

A Hand-held Device for Non-invasive Assessment of Beef Quality

by

Saranyu Shankar Samanta

A thesis submitted in partial fulfillment of the requirements for the degree of

Master of Science

in

Photonics and Plasmas

Department of Electrical and Computer Engineering  
University of Alberta

© Saranyu Shankar Samanta, 2014

## Abstract

Quantification of important biochemical (e.g. intramuscular fat content, toughness) properties of beef *m. longissimus thorasis* (LT) using technologies of optical spectroscopy and digital image analysis was examined in this thesis research. The main objective of this thesis work focused on the instrumentation of such technologies for industrial application. Effects of biochemical properties on optical spectroscopy and digital image analyzed results were investigated. Separate analyses with visible and near infrared light spectroscopy and image processing revealed the true potential of those technologies individually. Statistical analyses were performed to identify various correlations that are significant enough to quantify those biochemical properties effectively. Design and performance of a hand-held prototype device incorporating optical spectroscopy technology were tested to evaluate the possibilities of industrial application. Experimentation with hand-held device obtained equivalent results to that found by visible light spectroscopy using a commercial spectrophotometer. Visible light spectroscopy was significantly affected by various color components (e.g. L\*a\*b\*, RGB) of lean meat color in a multidimensional way. This affected the consistency and reliability of the quantification of biochemical properties of beef using visible light. However, near infrared light spectroscopy showed potential to be used as a possible method of quantification of various biochemical properties of beef. Partial least square analysis of near infrared spectroscopy data showed consistency with R<sup>2</sup> values between 0.65 to 0.80 to estimate intramuscular fat content and toughness of beef LT muscle. Addition of a polarizer increased the accuracy of beef toughness estimation by 20% using near infrared light. These results indicated that near infrared light spectroscopy has the potential to be utilized in a hand-held device for industrial application.

## **Acknowledgments**

First and foremost I would like to graciously thank my supervisor Prof. Abdul Y. Elezzabi and my co-supervisor Prof. Heather L. Bruce for their endless help and support over the course of this degree. Their endless encouragement, helpful criticism and precious guidelines helped me to develop as a researcher.

Secondly, I would like to thank Alberta Beef Producers, Alberta Innovates Bio Solutions, the Canadian Cattlemen's Association and the Alberta Livestock and Meat Agency Ltd for providing funding for this research.

I would like to thank my colleague and friend José Angel Puente Zamarripa for his help and support throughout the course of this research. I also thank all the members of the Bruce laboratory for providing helps and guidance on countless occasions. I would like to thank the laboratory personnel and scientists at Agriculture and Agri-Food Canada at the Lacombe Research Center and Agri-Food Discovery Place at the University of Alberta for their cooperation and support during many experiments during this research.

Thank you to the excellent academic and support staff of the Departments of Electrical and Computer Engineering department and Agricultural, Food and Nutritional Science. I would also like to thank and acknowledge the excellent work of Herbert Dexel, Reiner Schwarze, and Martin Riedner and for their support and cooperation in building the hand-held device and other parts. I would like specifically to thank Rick McGregor for helping me ordering various parts and guiding me in that regard.

Finally, I would like to thank my family and friends for their support, valuable guidance, encouragement and their prayers.

# Table of Contents

Abstract.....	ii
Acknowledgments.....	iii
List of Tables .....	ix
List of Figures.....	xiii
Chapter 1.....	1
Introduction.....	1
1.1 Motivation.....	1
1.2 Previous Research.....	2
1.3 Objectives.....	5
1.4 Thesis Structure.....	5
Chapter 2.....	8
Hand-held Device to Estimate Fat in Meat.....	8
2.1 Introduction.....	8
2.2 Theoretical Background.....	10
2.2.1 Spectroscopy.....	10
2.2.2 LED-Spectroscopy.....	11
2.2.3 Lock-In Amplifier.....	13
2.3 The Hand-held Device.....	14
2.3.1 Hardware Circuit Design.....	15
2.3.2 Software Design.....	30
2.4 Device Design Specifications.....	35
2.5 Future Improvements.....	36
2.6 Conclusion.....	37
Chapter 3.....	39
Development of an Intramuscular Fat Estimation Model for the Hand-held Device.....	39
3.1 Introduction.....	39
3.2 Materials and Methods.....	40
3.2.1 Experimental Samples.....	40
3.2.2 VIS Spectroscopy.....	41

3.2.3 NIR Spectroscopy.....	44
3.2.4 Hand-held Device Spectrometry .....	46
3.2.5 Experimental Setup.....	47
3.3 Data analysis: .....	54
3.4 Results: .....	57
3.4.1 Experiment on 12/11/10 .....	57
3.4.2 Experiment on 17/11/10 .....	61
3.4.3 Experiment on 25/11/10 .....	64
3.4.4 Experiment on 8/2/11 .....	68
3.4.5 Experiment on 6/4/11 .....	72
3.4.6 Experiment on 4/7/11 .....	73
3.4.7 Experiment on 20/7/11 .....	74
3.5 Discussion .....	75
3.5 Conclusion.....	75
Chapter 4.....	77
Spectroscopy on whole beef with known differences in intramuscular fat .....	77
4.1. Introduction .....	77
4.2 Materials and Methods.....	81
4.2.1 Materials .....	81
4.2.2 Experimental Setup and Measurements .....	85
4.2.3 Sample Preparation for Crude Fat Extraction.....	92
4.2.4 Crude Fat Extraction.....	93
4.3. Data Handling and Analysis.....	94
4.3.1 Digital Image Processing.....	94
4.3.2 VIS Spectroscopy .....	101
4.3.3 NIR Spectroscopy.....	103
4.3.4 LED-spectroscopy Using Hand-held Device .....	104
4.3.5 Statistical Analysis .....	104
4.4. Results .....	105
4.4.1 Color.....	105
4.4.2 Crude Fat and Image Processed Fat .....	107

4.4.3 Slope of Reflectivity .....	110
4.4.4 Correlation Coefficients .....	113
4.4.5 Spectroscopic Data Analysis Using PLS Method .....	115
4.5 Discussion .....	115
Chapter 5 .....	121
Modelling of Visible Light Reflectance and Surface Fat Content of Meat: A Paper Model Experiment.....	121
5.1 Introduction .....	121
5.2. Materials and Methods .....	126
5.2.1 Materials .....	126
5.2.2 Experimental Setup.....	129
5.2.3 Spectroscopic Measurement .....	131
5.2.4 Light Source Test Experiments .....	131
5.2.5 Data Analysis.....	132
5.2.6 Statistical Analysis .....	133
5.3. Results .....	134
5.3.1 Light Source Test Results.....	134
5.3.2 Spectroscopic Measurement Results .....	135
5.3.3 PLS Analysis Results.....	140
5.3.4 Analysis Results of Data Obtained from Meat Sample .....	141
5.4. Discussion .....	141
5.4.1 Light Source Test.....	146
5.4.2 Spectral Data Analyses .....	146
5.4.3 Analyses Using Data Obtained from Meat Sample.....	149
5.5. Conclusion.....	149
Chapter 6 .....	151
Comparison of NIR Prediction of Fat Content in Whole and Homogenize Beef.....	151
6.1 Introduction .....	151
6.2 Materials and Methods .....	153
6.2.1 Materials .....	153
6.2.2 Sample Preparation.....	156

6.2.3 Measurement on Whole Sample.....	157
6.2.4 Preparation of Ground Beef Samples.....	161
6.2.5 Measurements of Ground Beef Sample.....	162
6.2.6 Crude Fat Sample Preparation.....	162
6.2.7 Crude Fat Extraction.....	163
6.3. Data Analysis.....	163
6.3.1 Digital Image Processing.....	163
6.3.2 Spectroscopy.....	172
6.3.3 Statistical Analysis.....	173
6.4. Results.....	174
6.4.1 Color.....	174
6.4.2 Crude Fat and Image Processed Fat.....	174
6.4.3 Correlation Coefficients.....	175
6.4.4 VIS Spectroscopy.....	177
6.4.5 NIR Spectroscopy.....	179
6.5. Discussion.....	180
Chapter 7.....	187
Estimation of Beef Toughness Using NIR.....	187
7.1 Introduction.....	187
7.2 Materials and Methods.....	188
7.2.1 Experimental Design.....	188
7.2.2 Sample Preparation.....	189
7.2.3 NIR Spectroscopy.....	193
7.2.4 Experimental Setup.....	196
7.2.5 NIR Spectroscopic Measurement.....	196
7.2.6 Warner-Bratzler Shear Force (WBSF).....	196
7.3. Data and Statistical Analyses.....	197
7.3.1 NIR Spectroscopy.....	197
7.4 Results.....	199
7.5 Discussion.....	202
7.6 Conclusion.....	207

Chapter 8.....	208
Visible Light and Near-infrared Spectroscopy on Whole Beef Rib Eye Steaks.....	208
8.1 Introduction.....	208
8.2 Materials and Methods.....	208
8.2.1 Materials.....	208
8.2.2 Experimental Setup.....	210
8.2.3 Sample Preparation.....	212
8.2.4 Measurement on Whole Sample.....	212
8.2.5 Crude Fat Extraction.....	213
8.3 Data Analysis.....	214
8.3.1 Digital Image Processing.....	214
8.3.2 VIS and NIR Spectroscopy.....	214
8.4 Results.....	215
8.5 Discussion.....	219
8.6 Conclusion.....	222
Chapter 9.....	223
General Summary.....	223
Appendices.....	230
Appendix A: ATmega32 Program for Hand-held Device.....	230
Appendix B: Programs for VIS, NIR, and LED Spectroscopy.....	238
Appendix C: Programs for Image Processing and Spectrum Data Calculation.....	249
Appendix D: Programs to Calculate L*a*b* Value from Paper Model Sample Image.....	255
Appendix E: Programs for Image Processing.....	256
References.....	262

## List of Tables

Table 2.1: Pin diagram, logic levels and functions of each LCD pin. ....	30
Table 2.2: Connection configuration of keypad switches.....	34
Table 2.3: Voltage, current and power consumption values of analog and digital circuit. ....	36
Table 3.1: List of experimentation on the LED sensor unit of hand-held device.....	51
Table 3.2: R <sup>2</sup> values of linear regression between slope of reflectivity and number of fat pieces at wavelengths from 588.09 to 612.17 nm.....	60
Table 3.3: R <sup>2</sup> values of linear regression between slope of reflectivity and number of fat pieces at wavelengths from 588.09 to 605.05 nm.....	67
Table 3.4: R <sup>2</sup> values of linear regression between slope of reflectivity and number of fat pieces (big and small fat pieces) at wavelengths from 588.09 to 605.05 nm using smoothing coefficient of 51. ....	70
Table 3.5: R <sup>2</sup> values of linear regression between slope of reflectivity and number of fat pieces (big and small fat pieces) at wavelengths from 592.19 to 600.16 nm using smoothing coefficient of 151. ....	71
Table 3.6: R <sup>2</sup> values of linear regression between slope of reflectivity of LED-spectroscopy and number of fat pieces (big and small fat pieces) at LED wavelengths from 592 to 601 nm.....	71
Table 3.7: R <sup>2</sup> values of linear regression between slope of reflectivity and number of fat pieces at wavelengths from 592.19 to 600.16 nm using smoothing coefficient of 51.....	73
Table 3.8: R <sup>2</sup> values of linear regression between slope of reflectivity of LED-spectroscopy and number of fat pieces at LED wavelengths from 592 to 601 nm. ....	73
Table 3.9: R <sup>2</sup> values of linear regression between slope of reflectivity of LED-spectroscopy and number of fat pieces at LED wavelengths from 592 to 601 nm. ....	74
Table 4.1: Minimums (Min), maximums (Max), means, and standard deviations (SD) of L*, a*, b* color coordinate values of first and second block of beef rib eye samples.....	106

Table 4.2: Minimums (Min), maximums (Max), means, and standard deviations (SD) of L*, a*, b* color coordinate values of third and fourth block beef rib eye samples. ....	106
Table 4.3: Minimums (Min), maximums (Max), means, and standard deviations (SD) of L*, a*, b* color coordinate values of all beef rib eye samples. ....	106
Table 4.4: Minimums (Min), maximums (Max), means, and standard deviations (SD) of calculated fat using different methods for all beef rib eye samples. The crude fat was calculated for all (n=48) beef rib eye samples but image processed fat was calculated for only third and fourth block beef rib eye samples (n=24). ....	108
Table 4.5: Minimums (Min), Maximums (Max), Means, and standard deviations (SD) of calculated fat using different methods for all beef rib eye samples at different marbling grade. The crude fat was calculated for all (n=12 in each grade) beef rib eye samples but image processed fat was calculated for only third and fourth block beef rib eye samples (n=6 in each grade). ....	108
Table 4.6: Pearson Correlation coefficient (r) values among color, slope, and fat. ....	114
Table 4.7: Pearson Correlation probability (p) values among color, slope, and fat with highlighted in green for $p < 0.05$ . ....	114
Table 4.8: Effect of different data (NIR spectroscopy and crude fat) transformations (e.g. normalization, dark current subtraction, smoothing) on calibration and validation $R^2$ means and standard deviations using PLS method. ....	116
Table 4.9: Calibration and validation $R^2$ means and standard deviations of different spectroscopic analysis of beef rib eye samples using PLS method. ....	117
Table 5.1: Linear fit equations, R, G, B, L*, a*, b*, Y intercept, Slope of slopes at 595.05 nm for each different myoglobin color model. ....	137
Table 5.2: Linear fit equations, R, G, B, L*, a*, b*, Y intercept, and slope of reflectivity regression for each different color model. ....	140
Table 6.1: Minimums (Min), maximums (Max), means, and standard deviations (SD) of L*, a*, b* color component values of all beef samples (n=48). ....	174
Table 6.2: Means and standard deviations (SD) of fat detected chemically and with surface image processing for each Canada beef grade. ....	177

Table 6.3: Pearson Correlation coefficient (r) values among color, crude fat, and image processed fat. ....	178
Table 6.4: Pearson Correlation probability (p) values among color, crude fat, and image processed fat with correlations highlighted in green for $p < 0.05$ . ....	178
Table 6.5: Calibration and validation $R^2$ for VIS spectroscopic prediction of crude and image identified (WHOLE and CIRCLED) fat. ....	179
Table 6.6: Calibration and validation $R^2$ for NIR spectroscopic prediction of crude and image identified (WHOLE and CIRCLED) fat. ....	181
Table 7.1: various data sets calculated for PLS analysis. ....	199
Table 7.2: Minimum (Min), maximum (Max), Mean and standard deviation (SD) values of WBSF measured on after 3 days of storage of beef samples (processed on second slaughter date) with different treatments (n=5). ....	200
Table 7.3: Minimum (Min), maximum (Max), Mean and standard deviation (SD) values of WBSF measured on after 3 and 14 days of storage (ageing treatment) of beef samples (n=40). ....	200
Table 7.4: Calibration and validation regression coefficient ( $R^2$ ) values of various PLS analysis. ....	201
Table 8.1: Descriptive statistics of image detected and chemically extracted crude fat. ....	216
Table 8.2: Descriptive statistics (minimum (min), maximum (max), mean and standard deviation (SD)) of image and crude fat (%) within each grade category (n = 12 /grade). ....	216
Table 8.3: Descriptive statistics for $L^*$ , $a^*$ and $b^*$ color coordinate values. ....	216
Table 8.4: Pearson Correlation coefficient (r) values among color and percentage fat (crude fat and image processed fat). ....	217
Table 8.5: Pearson Correlation probability (p) values among color and percentage fat (crude fat and image processed fat) with correlations highlighted in green for $p < 0.05$ . ....	218

Table 8.6: Mean calibration and validation  $R^2$  values with standard deviations (in parentheses) for prediction of image processed and chemically extracted crude fat for VIS and NIR reflectance. .... 218

## List of Figures

Figure 2.1: Spectrum of a 592 nm LED (Super Bright LEDs Inc. St. Louis Missouri, USA) (maximum intensity at 592 nm) used in the device. ....	13
Figure 2.2: Device block diagram.....	14
Figure 2.3: Side view, top view and bottom view (from left to right) of the handheld device.....	16
Figure 2.4: Complete PCB and design of the sensor unit. Left image is showing the bottom side and right image is showing the top side of the sensor unit. ....	17
Figure 2.5: Servo motor control signal (frequency 61.04 Hz) with maximum pulse width (upper) and minimum pulse width (lower). ....	18
Figure 2.6: Circuit schematic of analog circuit.....	22
Figure 2.7: Complete PCB of analog circuit.....	23
Figure 2.8: Reference signal for LIA generated by MCU before filter capacitor. ....	23
Figure 2.9: Reference signal for LIA after filter capacitor. ....	24
Figure 2.10: LIA output signal after the second stage low pass filter with transition between two different LEDs (upper) and magnified transition portion (lower). ....	24
Figure 2.11: Complete PCB of digital circuit. ....	26
Figure 2.12: Circuit schematic of digital circuit. ....	27
Figure 2.13: Modulated signal for LED before ULN2003 (upper) and one magnified LED ‘ON’ to ‘OFF’ transition. ....	28
Figure 2.14: USBasp programmer for ATmega32 MCU.....	31
Figure 3.1: A general procedure used in the experiments for Preparation of the sample. Top: unpacked steak bought from local store, bottom left: cork borer used on the inter-muscular fat of the steak to cut fat pieces, and bottom right: pieces of fat cut from inter-muscular fat of the beef steak. ....	41

Figure 3.2: Halogen light source (OceanOptics HL-2000 Tungsten Halogen Light Source) (left image) and its spectrum with wavelength (nm) on x-axis and power ( $\mu\text{W}/\text{cm}^2/\text{nm}$ ) on y-axis (Ocean Optics, Dunedin, Florida, USA) (right image).....	42
Figure 3.3: (a) Ocean Optics USB4000 Spectrometer, (b) Ocean Optics R600-7-VIS-125F bifurcated fiber optic cable, and (c) black mask cover. ....	43
Figure 3.4: Front view (left) and side view (right) of the custom stand to hold the fiber optic stainless steel probe.....	44
Figure 3.5: Yokogawa AQ6370C Optical Spectrum Analyzer. ....	45
Figure 3.6: Left: SMA to FC custom adapter, middle: SMA to FC adapter attached to optical fiber cable, and right: optical fiber cable is connected to AQ6370C using the SMA to FC adapter. ....	46
Figure 3.7: Design and development cycle of the device. ....	47
Figure 3.8: Meat Sample with sequential increment of fat pieces for spectroscopic measurements. From one pieces of fat (top left) to five pieces of fat (bottom right) and the sample was placed under the black mask cover to exclude entire surface regions on the measurement surface except the area that was intended to be measured.....	48
Figure 3.9: Spectroscopic measurements using VIS light spectrometer were taken in a dark room. The left image is showing a measurement is being taken in a dark room, and the right image is showing the VIS light illuminated sample with two pieces of fat on the measurement surface ..	49
Figure 3.10: The side view (left) and the front view (right) of the hand-held device attached to a stand placed over the sample with the black mask for measurements using hand-held device....	50
Figure 3.11: The hand-held device with fixed base LED sensor unit is being used to take measurements. Illumination of the sample measurement surface using three different LEDs of non-rotating sensor unit is presented in the figures from left to right. ....	50
Figure 3.12: Plot of the reflectivity as a function of wavelength for up to 20 fat pieces with a smoothing coefficient of 51. The legends Rf 0 – Rf 20 represents reflectivity plots at 0 to 20 fat pieces.....	58

Figure 3.13: Magnified plot of the reflectivity as a function of wavelength for up to five fat pieces at wavelengths from 550 to 650 nm with a smoothing coefficient of 51. The legends Rf 0 – Rf 5 represents reflectivity plots at 0 to 5 fat pieces..... 58

Figure 3.14: Plot of the slop of reflectivity as a function of wavelength for up to five fat pieces with a smoothing coefficient of 51. The legends m 0 – m 5 represents slope of reflectivity plots at 0 to 5 fat pieces. .... 59

Figure 3.15: Magnified plot of the slop of reflectivity as a function of wavelength for up to five fat pieces at wavelengths from 585 to 615 nm with a smoothing coefficient of 51. The legends m 0 – m 5 represents slope of reflectivity plots at 0 to 5 fat pieces..... 59

Figure 3.16: Slope of reflectivity as a function of number of fat pieces at 595.05 nm (spectrometer wavelength)..... 60

Figure 3.17: Slope of reflectivity as a function of number of fat pieces (20 pieces) at 595.05 nm. .... 61

Figure 3.18: Light intensities of 588, 593, and 605 nm LED as a function of wavelength plot... 62

Figure 3.19: Normalized intensities of 588, 593, and 605 nm LED as a function of wavelength plot. .... 62

Figure 3.20: The plot of the simulated reflectivity as a function of LED wavelength for up to five fat pieces. The legends Rf 0 – Rf 5 represents simulated reflectivity plots at 0 to 5 fat pieces.... 63

Figure 3.21: Slope of simulated reflectivity as a function of number of fat pieces at 588 nm (LED wavelength)..... 63

Figure 3.22: Slope of simulated reflectivity as a function of number of fat pieces at 593 nm (LED wavelength)..... 64

Figure 3.23: Plot of the reflectivity as a function of wavelength for up to five fat pieces with a smoothing coefficient of 51. The legends Rf 0 – Rf 5 represents reflectivity plots at 0 to 5 fat pieces..... 65

Figure 3.24: Magnified plot of the reflectivity as a function of wavelength for up to five fat pieces at wavelengths from 550 to 650 nm with a smoothing coefficient of 51. The legends Rf 0 – Rf 5 represents reflectivity plots at 0 to 5 fat pieces..... 65

Figure 3.25: Plot of the slop of reflectivity as a function of wavelength for up to five fat pieces with a smoothing coefficient of 51. The legends m 0 – m 5 represents slope of reflectivity plots at 0 to 5 fat pieces. .... 66

Figure 3.26: Magnified plot of the slop of reflectivity as a function of wavelength for up to five fat pieces at wavelengths from 585 to 615 nm with a smoothing coefficient of 51. The legends m 0 – m 5 represents slope of reflectivity plots at 0 to 5 fat pieces. .... 66

Figure 3.27: Slope of reflectivity of LED-spectroscopy as a function of number of fat pieces at 588 nm (LED wavelength as specified by manufacturer). .... 67

Figure 3.28: Slope of reflectivity of LED-spectroscopy as a function of number of fat pieces at 593 nm (LED wavelength as specified by manufacturer). .... 67

Figure 3.29: Plot of the slop of reflectivity as a function of wavelength for up to six big fat pieces with a smoothing coefficient of 51. The legends m 0 – m 6 represents slope of reflectivity plots at 0 to 6 fat pieces. .... 69

Figure 3.30: Plot of the slop of reflectivity as a function of wavelength for up to eight small fat pieces with a smoothing coefficient of 51. The legends m 0 – m 8 represents slope of reflectivity plots at 0 to 8 fat pieces. .... 69

Figure 3.31: Plot of the slop of reflectivity as a function of wavelength for up to six big fat pieces with a smoothing coefficient of 151. The legends m 0 – m 6 represents slope of reflectivity plots at 0 to 6 fat pieces. .... 70

Figure 3.32: Plot of the slop of reflectivity as a function of wavelength for up to eight small fat pieces with a smoothing coefficient of 151. The legends m 0 – m 8 represents slope of reflectivity plots at 0 to 8 fat pieces. .... 71

Figure 3.33: Plot of the slop of reflectivity as a function of wavelength for up to nine fat pieces with a smoothing coefficient of 51. The legends m 0 – m 9 represents slope of reflectivity plots at 0 to 9 fat pieces. .... 72

Figure 3.34: Magnified plot of the slop of reflectivity as a function of wavelength for up to nine fat pieces at wavelengths from 585 to 615 nm with a smoothing coefficient of 51. The legends m 0 – m 9 represents slope of reflectivity plots at 0 to 9 fat pieces. .... 72

Figure 3.35: NIR reflectance spectra from 1100 to 1500 nm for up to ten fat pieces. The legends Int 0 – Int 10 represents intensity plots at 0 to 10 fat pieces. .... 74

Figure 4.1: Meat surface with uneven meat marbling. ....	79
Figure 4.2: Beef rib-eye (a) one rib-eye steak, (b) whole rib-eye section. ....	80
Figure 4.3: Rib section detailing locations of experimental steaks. ....	82
Figure 4.4: (a) Chroma Meter CR-400, (b) CR-A43 Calibration Plate .....	83
Figure 4.5: (a) polarizer, (b) custom made connector to hold polarizer, and (c) the connector is connected to the collection fiber of the optical fiber. ....	85
Figure 4.6: Sample labeling scheme (left), and whole rib eye steak with three specific locations of measurements (right). ....	89
Figure 4.7: A sample image recorded by a digital camera (Logitech webcam C905). ....	91
Figure 4.8: (a) Scanned digital image of a typical sample, (b) cropped digital image at location one (Figure 4.6) of the same sample. ....	92
Figure 4.9: Cropped image region of a sample (sample ID: 143YS1). ....	95
Figure 4.10: RGB values of different pixels of the cropped sample image (sample ID: 143YS1), (a) selected pixel inside lean muscle region, (b) selected pixel correspond to the lean muscle and located at the boundary of lean muscle and fat region, (c) selected pixel correspond to the fat region, (d) selected pixel correspond to the lean muscle region, (e) selected pixel correspond to the fat region. ....	99
Figure 4.11: (a) Original cropped image of the sample (sample ID: 143YS1); (b) identification of the fat and lean muscle regions of the cropped image, the identified fat regions were marked with black and lean muscle were kept unchanged. ....	100
Figure 4.12: (a) Scatter plot of crude fat and image processed fat (SMALL), (b) Scatter plot of crude fat and image processed fat (SMALL). ....	109
Figure 4.13: Plots of slope of reflectivity at 595 nm and percentage fat measured using different methods and different instruments from samples of the third and fourth block, (a) plots of slope of reflectivity at 595.05 nm wavelength of VIS spectroscopy using spectrometer with crude fat, (b) plots of slope of reflectivity at 595.05 nm wavelength of VIS spectroscopy using spectrometer with image processed fat (SMALL), (c) plots of slope of reflectivity at 595.05 nm	

wavelength of VIS spectroscopy using spectrometer with image processed fat (LARGE), (d) plots of slope of reflectivity at 595 nm wavelength of LED spectroscopy using handheld device with crude fat, (e) plots of slope of reflectivity at 595 nm wavelength of LED spectroscopy using handheld device with image processed fat (SMALL), (f) plots of slope of reflectivity at 595 nm wavelength of LED spectroscopy using handheld device with image processed fat (LARGE). 113

Figure 5.1: Inter reactions among three major myoglobin states and associated color of the states. .... 121

Figure 5.2: Digital JPEG image taken by (a) Logitech camera (webcam C905), and (b) EPSON PerfectionV33 flatbed scanner. .... 126

Figure 5.3: Eight different color circles used for the paper model experiment with white small circles simulating the surface fat or marbling on the beef. .... 127

Figure 5.4: Different marbling grades and increments in surface fat content are modeled by varying the number and pattern of small white circles for testing of fat quantification, detection of uniformity and consistency of light source. .... 128

Figure 5.5: Two paper model where (a) modeled metmyoglobin color and (b) modeled oxymyoglobin color with white small circles representing the intramuscular fat in lean meat. 128

Figure 5.6: (a) The fiber optic probe is attached to a standard laboratory stand using a custom made height adjustment holder with light source, white cutting board and black mask attaché to table with tape. This experimental setup was used for VIS spectroscopic measurements, (b) measurement area on sample (beef rib eye steak or paper model) with black mask cover and white fat pieces (white small circles for paper model) in the measurement area. .... 130

Figure 5.7: Reflectivity plots of five samples with same amount of model fat and same color tone (model myoglobin color tone of CL1) but different positioned fat pieces with smoothing coefficient of 91. .... 135

Figure 5.8: Reflectivity as a function of wavelength plot for varying number of fat pieces (small white circles) from 0 to 23 on the same color tone (CL1) samples with smoothing coefficient 51. .... 136

Figure 5.9: Slope of reflectivity at 595.05 nm as a function of the percentage of modeled fat (percentage small white circle area) from color tone CL1 samples. .... 136

Figure 5.10: Slope of reflectivity (at 595.05 nm) as a function of percentage of fat for different background color tones (modeled as myoglobin color).....	137
Figure 5.11: Reflectivity at 525.12 nm wavelength as a function of percentage of modeled fat (percentage white dot area) from color tone SCL1 samples.....	138
Figure 5.12: Reflectivity (at 525.12 nm) as a function of percentage of fat of different background color tone (modeled as myoglobin color). .....	139
Figure 5.13: X-variance and Y-variance explained by each PLS calculated factor in the PLS descriptive model (Blue: Calibration, Red: Validation). (a) X-variance and Y-variance explained by Factor 2 and Factor 1 with their scores in the scatter plot, (b) X-variance and Y-variance explained by Factor 3 and Factor 1 with their scores in the scatter plot, and (c) X-variance and Y-variance explained by Factor 4 and Factor 1 with their scores in the scatter plot. ....	144
Figure 5.14: Y-variance explained by four factors using four wavelength model predicting percentage of visible fat. ....	145
Figure 5.15: Relationships between slope of reflectivity at 595.05 nm and the number of fat pieces added to the surface of three beef rib steaks of experiments performed on 12/11/10, 25/11/10, and 6/4/11. ....	145
Figure 6.1: (a) Satco S4750-125 watt infrared heating lamp, (b) Medium Base Socket–PLT 243201, (c) Infrared heating lamp with cover and heat protection.....	155
Figure 6.2: (a) FGL850S – 5.08 cm square RG 850 colored glass filter, (b) Transmission characteristics graph of FGL850S filter.....	156
Figure 6.3: (a) Modified sample (rectangular portion of <i>longissimus</i> muscle removed from the whole rib eye steak), and (b) Whole rib eye steak.....	157
Figure 6.4: (a) Experimental setup with VIS light source, fiber optic cable, optical probe, and (b) cardboard partition to prevent light from computer and NIR spectrometer screens.....	158
Figure 6.5: The fiber optic probe is attached to a standard laboratory stand using a custom made height adjustment holder with the NIR light source, white cutting board and black mask attached to table with tape. This experimental setup was used for NIR spectroscopic measurements.....	160
Figure 6.6: (a) Original scanned digital image (unmarked) of a sample (sample ID: 111YG), and (b) marking was done on a separate copy of the same digital image of the same sample.....	161

Figure 6.7: Petri Dish filled with ground meat. .... 161

Figure 6.8: (a) A beef Sample (sample ID: 132YG) image just after scanning and resolution reduction, and (b) a portion of the same scanned image that was cropped using MATLAB™ program for image processing purposes. .... 164

Figure 6.9: A beef sample image with identified reference boundary and marked with green color using MATLAB™ image processing program..... 165

Figure 6.10: (a) The ROI boundary pixels were isolated as white pixels by transforming the sample image of Figure 6.9 into B/W image, and (b) the ROI was filled with white pixels using “imfill” function..... 165

Figure 6.11: Isolated ROI of original image. .... 166

Figure 6.12: Identification of the fat and lean muscle regions of ROI of the original beef sample image. (a) Identified Fat regions (marked with green), and (b) identified lean muscle regions (marked with blue). .... 167

Figure 6.13: RGB values of different pixels of the sample, (a) selected pixel outside sample boundary, (b) selected pixel correspond to the sample and located at the brighter boundary of sample surface, (c) selected pixel outside sample boundary, (d) selected pixel correspond to the sample and located at the darker boundary of sample surface..... 168

Figure 6.14: Identification of the entire sample surface, (a) cropped image of the original sample, (b) Identified sample surface (marked with white), and (c) Isolated sample surface from the original cropped image. .... 171

Figure 6.15: Identification of the fat and lean muscle region over entire sample surface, (a) Identified fat regions (marked with green), (b) Identified lean muscle regions (marked with blue). .... 171

Figure 6.16: Relationships between percentage crude fat as predicted using WHOLE and CIRCLED images and crude fat then extracted chemically. (a) Crude fat and image processed fat (WHOLE), (b) crude fat and image processed fat (CIRCLED), and (c) crude fat measured in the current experiment and crude fat measured from first rib eye measured during experiment reported in Chapter 4. .... 176

Figure 7.1: Split-Split-Plot experimental design to achieve sufficient variation of beef tenderness to obtain a robust statistical model for tenderness estimation using NIR spectroscopy. .... 189

Figure 7.2: Electrical Stimulation of beef carcass; (a) a beef carcass, hanged from the roof rails was connected to the electrodes of the electrical stimulator; (b) electrical stimulator control panel to set the voltage and current that was conducted through the beef carcass. .... 190

Figure 7.3: Image of the carcass pasteurization unit; (a) front view; (b) side view. .... 191

Figure 7.4: Hot and cold gel-packs on the carcass surface; (a) hot gel-packs; (b) cold gel-packs. .... 192

Figure 7.5: Distribution of rib eye steaks for different measurements. .... 193

Figure 7.6: (a) Polarizer holder adapter assembly; (b) Front view of unassembled small and large cylinder; (b) Back view of unassembled small and large cylinder; (c) Polarizer holder adapter assembly attached to the fiber optic probe. .... 195

Figure 8.1: Images are illustrating the experimental setup with light source, fiber optic cable, optical probe and card board partition; (a) experimental setup in normal room light; (b) close up of experimental setup in normal room light; (c) experimental setup in dark room with light source on; (d) close up of experimental setup in dark room with light source on. .... 211

Figure 8.2 (a) Digital image of a sample (sample ID: 843N); (b) Marked digital image of the same sample. .... 213

Figure 8.3: Linear relationship between image processed fat (CIRCLED) and crude fat percentages. .... 217

# Chapter 1

## Introduction

### 1.1 Motivation

Meat is a very common and valuable nutritious food commodity in our daily life. It is also more expensive than other food products because meat protein is costly to produce and is highly valued for its unique taste and texture. Meat consists of fat, protein, water, minerals and vitamins. The various chemical compositions in meat are also used to describe the eating qualities of meat. The Canadian beef grading system is a good example of this because the value of carcasses is determined by the amount of fat in the meat (Canadian Beef Grading Agency, [www.beefgradingagency.ca](http://www.beefgradingagency.ca)). The chemical compositions in meat are greatly influenced by different animal and carcass factors. Pre-slaughter factors such as breed, sex and age affect fat content while post-mortem factors such as carcass storage time and temperature affect protein functionality and the availability of protein nutritionally (Andres et al., 2007; Lawrie, 1985; Venel et al., 2001). Meat consumers are very concerned about the various quality characteristics of meat product because they affect the flavor and sensory acceptability and perceived healthfulness of meat (Dransfield, 1994; Leroy et al., 2003). Meat is usually cooked at home but is also available in the market already cooked and ready to eat (Prieto et al., 2009) as high valued ready-to-eat commercially available processed meat products (Downey and Beauchene, 1997). Hence, it is important and necessary to provide guarantee that the meat consumer will receive the appropriate quality for which they are paying. Various quality control measures should be implemented to ensure that the consumer obtains the appropriate quality of meat according to their preference (Prieto et al., 2009).

There are various methods that can be implemented to ensure satisfactory meat quality description. Chemical analysis, sensory analysis and screening methods are unsuitable because they are destructive to the sample and too time consuming for industrial online meat processing environments (Liu et al., 2004). Ideally, a method that is suitable for industrial meat processing environments should be non-destructive and should require little time to measure the characteristics that are indicative of eating quality. In this quest for ideal meat quality assessment technique, many researchers have proposed spectroscopic analysis. The optical and spectroscopic analysis of meat quality has been widely chosen as the best method for the replacement of conventional techniques. Spectrometric and optical analysis is non-invasive, non-destructive and less time consuming than other techniques. Also these techniques can be utilized for simultaneous assessment of different meat qualities (Osborne et al., 1993).

## **1.2 Previous Research**

Many studies have examined different light wavelengths to find correlations between meat properties and reflected light intensity. Light wavelengths in the visible (VIS) and near-infrared (NIR) region (400 nm to 700 nm and 700 nm to 2500 nm, respectively) have been of particular interest. Pearson correlation ( $r$ ) values between NIR measurement data and Warner-Bratzler shear force (WBSF) values greater than 0.8 have been obtained (Mitsumoto et al., 1991; Park et al. 1998a). As a result, the study of NIR spectroscopic analysis has been the subject of many recent papers and the use of NIR for estimation of various different characteristics of ground meat including moisture, protein, fat and collagen content has been commercialized (FoodScan<sup>TM</sup> Meat Analyzer, FOSS, Hillerød, Denmark). Prieto et al. (2009) indicated that NIR

spectroscopy was very effective at quantitative measurement of the important meat constituents (moisture, protein and fat) and this technology was reviewed by Prevolnik et al. (2004).

The use of VIS region (400 nm to 700 nm) also indicates correlations between intramuscular fat and certain wavelength regions (Swatland, 1989). In fact, the combination of VIS and NIR together has strengthened many correlations between light and meat quality characteristics (Swatland, 1988), suggesting either complementary or additive relationships exist in the two light regions. For this reason, the VIS wavelength range should be included in subsequent studies involving light spectroscopy and meat quality characteristics.

Among meat quality characteristics, meat tenderness is an essential factor and plays an important role in determining eating quality. Since the 1930's, Warner-Bratzler shear force (WBSF) has been used to measure the toughness of meat (Bratzler, 1958) but it is a time consuming and destructive method. For the WBSF method, a meat sample is cut from a carcass, cooked and is used to measure toughness. This leads to wastage of valuable and quality meat products. Different methods have been tested to measure meat toughness but have not proven as promising in accuracy as WBSF (Voisey, 1976). As a result, the development of non-invasive and non-destructive methods of assessing meat toughness has been difficult.

The BeefCam System, which is a video imaging analysis system (Vote et al., 2003; Wyle et al., 2003), used color to quantify beef eating quality; however, the BeefCam System has not been completely successful in measuring and categorizing beef by tenderness (Wyle et al., 2003). Vote et al. (2003) found that 36% of the meat classified as tender was actually very tough. Predicting tenderness has been shown to be more accurate with a colorimeter than a prototype BeefCam (Wheeler et al., 2002). According to the study of Wulf and Page (2000), color can be

used to describe 15 to 23% of the variation in beef eating quality, indicating that although related to beef tenderness, color is not completely appropriate for measuring meat quality.

Meat toughness is greatly influenced by the connective tissue and myofibrillar proteins (Maltin et al., 2003; Wheeler et al., 2000) and these tissue structures are responsible for optical scattering of meat (Xia et al., 2007). Light scattering could be a way to estimate beef toughness (Hildrum et al., 1994). Scattering coefficients appear to provide better estimation of toughness than absorption coefficient when compared to WBSF (Xia et al., 2007). In the studies of Xia et al. (2007), they observed correlation between scattering coefficients and WBSF at 721 nm with a  $R^2$  value 0.59 and the coefficient of determination improved to 0.67 using 19 *longissimus dorsi* muscles. They found similar results at other wavelengths from 650 nm to 850 nm.

Despite achieving modest correlation values between VIS-NIR and meat tenderness, VIS-NIR wavelengths still hold promise for measuring and estimating WBSF of cooked beef. In VIS-NIR, the 2<sup>nd</sup> derivative of the absorbance data had a better prediction equation with a  $r$  value between 0.80 to 0.86 and a  $R^2$  value between 0.64 to 0.74 (Yancey et al., 2010). In the estimation of toughness, it has been reported in many reviews that VIS-NIR technique is much more accurate than WBSF (Yancey et al., 2010). In addition, it may be possible that a VIS-NIR technique could estimate the changes in protein functionality and moisture in meat simultaneously (Yancey et al., 2010).

The increased sensitivity of VIS-NIR in the estimation of beef toughness compared to that of WBSF was also shown in the study of Rosenvold et al. (2009). These authors found a  $R^2$  value of 0.58 between VIS-NIR (400 nm -1700 nm) and WBSF values. The possible reason for a lower  $R^2$  than other studies indicated that WBSF measurement was less sensitive than the VIS-NIR measurement (Rosenvold et al., 2009). In the case of very tough beef, VIS-NIR underestimated

the toughness (Rosenvold et al., 2009). Xia et al. (2007) found that optical scattering was related to meat structural properties at VIS-NIR wavelengths ranging from 450 nm to 950 nm. However, they predicted WBSF using scattering coefficients with an  $R^2$  value ( $R^2 = 0.59$ ) similar to that of Rosenvold et al. (2009). In other research,  $R^2$  values between WBSF values and VIS-NIR values ranged from 0.18 to 0.72 and varied with the number of days post mortem (Liu et al., 2003).

### **1.3 Objectives**

Further investigation of the relationship between VIS-NIR wavelengths and meat quality characteristics was the primary objective. Therefore, a series of experiments with meat samples were required. These experiments would help to establish algorithms and obtain equations to describe and predict various meat quality characteristics. In addition, investigation of commercialization potential of this technology was the final objective of this study. Hence, design and construction of a handheld meat quality measurement device based on this technology was essential. The objective of this device construction was to deliver this technology effectively to the meat industry. Finally, the hypothesis of this study was that VIS-NIR spectroscopy can predict percentage of fat content and WBSF values in beef.

### **1.4 Thesis Structure**

The purpose of this thesis was to provide information regarding the experiments that were conducted during the course of this study. These experiments helped justify the validity of the hypothesis of this study. This thesis is organized in nine chapters including an introduction in Chapter 1 and a general summary in Chapter 9.

In Chapter 2, the design and construction of a prototype hand held device to measure fat content in beef using VIS spectroscopy is presented. The important objectives and challenges in

the design of such device were highlighted. Possible solutions to overcome the design challenges and meet the design objectives were described. Finally, scopes of future improvements of the prototype were discussed.

In Chapter 3, the development of a fat estimation model for the hand held device was investigated. Information regarding experimentation with VIS light, meat sample characteristics and the results obtained after each experiment, are explained. A fat estimation mathematical model was identified during the first couple of experiments. These experiments were conducted before the construction of the handheld device. Further experiments were conducted to investigate the potential of the mathematical model in the design of the handheld device. This chapter also describes various improvements on the design of the device at different stages to improve the performance of the device.

In Chapter 4, the mathematical model developed in Chapter 3 and used in the handheld device performance was tested. The results from the experiments indicated that the mathematical model was unable to predict fat contents in the beef samples. Here, NIR spectroscopy data and digital image data were also collected during the experiments. Finally, the results of statistical analysis on the collected data using partial least square technique were discussed.

In Chapter 5, the failure of the mathematical model was investigated. An artificial color model (paper model) experiment was conducted to investigate the hypothesis that color affected the accuracy of the mathematical model. An important aspect regarding prediction of fat using VIS spectroscopy was discovered. In addition to that some important facts about the experimental setup were noticed and assessed to improve the experimental setup in future similar experiments. The results, found in the model experiment were also validated by performing data analysis on data collected from real meat samples.

In Chapter 6, a comparison of prediction of fat content in whole and homogenized meat using optical spectroscopy was presented. The main purpose of this chapter was to validate the experimental setup used in all the previous experiment explained in previous chapters. This validation was conducted by comparing the forecasted accuracy of NIR spectroscopy to the predicted fat content in homogenized meat with results found by other researcher.

In Chapter 7, the viability of NIR spectroscopy to predict beef toughness was investigated. In addition to that, this chapter investigates the potential use polarization optics to improve prediction accuracy.

In Chapter 8, a similar experiment that of the previous experiment in Chapter 4 was described. However, there were some minor improvements in the experimental setup. The purpose of this experiment was to compare and validate the results with previous results that were presented in Chapter 4.

## **Chapter 2**

### **Hand-held Device to Estimate Fat in Meat**

#### **2.1 Introduction**

Beef industries in Canada are looking for effective solutions to achieve their goal of full instrument assessment of quality grades in fast, cost effective and non-invasive way (Canadian Beef Grading Agency, personal communication). A key criterion for any solution is that it must be suitable for the industrial meat processing environment. Determination of fat content in meat is an important aspect of meat grading system. In the past, certified human graders used a visual inspection technique, in conjunction with a predetermined grading scale, to grade meat by estimating the amount of visible fat on the meat surface (also known as ‘meat marbling’). This method was adequate until recently, when it was realized an instrument assessment of meat marbling must be standardized to ensure that the grading process is immune to human error. Various digital image processing technologies (e.g. CVS BeefCam<sup>®</sup> or e+v<sup>®</sup> model VBG 2000) were implemented to assess the amount of surface marbling. These technologies require an adequate amount of computing power to process the high resolution digital images. Clearly, affordability of such expensive equipment and software technologies was out of question for the small production lines of provincial abattoirs. The beef industries in Canada are desperately looking for a cost effective solution to develop a grading assessment system, which would be easier to operate and possesses similar or better accuracy than the digital image processing technologies (Canadian Beef Grading Agency, personal communication). The efficiency in terms of energy saving and reduced work space would be an asset.

Previous experimentation using visible light spectroscopy proved to be very effective in estimating meat marbling. A visible light spectroscopy fat estimation mathematical model,

developed through past experiments, was sufficiently promising to be incorporated in a hand-held device. However, developing a hand-held device posed several design challenges to meet the required objectives successfully. To operate in the visible spectrum, the device must have bright light sources at certain wavelengths and optical sensor(s) to measure reflected intensity at those specified wavelengths. The source light and the collected light must also be focused at a fixed region on the measurement surface at each wavelength. The size of the device is very important as it must have adequate space to accommodate all the sensing and electronic components within which to work effectively. Furthermore, the device must be agile, light weight, robust, and small enough to work as an effective hand-held device. A key challenge in designing a light sensitive device is the “dark noise” or “dark current”. This artefact light signal is due to ambient stray light and electrical noise generated by various electronic components (e.g. reverse biased leakage current from transistors and diodes). As such, designing an efficient filter to discriminate against such unwanted artefact signals, is a key factor to the accuracy in the performance of the hand-held device. To estimate the amount of fat on meat, a mathematical model must be developed and incorporated within a built-in microprocessor. This model utilizes the raw data, collected from instrument's sensor system, to calculate certain instrument variables (e.g. reflectivity of the measurement surface at specific wavelength and estimate amount of fat content on the measurement surface). The instrument should also incorporate a computing system powerful enough to compute the mathematical model and process the sensor data to estimate amount of fat content. Furthermore, the hand-held device has to be energy efficient to be operated using on board battery power. Finally, the device has to be properly calibrated, according to Canada grading guidelines, for marbling estimation. Proper calibration of the device and implementation of the calibration model into the device is yet another important design

aspect for the optimum performance and accuracy of the device operation.

The important objectives of the device design are to have a bright light source and to be able to collect the reflected light at specific wavelength. The collected light has to be in the form of an analog electrical signal. The device must incorporate an efficient and effective analog filter to remove optical and unwanted electrical noise. The electrical signal might need to be amplified at different stages of the electrical circuit. The signal has to be converted to digital signal to be processed by an onboard microprocessor. This microprocessor must be powerful enough to compute the fat estimation mathematical model using reflected light intensity data. Finally, the hand-held device has to display the results to be read by the operator. The overall design objective of the device should be accomplished in an energy efficient manner; as such, the device must be battery powered.

## **2.2 Theoretical Background**

### **2.2.1 Spectroscopy**

Spectroscopy is a study of electromagnetic radiation (EMR) in which EMR is dispersed into its wavelengths components. Spectroscopy is often used to understand interactions of light with matter by analyzing the light frequencies, reflected, transmitted, absorbed, or amplified by the material. Spectroscopy had been widely used as a non-invasive method to study physical and chemical properties of matter.

The entire wavelength range of EMR is known as the electromagnetic spectrum. The human eye can detect the wavelength range from 400 nm to 700 nm of EMR. That is why it is referred to as the visible spectrum (VIS). The 700 nm to 2500 nm range is referred to as the near-infrared spectrum (NIR), and is not visible to the human eye. Certain EMR spectra are absorbed by matter if it is placed in the path of EMR. Emission spectrometers are used to study the EMR

spectrum that is emitted from a source object and an absorption spectrometer is used to study EMR spectrum that is reflected back from or transmitted through an object. A spectrometer segregates an EMR spectrum into its wavelength components and quantifies the number of photons presence in each wavelength using a charge-coupled device (CCD) or a similar optical sensor. The intensity of any EMR is proportional to the number of photon it carries (photon flux).

In this investigation, reflectance or reflected intensity spectral analysis was performed by converting the raw intensity from the spectrometer into normalized intensity (reflectivity). The normalization was done by dividing the detected reflectance by a reference reflectance, which was recorded from a uniformly reflective calibration standard. In this study both VIS and NIR spectrometers were used to analyze reflectance spectrum. The VIS and NIR spectra were analyzed to deduce any relationship that may exist between intensities at various wavelengths and to search for either biochemical or structural properties of beef muscle and intramuscular fat. Detailed description of the spectrometers and experimental setup used in this study can be found in subsequent chapters.

### **2.2.2 LED-Spectroscopy**

In light emitting diode (LED) spectroscopy, an LED of a specific wavelength is used to measure light intensity of a specific wavelength. A typical LED spectrum is in the form of a normal light intensity distribution curve or a Gaussian distribution curve. As a consequence, a specific peak wavelength [ $\lambda$  (nm)] LED light spectra contains light from wavelength ( $\lambda+x$ ) nm to wavelength ( $\lambda-x$ ) nm where  $x$  is the range of the LED spectra on the wavelength axis with maximum peak intensity at  $\lambda$  nm. A representative LED spectrum is shown in Figure 2.1.

In this study, LED spectroscopy was used for the sensor system of the hand-held device. In the spectrometric sensor design, the advantages of LED based spectroscopy have already been discussed in the literature (Degner et al., 2012). An LED based sensor may not be as good as a high-resolution spectrometer instrument; however, in many cases, LED spectroscopy performs well for fast online measurement (Degner et al., 2010). Degner et al. (2010) employed LED-based spectroscopy using standard LEDs to design chemical sensors for application in harsh environments (e.g. exhaust system of an automobile). It was realized that this type of sensor design was low cost, required a small footprint, had a long life and was well suited to many applications from small battery powered hand-held devices to industrial process control implementation (Degner et al., 2010). In most optical spectroscopy applications, the spectral absorption band for a particular substance is used to identify the chemical and structural properties of the material. However, in this study the reflectivity property of substance was utilized to formulate a fat estimation mathematical model.

Reflectivity is defined as a fraction of the incident EMR that is reflected by a surface. Reflectivity can be described as the ratio between the reflected light intensity and the incident light intensity integrated over all solid angles:

$$\text{Reflectivity} = \frac{\text{Reflected light intensity}}{\text{Incident light intensity}} \quad (2.1)$$

Reflectivity is known as a property of matter and the device was designed to measure the reflectivity of the meat samples. To make the device feasible, a reference reflectivity must be established. Here, a white Teflon<sup>TM</sup> (DuPont, USA) sheet of high uniform reflectivity was used to calculate the incite reflectivity. As such, all the measured reflectivity data collected in this work used this as a reflectivity baseline.

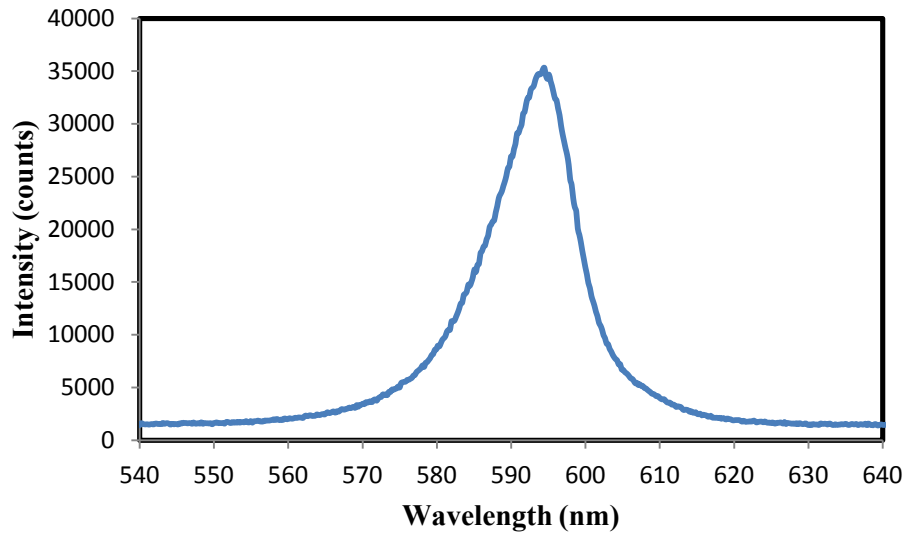


Figure 2.1: Spectrum of a 592 nm LED (Super Bright LEDs Inc. St. Louis Missouri, USA) (maximum intensity at 592 nm) used in the device.

In this design, multiple LEDs were used to incorporate different wavelength regions that showed strong correlation with the measurement parameters, particularly the amount of surface fat and meat tenderness. Detailed design of the sensor unit was explained in the hardware design section of this chapter.

### 2.2.3 Lock-In Amplifier

A lock-in amplifier (LIA, also known as a phase-sensitive detector) is a type of electronic amplifier that can extract an input signal from an extremely noisy environment using a modulated signal at a fixed reference frequency. A LIA uses a reference signal that can be generated by the same instrument or generated externally. When the reference signal is generated externally, the LIA employs a phase-locked loop (PLL) to internally generate a waveform at the same frequency and phase of the reference input, with very low distortion. The generated waveform is then used as a reference signal to multiply with the input signal (already modulated by the external reference signal). As a result, both the input and the reference signals contain

same phase and frequency information. The output signal of the multiplication stage is passed through a low pass filter to remove the high frequency components from the output signal. The output of the low pass filter only contains the DC component of the input signal which have equal phase and frequency of the reference signal. If the input signal contains noise, the LIA only outputs the DC component of the input signal, thus this noise is removed from the original signal.

### 2.3 The Hand-held Device

The hand-held device contained the following components: (1) light source (LED), (2) photodiode, (3) interface circuit, (4) LIA, (5) analog to digital converter (A/D), (6) microcontroller unit (MCU) (2009 Atmel Corporation, ATmega32, San Jose, California, USA) and (7) a display. The device block diagram is illustrated in Figure 2.2.

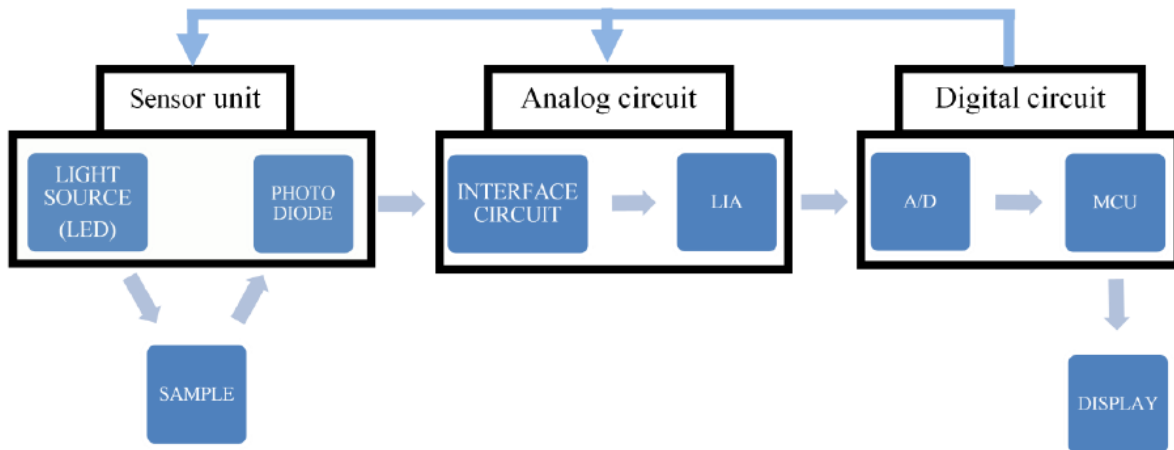


Figure 2.2: Device block diagram.

The light source had five LEDs (diameter 5 mm) of wavelengths 592, 593, 595, 601 and 605 nm (Super Bright LEDs Inc. St. Louis Missouri, USA; Optek Technology Inc., Carrollton, Texas, USA; Kingbright, City of Industry, California, USA). The LEDs serve as the sources of the various peak wavelengths. The LED light output was modulated using a reference signal generated by the MCU. This same reference signal was used in the LIA circuit. Hence, both LIA input signal and the reference signal had the same phase and frequency (i.e. synchronized). For signal detection, a silicon photodiode collects the reflected light from the sample surface and converts it into an electrical signal. The photodiode used was BPW34 (BPW34, Osram opto semiconductors, Regensburg, Germany). This photodiode had spectral sensitivity from 400 nm to 1100 nm. The electrical signal of BPW34 was a current signal. The interface circuit converted the current signal from BPW34 into a voltage signal. The LIA circuit used a bipolar voltage supply ranging from +12 volts to -12 volts. In this design, the LIA circuit incorporated amplifiers at both input and output stages. Because the LIA DC voltage signal is proportional to the intensity of the reflected light from the sample surface, the LIA extracted voltage signal represents a measure of the intensity of the reflected light. With a 10 bit resolution, the A/D converter transforms the DC voltage signal into digital signal. An average of 2000 consecutive readings from the A/D converter was recorded by the MCU. With a MCU preprogrammed fat estimation mathematical model, the fat percentage was calculated and displayed on a liquid crystal display (LCD). Figure 2.3 shows the first prototype of the handheld-device.

### **2.3.1 Hardware Circuit Design**

The device hardware consisted of five major components: (1) a sensor unit, (2) an analog circuit, (3) a digital circuit, (4) a battery and power circuit and (5) a display unit. The sensor unit incorporated a set of LED light sources on the rotating disk and the photodiode. The interface

circuit and the LIA were designed as analog circuits and were integrated in a printed circuit board (PCB). The A/D converter was a part of the microcontroller integrated circuit (IC). The digital circuit PCB contained the MCU, power supply regulator and control circuits for the sensor unit. The display unit was a standalone LCD which was interfaced with the MCU.



Figure 2.3: Side view, top view and bottom view (from left to right) of the handheld device.

### 2.3.1.1 The Sensor Unit

The sensor unit was comprised of two basic elements: (1) a movable light source unit and (2) a fixed reflected light receiving unit. The LEDs were placed on a rotating disk in a circular pattern (Figure 2.4). The LEDs of different wavelengths were arranged side by side along the perimeter of a 37.53 mm diameter circular PCB (Figure 2.4). The LEDs were rotated in such a way that they had overlapping illumination areas on the meat sample. The circular PCB was mounted on a plastic arm of a servo motor (2013 Hitec RCD USA, Inc., Poway, California, USA). The arm was connected to the shaft of the servo motor for actuation. The servo motor control circuit was driven by a square wave signal with a variable pulse width (Figure 2.5). The duration of the pulse width was directly proportional to the angular displacement of the servo

motor shaft. Here, the driving square wave signal of pre-set duration was generated by the MCU. The MCU was programmed to vary the pulse width in such a way that upon rotation of the PCB each LED would move in front of the fixed photodiode (placed on the bottom side of a static base PCB) at a specific interval [Figure 2.4 (bottom side)]. The photodiode was placed on a fixed circuit in front of the rotating disk [Figure 2.4 (bottom side)]. The servo motor was mounted upside down on the top side of the base PCB and the circular PCB was connected to the fixed base of the PCB via a flex cable wire. The sensor unit was connected to the digital circuit using two multi-pin connectors mounted on the top side of the base PCB [Figure 2.4 (top side)]. The servo motor was connected to the base PCB using a three pin connector. The ground connection of the servo motor was connected to the base PCB ground line. The positive voltage line of the servo motor and the servo motor control signal were connected to digital circuit via a two pin connector. LEDs and the photodiode were connected to the digital circuit via a ten pin connector mounted on the top edge of the base PCB.

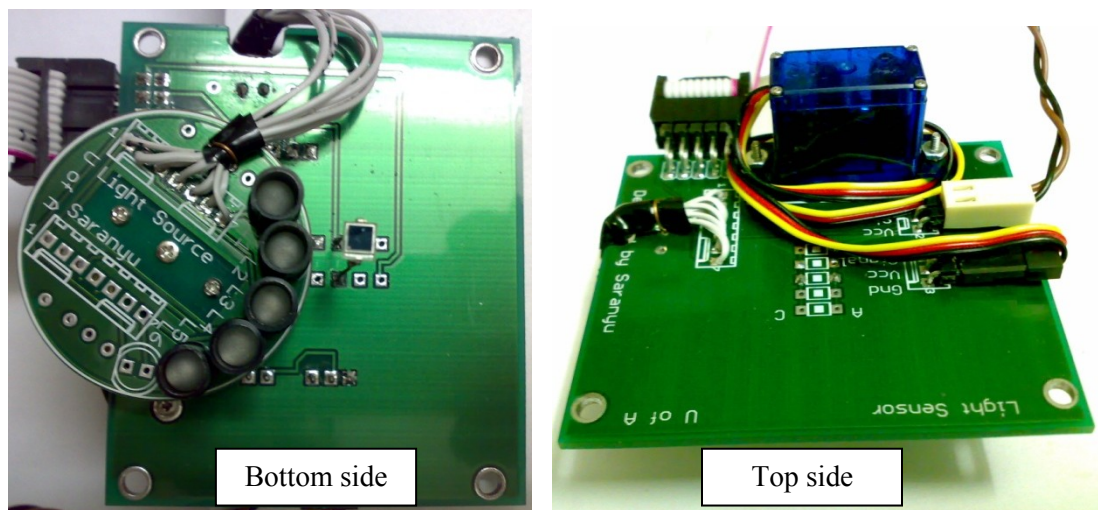


Figure 2.4: Complete PCB and design of the sensor unit. Left image is showing the bottom side and right image is showing the top side of the sensor unit.

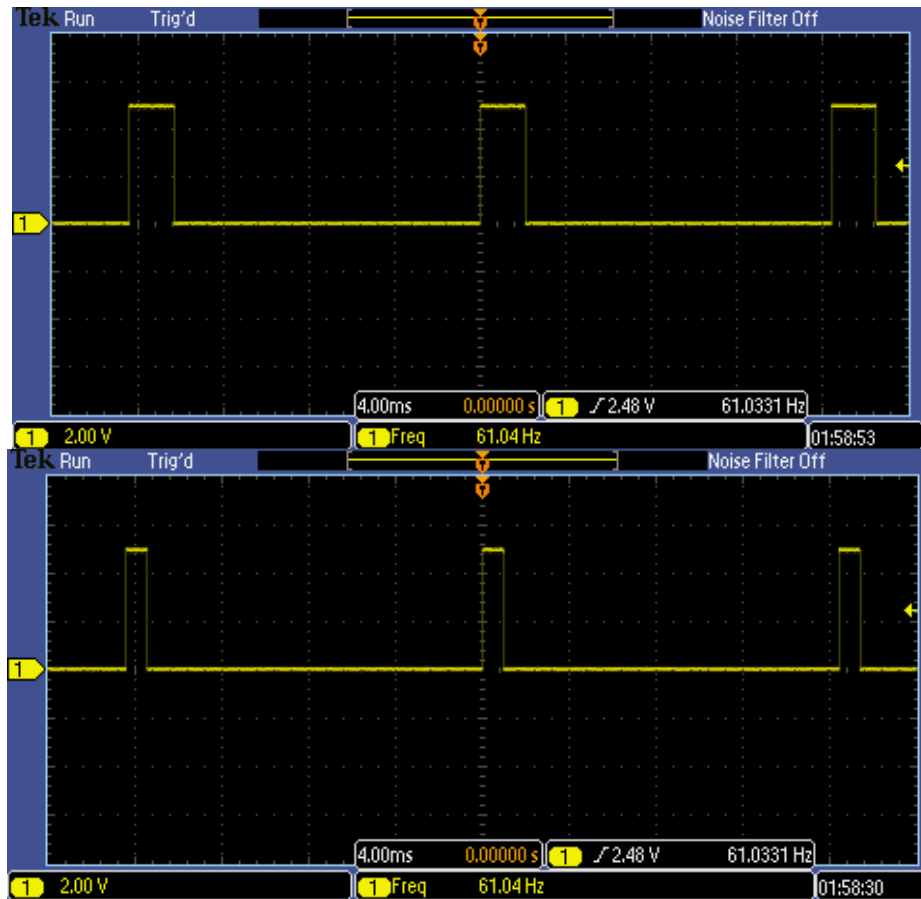


Figure 2.5: Servo motor control signal (frequency 61.04 Hz) with maximum pulse width (upper) and minimum pulse width (lower). (NOTE: voltage axis 2 volts per line division and time axis 4 ms per line division).

To achieve uniform diffused light from each LED, the LED's encapsulating clear plastic surface was roughened using fine sand paper. The LEDs were encircled with Teflon<sup>TM</sup> cylinders to prevent direct light from the LED contaminating the photodiode. In the current design, the following five LEDs models were used: (1) 592 nm (RL5-Y4523, 2002-2014 Super Bright LEDs Inc. St. Louis Missouri, USA), (2) 593 nm (OVLFY3C7, Optek Technology Inc., Carrollton, Texas, USA), (3) 595 nm (RL5-Y5030, 2002-2014 Super Bright LEDs Inc. St. Louis Missouri, USA ), (4) 601 nm (WP7113SEC, Kingbright, City of Industry, California, USA) and (5) 605 nm (RL5-O4030, Super Bright LEDs Inc. St. Louis Missouri, USA ). An additional design feature was that the circular PCB can be designed to accommodate additional LED if desired.

### 2.3.1.2 The Analog Circuit

The basic stages of the analog circuits were as follows: (1) a photodiode interfacing circuit, (2) an input amplifier, (3) a signal multiplier and (4) an active low pass filter. The complete circuit schematic and the complete PCB of the analog circuit are illustrated in Figure 2.6 and Figure 2.7 respectively. The output of the photodiode was delivered as a current signal; hence, an interface current to voltage converter circuit was designed to transform its output into voltage signal. The interfacing circuit of the photodiode (BPW 34) was built around a low power quad operational amplifier (op-amp) (LM324N, 2014 STMicroelectronics, Geneva, Switzerland) integrated circuit (IC). This op-amp was powered by a dual polarity power supply. The power supply (both positive and negative) was passed through a RC (R= resistor, C= capacitor) low pass filter. A 220  $\Omega$  resistor in series and a 0.1  $\mu\text{F}$  tantalum capacitor, which was in parallel, was used to design the low pass filter. To stabilize the output gain, a negative feedback was provided via a 10 K $\Omega$  resistor.

The output signal from this stage was fed into an input amplifier comprised of a triple op-amp instrumentation amplifier IC (INA114, 2009, Texas Instruments Incorporated, Dallas, Texas, USA). The resistor and capacitor values of this amplifier were kept similar to that designed by Sengupta et al. (2005). To achieve a unity gain, both pin number 2 and pin number 3 of INA114 were not connected to a gain resistor. However, the supply voltage +12 volts and -12 volts were used for this amplifier in contrary to that designed by Sengupta et al. (2005). One 0.1  $\mu\text{F}$  tantalum filter capacitor was connected in parallel to each power supply pin of this amplifier.

The amplified signal was multiplied with the reference signal (generated by the MCU to modulate the LED light outputs) using a balanced modulator/demodulator IC (AD630, Analog Devices, 2004 Analog Devices, Inc., Norwood, Massachusetts, USA). The amplified signal from

INA114 amplifier was directly connected to the AD630 IC. However, the reference signal was passed through a high pass filter designed by a series 0.1  $\mu\text{F}$  tantalum capacitor and a parallel 1M $\Omega$  resistor. The waveform of the reference signal before this capacitor and after this capacitor is depicted in Figure 2.8 and Figure 2.9 respectively. The positive and negative power supplies of AD630 were +10 volts and -10 volts respectively. One 0.1  $\mu\text{F}$  tantalum filter capacitor was connected to each power supply pin of AD630. An 180° phase shift and 0° phase shift can be selected by connecting the reference signal to pin number 9 and pin number 10 of the AD630 accordingly. However, in this design, a 0° phase shift was selected by connecting the reference signal to pin number 10 of the AD630 and connecting pin number 9 to ground.

The output of the multiplier was filtered using a single stage RC low pass filter. The value of resistors and capacitors were kept similar to that designed by Sengupta et al. (2005). A time constant of 0.01 s was achieved by using a 1 M $\Omega$  series connected resistor connected to a 0.01  $\mu\text{F}$  parallel connected ceramic capacitor to form the RC low pass filter stage. Hence, the cut-off frequency of the RC filter was 100 Hz. The reference signal had an approximate frequency of 980.4 KHz. The cut-off frequency of 100 Hz blocks any high frequency (980.4 KHz) component of the AD630 output signal. A lowered cut-off frequency was achievable by increasing the capacitor value but at the expense of a slowed response of the LIA circuit. It was found that a 100Hz cut-off frequency provided an optimum performance of the LIA.

The output of the low pass filter was passed through a DC amplifier designed using a low offset, low drift op-amp (operational amplifier) (OP07, 1995 National Semiconductor Corporation, USA). This amplifier was a negative feedback, non-inverting amplifier. The resistor and capacitor values of this amplifier were also kept similar to that designed by Sengupta et al.

(2005). However, the positive and negative supply voltages were +12 volts and -12 volts accordingly and bypass filter capacitors were used at each power supply pin of the OP07.

A second stage of RC low pass filter with a similar time constant (0.01 s) using a 100 K $\Omega$  series connected resistor and 0.1  $\mu$ F tantalum parallel connected capacitor was designed. The output of the DC amplifier stage was passed through this filter for improved noise reduction. It was also recommended by Sengupta et al. (2005) that a two stage filter would provide better performance. The analog circuit PCB used a 6-pin port ('ANALOG' in Figure 2.6) that was connected to another 6-pin port ('DIGITAL' in Figure 2.12) on the digital circuit PCB. The output waveform of the LIA after this stage is illustrated in Figure 2.10.

### **2.3.1.3 The Digital Circuit**

Digital control and processing was performed using an 8-bit AVR microcontroller (© 2009 Atmel Corporation, ATmega32, San Jose, California, USA). The digital circuit was built around this Microcontroller unit (MCU). The basic functions of this circuit were: (1) send control signal to the servo motor, (2) switch individual LED ON or OFF at required interval, (3) generate reference signal for LIA, (4) read data from ADC (A/D converter), (5) compute the fat estimation model using recorded data from ADC, (6) display results and various required information on the LCD display and (7) read switches as user input and execute pre-programmed function of each switch. The complete PCB and the complete circuit schematic of the digital circuit are presented in Figure 2.11 and Figure 2.12 respectively. The MCU circuit was designed using manufacturer recommended external circuit components based on required functions and performance. The reset circuit was designed to operate as 'power on reset' as well as user reset input via a push button switch. The MCU clock was provided using a 16 MHz external crystal oscillator (HC-49US-DN Extended Temp Range Crystal, ECS, INC. International, Ridgeview, Olathe, Kansas).

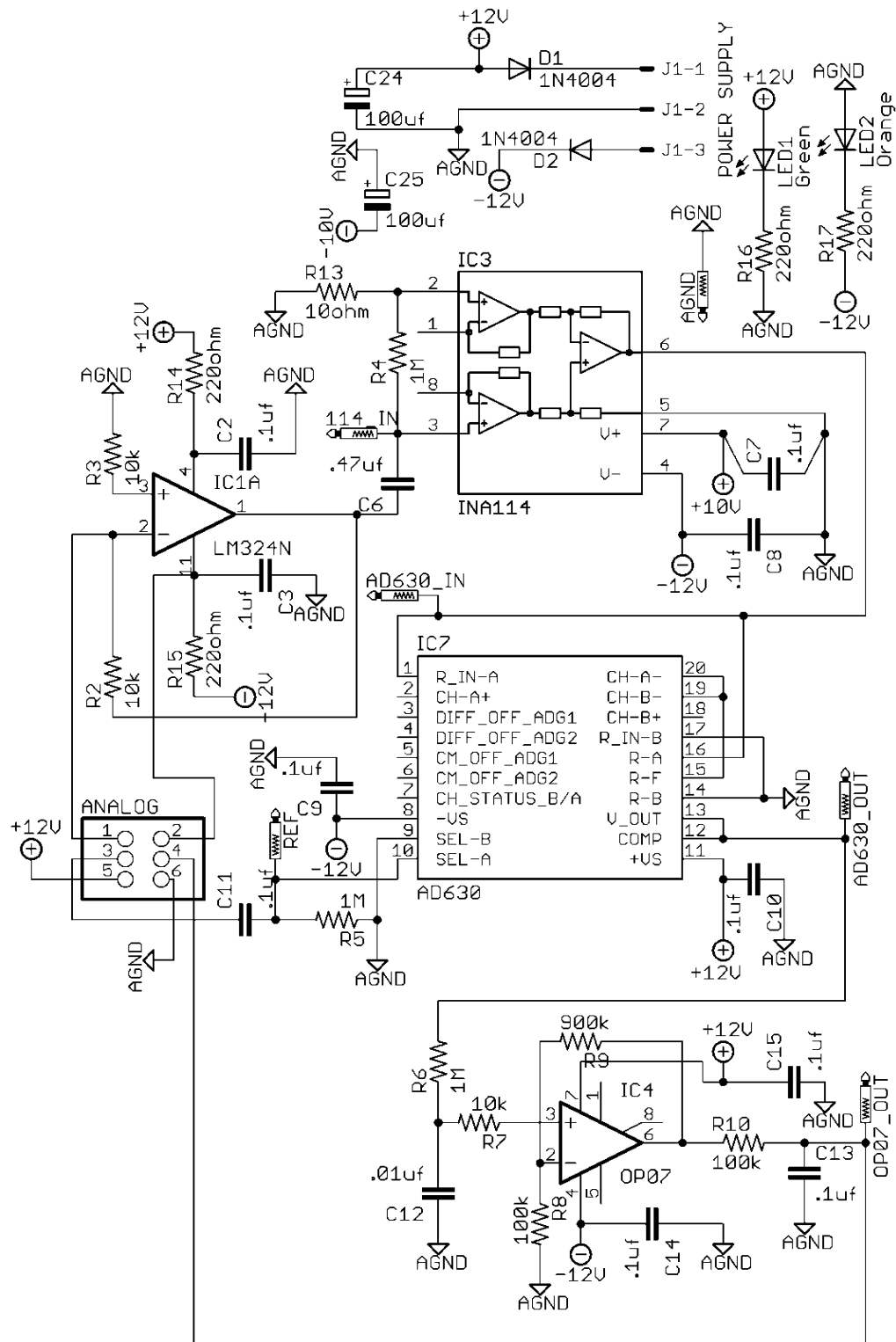


Figure 2.6: Circuit schematic of analog circuit.

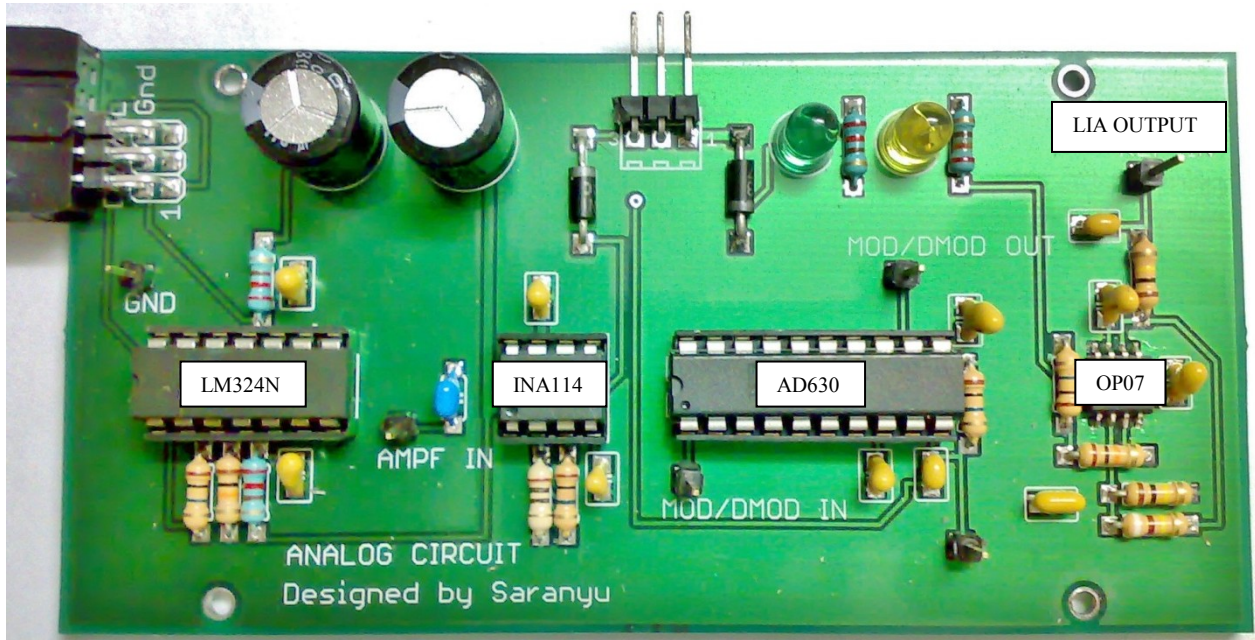


Figure 2.7: Complete PCB of analog circuit.

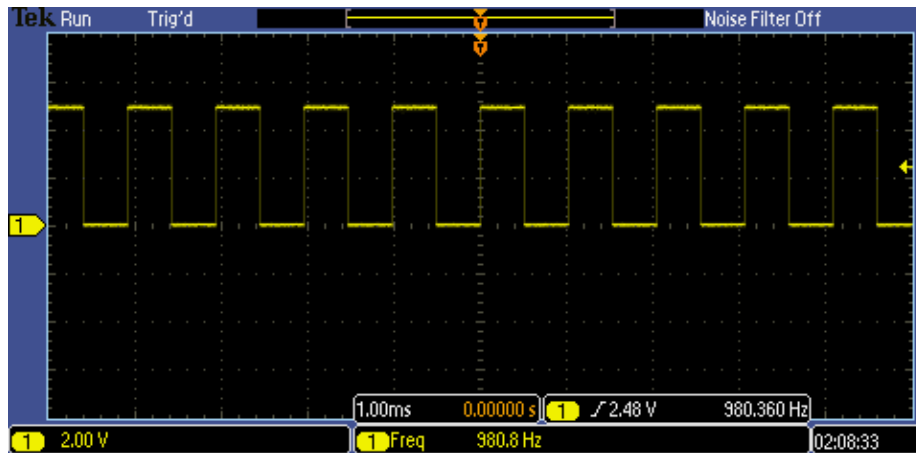


Figure 2.8: Reference signal for LIA generated by MCU before filter capacitor (NOTE: voltage axis 2volts per line division and time axis 1ms per line division).

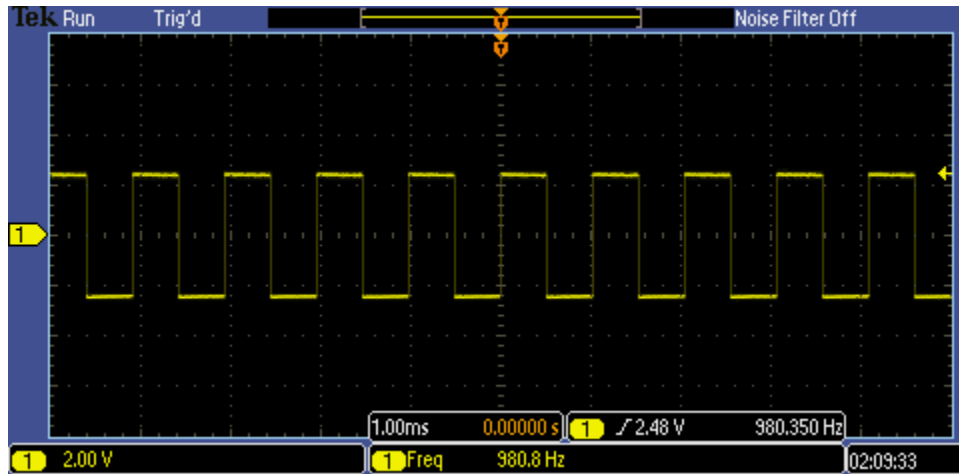


Figure 2.9: Reference signal for LIA after filter capacitor. (NOTE: voltage axis 2 volts per line division and time axis 1ms per line division).

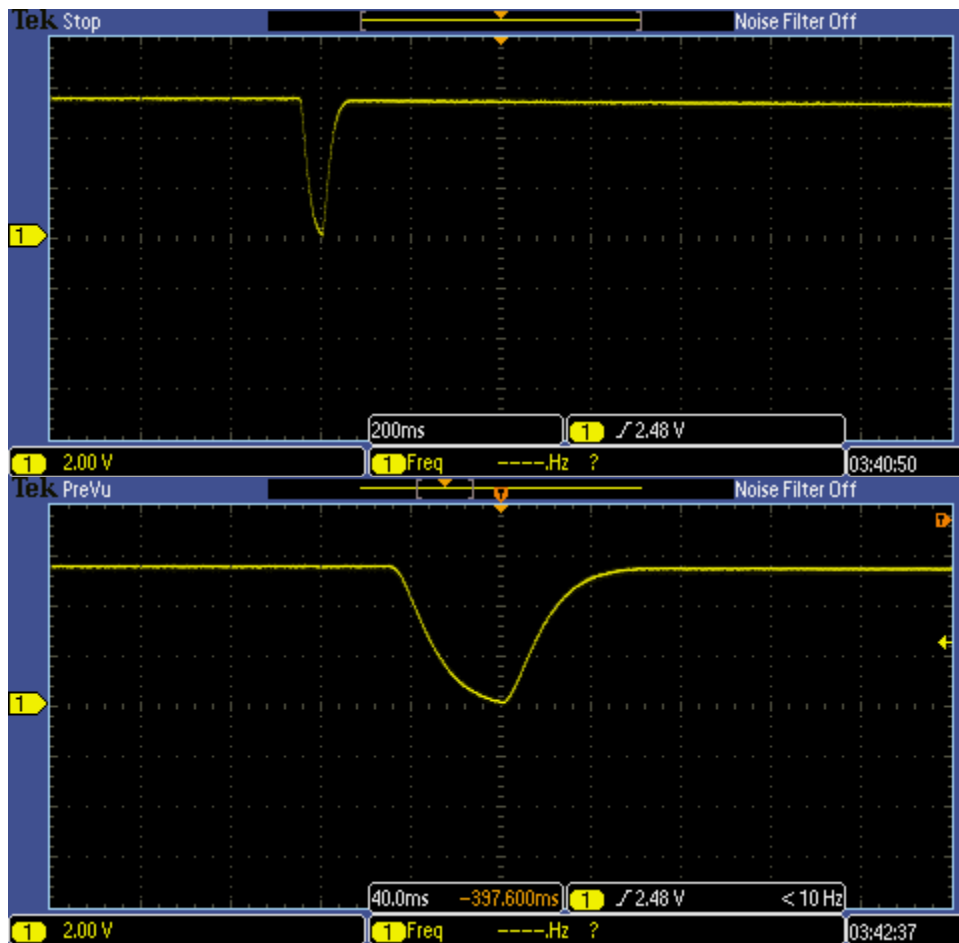


Figure 2.10: LIA output signal after the second stage low pass filter with transition between two different LEDs (upper) and magnified transition portion (lower). NOTE: voltage axis 2 volts per line division and time axis 200ms (upper) 40ms (lower) per line division.

The analog reference for the MCU ADC was provided from a voltage divider designed using a multi-turn 10 K $\Omega$  variable resistor. All power supply was bypassed with a 0.1  $\mu$ F tantalum filter capacitor. Digital ground and analog ground were separate and both were connected to power supply ground by a parallel filter capacitor of 470  $\mu$ F. The power supply was regulated to 5 volts. This arrangement helped the analog part (e.g. ADC and analog voltage reference) of this circuit to be free of high frequency noise from digital circuit components. The power supply was designed using a linear positive voltage regulator (LM7805C, 2006 Fairchild Semiconductor Corporation, Orchard Parkway, San Jose, California, USA). This voltage regulator was capable to provide 1 A (Ampere) current.

The servo motor control signal was generated from pin number 4 of port D (manufacturer specified name OC1B) of the MCU. The LEDs were driven by a seven channel ‘Darlington’ sink driver (ULN2003AG, Toshiba Corporation, Japan). LED switching signal from MCU was modulated by two ‘quad 2-input AND gate’ IC (DM74LS08N, 1995 National Semiconductor Corporation, Arlington, Texas) using digital pulse modulation technique. In this modulation the carrier signal was the reference signal from MCU which was generated for LIA (Figure 2.8). This reference signal was generated from pin number 7 of port D (manufacturer specified name OC2) of the MCU. The modulating signal was the ‘HIGH’ (binary ‘1’ or +5 volts) or ‘LOW’ (binary ‘0’ or Ground) signal from MCU to turn on or off the LED accordingly. The modulated signal from AND gate output (Figure 2.13) was used in ULN2003AG to drive the LEDs. ULN2003AG driver was controlled by modulated signal for switching ‘ON’ and ‘OFF’ appropriate LED at desired interval in synchronisation with servo control signal. The MCU sent ‘HIGH’ signal when a LED needed to turn on. This ‘HIGH’ signal passed through a modulation phase before being connected to a ULN2003AG control pin to drive the LED. The MCU

recorded reflected data of each specific LED by moving that LED in front of the photodiode using a servo motor control signal. The MCU used this data for computation of the fat estimation model. The results and various required information were displayed on a 20×4 segments (NOTE: 4 lines and 20 segments in each line within each segment were able to print one ASCII character) LCD (China) display. The LCD had four data lines and three control lines which were connected to the MCU using port B. The user operable five push button switches were connected to port C of the MCU. The digital circuit PCB used a 6 pin connector (‘MCU PROGRAMMING PORT’) for programming, a 12 pin connector (‘LCD’) to connect LCD, a 6 pin connector (‘DIGITAL’) to connect the analog circuit PCB and a 10 pin connector (‘SENSOR MODULE’) to connect the sensor unit PCB (Figure 2.12).

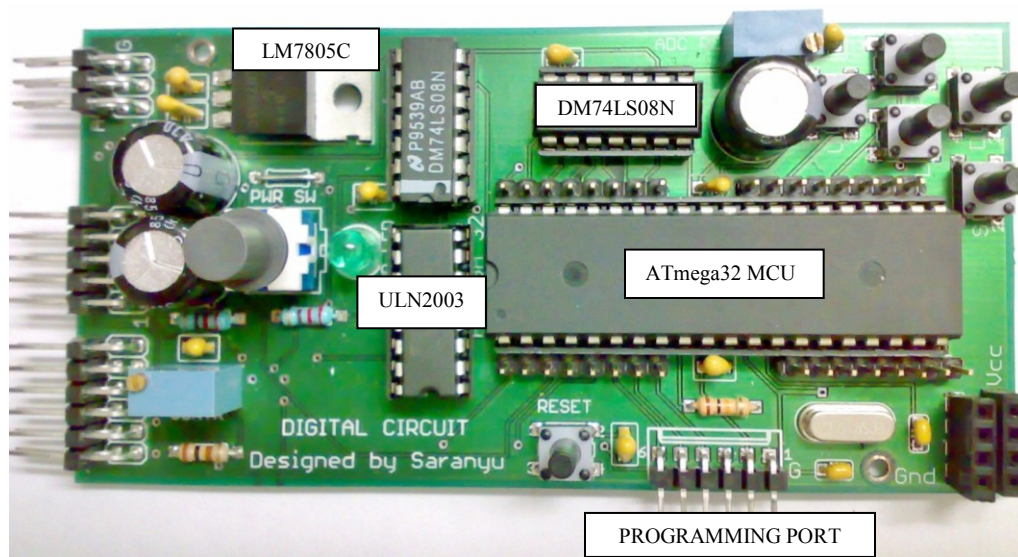


Figure 2.11: Complete PCB of digital circuit.

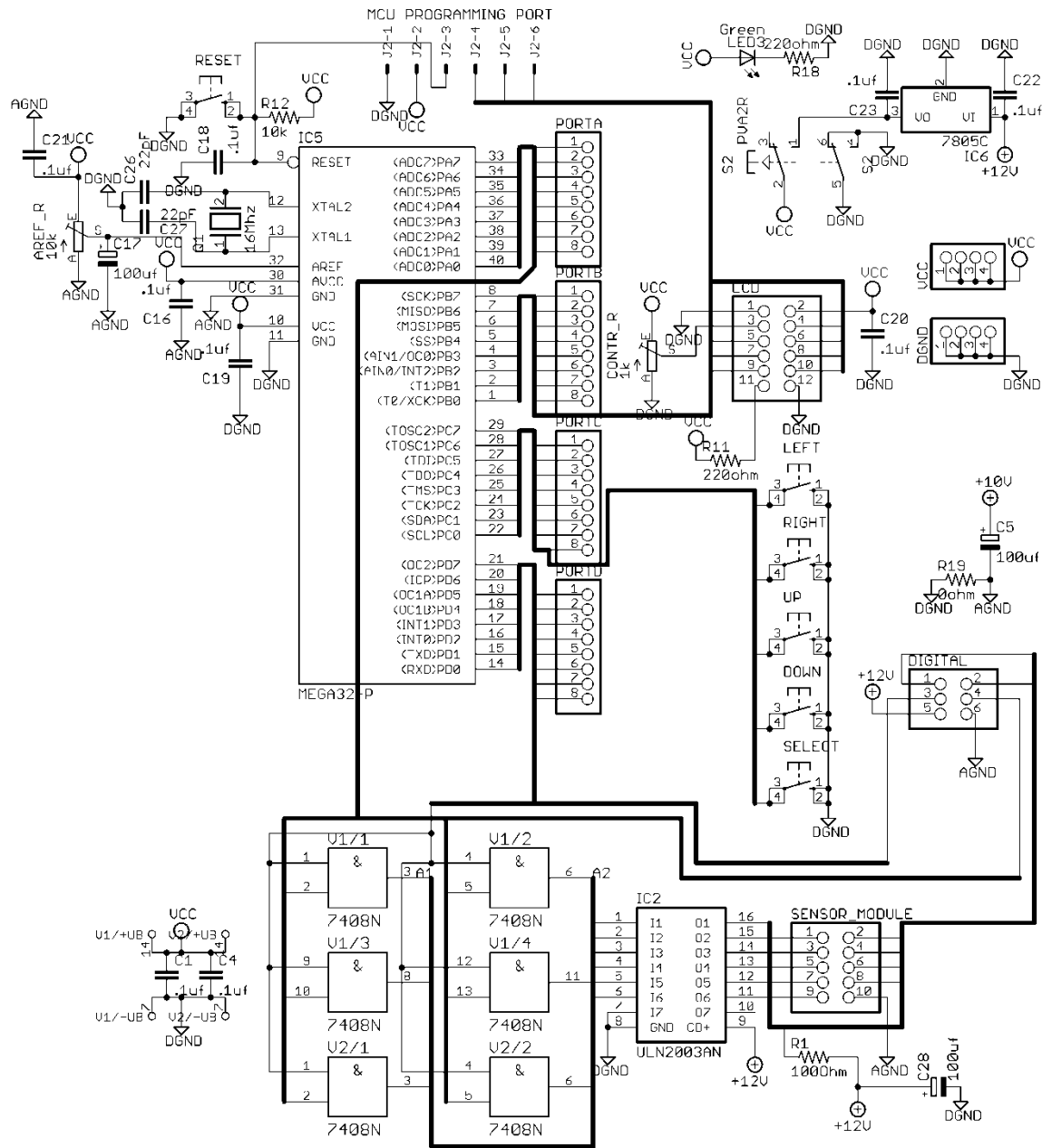


Figure 2.12: Circuit schematic of digital circuit.

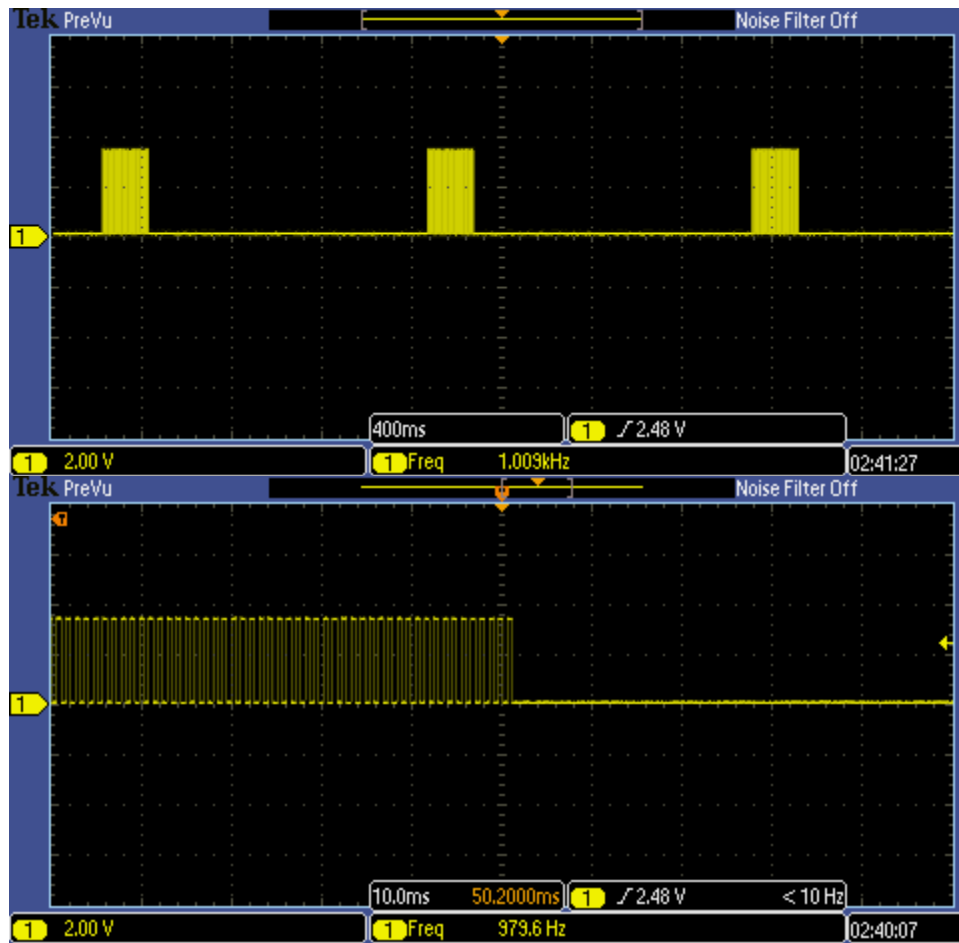


Figure 2.13: Modulated signal for LED before ULN2003 (upper) and one magnified LED ‘ON’ to ‘OFF’ transition (NOTE: voltage axis 2volts per line division and time axis 400ms (upper) and 10ms (lower) per line division).

### 2.3.1.4 Battery and Power Circuit

The battery and power circuit consisted of four 9.6 volts, 230 mAh (0.23 ampere hour) rechargeable NiMH (nickel-metal hydride) batteries (Powerex MHR9V, Maha Energy Corporation, City of Industry, California, USA), two variable positive voltage regulators (LM317T, 2014 STMicroelectronics, Geneva, Switzerland). In this circuit, two batteries were connected in series to generate 19.2 volts. A positive voltage regulator was used to regulate down the voltage from 19.2 volts to 11.96 volts. Similarly, the two remaining batteries and one

positive voltage regulator were used to generate another 11.96 volts. The negative side of the first supply of 11.96 volts was connected to the positive side of the second. This junction point became the common ground for the positive 11.96 volts supply (first regulator output) and negative 11.96 volts supply (second regulator output). Thus, a bipolar power supply of +11.96 volts and -11.96 volts was designed. This supply was used to power the analog circuit; however, only the positive power supply (+11.96 volts) was used for digital circuit. This circuit also contained a toggle switch to connect or disconnect the batteries. This allowed the batteries to conserve energy when the device was not in use. A voltage divider circuit using two resistors was utilized to reduce the series voltage of the two batteries from 19.2 volts to an acceptable voltage level of ADC. This voltage divider output was connected to one of the remaining ADC channels to monitor the battery voltage.

#### **2.3.1.5 Display Unit**

The display unit was a standalone 20×4 segment LCD (anonymous manufacturer, China). The LCD came with the required LCD interfacing circuit. The interfacing circuit provided came with a TTL (transistor-transistor logic) compatible 16 pin bidirectional port. The MCU had TTL logic, hence, the LCD could be directly connected to MCU using that port. The pin configuration was generic in nature. The LCD pins, their logic levels and functions are listed in Table 2.1. The compiler used special LCD instruction to multiplex the LCD data bus; therefore, only four data bus pins were required to send and receive data from LCD.

Table 2.1: Pin diagram, logic levels and functions of each LCD pin.

Pin number	Symbol	Logic level or volts	Function
1	VSS	0 volts	Power Ground
2	VCC	+5 volts	Power supply
3	VEE	-	Contrast adjustment
4	RS	H/L	H: Data L: Instruction
5	R/W	H/L	H: Read L: Write
6	E	H/L	Enable
7-14	DB0 – DB7	H/L	Data bus line
15	LEDA	+5 volts	Power supply for back light LED
16	LEDK	0 volts	

### 2.3.2 Software Design

The software for the MCU was written in C-language (Appendix A). A C-language compiler and integrated development environment (IDE) software (CodeVisionAVR, version: 2.04.4a Advanced, HP InfoTech S.R.L., Bucharest, Romania, European Union) was used to generate the HEX (hexadecimal) file for the Atmega32 MCU. The MCU contained a 32 KB (NOTE: 32,000 bytes = 32,000 × 8 bits) in-system self-programmable flash program memory (ATmega32 datasheet, revision. 2503O–AVR–07/09, 2009 Atmel Corporation). The Serial Peripheral Interface (SPI) port of MCU was used to upload the HEX file into the flash program memory. The SPI port was located at port B of MCU. An Atmel AVR microcontroller programmer (USBasp, open sourced free circuit, Internet) was built using open source information from the internet (Figure 2.14). This programmer used an ATmega8 (2009 Atmel Corporation, ATmega8, San Jose, California, USA) microcontroller. A programmer software (AVR8 Burn-O-Mat, version 2.1.1, author: Torsten Brischalle, 2009) was used to interface with a USBasp programmer connected to computer using an USB (Universal Serial Bus) port. The HEX file was

uploaded using this software. Various functions of the software were: (1) sensor interfacing, (2) display interfacing, (3) key pad interfacing and (5) computation and display of results. The header file 'mega32.h' was used to specify the use of ATmega32 MCU. This header file contained all the specific input/output registers of ATmega32 MCU. A standard input and output header file ('stdio.h') and a standard library function's header file ('stdlib.h') were used for general C language functions. A header file ('delay.h' CodeVisionAVR, version: 2.04.4a Advanced, HP InfoTech S.R.L., Bucharest, Romania, European Union) was used to incorporate delay functions for generating delay in terms of milliseconds ('void delay\_ms(unsigned int n)' CodeVisionAVR, version: 2.04.4a Advanced, HP InfoTech S.R.L., Bucharest, Romania, European Union) and microseconds ('void delay\_us(unsigned int n)' CodeVisionAVR, version: 2.04.4a Advanced, HP InfoTech S.R.L., Bucharest, Romania, European Union). The compiler generated code for ADC, input/output ports, MCU Timer/Counter and LCD initialization. The compiler used an automatic program generator graphical user interface (GUI) to take user input regarding various MCU components and generated code for ease of programming. This helped write programs faster without the need to memorize all the MCU registers and their specific configuration for various functions. Furthermore, description of each compiler generated function was given in the help section of the compiler.



Figure 2.14: USBasp programmer for ATmega32 MCU.

### 2.3.2.1 Sensor Interfacing

The sensor interfacing program had the following basic functions: (1) generate control signal for servo motor, (2) generate reference signal for LIA and modulation of LED light, (3) switch between LEDs, and (4) read data from ADC. The 16-bit timer/counter1 was used to generate control signal for the servo motor. The servo motor arm position was adjusted by tuning the pulse width of the control signal. In general, a servomotor achieves its initial position or 0° position by a pulse width of 1 ms, its 90° position by a pulse width of 1.5 ms and a 180° position by a pulse width of 2 ms. The value of a timer configuration register of the MCU (manufacturer specified name 'OCR1B') was used to modify the pulse width of the control signal. The reference signal was generated using the 8-bit timer/counter2 of the MCU. Both the phase and frequency of this signal were kept constant at all time.

An interface program switched the individual LED on after rotating the servo arm to the appropriate angle such that the photodiode read only the light reflected from the specific LED. For ease of programming, the MCU pins that were connected to each individual LED were defined by new names, specifically LED\_L1 to LED\_L5, at the beginning of the program. Once the LED was in position, the program read the ADC data and stored it in a variable for the next computation. The ADC read function ('unsigned int read\_adc(unsigned char adc\_input)') CodeVisionAVR, version: 2.04.4a Advanced, HP InfoTech S.R.L., Bucharest, Romania, European Union) was used to read data from ADC. Two thousand (2000) such consecutive readings were recorded and the average value of the 2000 readings were calculated and stored in a variable for next step. Readings were taken from other LEDs in the same manner.

### **2.3.2.2 Display Interfacing**

A generic instruction set of a 20×4 segment LCD display was already built into the compiler. The compiler used these instructions and created some functions in C-language for read, write and delete operations. The header file 'lcd.h' had the function declarations for the LCD. This header file was used to incorporate the LCD functions in the main program. The function 'void lcd\_gotoxy(unsigned char x, unsigned char y)' (CodeVisionAVR, version: 2.04.4a Advanced, HP InfoTech S.R.L., Bucharest, Romania, European Union) was used to select each individual segment in the LCD. Data located in the flash memory and SRAM (Static Random Access Memory) were displayed on the LCD using 'void lcd\_putsf(char flash \*str)' and 'void lcd\_puts(char \*str)' functions (CodeVisionAVR, version: 2.04.4a Advanced, HP InfoTech S.R.L., Bucharest, Romania, European Union) accordingly. A standard library function ('void ftoa(float n, unsigned char decimals, char \*str)' CodeVisionAVR, version: 2.04.4a Advanced, HP InfoTech S.R.L., Bucharest, Romania, European Union) was used to convert floating point number to characters in string. This helped to display floating point numbers on the LCD because LCD display functions were able to take only 'string' type variables.

### **2.3.2.3 Key pad Interfacing**

The key pad of the device consisted of five push button switches. They were placed on top of the device handle in 'UP', 'DOWN', 'LEFT', and 'RIGHT' orientation and another one as 'SELECT/ENTER' key beside the 'DOWN' key. Each individual key button was connected to an individual pin of port C of the MCU as active low configuration. In active low configuration, a 'LOW' signal (binary '0' or ground) was sent to the MCU pin when a key was pressed. The keys were connected to pin numbers 3-7 of port C of the MCU. The connection configuration of each key is given in Table 2.2. A key pad interfacing program was written to detect each key

press. Each individual key of the key pad was constantly monitored and each time an active low signal (binary ‘0’ or ground) was detected a while loop after a delay of 100 ms was initiated until the key was released or a ‘HIGH’ (binary ‘1’ or +5 volts) was detected. This programming technique helped to solve the ‘key bouncing’ problem of a push button switch. When a push button switch is pressed the contact surfaces inside the switch starts bouncing in a damping oscillation pattern (e.g. damping oscillation of a small metal ball dropped on a metal plate from a certain height). This problem is referred to as ‘key bouncing’.

Table 2.2: Connection configuration of keypad switches.

Pin number of port C	Key
3	’LEFT’
4	’RIGHT’
5	’UP’
6	’DOWN’
7	’SELECT/ENTER’

#### 2.3.2.4 Computation and Display of Results

Various numerical steps of the fat estimation mathematical model were performed using basic mathematical functions available in C-language. The ADC data was averaged and displayed on the LCD for testing of the fat estimation model manually. The computations of the various numerical steps were pre-programmed in the MCU.

#### 2.3.2.5 Power Monitoring

It was important to ensure that the power supply voltage was accordance with the calibration factors that were pre-programmed in the MCU. As such, monitoring of the battery voltage was

essential during the operation of the device. The reference voltage (voltage at MCU analog reference pin) of the ADC must be at constant voltage (+5 volts) at all time during the measurement process. The purpose of the power monitoring program was to stop the device operation and initiate error message in case of a problem in the power supply or a low battery voltage. However, this program was not included in the test prototype.

## **2.4 Device Design Specifications**

The devices consisted of three major parts: a sensor unit, an analog circuit and a digital circuit. Both the sensor unit and the display unit were powered directly from the digital circuit board. Approximate voltage, current and power consumption values of analog circuit and digital circuit are shown in Table 2.3. The current and power consumption by the analog circuit were constant. The digital circuit maximum power consumption was about 3 watts when the servo motor was in moving condition. However, the average power consumption was much less than 3 watts due to the fact that servo motor motion lasted less than a second. Furthermore, the servo motor was static when readings from all LEDs were recorded.

The waveform of LIA output (Figure 2.10) showed that there was a requirement for a 100 ms time delay because the LIA output required approximately 100 ms to stabilize between switching off of one LED and switching on to the next LED. This time delay was added in the MCU program using a delay function ('void delay\_ms(unsigned int n)' CodeVisionAVR, version: 2.04.4a Advanced, HP InfoTech S.R.L., Bucharest, Romania, European Union). The height of the device sensor from the sample surface was kept between 5 cm to 7 cm. A height of more than 7 cm reduced the reflected light intensity from the sample surface, which affected the optimum device performance. This was due to ambient noise suppressing the signal to a level that the LIA

was not able to recover. A height below 5 cm adversely affected the performance of the device because the reflected light intensity saturated the ADC.

The approximate dimensions of the device were 22.5 cm in length, 11.6 cm in width and 6.5 cm in height, and the weight of the device was approximately 722 g.

Table 2.3: Voltage, current and power consumption values of analog and digital circuit (NA = not applicable).

	<b>Power supply</b>	<b>Servo motor arm</b>	<b>Voltage (Volts)</b>	<b>Current (Milli-amperes)</b>	<b>Power (Watts)</b>
<b>Analog circuit</b>	Positive	NA	+11.96	+51.8	0.62
	Negative	NA	-11.96	-49.6	0.59
<b>Digital circuit</b>	Positive	Static	+11.96 (before LM7805) +4.94 (after LM7805)	85.2-164.2 (at +11.96 volts)	1.02-1.96
		Moving	+11.96 (before LM7805) +4.94 (after LM7805)	118.2-248.2 (at +11.96 volts)	1.41-2.97
	Negative	NA	NA	NA	NA

## 2.5 Future Improvements

The design of the device presented here was a prototype design. Therefore, many possibilities of improvement existed. Firstly, the servo motor based mechanical sensor unit could be replaced by a complete optical sensor without any moving parts. However, that may require additional

space. The same sensor unit, used in this prototype, could be designed using a more power efficient servo motor than the one used. Also, the connection between the rotating disk PCB and the static base PCB of the sensor unit was not sufficiently robust, and a cable connection with increased flexibility and durability should be incorporated in an improved design. Because having LEDs at close peak wavelengths is not possible, the design can be further improved by using a powerful white LED with optical band pass filter arrangement.. The LIA could be designed using filters and amplifiers of increased complexity or using a powerful DSP chip instead of the digital LIA for improved performance and noise immunity. The circuit could be made using surface mount technology (SMT) components to reduce space and accommodate a circuit of increased complexity and robustness. In the digital circuit, an external ADC with increased resolution could be implemented to improve the signal detection accuracy. Advanced MCU and high resolution graphics display could be added for more feature and robustness. Also, the batteries used in this prototype did not supply sufficient energy to power the device for an entire day of operation. This feature would be crucial for success in a commercial abattoir. If a high capacity lithium-ion battery were to be used, there would be enough stored energy to power the device for an entire day of operation.

## **2.6 Conclusion**

The design of the prototype achieved most of the design objectives successfully. The device was lightweight and small enough in dimension to be operated as a hand held device. No external power supply or computing power was needed in comparison with other machines currently being used in commercial abattoir. The important fact to be mentioned here would be the cost of this hand-held device was much less than currently available machines. The MCU unit was capable of executing 16 million instructions at 16 MHz clock. This MCU was powerful

enough for the computation and other functions to perform easily. This prototype was designed to work using visible light spectroscopy; however, NIR light spectroscopy could be implemented in this device by changing the VIS wavelength LEDs to NIR wavelength LED or by using optical filters. The testing of the device using meat samples (discussed in Chapter 3) showed results that were equivalent to those found using a complex and more expensive commercial spectrometer that that used in this study. However, complete testing, validation and calibration using a large number of samples in a commercial abattoir environment was the scope of the future research.

## Chapter 3

# Development of an Intramuscular Fat Estimation Model for the Hand-held Device

### 3.1 Introduction

Methods commonly used to measure the amount of intramuscular fat in beef include digital pattern recognition based upon visible color (CVS, Research Management System USA, Inc., Fort Collins, Colorado, USA), chemical extraction of the fat (AOAC, 1995) and subjective visual appraisal. Until recently, subjective visual appraisal was the method approved by the Canadian federal government for determining differences in intramuscular fat within the beef grading system because chemical extraction was destructive. The development and commercialization of digital pattern recognition technology in the form of the E + V Beef Grading System has increased the objectivity by removed human error from grading and was at the same time non-invasive, thus preserving meat quality. Although effective, this technology is prohibitively expensive, and only very large abattoirs can afford it. There is a need for small abattoirs to have access to comparable objective technology so that their beef products are similarly considered in the provincial markets.

Of the developing technologies available, estimation of meat quality using spectroscopy would be the most effective solution for a handheld device in order to estimate and quantify various qualities of beef. Light with wavelengths in the visible and near-infrared region (400 to 700 and 700 to 2500 nm, respectively) has shown particular promise, giving correlation values between NIR wavelengths and Warner-Bratzler shear force (WBSF) values greater than  $r = 0.8$  (Mitsumoto, Maeda, Mitsunashi & Ozawa 1991; Park, Chen, Hruschka, Shackelford & Koohmaraie 1998a). Dian et al. (2008) used VIS and NIR reflectance of peri-renal fat to

differentiate the carcasses of pasture-fed and concentrate-fed lambs and Liu et al. (2004) showed that tough and tender chicken breast could be differentiated based upon VIS-NIR spectra. The most compelling evidence of its promise is that NIR technology exists commercially for the laboratory assessment of meat fat, water and protein content, with laboratory-grade NIR technology best used to assess the chemical composition of minced or ground meat as it is calibrated for a homogenized product (Ripoll et al., 2008; Sierra et al., 2008). Moisture, fat and water concentrations have also been successfully predicted in whole pork using VIS-NIR (400 to 1700 nm) (Chan et al. 2002) and fat in whole beef (Rødbotten et al., 2000), but no commercial VIS-NIR product has been developed for use on whole meat. Because the efficacy of NIR is known, experimentation was conducted to test the hypothesis that VIS reflectivity can be used to predict the amount of intramuscular fat in whole beef cuts, and a series of experiments were performed to examine the relationship between visible fat in beef and VIS reflectivity.

## **3.2 Materials and Methods**

### **3.2.1 Experimental Samples**

A total of seven lean beef steaks and chunks of thick inter-muscular fat were obtained from a local grocery store at different times. Cork borers (4.5 and 7.5 mm diameter) were used to remove pieces of fat of two different sizes, small fat pieces (4.5 mm diameter) and large fat pieces (7.5 mm diameter), from the thick inter-muscular fat. Pieces of fat were placed on lean muscle regions of the steak in an additive sequence such that an increasing amount of visible intramuscular fat (marbling) was simulated on each steak (Figure 3.1).

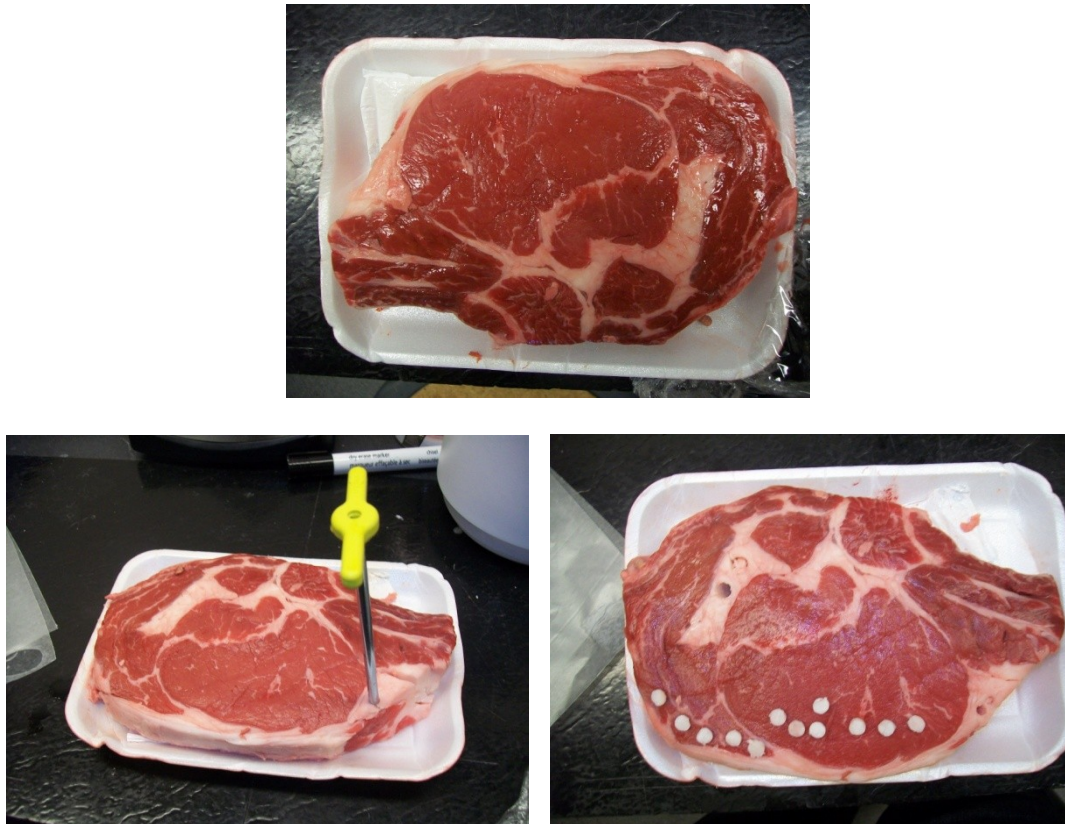


Figure 3.1: A general procedure used in the experiments for preparation of the sample. Top: unpacked steak bought from local store. Bottom left: cork borer used on the inter-muscular fat of the steak to cut fat pieces. Bottom right: pieces of fat cut from inter-muscular fat of the beef steak.

### 3.2.2 VIS Spectroscopy

The reflectance intensity of the VIS spectrum from the beef surface was measured using a USB spectrometer (USB4000, Ocean Optics, Dunedin, Florida, USA) [Figure 3.3 (a)]. This spectrometer produced spectrum with a wavelength range of 345.33 nm to 1055 nm, however, the functional wavelength range of the spectrometer was about 400 to 780 nm as the extreme wavelengths of the manufacturer specified wavelength range were too noisy to be useful. The typical signal to noise ratio expected according to manufacturer's specification was 300:1. The electronics in the spectrometer produced a small signal even at zero light which was designated as "dark noise" (also known as "dark current"). According to the manufacturer's specifications,

the dark noise was 50 root mean square (RMS) counts. The analog to digital converter (ADC) used had a resolution of 16 bit. The optical resolution was between 0.1 nm to 10.0 nm. This spectrometer required a fiber optic cable with an SMA 905 type connector to transmit and receive light signal.

An Ocean Optics tungsten halogen light source (HL-2000, Ocean Optics, Dunedin, Florida, USA) (Figure 3.2) was used. This light source had a broad spectrum from VIS range to NIR range (360-2400 nm) and covered the entire spectrum range of the VIS spectrometer used in these experiments.

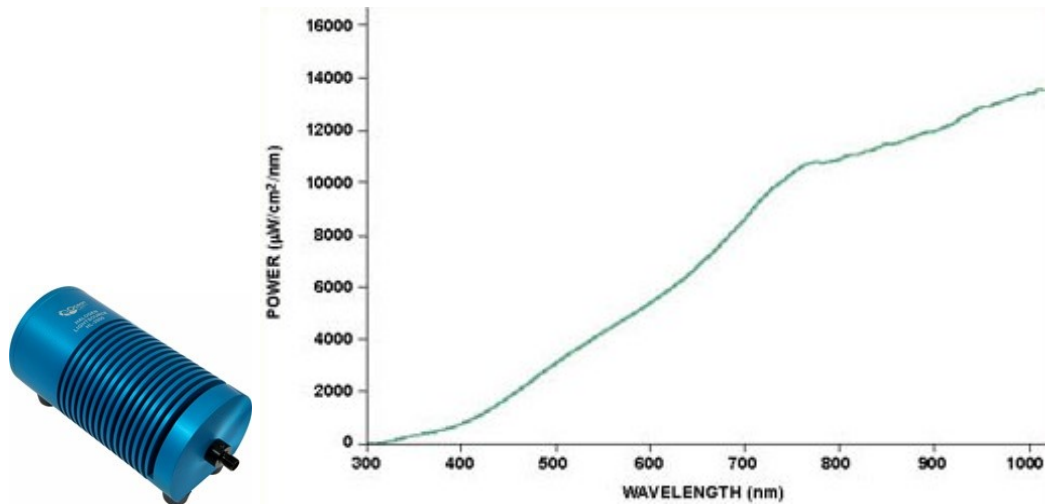


Figure 3.2: Halogen light source (OceanOptics HL-2000 Tungsten Halogen Light Source) (left image) and its spectrum with wavelength (nm) on x-axis and power ( $\mu\text{W}/\text{cm}^2/\text{nm}$ ) on y-axis (Ocean Optics, Dunedin, Florida, USA) (right image).

A bifurcated fiber optic cable (R600-7-VIS-125F, Ocean Optics, Dunedin, Florida, USA) [Figure 3.3 (b)] was used to transmit the light from the source onto the meat surface and return the reflected light to the spectrometer. According to manufacturer specifications, this fiber optic cable had a SMA 905 type connector at both ends (receiver and transmitter) of each fiber and a numerical aperture of 0.22  $\mu\text{m}$ . These specifications were essential to meet the compatibility requirements of USB4000 spectrometer. This cable had six illumination fibers surrounding one

read fiber for carrying source light on to the measurement surface. The optical read fiber in the middle was used to collect the reflected light. The receiving end of the optical fiber had a 10 cm stainless steel probe for improved protection. The height from the measurement surface to the end of the probe was held constant at 6 cm or 8 cm (depending on the experimental setup) during any measurement. A stand with a custom holding mechanism (Figure 3.4) and height adjustment feature was used to attach and hold the metal probe.

A Teflon<sup>TM</sup> sheet 1.66 mm thick was used as a reference for normalization. The Teflon<sup>TM</sup> sheet had a uniform distribution of spectral intensity with high reflectivity and was therefore suitable for use as a reference. A black mask (a plastic black cover with a circular opening in the center of diameter approximately 4.5 cm) [Figure 3.3 (c)] was used to exclude entire surface regions on the measurement surface except the area that was intended to be measured. The “dark current” noise spectrum was recorded by covering the probe with a black plastic cap.

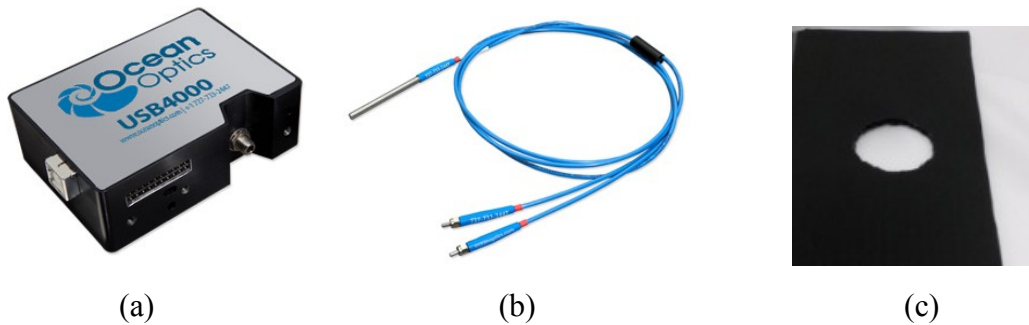


Figure 3.3: (a) Ocean Optics USB4000 Spectrometer, (b) Ocean Optics R600-7-VIS-125F bifurcated fiber optic cable, and (c) black mask cover.

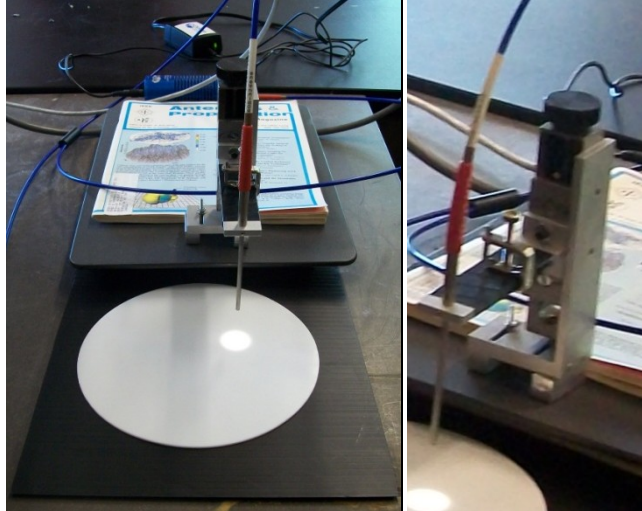


Figure 3.4: Front view (left) and side view (right) of the custom stand to hold the fiber optic stainless steel probe.

### 3.2.3 NIR Spectroscopy

An Optical Spectrum Analyzer (AQ6370C, Yokogawa, Tokyo, Japan) (Figure 3.5) was used for measurement of NIR light spectrum. The wavelength range of this spectrometer was 600 to 1700 nm. This spectrometer had an internal calibration source for wavelength calibration and optical alignment. It had wavelength resolution of 0.02 nm with typical wavelength accuracy of  $\pm 0.01$  nm. Sensitivity levels could be adjusted using the sensitivity level setting, as “MID” and “HIGH1” to “HIGH3” (Manufacturer specified terms). The typical level sensitivity was -90 dBm (1300-1620 nm), -85 dBm (1000-1300 nm), -60 dBm (600-1000 nm) at the “HIGH3” level sensitivity setting (AQ6370C datasheet, Yokogawa, Tokyo, Japan). The sweep time (measurement time) increased with increased sensitivity level setting and it required a fiber with PC type connector (e.g. FC, SC or ST (manufacturer specified terms) type connectors). The spectrum analyzer had a stray light suppression ratio of 73 dB with an auto resolution correction, auto reference level and a built in smoothing filter function. According to manufacturer’s specifications, a ‘warm up’ time of one hour was required. After warm up an optical alignment

followed by a wavelength calibration using the internal calibration light source was mandatory for guaranteed performance and accuracy of the spectrometer.



Figure 3.5: Yokogawa AQ6370C Optical Spectrum Analyzer.

Wavelength resolution of 1 nm was used for convenience of data analysis. Auto reference level, auto resolution correction, and the smoothing function of the instrument were used for best measurement results but these functions increased measurement time. NIR readings were recorded in the full wavelength range from 600 to 1700 nm and all measurements were performed in a dark room.

The light source for NIR spectroscopy was the same light source used for VIS spectroscopy. The light source had a broad spectrum range and it covered the spectrum range of the NIR spectrometer as well.

The fiber optic cable used was the same cable used in the VIS spectroscopic analysis (Ocean Optics R600-7-VIS-125F bifurcated fiber optic cable). This fiber optic cable had a SMA905 connector, thus a custom made SMA to FC (PC type connector which is compatible with AQ6370C) adapter was used to connect the cable with the AQ6370C Optical Spectrum Analyzer. This SMA to FC adapter was designed and manufactured in the Electrical Engineering workshop at the University of Alberta.



Figure 3.6: Left: SMA to FC custom adapter, middle: SMA to FC adapter attached to optical fiber cable, and right: optical fiber cable is connected to AQ6370C using the SMA to FC adapter.

The same white Teflon<sup>TM</sup> sheet and black mask cover [Figure 3.3 (c)] used in the visible spectroscopic analysis were also used in the NIR analyses for the same purposes. Similarly “dark current” noise was recorded. The recorded spectrum data was stored during the measurement directly in the AQ6370C internal memory using a ‘.CSV’ (Comma-separated values) file extension and data were transferred from AQ6370C to a personal computer for data analysis as the ‘.CSV’ files were compatible with Microsoft Office Excel<sup>TM</sup>.

### 3.2.4 Hand-held Device Spectrometry

The handheld device was tested during these experiments. During the design and development phase of the device these experiments were performed to test various design aspects of the device such as sensor design, height of the sensor from measurement surface, photo diode response, effect of LED spectrum, placement of LEDs surrounding the photo diode, performance of the LIA filter, ADC performance, noise and error margin. After each experiment, results were analyzed and if required, necessary modifications were made in design as well as in the fat estimation model to improve the overall performance of the system. This design and development cycle of the device was continued until a satisfactory overall performance was achieved (Figure 3.7).

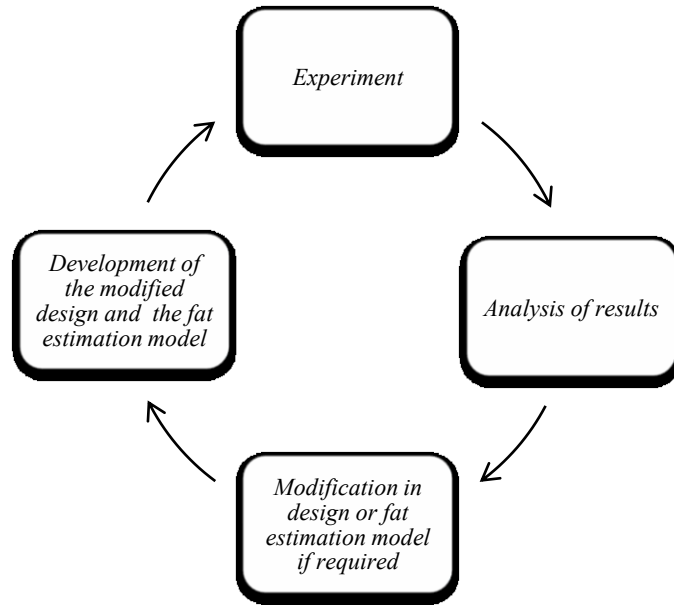


Figure 3.7: Design and development cycle of the device.

### 3.2.5 Experimental Setup

Seven individual experiments were performed without replication to complete all the assessment and achieve satisfactory performance of the estimation model as well as the hand-held device. One beef steak was purchased for each experiment and incremental increase in the amount of surface fat was simulated by increasing the number of fat pieces sequentially. Notably, the beef sample and the measurement area was constant at different amount of surface fat. There were different parameters and purposes for the individual experiments, and these are listed in Table 3.1. The size of the fat pieces along with the height of the probe or optical sensor from the measurement surface was varied to investigate performance difference in the system. The VIS spectrometer, NIR spectrometer and the hand-held device were tested and studied in these experiments.

The optical fiber cable probe was adjusted to a height of 60 or 80 mm from the surface of the meat, and had light circle diameters of 32.5 and 36.5 mm, respectively, on the measurement

surface and the height varied between individual experiments. The hand-held device sensor module had either three (588, 593, and 605 nm) or five (592, 593, 595, 601, and 605 nm) LEDs and all LEDs were focused onto a common region on the meat surface. The LEDs were angled (for the non-rotating LED sensor unit) or rotated (for the rotating LED sensor unit) in such a way that they had an overlapping illumination area on the meat sample at a distance  $x$  cm (where  $x$  cm was set depending on the experimental setup) away from the LEDs. To achieve increased amount of surface fat, fat pieces were added sequentially after each measurement as shown in Figure 3.8. The basic setup for all the VIS-NIR spectroscopic measurement was identical. The probe of the fiber optic cable was secured in place with the custom made stand (Figure 3.4). The other ends of the fiber optic cable were connected to spectrometer and light source according to manufacturer specifications. All spectroscopic measurements were taken in a dark environment (Figure 3.9 and 3.11) to reduce the effect of ambient light. Minor changes to experimental setup were made during a series of unreplicated experiments to address new hypotheses and these are detailed in Table 3.1.

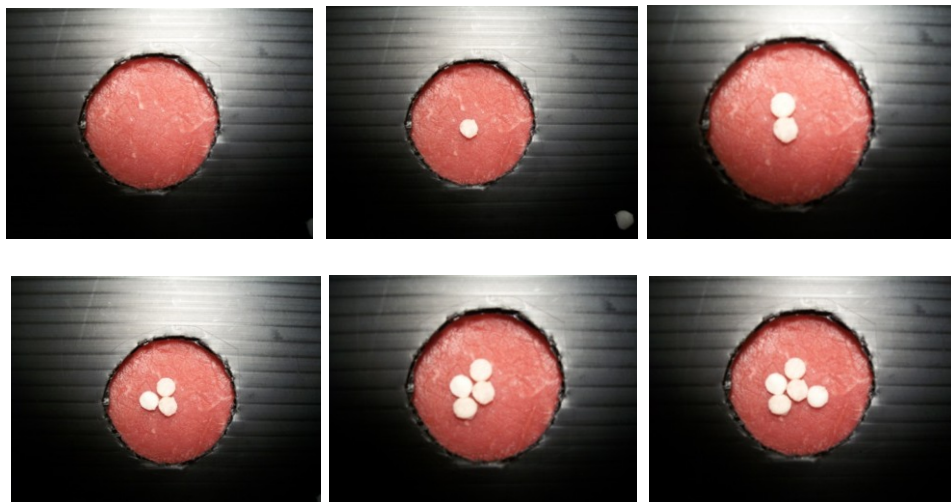


Figure 3.8: Sequential increment of fat pieces for spectroscopic measurements on a beef steak to simulate increased surface fat from none (top left) to five pieces of fat (bottom right). The steak was placed under a black mask cover to exclude entire surface regions on the measurement surface except the area that was intended to be measured.



Figure 3.9: Spectroscopic measurements using VIS light spectrometer were taken in a dark room. The left image is showing a measurement taken in a dark room, and the right image is showing the VIS light illuminated sample with two pieces of fat on the measurement surface.

To accommodate testing of design modifications, setups differed for the individual LED, sensor module or handheld device across experiments. A small PCB was used to mount three LEDs (manufacturer specified wavelength 588, 593, and 605 nm) along with the BPW34 photodiode to build the sensor unit. This sensor unit was used during the experiment performed on 25/11/10 and 17/11/10 (Table 3.1). During these experiments the LIA filter was designed and built on a large “Breadboard” or “Protoboard” by combining three “Breadboards” together and the digital control unit was a custom made general purpose ATmega32 microcontroller board built on a Veroboard<sup>TM</sup>. A new sensor module was designed and built using five different LEDs (manufacturer specified wavelengths of 592, 593, 595, 601 and 605 nm) to acquire more wavelength data to use with the fat estimation model. This new sensor was used during experiments on 8/2/11 and 6/4/11. A temporary sensor module with LEDs mounted on a rotating disk of PCB was designed and tested and the hand-held device fitted with rotating LED sensor unit, LIA filter, and digital control circuit was designed for the experiment on 4/7/11 as shown in Figure 3.10. The setup of each steak with fat pieces for measurement using LED or LED sensor was identical to that used in VIS-NIR spectroscopy measurements. Notably, the measurement

using the LED sensor unit did not require a dark environment as it used a LIA filter to filter and remove any ambient noise. However, to be cautious, fluorescent light sources in the room were turned off.

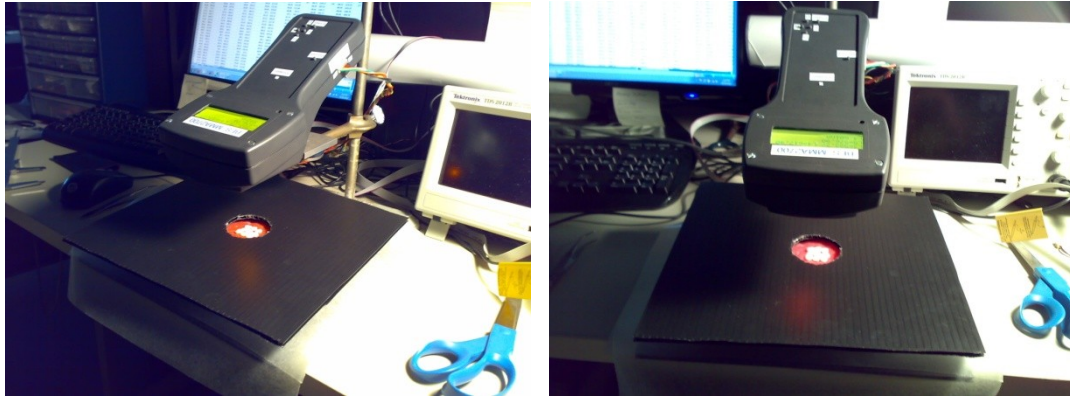


Figure 3.10: The side view (left) and the front view (right) of the hand-held device attached to a stand placed above the sample with the black mask in place for measurements.

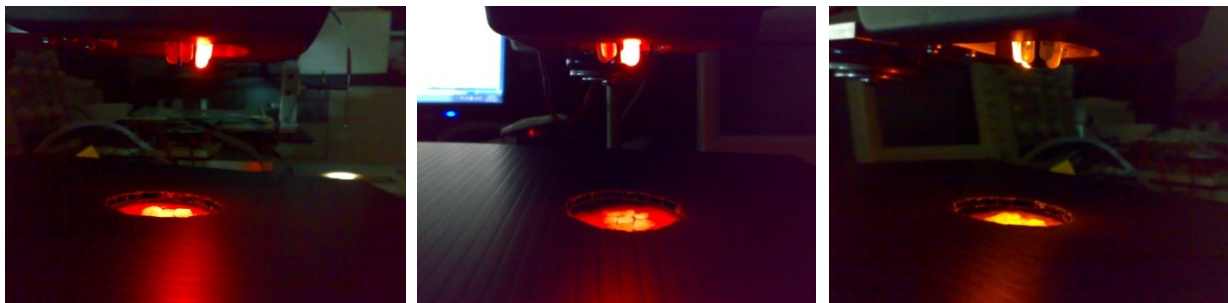


Figure 3.11: Experimental set up of the hand-held device with the fixed base LED sensor unit for measurements. Illumination of the sample measurement surface using three different LEDs on the non-rotating sensor unit is presented from left to right.

Table 3.1: Unreplicated experiments performed on single steaks using the LED sensor unit on the hand-held device.

Experiment Date (d/m/y)	Purposes	Modifications				Sensor of the hand-held device
		Height	Light circle diameter (Approximate)	Small pieces of fat (Diameter 4.5 mm)	Big pieces of fat (Diameter 7.5 mm)	
12/11/10	Formation of the fat estimation model. Performance study of the VIS spectrometer using the fat estimation model.	Probe distance from the measurement surface: 60 mm	VIS light: 32.5 mm	0	20	NA
17/11/10	Study of the fat estimation model using spectrum bands of chosen LEDs and sample data collected in the experiment on 12/11/10 by integration method (explained in data analysis section).	Probe distance from the measurement surface: 60 mm  LED distance from the measurement surface: 60 mm (Estimated)	LED light: (not recorded!)	NA	NA	Individual LED of 588 nm, 593 nm and 605 nm (wavelengths of LEDs as specified by manufacturer)
25/11/10	Study of the fat estimation model using VIS spectrometer and the electronic setup of the device with its sensor, LIA filter and digital processing unit.	Probe distance from the measurement surface: 60 mm Sensor distance from the measurement surface: 60 mm	VIS light: 32.5 mm	0	5	Sensor module had three LEDs of 588 nm, 593 nm and 605 nm (wavelengths of LEDs as specified by manufacturer) and a photodiode (BPW34). This module had static sensor PCB with all the LEDs focused onto a common region on the measurement surface.

8/2/11 part 1	Study of the new sensor module with 5 different LED and performance of the system using increased sensor and probe height.	Probe distance from the measurement surface: 80 mm Sensor distance from the measurement surface: 80 mm	VIS light: 36.5 mm	8	0	Static sensor module with five different LEDs of 592nm, 593nm, 595nm, 601nm and 605nm (wavelengths of LEDs as specified by manufacturer) and the BPW34 photodiode.
8/2/11 part 2	Study of both VIS spectrometer and handheld device system using increased size of fat pieces.	Probe distance from the measurement surface: 80 mm Sensor distance from the measurement surface: 80 mm	VIS light: 36.5 mm	0	6	Same as the sensor used in part 1 of this experiment.
6/4/11	Study of both VIS spectrometer and handheld device system using decreased probe and sensor height.	Probe distance from the measurement surface: 60 mm Sensor distance from the measurement surface: 60 mm	VIS light: 29 mm	0	9	Same as the sensor used in experiment on 8/2/11.
4/7/11	Study of both VIS spectrometer and handheld device system in order to test the performance of linear fit on spectrum data for denoising and new rotating sensor.	Probe distance from the measurement surface: 60 mm Sensor distance from the measurement surface: 60 mm	VIS light: 29 mm (Estimated)	0	9	Rotating sensor module with five different LEDs of 592nm, 593nm, 595nm, 601nm and 605nm (wavelengths of LEDs as specified by manufacturer) and a photodiode (BPW34).

20/7/11	Study of NIR spectrometer and NIR spectroscopy using fat pieces to simulate increase or decrease in fat.	Probe distance from the measurement surface: 40 mm.	VIS light: 25 mm(recorded by passing VIS light and measuring the diameter)	0	10	NA
---------	--	---	--	---	----	----

### 3.3 Data analysis:

All measurement data were saved in Excel™ files. The data analysis was performed in MATLAB™ using the data saved in Excel™ files. Three generic MATLAB™ programs were written (Appendix B) to analyze VIS, NIR and LED spectroscopy data. Minor changes in parameters and functions were made to these programs during the various experiments. Reflectivity of each wavelength was calculated using the following formula:

$$R = \frac{I_{reflected} - I_{dark}}{I_{reference} - I_{dark}} \times 100 \quad (3.1)$$

In this equation, R is the reflectivity of each wavelength,  $I_{reflected}$  is the light intensity of each wavelength reflected back from the sample,  $I_{reference}$  is the light intensity of each wavelength reflected back from the white reference (Teflon™ sheet) and  $I_{dark}$  is the dark noise which was measured when there was no light (the probe was covered with a cap). Great care was taken during recording of  $I_{reflected}$  and  $I_{reference}$  to ensure that experimental setup and all other measurement conditions were constant. A substantial amount of noise can be removed by subtracting the dark current noise ( $I_{dark}$ ) from the  $I_{reflected}$  and  $I_{reference}$ . The dark current noise and other noises are random in nature and so application of a smoothing filter can remove this noise but it will also reduce the high contrast peaks. The slope of reflectivity (m) at wavelength  $\lambda$  was calculated using the following formula:

$$m = dR/d\lambda \quad (3.2)$$

In this equation, R is the reflectivity at wavelength  $\lambda$ . It was understood that the slope of reflectivity at certain wavelengths in the range 588 to 605 nm could be utilized to predict the

amount of fat in beef. In this method it was clear that the high contrast peaks were not necessary as the slope of reflectivity was the key component for the fat estimation model. A moving average filter was used to smooth the spectroscopy data. The calculation steps for slope of reflectivity using smoothing filters were as follows;

1.  $I_{\text{vis}}$  = VIS light spectra collected from meat surface at different number of FAT pieces.
2.  $I_{\text{visf}}$  = Filtered  $I_{\text{vis}}$  using moving average filter with 51 (11 nm, as the resolution was 0.22 nm) data points (smoothing coefficient).
3.  $I_{\text{visref}}$  = Reference VIS light spectra collected from Teflon<sup>TM</sup> sheet.
4.  $I_{\text{visreff}}$  = Filtered  $I_{\text{visref}}$  using moving average filter with 51 (11 nm, as the resolution was 0.22 nm) data points (smoothing coefficients).
5.  $I_{\text{visdark}}$  = Dark current noise measured during the VIS spectrum measurement.
6.  $I_{\text{visdarkf}}$  = Filtered  $I_{\text{visdark}}$  using moving average filter with 51 (11 nm, as the resolution was 0.22 nm) data points (smoothing coefficients).
7.  $R$  (reflectivity) =  $(I_{\text{visf}} - I_{\text{visdarkf}}) / (I_{\text{visreff}} - I_{\text{visdarkf}}) \times 100$ .
8.  $m$  (slope of reflectivity) =  $dR/d\lambda$ .
9.  $m_f$  = Filtered  $m$  using moving average filter with 51 (11 nm, as the resolution was 0.22 nm) data points (smoothing coefficient).

A smoothing coefficient of 51 data points was used in general but smoothing coefficients of 90 (data not shown) and 151 data points were also tested during different experiments. Similar equations were used to transform NIR spectrum data for analysis. The reflectivity of each LED was calculated using Equation 3.1 but without subtracting the dark current. The wavelengths of individual LEDs were approximated to be equal to the peak intensity wavelength (specified by manufacturer) of that specific LED. Slope of reflectivity was calculated using Equation 3.2. The

calculated LED reflectivity data was analyzed in MATLAB<sup>TM</sup> as three or five wavelengths spectrum as required. A separate MATLAB<sup>TM</sup> program (Appendix B) was used for this purpose.

The experiment performed on 17/11/10 was focused on finding the viability of using LED at specific individual wavelengths. The LED spectrum showed its highest intensity near to the peak wavelength as specified by the manufacturer. It was assumed that these LED spectrums could be approximated to be a single wavelength light source at peak wavelength. In this experiment each LED spectrum was recorded using VIS spectrometer (Ocean Optics USB400) and normalized by the maximum intensity value (number of photons) at peak wavelength. This normalized spectrum of each LED was multiplied with the reflectance spectrum of VIS light, collected during Experiment 12/11/10. Each result of the multiplication was integrated over the entire range of wavelength of VIS spectrometer. These integrations helped to obtain simulated LED reflectance from the VIS light spectrums of different fat pieces. These simulated reflectances were normalized using simulated reflectance of Teflon<sup>TM</sup> sheet to obtain simulated reflectivity for various amounts of fat pieces. Results of this experiment are presented in the result section. A MATLAB<sup>TM</sup> program (Appendix B) was used in this experiment for various calculations. A smoothing filter with a smoothing coefficient of 51 was used to filter all spectrum data from the spectrometer. “Dark current” was subtracted from all LED spectrums as well as from all VIS spectrums.

The linear relationships between slope of reflectivity and number of fat pieces were presented in graphs using linear regression equation lines (dashed black lines) and regression coefficient ( $R^2$ ) values were included on each graph. Results from different measurement systems were analyzed individually and compared to each other to identify any discrepancies that may exist.

This technique helped identify similarities and differences not only in different measurement systems but within individual wavelengths.

### **3.4 Results:**

#### **3.4.1 Experiment on 12/11/10**

A graph of reflectivity over the entire spectrum of the spectrometer plotted for 20 fat pieces (Figure 3.12) showed that as the number of fat pieces increased the initial relationship with the amount of fat that was present was lost above six or seven fat pieces. Examination of the same reflectivity data for one to five fat pieces indicated that changes in the slope of the reflectivity were apparent around 600 nm (Figure 3.13). A graph of the slope of reflectivity (first order derivative of reflectivity,  $dR/d\lambda$ ) at each wavelength confirmed this hypothesis (Figure 3.14 and 3.15). Linear relationships between slopes of reflectivity with number of fat pieces were examined by scatter plots and linear regression  $R^2$  values at wavelengths between 588 and 612 nm (Figure 3.16). Linear regression  $R^2$  values at wavelengths from 588 to 612 nm are presented in Table 3.2.

The area of the circular opening (assuming an ideal circle) of the black mask cover was approximately  $1590 \text{ mm}^2$  ( $A = \pi r^2, r = \text{diameter}/2$ ), area covered by each small fat pieces (assuming ideal circle) was about  $15.9 \text{ mm}^2$ , and the area covered by each big fat pieces (assuming ideal circle) was about  $44 \text{ mm}^2$ . Hence, the percentage area covered by each big fat piece was about 2.78% and each small fat piece was about 1%.

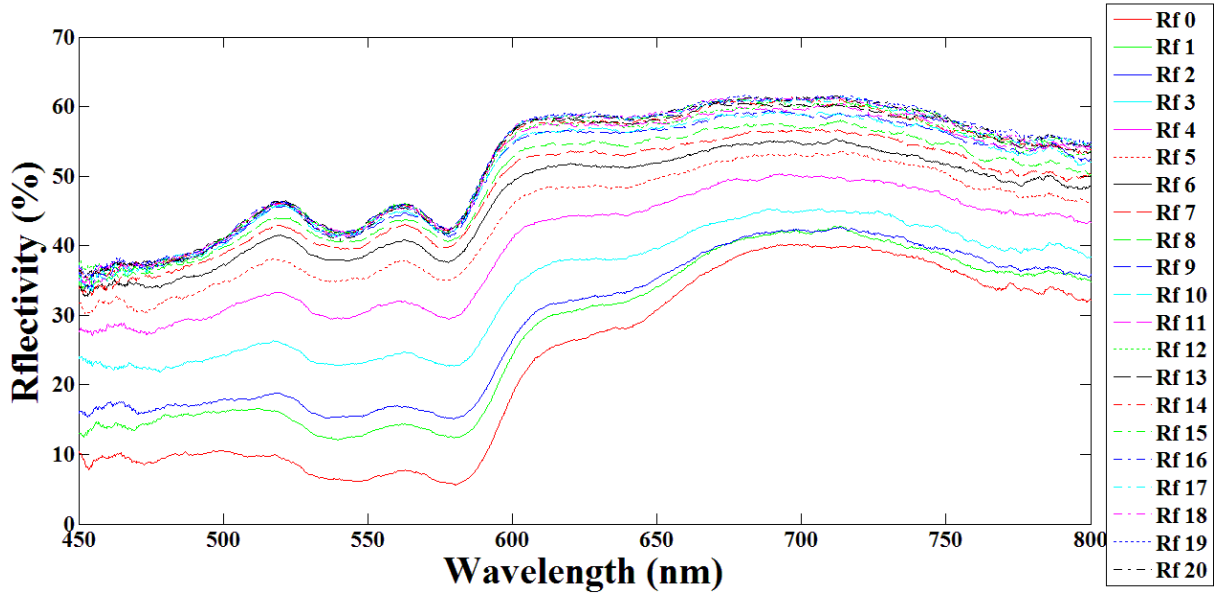


Figure 3.12: Plot of the reflectivity as a function of wavelength for zero (0) to twenty (20) fat pieces with a smoothing coefficient of 51. The legends Rf 0 to Rf 20 represent reflectivity plots for 0 to 20 fat pieces.

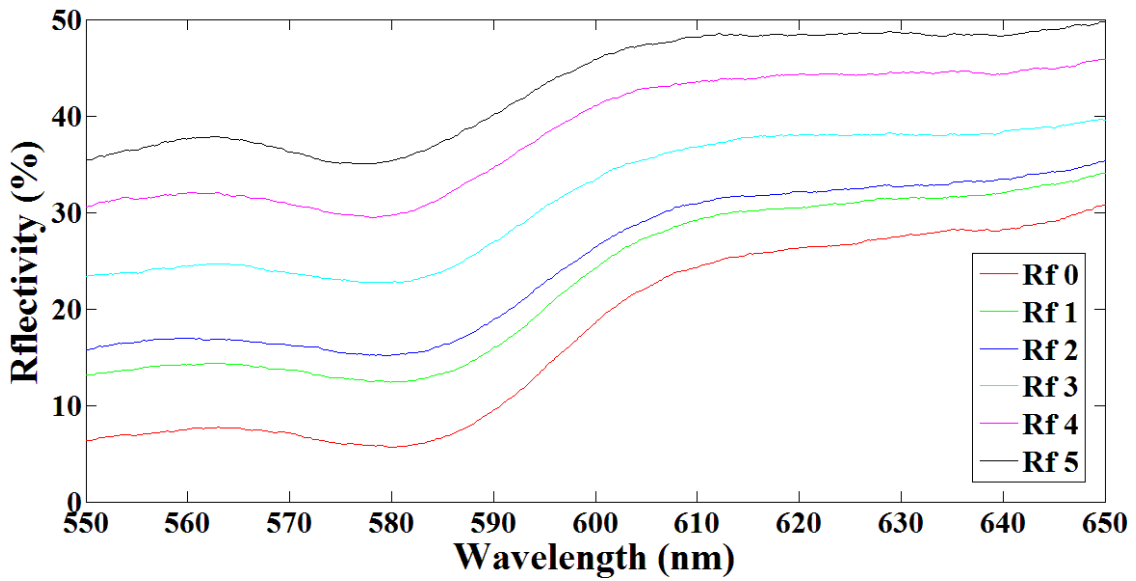


Figure 3.13: Magnified plot of the reflectivity as a function of wavelength for zero (0) to five (5) fat pieces at wavelengths from 550 to 650 nm with a smoothing coefficient of 51. The legends Rf 0 to Rf 5 represent reflectivity plots for 0 to 5 fat pieces.

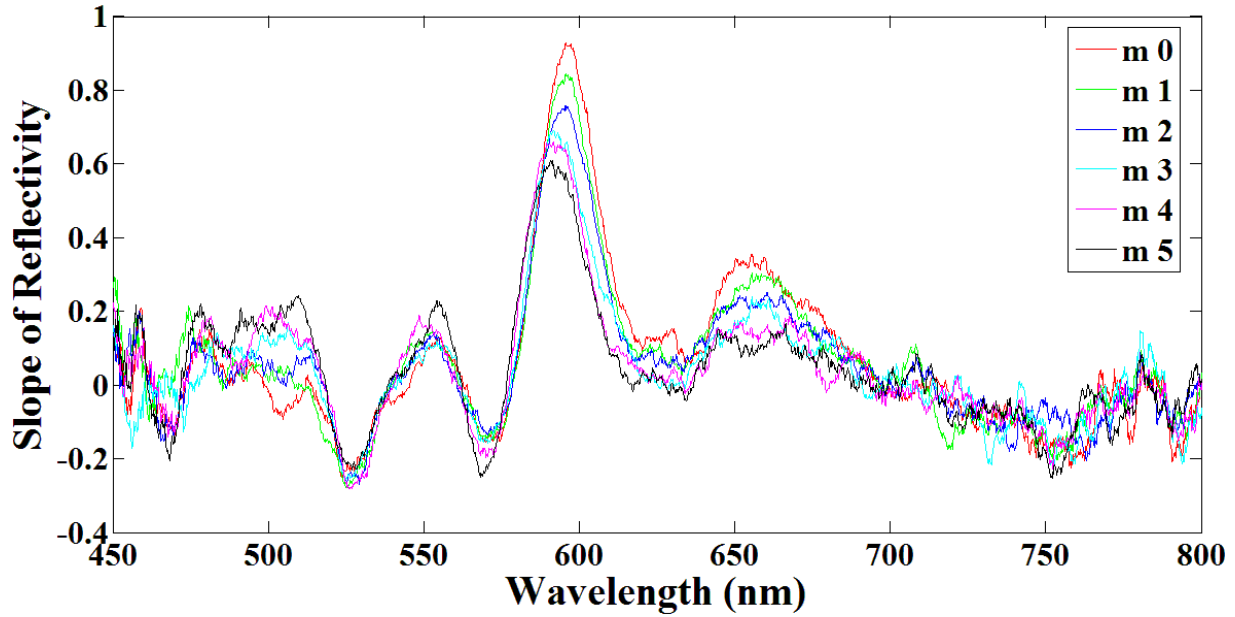


Figure 3.14: Plot of the slope of reflectivity as a function of wavelength for zero (0) to five (5) fat pieces with a smoothing coefficient of 51. The legends m 0 to m 5 represent slope of reflectivity plots for zero to five fat pieces.

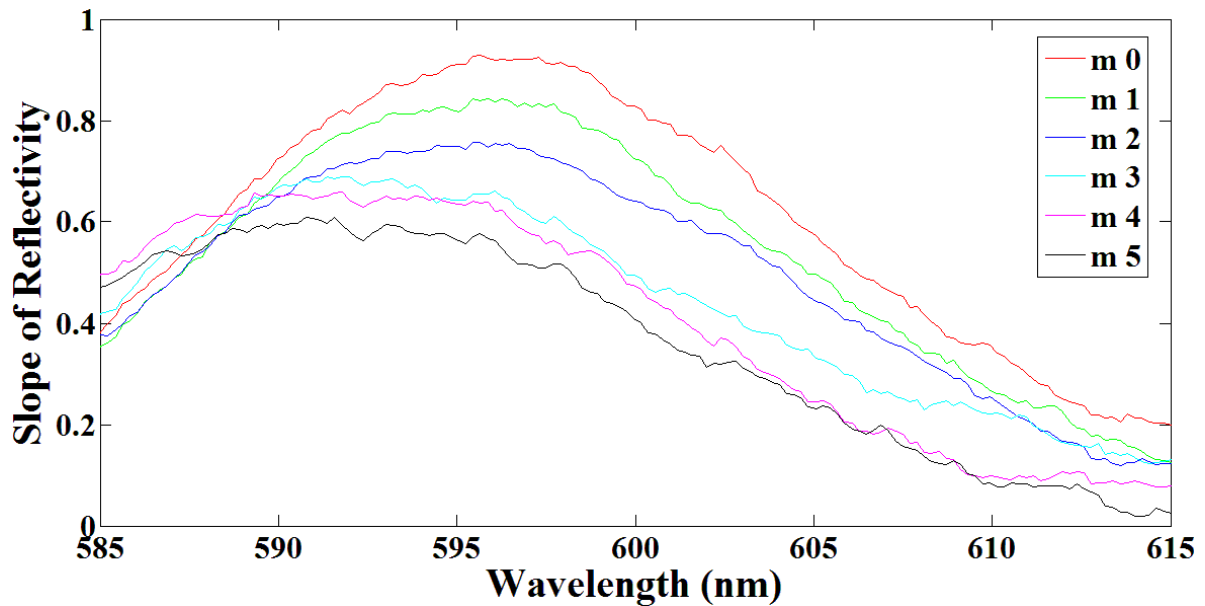


Figure 3.15: Magnified plot of the slope of reflectivity as a function of wavelength for zero (0) to five (5) fat pieces at wavelengths from 585 to 615 nm with a smoothing coefficient of 51. The legends m 0 to m 5 represent slope of reflectivity plots for 0 to 5 fat pieces.

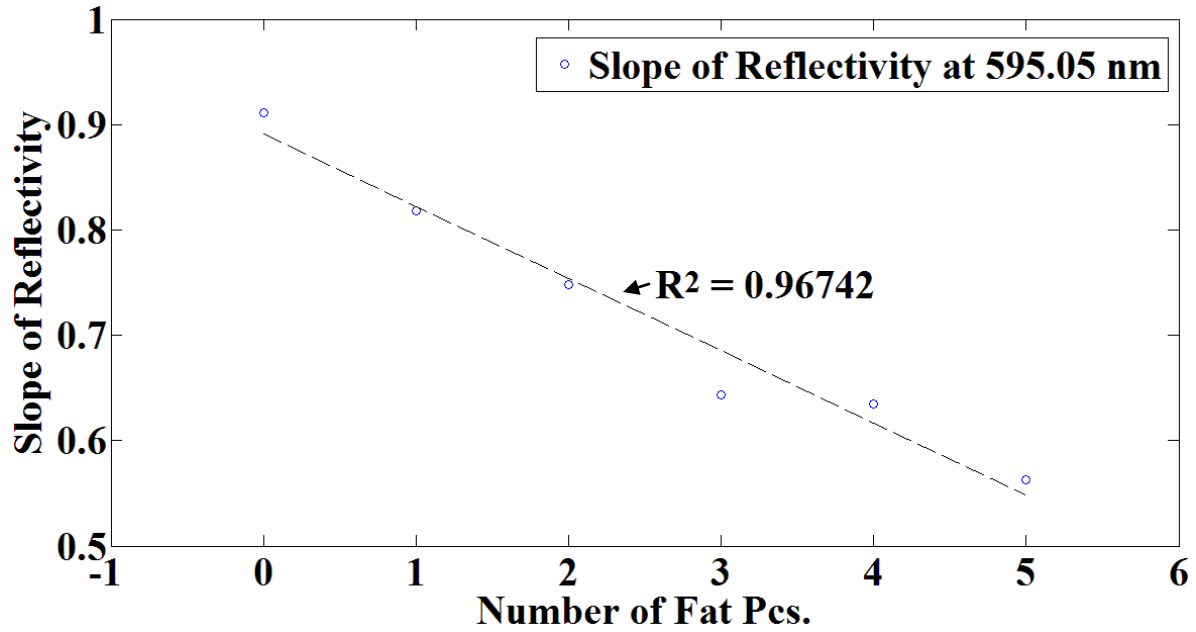


Figure 3.16: Slope of reflectivity as a function of number of fat pieces at 595.05 nm (spectrometer wavelength).

Table 3.2:  $R^2$  values for linear regression between slope of reflectivity and number of fat pieces at wavelengths from 588.09 to 612.17 nm.

Spectrometer Wavelength (nm)	$R^2$
588.09	0.003
590.14	0.83
592.19	0.99
593.01	0.99
595.05	0.97
597.09	0.98
600.16	0.97
601.99	0.98
603.01	0.96
605.05	0.97
607.08	0.96
610.13	0.93
612.17	0.97

These  $R^2$  values substantiated that a linear relationships existed at wavelengths from 592 to 612 nm between the slope of reflectivity and the amount of fat. However, the slope of reflectivity plot for 595 nm (Figure 3.17) for the 20 fat pieces revealed that after six pieces of fat the system appeared saturated and differentiation between various amounts of fat on the surface of the meat was lost.

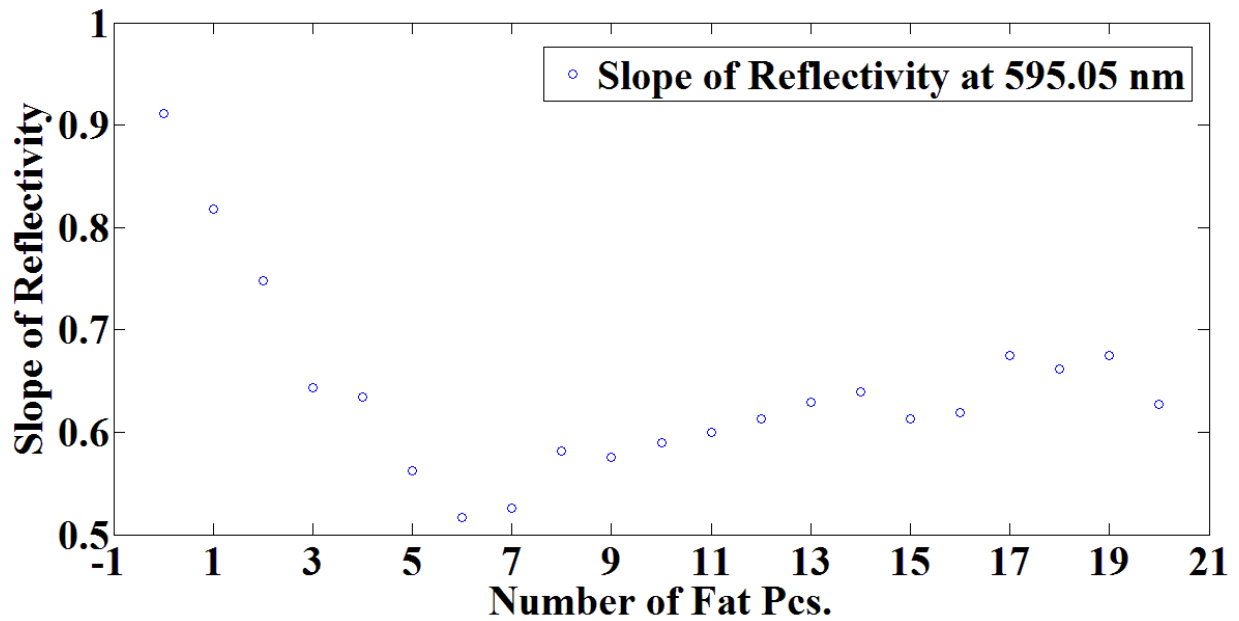


Figure 3.17: Slope of reflectivity as a function of number of fat pieces (20 pieces) at 595.05 nm.

### 3.4.2 Experiment on 17/11/10

The light intensities of the 588, 593, and 605 nm LEDs as recorded by VIS spectrometer are presented in Figure 3.18.

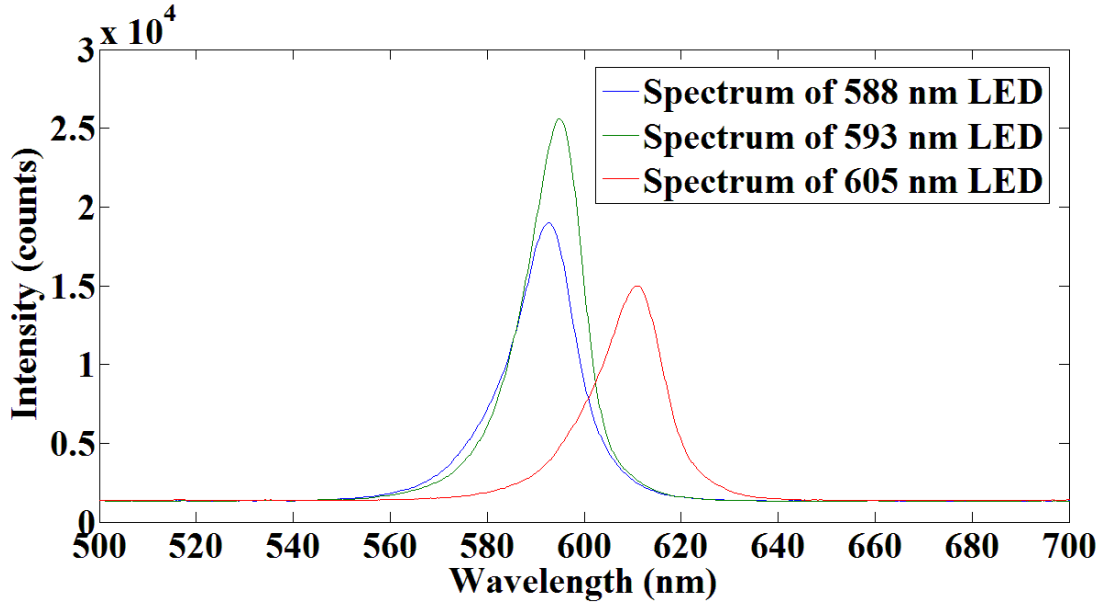


Figure 3.18: Light intensities of 588, 593, and 605 nm LED as a function of wavelength plot.

The normalized light intensity as a function of wavelength of each LED is plotted in Figure 3.19. Simulated reflectivity as a function of LED wavelength for five fat pieces at each LED wavelength is plotted in Figure 3.20.

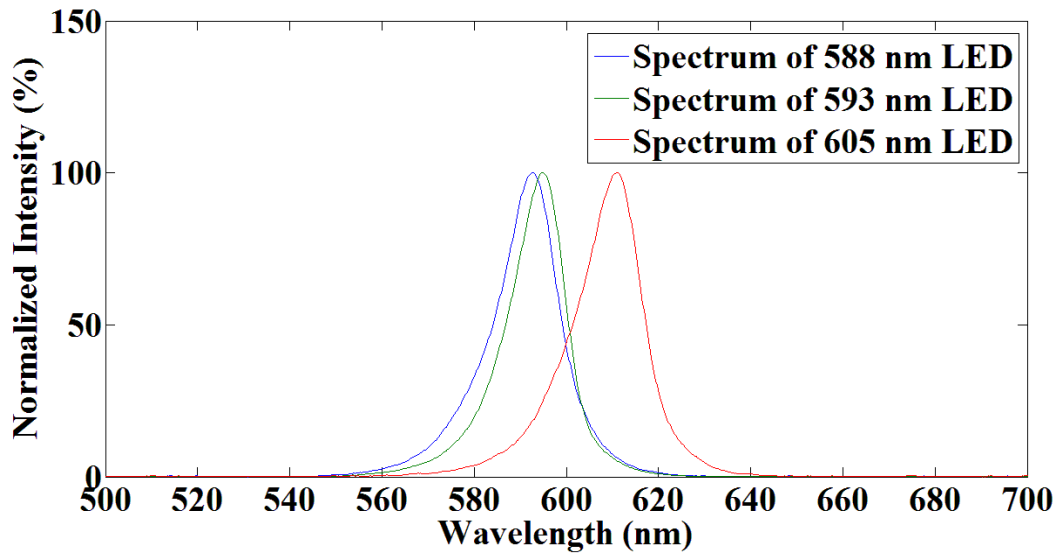


Figure 3.19: Normalized intensities of 588, 593, and 605 nm LED as a function of wavelength plot.

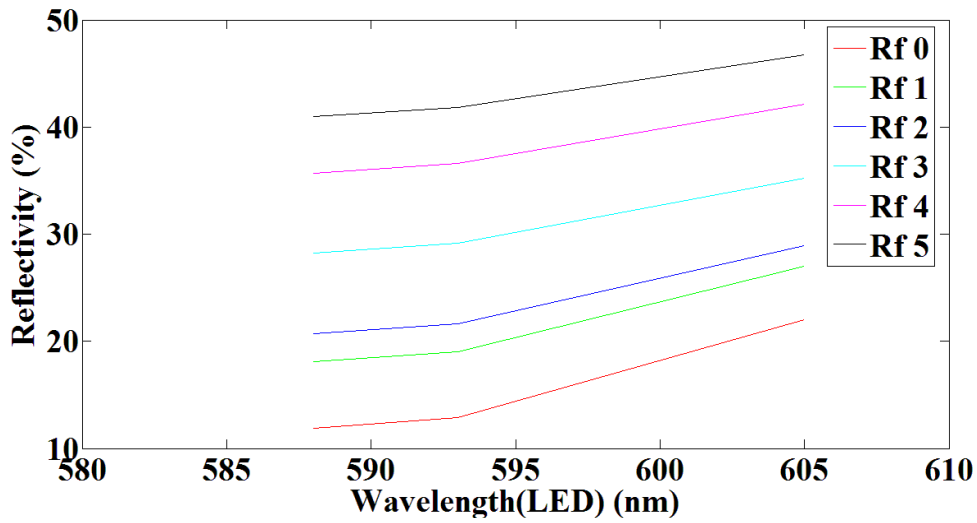


Figure 3.20: Plot of simulated reflectivity as a function of LED wavelength for zero (0) to five (5) fat pieces. The legends Rf 0 to Rf 5 represent simulated reflectivity plots for 0 to 5 fat pieces.

The plot of the slope of simulated reflectivity as a function of number of fat pieces at 588 and 593 nm LED showed linear relationship with number of fat pieces (Figures 3.21 and 3.22).

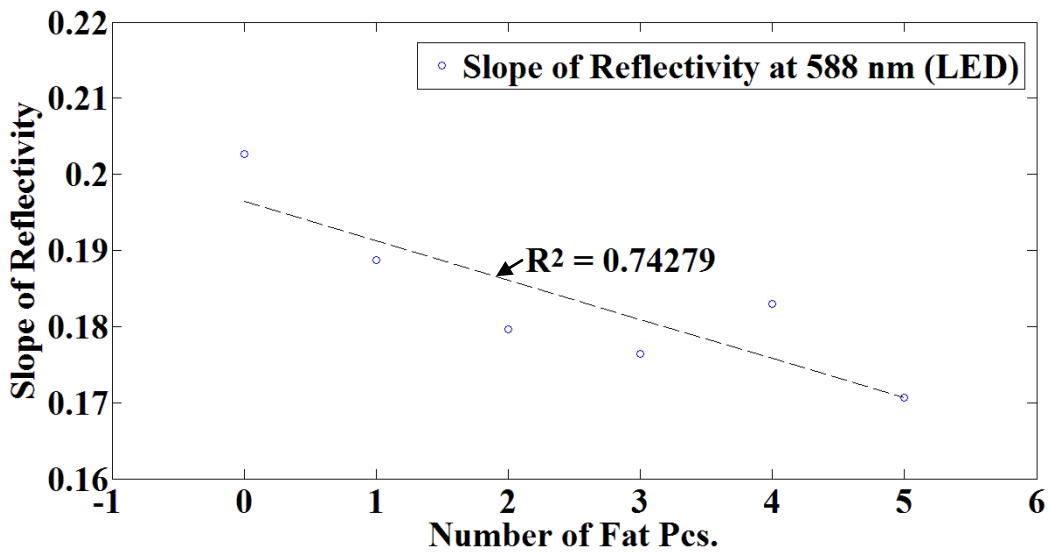


Figure 3.21: Slope of simulated reflectivity as a function of number of fat pieces at 588 nm (LED wavelength).

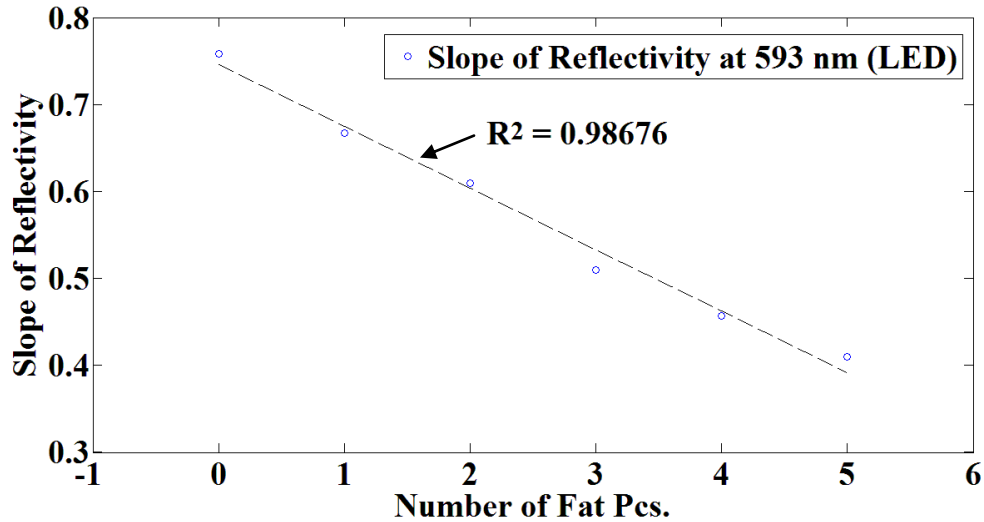


Figure 3.22: Slope of simulated reflectivity as a function of number of fat pieces at 593 nm (LED wavelength).

### 3.4.3 Experiment on 25/11/10

The reflectivity plots in Figures 3.23 and 3.24 indicated that the slope of each reflectivity plot in the wavelength range of 588 to 605 nm was changing as the number of fat pieces increased. This hypothesis was confirmed by plotting the slope of reflectivity as a function of wavelength for zero to five fat pieces (Figures 3.25 and 3.26). Results ( $R^2$  values) indicated that the data gathered at 588.09 nm did not show strong linearity with the amount of fat but that at 592.19, 593.01, 595.05, 600.16, and 605.05 nm had promising linear relationships with the amount of fat (Table 3.3). The 593 nm LED wavelength (manufacturer specified) did exhibit some linearity between the slope of reflectivity and the number of fat pieces but the 588 nm LED wavelength showed poor linearity and provided results directly opposed to what had been observed in a previous experiment (Figures 3.27 and 3.28).

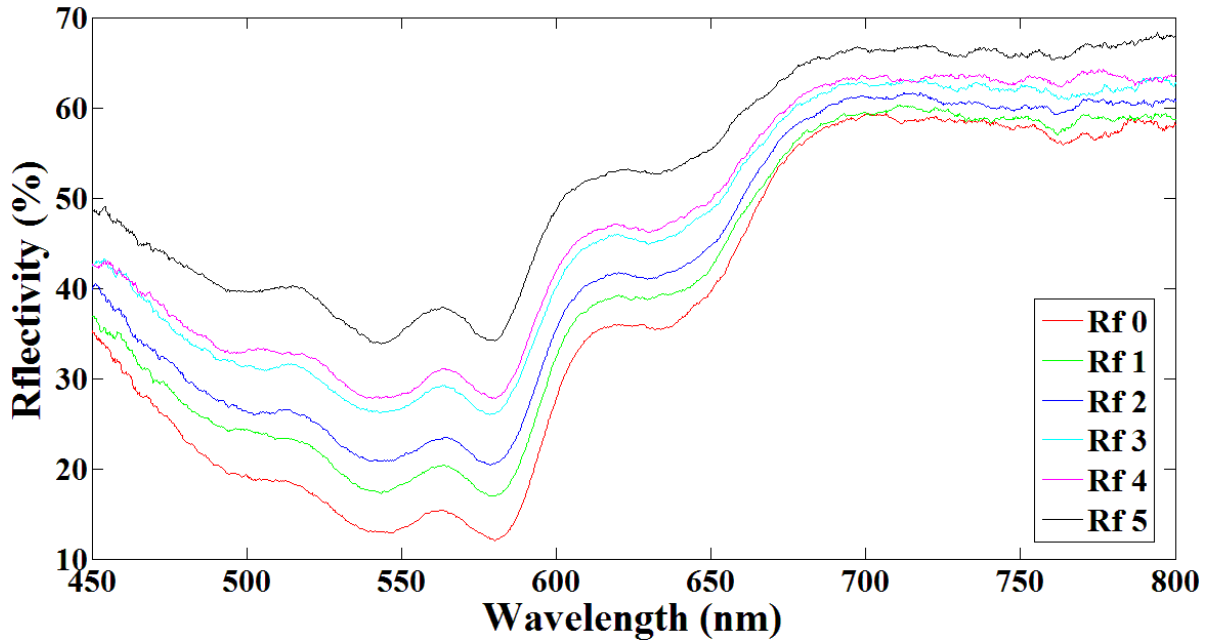


Figure 3.23: Plot of the reflectivity as a function of wavelength for zero (0) to five (5) fat pieces with a smoothing coefficient of 51. The legends Rf 0 to Rf 5 represent reflectivity plots for 0 to 5 fat pieces.

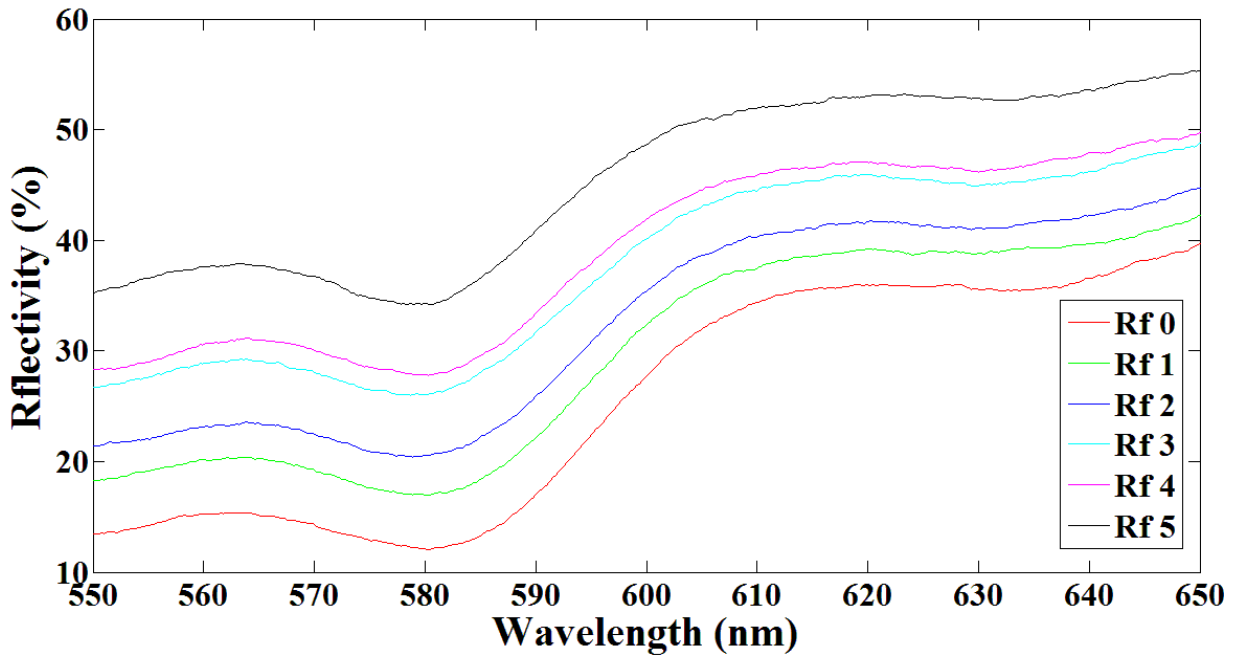


Figure 3.24: Magnified plot of the reflectivity as a function of wavelength for zero to five fat pieces at wavelengths from 550 to 650 nm with a smoothing coefficient of 51. The legends Rf 0 to Rf 5 represent reflectivity plots for 0 to 5 fat pieces.

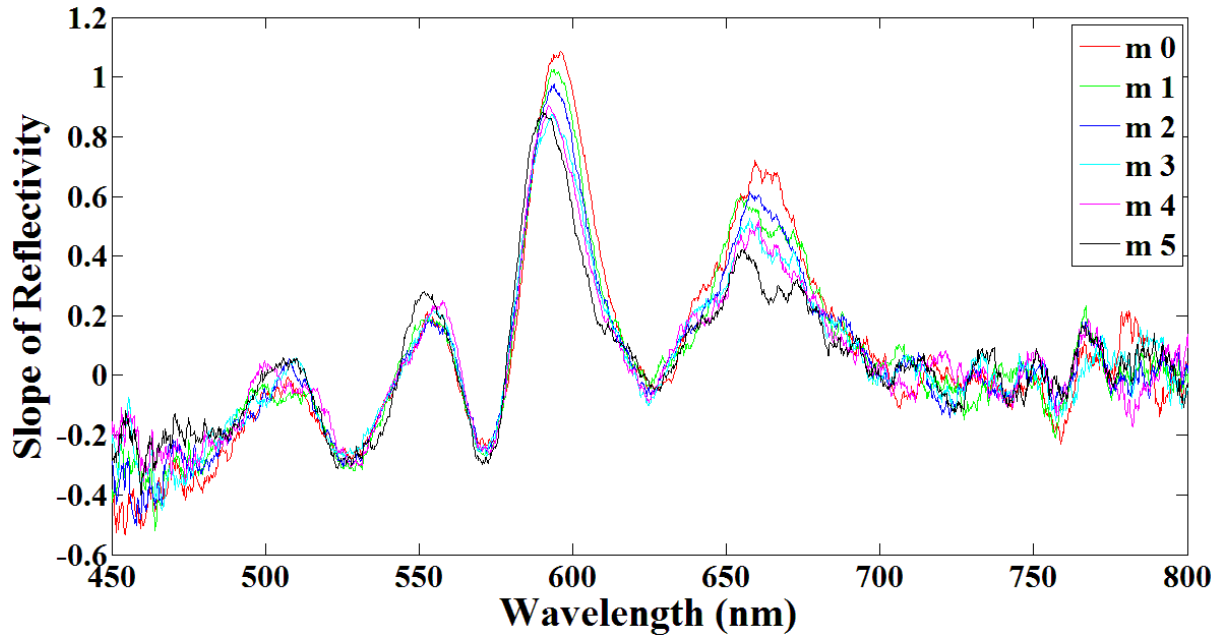


Figure 3.25: Plot of the slope of reflectivity as a function of wavelength for zero to five fat pieces with a smoothing coefficient of 51. The legends m 0 to m 5 represent slope of reflectivity plots for zero to five fat pieces.

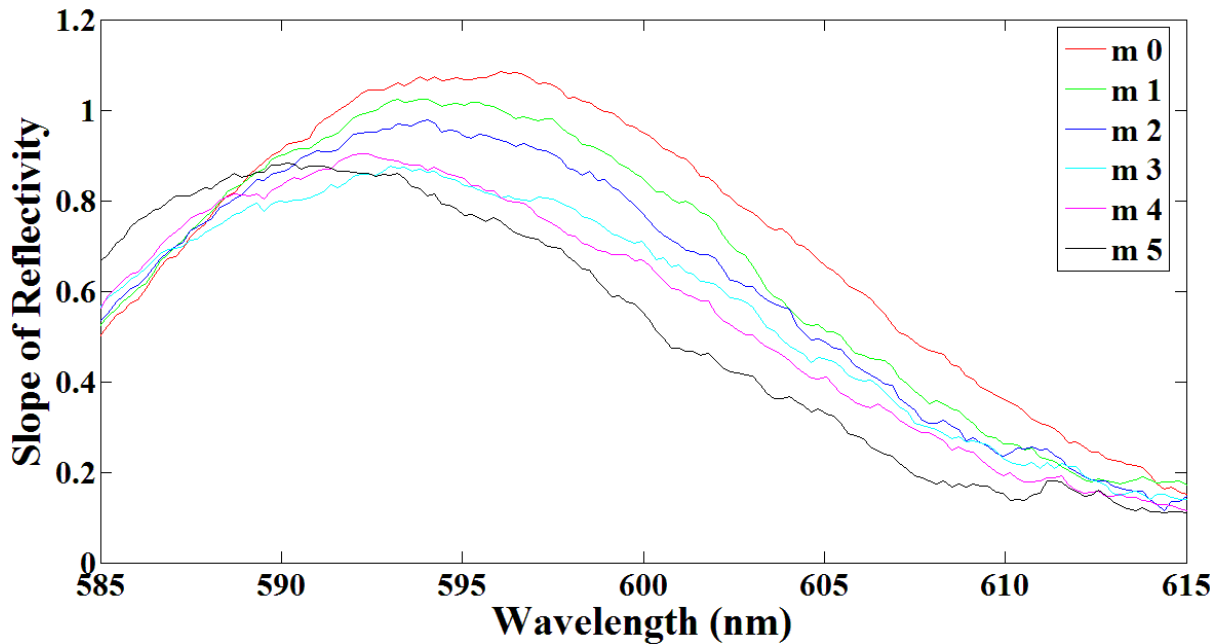


Figure 3.26: Magnified plot of the slope of reflectivity as a function of wavelength for zero (0) to five (5) fat pieces at wavelengths from 585 to 615 nm with a smoothing coefficient of 51. The legends m 0 to m 5 represent slope of reflectivity plots for zero to five fat pieces.

Table 3.3:  $R^2$  values of linear regression between slope of reflectivity and number of fat pieces at wavelengths from 588.09 to 605.05 nm (spectrometer results).

Spectrometer Wavelength (nm)	$R^2$
588.09	0.26
592.19	0.83
593.01	0.91
595.05	0.95
600.16	0.98
605.05	0.93

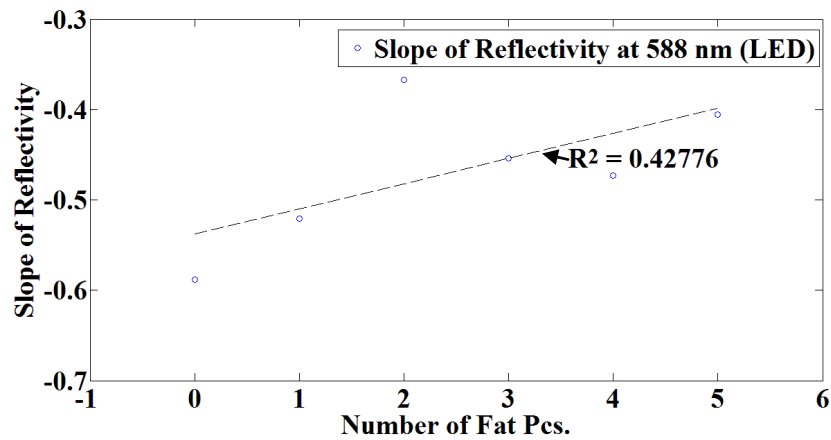


Figure 3.27: Slope of reflectivity from LED-spectroscopy as a function of number of fat pieces at 588 nm (LED wavelength as specified by manufacturer).

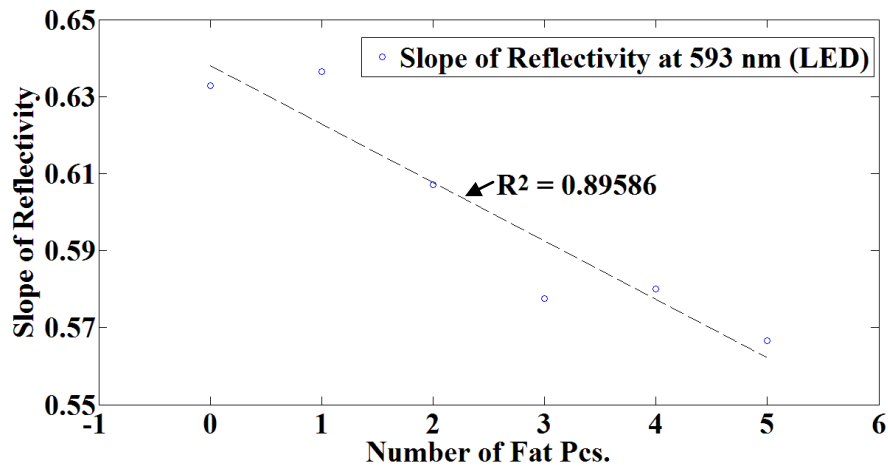


Figure 3.28: Slope of reflectivity from LED-spectroscopy as a function of number of fat pieces at 593 nm (LED wavelength as specified by manufacturer).

#### **3.4.4 Experiment on 8/2/11**

The height of the probe and LED sensor was increased to widen the area of measurement on the surface of the meat with an expectation of achieving improved prediction at more than seven fat pieces. This was not realized as the slope of reflectivity against wavelength plots (Figures 3.29 and 3.30) had increased noise due to the increase in probe height. Results of linear regression between the slope of reflectivity and number of fat pieces (big and small fat pieces) at 592.19, 593.01, 595.05, 600.16, and 605.05 nm using a smoothing coefficient of 51 had decreased linearity (Table 3.4). As a result, a smoothing coefficient of 151 rather than 51 was used to reduce the influence of the increased noise (Figures 3.31 and 3.32). Some increased linearity between fat piece numbers and slope of reflectivity was observed with higher order smoothing coefficients at 592.19, 593.01, 595.05, and 600.16 nm (Table 3.5), but linearity differed dramatically between large and small fat pieces at each wavelength. Unexpectedly, the amount of linearity of slope of reflectivity with number of fat pieces differed between the VIS spectroscopy and LED-spectroscopy (Table 3.6), indicating that the visible light source and the LED-spectroscopy performed or detected reflectance dissimilarly in this experiment.

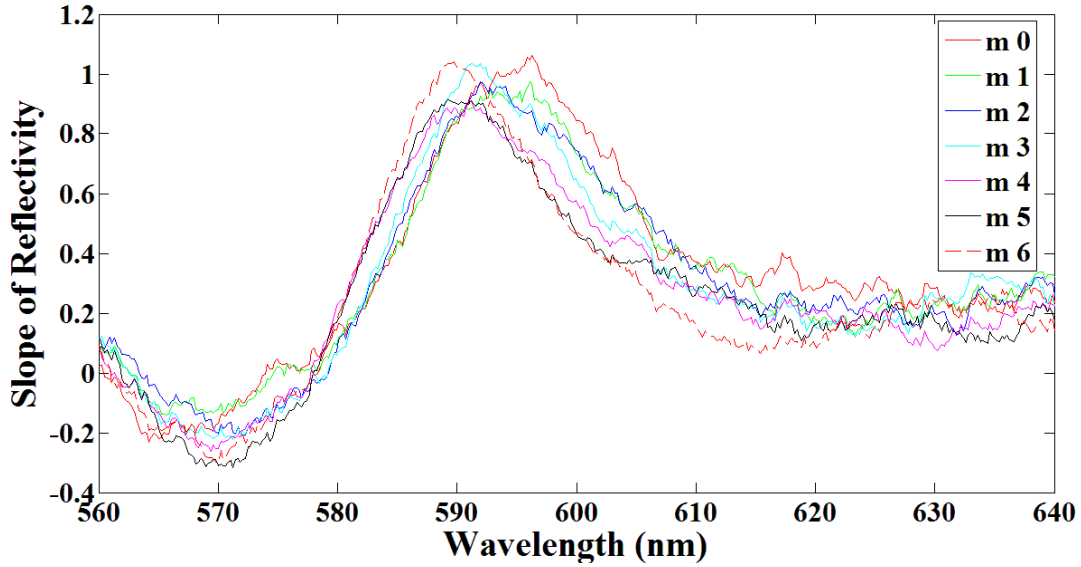


Figure 3.29: Plot of the slope of reflectivity as a function of wavelength for zero to six large fat pieces with a smoothing coefficient of 51. The legends m 0 to m 6 represents slope of reflectivity plots for 0 to 6 fat pieces.

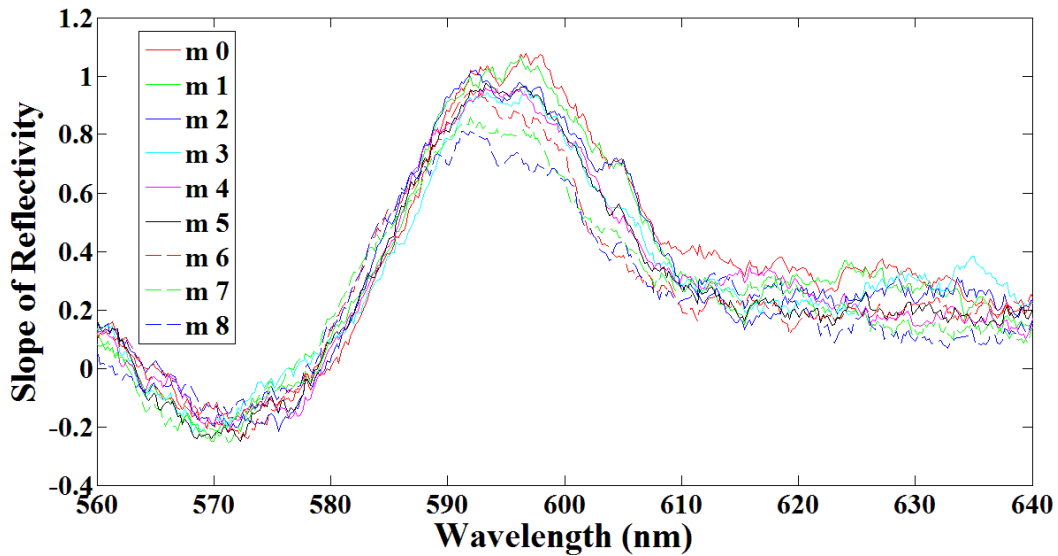


Figure 3.30: Plot of the slope of reflectivity as a function of wavelength for zero to eight small fat pieces with a smoothing coefficient of 51. The legends m 0 to m 8 represent slope of reflectivity plots for 0 to 8 fat pieces.

Table 3.4:  $R^2$  values of linear regression between slope of reflectivity and number of fat pieces (big and small fat pieces) at wavelengths from 588.09 to 605.05 nm using a smoothing coefficient of 51.

Spectrometer Wavelength (nm)	$R^2$ (big fat pieces)	$R^2$ (small fat pieces)
592.19	0.05	0.72
593.01	0.47	0.84
595.05	0.85	0.79
600.16	0.95	0.90
605.05	0.93	0.85

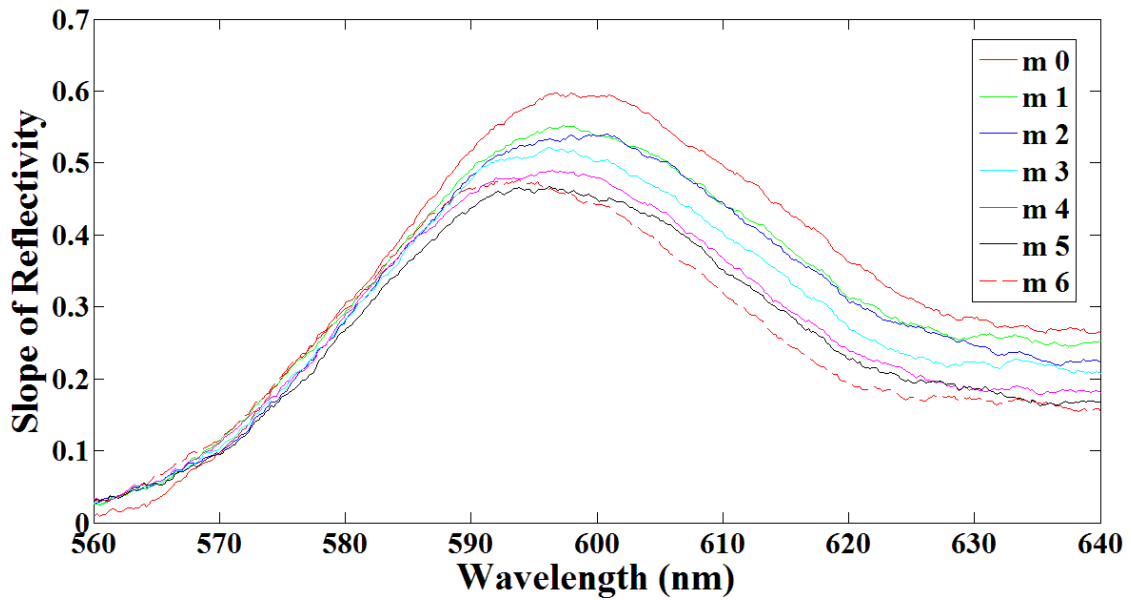


Figure 3.31: Plot of the slope of reflectivity as a function of wavelength for zero to six large fat pieces with a smoothing coefficient of 151. The legends m 0 to m 6 represent slope of reflectivity plots for 0 to 6 fat pieces.

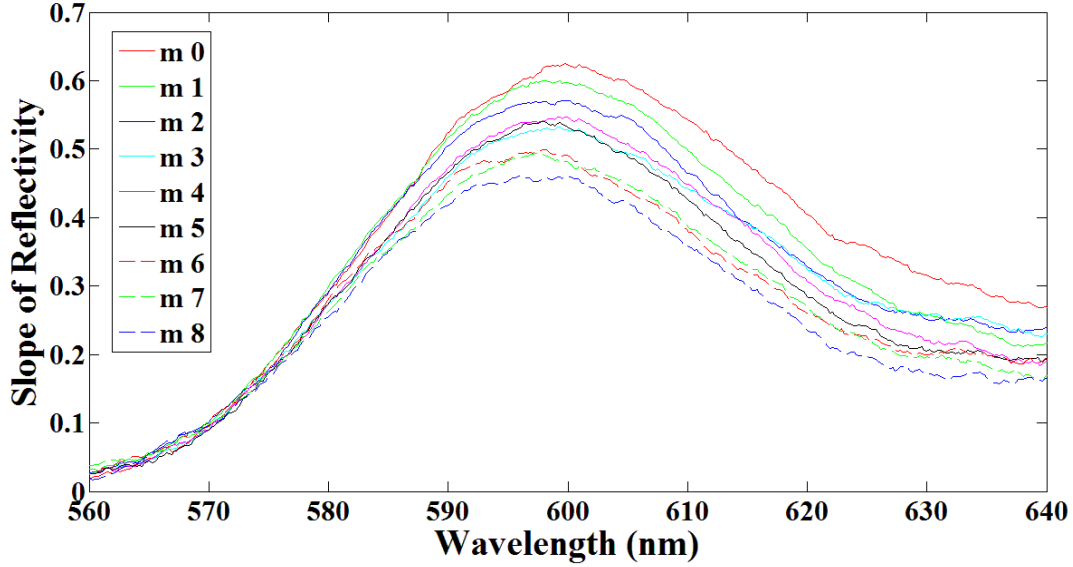


Figure 3.32: Plot of the slope of reflectivity as a function of wavelength for zero to eight small fat pieces with a smoothing coefficient of 151. The legends m 0 to m 8 represent slope of reflectivity plots for 0 to 8 fat pieces.

Table 3.5:  $R^2$  values of linear regression between slope of reflectivity and number of fat pieces (large and small fat pieces) at wavelengths from 592.19 to 600.16 nm using smoothing coefficient of 151.

Spectrometer Wavelength (nm)	$R^2$ (large fat pieces)	$R^2$ (small fat pieces)
592.19	0.88	0.94
593.01	0.90	0.95
595.05	0.93	0.94
600.16	0.96	0.95

Table 3.6:  $R^2$  values of linear regression between slope of reflectivity of LED-spectroscopy and number of fat pieces (large and small fat pieces) at LED wavelengths from 592 to 601 nm.

LED Wavelength (nm)	$R^2$ (large fat pieces)	$R^2$ (small fat pieces)
592	0.88	0.83
593	0.97	0.74
595	0.94	0.39
601	0.71	0.75

### 3.4.5 Experiment on 6/4/11

Returning the probe and LED sensor height to 60 mm decreased noise level (Figures 3.33 and 3.34) so a smoothing coefficient of 51 was re-adopted.

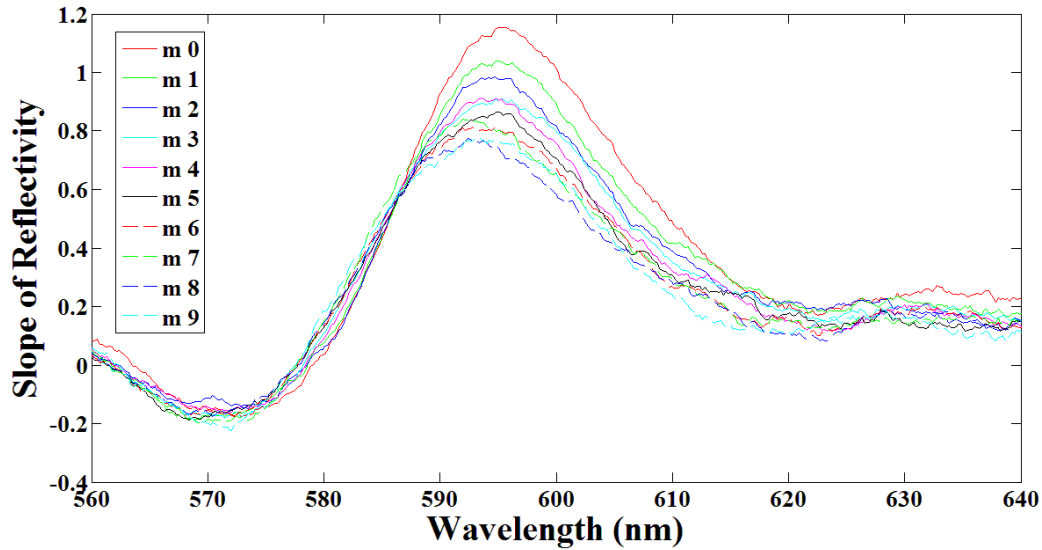


Figure 3.33: Plot of the slope of reflectivity as a function of wavelength for zero (0) to nine (9) fat pieces with a smoothing coefficient of 51. The legends m 0 to m 9 represent slope of reflectivity plots for 0 to 9 fat pieces.

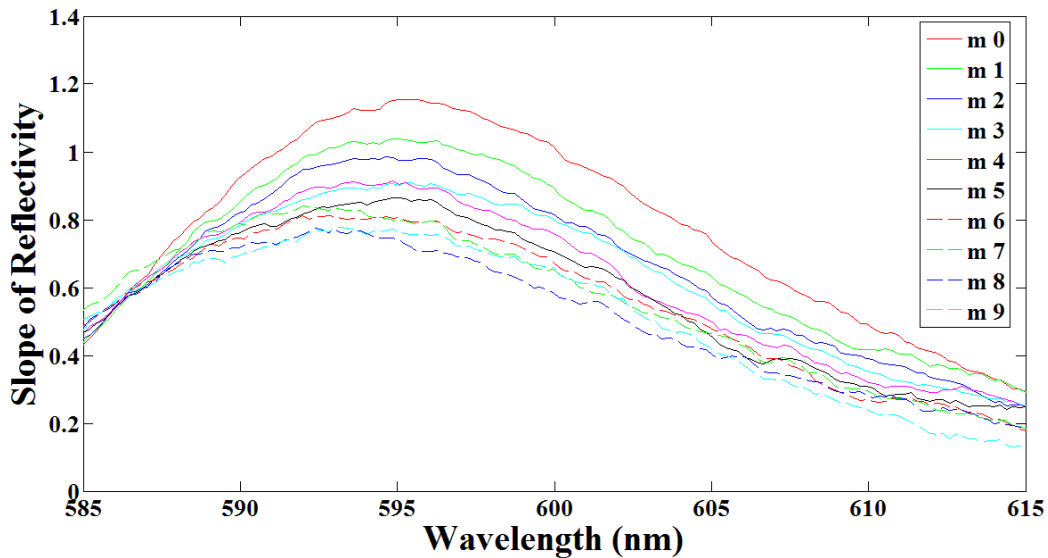


Figure 3.34: Magnified plot of the slope of reflectivity as a function of wavelength for zero to nine fat pieces at wavelengths from 585 to 615 nm with a smoothing coefficient of 51. The legends m 0 to m 9 represent slope of reflectivity plots for 0 to 9 fat pieces.

As a consequence, linear correlations obtained at various wavelengths between slope of reflectivity and the number of fat pieces improved (Table 3.7). LED-spectroscopy showed strong linear correlations between slope of reflectivity and number of fat pieces at 593 and 595 nm but 592 and 601 nm LED wavelengths showed poor linear correlations (Table 3.8).

Table 3.7:  $R^2$  values of linear regression between slope of reflectivity and number of fat pieces at wavelengths from 592.19 to 600.16 nm using smoothing coefficient of 51.

<b>Spectrometer Wavelength (nm)</b>	<b><math>R^2</math></b>
592.19	0.88
593.01	0.90
595.05	0.92
600.16	0.90

Table 3.8:  $R^2$  values of linear regression between slope of reflectivity of LED-spectroscopy and number of fat pieces at LED wavelengths from 592 to 601 nm.

<b>LED Wavelength (nm)</b>	<b><math>R^2</math></b>
592	0.58
593	0.97
595	0.96
601	0.66

### 3.4.6 Experiment on 4/7/11

The LED sensor unit with rotating PCB was tested in this experiment. Improved linear correlation was achieved in LED-spectroscopy using 9 large fat pieces at 592 and 601 nm LED wavelengths (Table 3.9). However, the 593 and 595 nm LED showed slightly reduced linear correlation.

Table 3.9:  $R^2$  values of linear regression between slope of reflectivity of LED-spectroscopy and number of fat pieces at LED wavelengths from 592 to 601 nm.

LED Wavelength (nm)	$R^2$
592	0.85
593	0.89
595	0.89
601	0.96

### 3.4.7 Experiment on 20/7/11

Results of NIR reflectance as a function of number of fat pieces in the NIR spectral range are presented in Figure 3.35. Results indicated that there were differences in reflectance amplitude and reflectance slope as the number of fat pieces increased on the surface of the beef steak. Differences appeared to be sufficiently large for development of an algorithm to describe the amount of fat in whole steak.

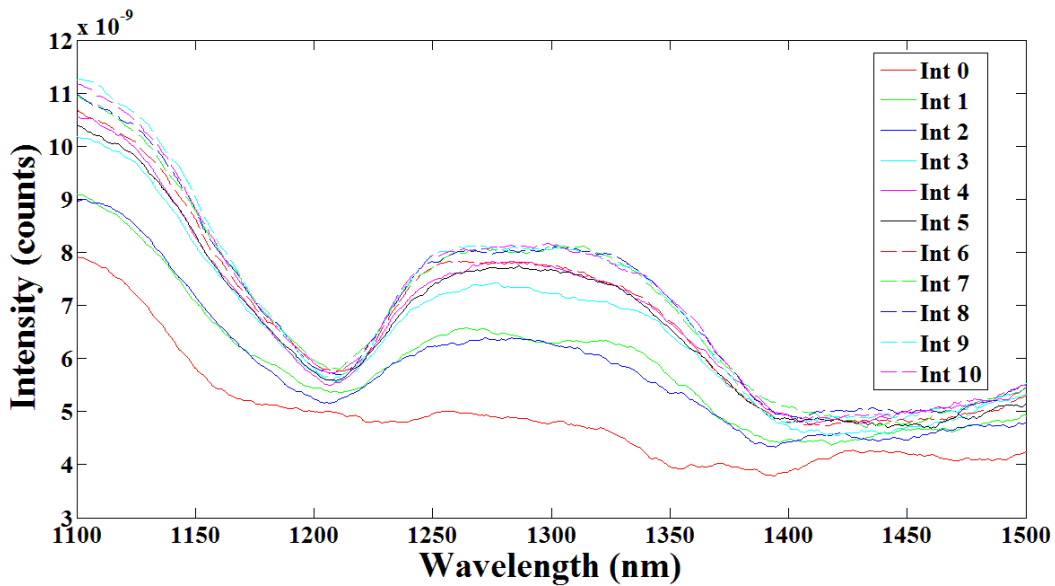


Figure 3.35: NIR reflectance spectra from 1100 to 1500 nm for zero to ten fat pieces added to the beef steak from experiment 20/7/11. The legends Int 0 to Int 10 represent intensity plots for 0 to 10 fat pieces.

### **3.5 Discussion**

Results regarding the relationship between VIS slope of reflectivity and number of fat pieces were similar across VIS spectroscopy experiments (12/11/10 and 25/11/10). The 588 and 590 nm wavelengths did not show strong linearity with the amount of fat but 592, 593, 595, 600 and 605 nm showed promising linearity with the amount of fat. The results of the LED-spectroscopy in this experiment also showed good agreement with the results of the simulation experiment on 17/11/10.

Fat estimation using slope of reflectivity showed promising results within each particular sample. At probe and LED sensor height 60 mm and wavelengths of 592, 593, 595, 600 and 605 nm the fat estimation model worked well using a smoothing coefficient of 51 for VIS spectroscopy. In the case of LED-spectroscopy, the effect of noise was less than that associated with VIS spectroscopy as an LIA filter was used for LED spectroscopy. One disadvantage in the LED spectroscopy was the opposing correlations among the different wavelengths and why this occurred was unclear. Further experimentation will be necessary to reveal an explanation of the results, but these experiments indicated that there is the potential to use specific LED wavelengths to estimate the slope of reflectivity for fat characterization and this will be the focus of additional investigation.

### **3.5 Conclusion**

VIS spectroscopy using VIS light or LED light can predict intramuscular fat on the surface of beef using slope of reflectivity. The results of VIS spectroscopy and LED-spectroscopy were equivalent using slope of reflectivity to estimate amount of fat in beef. This method can be delivered in the form of a hand-held device; however, further experiments are required to

validate and calibrate the LED sensor for effective commercial use to estimate intramuscular fat in beef.

## **Chapter 4**

### **Spectroscopy on whole beef with known differences in intramuscular fat**

#### **4.1. Introduction**

The Canadian Beef Grading Agency began implementation of grading beef carcasses using full instrument assessment in 2012, opening an opportunity to not only describe beef according to the characteristics stipulated in the current beef grading guidelines, but to also add additional measurements to characterize the eating quality of beef. The ability to objectively measure meat quality characteristics and sort according to these characteristics would improve Canada's ability to meet specific domestic and international market demands. Technology such as the Computer Vision System (CVS, Research Management System USA, Inc., Fort Collins, Colorado, USA), which captures images of the carcass and the loin eye muscle, were at the forefront of beef description instrumentation, and were used primarily to calculate carcass yields, rib eye areas and intramuscular grade fat at beef abattoir line speeds. The CVS with its BeefCam module had been used to sort beef loins according to toughness, but had only been able to achieve 64% accuracy (Vote et al., 2003). Recently, near infra-red (NIR; 700 to 1200 nm wavelength) has been developed to estimate the toughness and fat content of beef so that beef carcasses may be sorted according to predicted consumer acceptability. NIR technology is rapid, robust and non-invasive and is amenable to use in the processing line has the potential to describe beef with more objectivity and consistency than trained grading personnel. It also has the advantage of using less computer memory space than captured digital images and the data can be exported to common software spreadsheet programs. The ability of current light spectroscopy and imaging technology to predict beef toughness has been variable, however, with

accuracy ranging from 67 to 93% using crude NIR instrumentation (Cluff et al., 2008; Price et al., 2008; Rust et al., 2008). Results from Leroy et al. (2003) and Xia et al. (2007) suggested that inclusion of visible (VIS) light in a spectral scan of meat improves meat quality prediction. As a result, there is an opportunity to improve upon NIR technology by including visible light (400 to 700 nm) and to include polarization, which may allow detection of structural differences in muscle proteins (Luc et al., 2008).

The most important characteristic to measure during beef grading in Canada is intramuscular fat or marbling, which is the fat visible on the cut meat surface. According to the study of Asplund et al. (2014) the penetration depth of VIS and NIR wavelengths varied depending on the characteristics of the biological sample. Visible light was significantly absorbed at low hemoglobin concentrations (Asplund et al., 2014) and so NIR wavelengths showed higher penetration depths than VIS wavelengths when biological samples contained hemoglobin. In beef samples, the visible light absorbed by myoglobin is comparatively higher than that absorbed by NIR light (Krzywicki, 1979; Khatri et al., 2012); therefore, NIR light is expected to penetrate more deeply into the beef muscle than VIS light. Spectral analysis using the VIS light region is anticipated to be dependent on surface marbling as the penetration strength of wavelengths at VIS region is comparatively less than that with light from the NIR region (700 to 2500 nm). This could compromise its efficacy as marbling on the meat surface is not evenly distributed over the whole surface of a steak (Figure 4.1). The spectral reading can be recorded at one or many different regions on the meat surface, however, depending upon the surface area available on the steak. These readings are then averaged to obtain an estimate of marbling on the whole surface. Despite averaging readings from multiple regions, the possibility exists that prediction of surface fat on a beef steak could be erroneous depending on regions

selected for spectral recording. It was notable that this problem has no effect in the measurement of fat with the current digital image processing technique (E + V Technology), as in this technology the whole meat surface is measured. A two dimensional light scan of the whole meat surface would resolve this problem in spectral analysis.



Figure 4.1: Meat surface with uneven meat marbling.

Another challenge to consider when using light to quantify or estimate the amount of marbling on the surface of beef is the location and concentration of fat across and along the whole rib-eye section [Figure 4.2 (b)]. Depending upon cross sectional angle and the position of the cross section on the whole rib-eye, the amount of marbling and surface fat concentration may vary. Usually, intramuscular fat is concentrated near the blood vessels inside a muscle and the concentration of fat and marbling in a cross section will be artificially increased if measurement is made near such a region. Representativeness of measurement can be verified by determining the amount of marbling on the surface digitally or through chemical analysis of meat to estimate the ‘crude’ solvent-extractable fat in a steak.

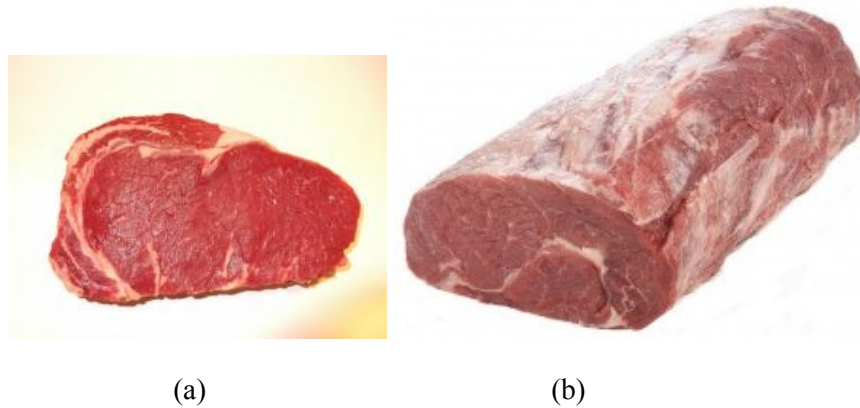


Figure 4.2: Beef rib-eye (a) one rib-eye steak, (b) whole rib-eye section.

Near-infrared spectroscopy is already commercially available and used to estimate sensory acceptability and nutrient content estimation of food products (Osborne, 1981). NIR spectroscopy is successfully used for assessment of chemical components and their relative percentage in meat (Kruggel et al., 1981). Recently, NIR spectroscopy has been shown to have the potential to measure and estimate different quality attributes in meat (Leroy et al., 2003); however, commercial NIR spectroscopy only has the ability to predict the amount of fat, moisture, and protein in ground or homogenized meat products (Ripoll et al., 2008; Sierra et al., 2008). Togerson et al. (2003) showed the capability of NIR to predict fat, moisture and protein content of ground beef in an online experiment, but this method is not suitable for meat processing plants because it is time consuming and destructive. A fast and non-destructive method for fresh intact meat is needed for on-line prediction of the technological and sensory qualities of beef (Leroy et al., 2003). To this end, a study was undertaken to investigate the relationship between VIS and NIR spectroscopic reading and marbling in whole beef, as Rodbotten et al. (2000) indicated that fat has been successfully predicted using VIS-NIR (400 to 1700 nm) in whole beef. Despite being mentioned in some literature, it was still unclear the appropriate method, prediction accuracy and percentage of correlation to predict fat in whole

meat using NIR technology. The final objective was to determine if fat content could be predicted in whole or intact meat using NIR alone. Once these relationships have been established, the construction of a working prototype (a handheld device) will be possible so that the amount of fat in whole meat can be estimated in an industrial environment.

## **4.2 Materials and Methods**

### **4.2.1 Materials**

The surface of the *m. longissimus thoracis* (LT) muscle between the 12th and 13th rib of the beef carcass was graded at the abattoir by Canadian Beef Grading Agency staff and therefore was the surface used for all the light measurements in this experiment. Forty-eight (48) rib sections containing LT muscle were purchased from a large federally inspected Alberta abattoir, with 12 rib eyes obtained from each of the four marbling grades (A, AA, AAA and Prime). Total sample population was ordered in 4 blocks with each block containing 3 replicates of each marbling grade.

Each rib section was trimmed of excess fat and bone and cut into rib-eye steaks for experimentation as shown in Figure 4.3. Four 2.5 cm thick steaks were taken from each rib section; the first was used for spectroscopic and color measurements while the second was used for crude fat analysis. The third and fourth steaks were used for cooking loss and Warner–Bratzler Shear Force (WBSF) and for pH and drip loss, respectively, in another study (Zamarripa, 2014). The first steaks were analyzed 3 to 4 days post mortem and the remainder of each rib section was aged in plastic bags under vacuum for 14 days at 4 °C. The first steak, which was used for light measurement at 3 to 4 days post mortem, was aged for 14 days at 4 °C under vacuum after light spectroscopy measurements. Following the 14 day aging period, the

remainder of each rib section was cut similar to the 3 day section and meat quality measurements performed as described by Zamarripa (2014).

Rib eye steak surface color on the posterior surfaces of both non-aged and aged samples was captured and described using a colorimeter (Chroma Meter CR-400, Konica Minolta, Osaka, Japan) [Figure 4.4 (a)] and a digital scanner (EPSON PerfectionV33 Flatbed scanner, Seiko Epson Corporation, Suwa, Japan). The Konica Minolta CR-400 Chroma Meter is a color measurement instrument with aperture diameter of 8 mm. It uses silicon photocell sensors as detectors and a pulsed xenon lamp as a light source. Measurement time of the CR-400 is 1 second and the minimum measurement interval 3 seconds. Instrument measurement area was 8 mm (diameter) and instrument illumination area was 11 mm (diameter). A white calibration unit (CR-A43 Calibration Plate, Konica Minolta, Osaka, Japan) [Figure 4.4 (b)] was used for instrument calibration purposes and the instrument was calibrated immediately before measurements were taken.

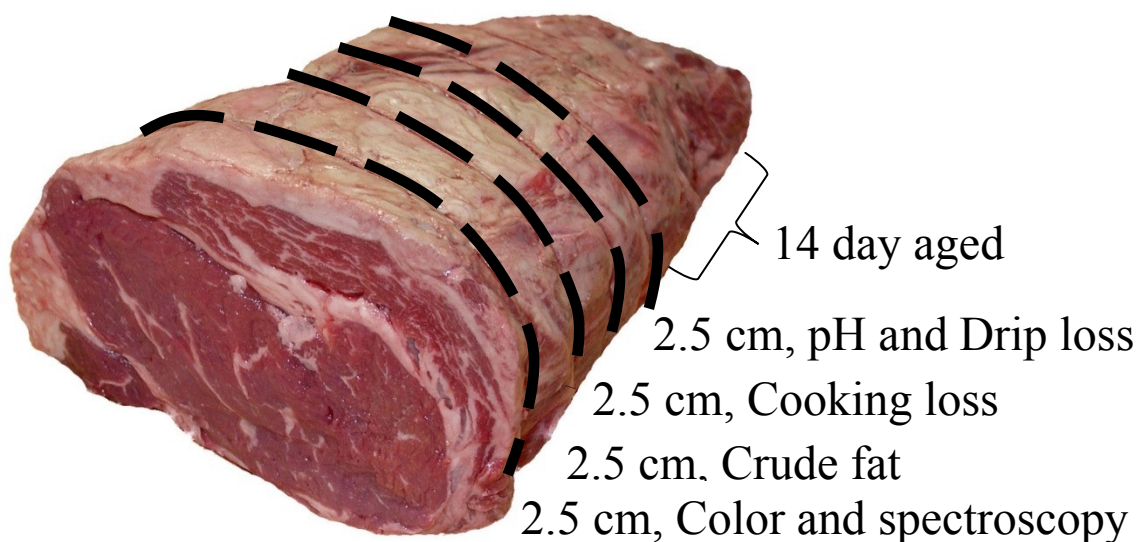


Figure 4.3: Rib section detailing locations of experimental steaks.



Figure 4.4: (a) Chroma Meter CR-400, (b) CR-A43 Calibration Plate

A digital color image scanner (EPSON PerfectionV33 Flatbed scanner, Seiko Epson Corporation, Suwa, Japan) was used to scan the surface of the samples to acquire digital images for image processing. This color image scanner was 285 mm  $\times$  429 mm in dimension and used a CCD sensor and an innovative LED light source. It had a 48 bit color depth and 4800  $\times$  9600 dots per inch (dpi) hardware resolution.

The intensity of the visible light reflectance from the rib eye surface was measured using the VIS spectrometer (Ocean Optics USB4000) as described in Section 3.2.2 of Chapter 3. The tungsten halogen light source HL-2000 was used as a broad spectrum light source that emitted well into the NIR region and covered the entire spectrum range of the spectrometers used in this experiment.

The bifurcated fiber optic cable (Ocean Optics R600-7-VIS-125F) (Section 3.2.2 of Chapter 3) was used to transmit light from the source onto the meat surface and return the reflected light to the spectrometer. A standard laboratory stand used to attach and hold the metal probe of the fiber optic cable at a fixed distance from the measurement surface.

The Teflon<sup>TM</sup> sheet (1.66 mm thick; Section 3.2.2 of Chapter 3) was used as a reference measurement for normalization. The black mask (a plastic black cover with a hole in the center of diameter approximately 4.5 cm; Section 3.2.2 of Chapter 3) was used to exclude surface regions on the measurement surface except for the region intended to be measured.

The Yokogawa AQ6370C Optical Spectrum Analyzer (Section 3.2.3 of Chapter 3) was used for NIR spectroscopy measurements. Wavelength resolution of 1 nm was used for convenience of data analysis. The level sensitivity was set to “HIGH2” for a moderate measurement speed and moderate sensitivity level. With these settings, the sweep time was approximately 20 seconds. Auto reference level, auto resolution correction, and smoothing function were used for optimum measurement results but these functions increased measurement time. Reflected NIR light spectra were recorded in the full wavelength range from 600 to 1700 nm and all measurements were performed in a darkened room. The light source for NIR spectroscopy was the same as that used for VIS spectroscopy. The light source had a broad spectrum range and it covered the spectrum range of the NIR spectrometer.

In conjunction with the light source, a polarizer (LPIRE050-C linear polarizer, Thorlabs, Newton, New Jersey, USA) of diameter 1.27 cm was used to collect polarized reflectance light from the sample [Figure 4.5 (a)]. The polarizer was used to investigate the relationship between meat quality measurement and polarized light. A custom made connector, designed and built in the Electrical Engineering department workshop of the University of Alberta, was used to maintain the polarizer between the collection fiber of the bifurcated fiber optic cable and the receiver terminal of the spectrometer (Figure 4.5 (b) and Figure 4.5 (c)).

The fiber optic cable used was the same cable (Ocean Optics R600-7-VIS-125F bifurcated fiber optic cable) as used in the visible spectroscopic analysis. The custom made SMA to FC (PC

type connector which is compatible with AQ6370C) adapter (Section 3.2.3 of Chapter 3) was used to connect the cable with the AQ6370C Optical Spectrum Analyzer. The same white Teflon™ sheet and black mask cover used for VIS spectroscopic analysis were also used for NIR measurements. The recorded spectrum data was stored directly in the AQ6370C internal memory during the measurement. A USB flash drive was used to transfer the data from AQ6370C to computer for data analysis.

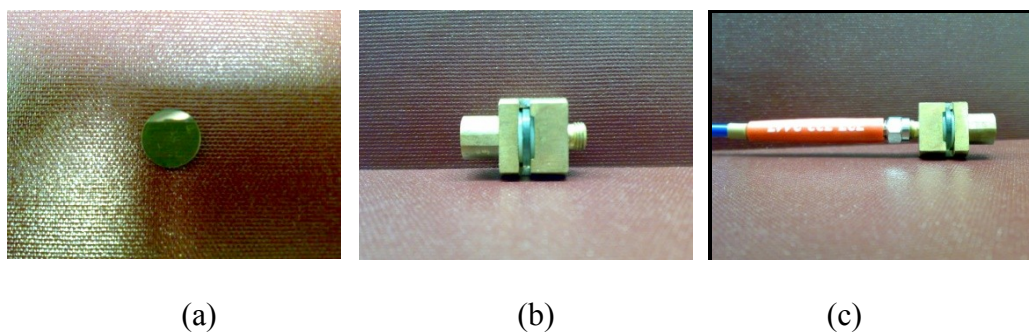


Figure 4.5: (a) Polarizer, (b) custom made connector to hold the polarizer, and (c) the connector connected to the collection fiber of the optical fiber.

The hand-held device with rotating sensor unit was used to take measurements at wavelengths 592, 593, 595, 601, and 605 nm. The reflectance of each wavelength was normalized using the same Teflon™ sheet used in VIS and NIR spectroscopy to calculate reflectivity data at each wavelength. The black mask cover was also used during measurements of hand-held device.

#### 4.2.2 Experimental Setup and Measurements

Light spectroscopy was performed in two locations due to laboratory scheduling conflicts, with experimentation performed in one laboratory location for blocks one and two ( $n = 12$  samples per block) and in another location for blocks three and four (last 24 samples).

#### 4.2.2.1 First and Second Block

For the first and second blocks, the measurement area was covered with black (non-transparent) plastic bags to prevent any interference due to stray light in the lab room. The room temperature was constant (21 to 22 °C) according to the thermostat inside the room. A digital camera (Webcam C905, Logitech, California, USA) was used to take pictures of the samples to calculate the percentage fat with the help of image processing. The light source for the camera was made using special LEDs with specific wavelengths and placed over the sample in proper angle with the camera so that the reflected light from the sample would go towards the camera.

The light source for the spectroscopic measurement was the Ocean Optics halogen light source (HL-2000, Ocean Optics, Dunedin, Florida, USA). The VIS spectroscopy measurement setup was similar to that described in Section 3.2.5 of Chapter 3. The VIS spectrometer was connected to a Netbook Computer (Aspire one 532h-2630, Acer, China). The interface software (SpectraSuite™, Ocean Optics, Dunedin, Florida, USA) installed in the Netbook was used to set different parameters of the spectrometer and for collecting measurement readings from spectrometer. The integration time for the spectrometer was set at 100 ms and an option for dark current reduction in the interface software was set to 'ON' for all the VIS spectroscopic measurements. A white plastic cutting board was placed on the table and was used to position the samples. The reflectance data of entire spectrum from the spectrometer was saved to an Excel™ file for further processing. The reflectance data was then processed and analyzed in MATLAB™ (Mathworks, Massachusetts, USA) and Unscrambler™ software (CAMO, Woodbridge, New Jersey, USA).

During NIR measurement, the transmitter end of the fiber optic cable was connected to the NIR spectrometer AQ6370C and the other end of the cable with multiple fiber channels for

carrying light from light source was connected to the Ocean Optics light source. During non-polarized measurements the SMA905 to FC converter adapter was used and during polarized measurement the custom made connector with polarizer holder was used. Other than these conditions, experimental setup was unchanged from VIS light measurements. The recorded measurement data were stored in the AQ6370C's internal memory as "CSV" (comma-separated values) file format. CSV files are compatible with Microsoft Excel™. The NIR spectrometer data was transferred to a computer using a USB flash drive for further data analysis. The reflectance data was then processed and analyzed in MATLAB™ and Unscrambler™ software (CAMO, Woodbridge, New Jersey).

The hand-held device was attached to the stand by removing the fiber optic probe. Height of the sensor unit was adjusted and verified using ruler. Measurement data (reflectance of each LED wavelength) were recorded in an Excel™ file.

#### **4.2.2.2 Third and Fourth Block**

The remaining sample measurements (third and fourth block) were performed in a dark lab room with no windows. The room temperature was constant (21 to 22 °C) over time, according to the thermostat, inside the room. For these blocks, digital images were generated using the desktop scanner, EPSON PerfectionV33 Flatbed connected to a laptop computer (ThinkPad X220, Lenovo, China). Isopropyl alcohol and soft tissues (Kimwipes™, Fisher Scientific, Edmonton, Canada) were used to clean the glass screen of the scanner between samples. An A4 size sheet (transparent plastic paper) was used to cover the sample after placing it on the scanner glass screen. This sheet was used to prevent the white reflector and calibration plate of the scanner, which was attached to the cover plate of the scanner, from touching the samples directly. The direct contact of the reflector and calibration plate of the scanner with the samples

may have resulted in loss of calibration property and accuracy. Fiber optic probe set up, hand-held device setup, reflectance recording devices and electronic data storage were identical to that of VIS and NIR spectroscopic measurements conducted on the first and second block samples.

#### **4.2.2.3 Sample Preparation**

Rib eye steaks 2.5 cm thick were removed from the rib sections as described in Section 4.2.1 and labelled according to source rib section, block number, quality grade (A, AA, AAA, Prime), sample number, and aging treatment (Y for aged and N for non-aged sample). Electronic data were also similarly labeled for type of measurement (N for non-polarized NIR reading, P for polarized NIR reading with polarizer grating parallel to the muscle fiber, R for polarized NIR reading with grating perpendicular to the muscle fiber, C for camera images, S for scanner and V for VIS reading) and location of the measurement region on the meat surface (Figure 4.6). The labeled sample was then loosely covered in plastic wrap to prevent moisture loss. The samples were kept in the laboratory cooler at 4 °C until just prior to the measurement and then removed from the cooler one by one for measurement.

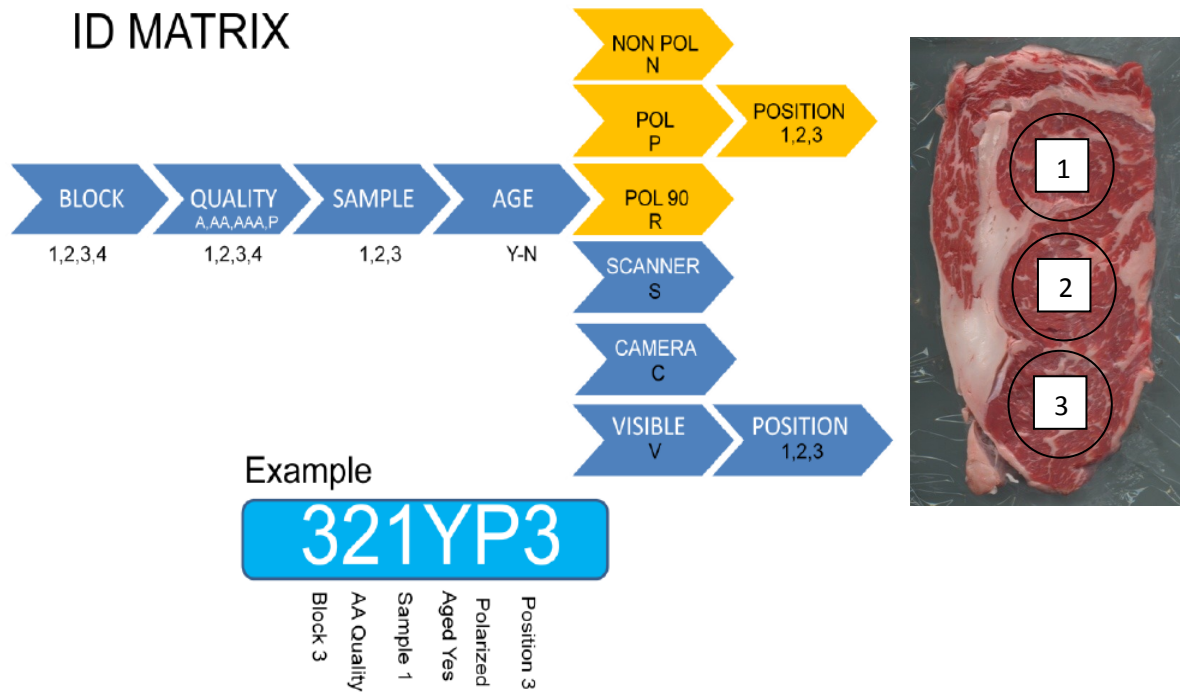


Figure 4.6: Sample labeling scheme (left), and whole rib eye steak with three specific locations of measurements (right).

#### 4.2.2.4 Measurements on Samples

Immediately prior to measurement, steaks were removed from refrigeration and placed uncovered on a white cutting board. Lightness ( $L^*$ ), green-red ( $a^*$ ) and blue–yellow ( $b^*$ ) color component values of the color system established by the Commission Internationale de L’Eclairage (CIE) were recorded for visually fat free lean at three different locations on the meat surface using the CR-400 Minolta colorimeter and have been presented previously (Zamarripa, 2014). Following colorimeter measurements, a digital image of each sample was recorded using a camera or scanner and the custom LED light sources.

Each sample was prepared for VIS and NIR spectroscopic measurement by placing it under the black mask cover with the measurement surface facing up. The fiber optic probe height was adjusted to a height of 5 cm for blocks one and two and 10 cm for blocks three and four from the

measurement surface and verified using a ruler. For recording Teflon™ reference readings for VIS and NIR spectroscopy, a piece of waxed paper was placed on the measurement surface to prevent the white Teflon™ reference from directly contacting the sample, and the same black mask cover used to cover samples during measurement was placed over the Teflon™ reference. One Teflon™ reference reading and one “dark current” noise reading were recorded for each measurement day. The “dark current” spectroscopic reading was taken by covering the fiber optic probe with a cap and recording spectrum data. VIS and NIR spectroscopy measurements were conducted similarly to that of the Teflon™ reference, with the black mask cover placed over the measurement surface of the sample and the light spectroscopic reading was recorded in same way as that of the Teflon™ reference. Two different positions were recorded [Positions one and three, Figure 4.6 (right)] were recorded once on each steak face. Electronic VIS data were stored in Excel™ files which contained all the measurement readings and were saved for further analysis. Electronic NIR data were stored as CSV files in the internal memory of AQ6370C. All spectroscopic measurements were later saved into Microsoft™ Excel files along with Teflon™ reference and “dark current” spectroscopy readings. These were used for calculation of reflectivity spectra of each sample.

The interface connector between the fiber optic cable and the NIR spectrometer was replaced with the custom made polarizer holder and connector for taking measurement readings using polarizer. The polarizer was connected at the spectrometer end of the fiber optic cable. Two sets of readings were taken using the polarizer; one with polarizer axis parallel to the muscle fiber and another with polarizer axis perpendicular to the muscle fiber. To change the polarizer axis orientation so that it was perpendicular to the muscle fiber direction, the polarizer was rotated 90 degree from its initial position (polarizer axis parallel to muscle fiber). The output polarization of

the polarizer was marked at the factory for ease of identification and another mark was added at perpendicular to the polarizer axis direction for ease of changing the orientation of the polarizer axis properly with respect to muscle fiber direction. To normalize the polarizer readings a set of white Teflon<sup>TM</sup> reference readings were taken with the polarizer at the same axis orientation of the reflectance and reference lights.

The hand-held device sensor height was adjusted to 6 cm for all samples. The Teflon<sup>TM</sup> reference readings were taken in a similar way to that of VIS and NIR spectroscopy. These reference readings were recorded before each sample reading. After completion of all spectroscopic measurements, steaks were individually packaged under vacuum stored at 4 °C for 14 days. Following the 14 day ageing period, spectroscopic measurement was performed as described for the day 3 samples. However, only the spectroscopic data collected from day 3 samples were analyzed in this study.

#### **4.2.2.5 Preparation of Digital Images**

The images (Figure 4.7) recorded by digital camera were of inferior quality as these images required sophisticated image processing to be able to estimate amount of surface fat on meat samples. The images obtained from scanner were of improved quality and ideal for estimation of surface fat using simple image processing.



Figure 4.7: A sample image recorded by a digital camera (Logitech webcam C905).

From the entire steak surface, two rectangular regions that contained the circular region of spectroscopic measurement were cropped from the scanned digital images using Microsoft Paint™ and were used for image processing (Figure 4.8). Two different types of region were cropped: one region (LARGE) covered most of the steak surface including the circular area of spectroscopic measurement while the second region (SMALL) contained just the circular spectroscopic measurement area. The original scanner digital image had resolution of  $5100 \times 7019$  pixels and resolution of the original image was reduced to  $1275 \times 1755$  pixels using the “Resize” function of Microsoft Paint™ to decrease image processing time by the computer. This reduction in resolution did not affect the fat percentage calculation because the ratio of the fat region and lean muscle region of meat remained constant (data not shown).

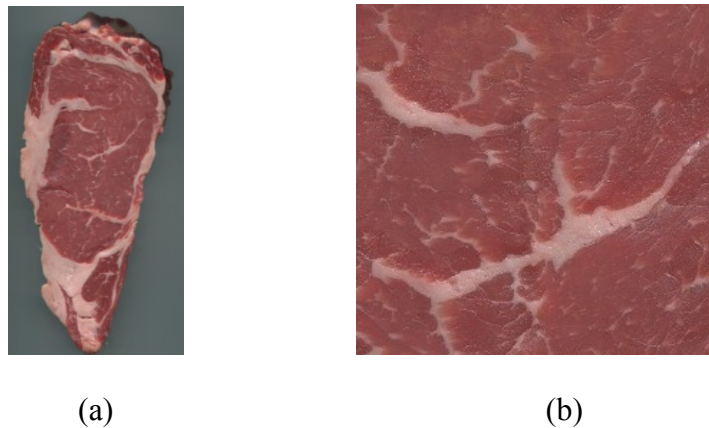


Figure 4.8: (a) Scanned digital image of a typical sample; (b) cropped digital image at location one (Figure 4.6) of the same sample.

#### 4.2.3 Sample Preparation for Crude Fat Extraction

Sample preparation for crude fat and crude fat extraction was performed similarly for all blocks as described by Zamarripa (2014). For crude fat estimation, each LT was trimmed of

inter-muscular fat and other small muscles and then diced into cubes for lyophilisation (freeze-dry). The weight of the diced sample was recorded using an electronic balance. The aluminum tray used to keep the sample during lypophilization was weighed and its weight was recorded. The diced samples were stored at -20 °C until lypophilization. Following lypophilization, the diced samples were weighed for calculation of moisture loss and ground with dry ice to a powder in a Waring blender with a stainless steel cup (Fisher Scientific, Mississauga). The powdered samples were stored at -20 °C in a labeled plastic pouch pack (Whirlpak™, Fisher Scientific, Mississauga) until crude fat extraction.

#### **4.2.4 Crude Fat Extraction**

The crude fat extraction was performed according to the AOAC Official Method 960.39 (AOAC, 1995). Crude fat was extracted from approximately 2 g of lyophilized and powdered muscle was weighed into a solvent-permeable thimble using petroleum ether into a clean glass beaker. The extraction was performed in the Goldfish Fat Extraction Apparatus (Model 35001, Labconco Corp. 35181 Revision I, 1997). The thimble was sealed using glass wool and each thimble was labeled using a graphite pencil. A blank thimble was prepared as a control, weighed and sealed with glass wool and included in each Goldfish extraction.

In a chemical fume hood approximately 40 mL of petroleum ether was poured in each clean, dry, labeled extraction beaker that had been accurately weighed. Sample thimbles were placed into the stainless steel thimble holder and attached to the condenser units. Each extraction beaker was attached to the condenser units using ring clamps according to appropriate thimble sample. The clamps were tightened carefully so that there were no leak between the beaker and the condenser unit. The water flow and the oven were turned on. Oven burners were raised near to

the beakers but with a distance maintained that would allow the petroleum ether to reflux during extraction and extraction was allowed to continue for 6 h.

After completion of the extraction process, heating was halted by lowering the oven burners and the extraction beakers were removed after visually confirming that the refluxing had come to a complete stop. Remaining petroleum ether was allowed to evaporate from the extraction beakers inside a fume hood at room temperature until the solvent evaporated completely (overnight). Once the solvent in the extraction beakers had dried completely, the extraction beakers were dried in an oven at 100-110 °C for 30 min to remove residual moisture. After completion of the baking process the extraction beakers were kept in desiccators to cool to room temperature. The extraction beakers were weighed and fat/lipid content of each sample was calculated as a percentage of the dry meat powder weight adjusted to wet weight using the moisture content. Moisture content was derived by subtracting freeze-dried weight from the original wet weight.

### **4.3. Data Handling and Analysis**

#### **4.3.1 Digital Image Processing**

Digital scanned images were only obtained from the samples of third and fourth block. For image processing purpose, all the regions of each sample used for spectroscopic measurement, were cropped (Figure 4.9). The results from each region within each sample were averaged and the average was correlated with the spectroscopic readings of the corresponding sample. The programming code for image processing was written in MATLAB<sup>TM</sup> (MathWorks, Natick, Massachusetts, USA) software [Version 7.9.0.529 (R2009b)] and images were represented in Red (R), Green (G) and Blue (B) color components. Each color component was described in 8 bit color depth (scale: 0 to 255). The data type, “uint8” was used to allocate memory for

variables of each color component. Variables with binary (Base-2 numeral system, uses two symbol; typically 0 and 1) data type were used to describe black and white image pixels (0 as black pixel and 1 as white pixel).The cropped image was loaded to MATLAB™ program memory using “imread” function. The MATLAB™ code for this image processing can be found in Appendix C.

The purpose of this image processing was to calculate the fat/lipid percentage (IMAGE PROCESSED FAT) of the cropped image region. The pixels of the cropped image (CI) were passed through a threshold setting that distinguished fat regions from lean muscle regions. In this threshold method, a range of RGB values were set to isolate the pixels representing lean muscle region from the entire image. It was observed that uneven meat surface had some bright regions (glare from uneven sample surface) and some dark regions (due to shadows formed by uneven sample surface). These bright and dark regions on the meat surface increased the difficulty in differentiating fat from lean muscle because of light scattering interference. These regions were identified and isolated from the cropped image using image thresholding. The remaining cropped image regions were processed to evaluate the percentage of fat region in the lean meat.

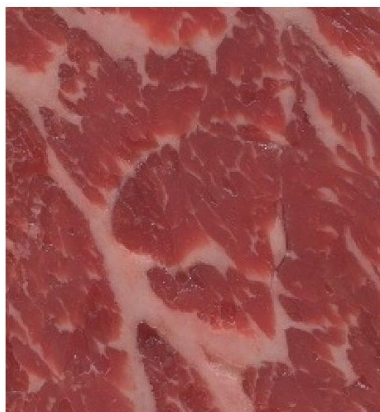
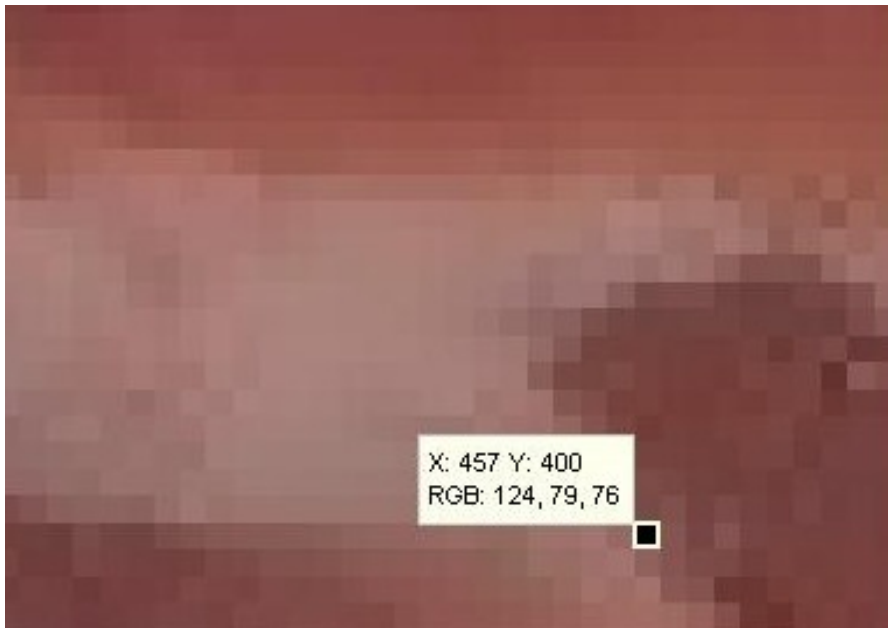
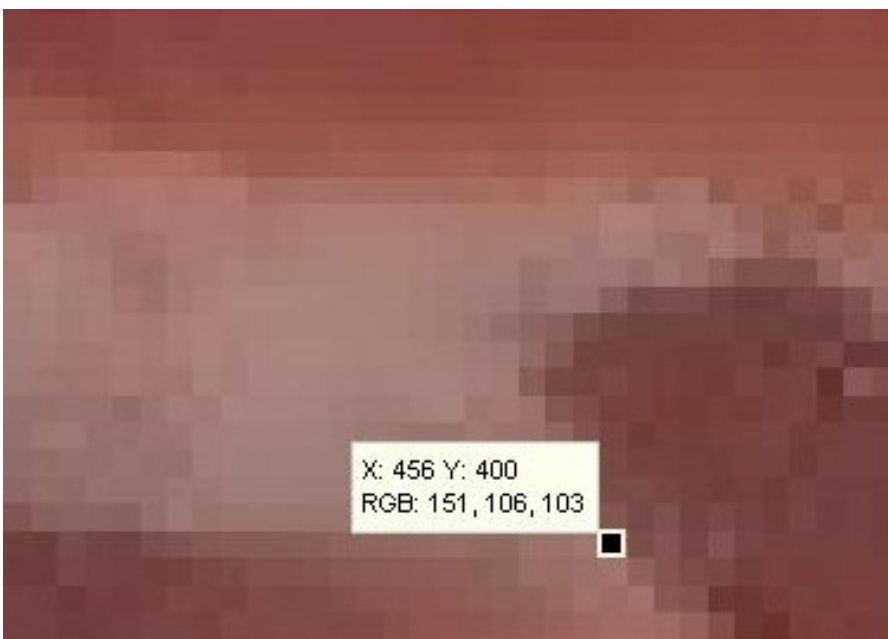


Figure 4.9: Cropped image region of a sample (sample ID: 143YS1).

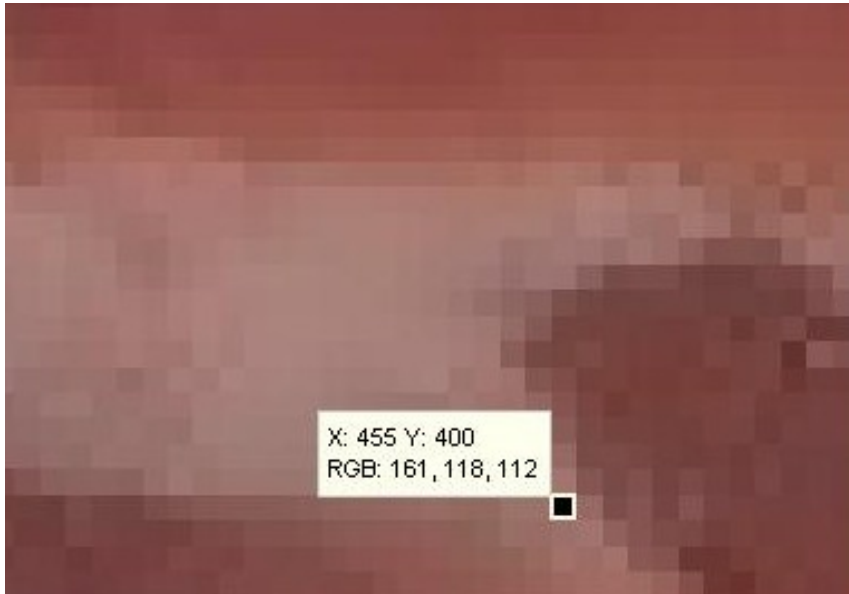
In Figure 4.10 (a) the selected pixel had RGB values of R=124, G=79, B=76 and corresponded to a lean muscle region of the sample. The selected pixel in Figure 4.10 (b) belonged to lean muscle as well but it was located at the boundary of lean and fat and the RGB values of this pixel were R=151, G=106, B=103. The adjacent pixel to this pixel was located in the fat region as shown in Figure 4.10 (c) and the RGB values of this pixel were R=161, G=118, B=112. There was another set of pixels that corresponded to the lean muscle region as shown in Figure 4.10 (d) and Figure 4.10 (e). The pixel selected in Figure 4.10 (d) that was located at the boundary of a lean muscle and fat region was located in the lean muscle region. The RGB values of this pixel were R=164, G=110, B=100. Another pixel adjacent to this pixel was selected in the fat region as shown in Figure 4.10 (e) and the RGB values of this pixel were R=172, G=124, B=114. It was observed that from lean muscle to fat that pixel R values increased along with the G and B values. Also, the lean muscle nearest to fat was comparatively brighter than the previous pixel shown in Figure 4.10 (a), (b) and (c) and therefore a thresholding condition was required to identify the boundary between lean muscle region and the fat region. Through visual inspection of different color variation across samples, RGB values R=130, G=110, B=100 appeared to best describe this regional boundary between fat and lean muscle. Specifically, when R values were below 130 and the G and B values were below 110 and 100, respectively, the pixel was likely in a lean muscle region. Additionally, when the R values were above 130, the G and B values needed to remain under 110 and 100 respectively for that pixel to belong to a lean muscle region. These RGB value conditions were used as the threshold for determining if a pixel represented fat or lean muscle.



(a)



(b)



(c)



(d)



(e)

Figure 4.10: RGB values of different pixels of the cropped sample image (sample ID: 143YS1), (a) selected pixel inside lean muscle region, (b) selected pixel correspond to the lean muscle and located at the boundary of lean muscle and fat region, (c) selected pixel correspond to the fat region, (d) selected pixel correspond to the lean muscle region, (e) selected pixel correspond to the fat region.

Fat regions were isolated using two thresholding conditions. Figure 4.11 shows that the fat regions were identified and marked with black while lean muscle regions were left unchanged. The resolution of any image was uniform over the entire image. These images were obtained by scanning the sample using a digital scanner and with this method each point of the meat surface was equidistance from the scanner image sensor. As a result, a measure of the surface area could be evaluated by the number of pixels on the image. If the number of pixel counts of a given area A was P and the pixel area constant was s, then

$$A = P \times s \quad (4.1)$$

The constant  $s$  was defined as the amount of meat surface area that a single image pixel represented on the meat surface. If  $A_f$  was assumed to be the total fat region surface area, then  $A_{lm}$  was assumed to be the total lean muscle region surface area,  $P_f$  was assumed to be total number of pixels of all fat regions and  $P_{lm}$  was assumed to be the total number of pixels in the entire lean muscle region. With these assumptions, the percentage of cropped image was obtained by the following formulae.

$$\% \text{Fat of CI} = \frac{A_f}{A_f + A_{lm}} \times 100 \quad (4.2)$$

$$\% \text{Fat of CI} = \frac{P_f \times s}{P_f \times s + P_{lm} \times s} \times 100 \quad (4.3)$$

$$\% \text{Fat of CI} = \frac{P_f}{P_f + P_{lm}} \times 100 \quad (4.4)$$

Thus, the amount of percentage fat of the cropped image could be calculated using the total number pixels in fat region ( $P_f$ ) and total number of pixels in lean muscle region ( $P_{lm}$ ).

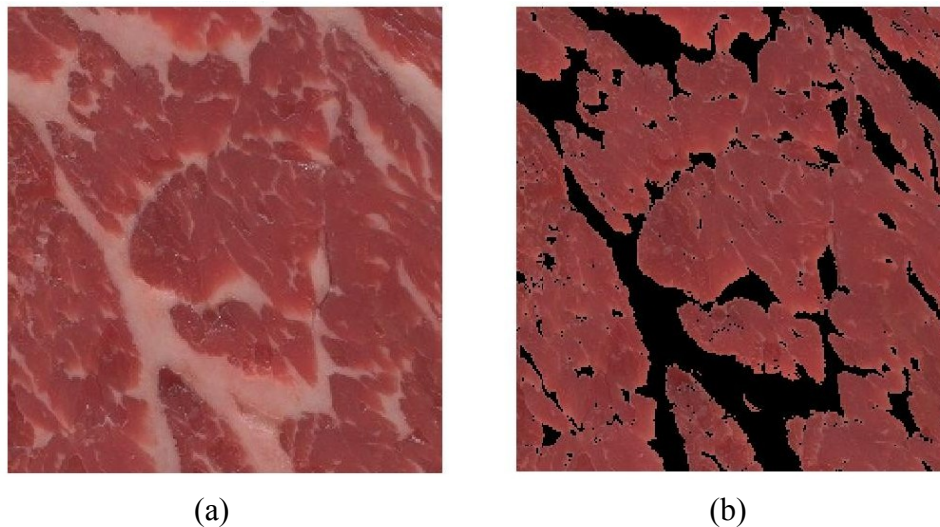


Figure 4.11: (a) Original cropped image of the sample (sample ID: 143YS1); (b) identification of the fat and lean muscle regions of the cropped image, the identified fat regions were marked with black and lean muscle were kept unchanged.

### 4.3.2 VIS Spectroscopy

All recorded data from VIS spectroscopy was stored in Excel<sup>TM</sup> files. The Excel<sup>TM</sup> files were named according to each sample identification number. The data files were then loaded in MATLAB<sup>TM</sup> and processed using MATLAB<sup>TM</sup> program. Different MATLAB<sup>TM</sup> library functions were used to calculate and process the data according to desired algorithms and formulae. The MATLAB<sup>TM</sup> code is presented in Appendix C.

The white light spectroscopic measurement was performed on the whole steak. The purpose of this data analysis was to find the amount of correlation that may exist between the slopes of the surface reflectivity curve (as indicated in Chapter 3) at various wavelengths and crude fat or image processed fat values. The reflected light intensity spectrum data were first filtered using MATLAB<sup>TM</sup> library function “smooth”. This library function was a moving average filter. The “smoothing coefficient” was a user defined parameter that can be passed on to the function as a constant. The value of this coefficient was set to determine the span of the moving average filter. The VIS spectrometer was set to produce VIS spectrum of resolution 0.22 nm. A smoothing coefficient of 51 (span = 51 × 0.22 = 11.22 nm) was used to filter the VIS spectroscopic data. The reflectivity spectrum was calculated after filtering the reflected light spectrum, which was recorded directly from spectrometer, using the following formulae.

$$\text{Reflectance} = I_{\text{reflected}} - I_{\text{dark}} \quad (4.5)$$

$$R = \frac{I_{\text{reflected}} - I_{\text{dark}}}{I_{\text{reference}} - I_{\text{dark}}} \times 100 \quad (4.6)$$

Where R was the reflectivity of each wavelength,  $I_{\text{reflected}}$  was the light intensity of each wavelength reflected back from the sample,  $I_{\text{reference}}$  was the light intensity of each wavelength reflected back from the white reference (Teflon<sup>TM</sup> sheet) and  $I_{\text{dark}}$  was the ‘dark current’ noise which was measured when there was no light (the probe was covered with a cap). It was important that during recording of  $I_{\text{reflected}}$  and  $I_{\text{reference}}$  from each sample that all measurement conditions stayed constant. A substantial amount of noise was removed by subtracting the dark noise ( $I_{\text{dark}}$ ) from the  $I_{\text{reflected}}$  and  $I_{\text{reference}}$ . Reflectivity spectrum data for each location of a sample was first calculated and then averaged to get an average reflectivity of the sample surface. The slope of the reflectivity spectrum was calculated at each wavelength using the following formula and used for calculation of correlation with crude fat or image processed fat.

$$m_{\lambda} = \frac{d(R)}{d(\lambda)} = \frac{R_{\lambda+1} - R_{\lambda}}{(\lambda+1) - \lambda} \quad (4.7)$$

Where  $m_{\lambda}$  was denoted as the slope of the reflectivity at wavelength  $\lambda$ ,  $R_{\lambda}$  was denoted as averaged reflectivity at wavelength  $\lambda$ ,  $R_{\lambda+1}$  was denoted as averaged reflectivity at wavelength  $\lambda+1$ . The slope of reflectivity data for each sample was first calculated and then filtered using same MATLAB<sup>TM</sup> library function “smooth” using smoothing coefficient of 51. The filtered slope of reflectivity data was stored in another Excel<sup>TM</sup> file along with other data (e.g. crude fat data and image processed fat data). This new Excel<sup>TM</sup> data sheet was used for calculation of different correlations.

Separate data sets of VIS spectroscopy were created for statistical analysis using Partial Least Squares (PLS) method. The reflectivity spectrum data were calculated using the Equations 4.5 and 4.6 but without the multiplication by 100. The reflectivity spectrum data were filtered using

a smoothing coefficient of 50 ( $\text{span} = 50 \times 0.22 = 11 \text{ nm}$ ). After filtration of each reflectivity data, an average reflectivity of the sample surface was obtained by averaging the filtered reflectivity from each location of a sample. Two separate data sets of third and fourth block samples were created for statistical analysis of VIS spectroscopy and crude fat: one with “dark current” subtracted and another one without “dark current” subtraction. This helped understand the effect of “dark current subtraction” on PLS analysis results. No “dark current” was subtracted for the data sets used for PLS analysis of VIS spectroscopy and image processed fat.

### **4.3.3 NIR Spectroscopy**

The NIR spectroscopy data was only utilized in the statistical analysis using the PLS method. The NIR spectroscopy data set was processed in a similar manner to that performed with the VIS spectrum data set created for PLS analysis. NIR spectrometer produced NIR spectrum of resolution of 0.1 nm. During the analysis of NIR spectrum the resolution was reduced to 1 nm. The reflectance spectra were filtered using MATLAB<sup>TM</sup> library function “smooth”. A smoothing coefficient of 11 ( $\text{span} = 11 \times 1 = 11 \text{ nm}$ ) was used. The reflectivity of the NIR spectrum was calculated using a formula similar to that used in VIS spectroscopy data analysis of PLS method. The “dark current” noise was not measured during the spectroscopic measurement of first and second block so no adjustment for “dark current” noise was able to be performed. The NIR reflectivity data from two different positions of a sample were averaged to obtain an average reflectivity of the sample surface. During NIR data analysis, multiple data sets were created to test the effects of “dark current” subtraction, normalization and application of smoothing filter at different stages (e.g. before normalization, after normalization, after averaging) of calculations. These data sets were analyzed separately using the PLS method. No “dark current” was subtracted for the data sets used for PLS analysis of NIR spectroscopy and image processed fat.

Although collected, NIR polarized reflectivity spectrum was not analyzed in this study, but was retained for future analysis.

#### **4.3.4 LED-spectroscopy Using Hand-held Device**

The slope of reflectivity from LED-spectroscopy data was calculated using Equations 4.5, 4.6, and 4.7. However, no smoothing filter was applied in this data analysis. The slope of reflectivity data were used to calculate various correlations between crude fat, and image processed fat. Results are presented in the result section of this chapter.

#### **4.3.5 Statistical Analysis**

Correlations were calculated in MATLAB™ using MATLAB™ library functions. In these calculations MATLAB™ function “corr” was used to calculate r values (correlation coefficients) and p values. The r values were used to evaluate the amount of correlation exists between two random variables. The p values were used to identify the most significant correlations between two random variables, with significance at  $p < 0.05$ .

Statistical analysis was performed using the software package Unscrambler™ X [Version: 10.2 (64-bit)]. This analysis was performed using non-linear iterative partial least squares (NIPALS) algorithm of the PLS method. Weighted regression coefficient (WRC) plots were used to understand the amount of correlation present at each wavelength. In PLS analysis, different trends present in the dataset were denoted as factors. The number of factors was selected at the beginning of the PLS analysis, with the default value being seven.

Due to the changes in experimental parameters and setup environment between the first two and last two blocks, PLS analysis was performed separately on these blocks. PLS analysis used a segmented random cross validation method for the formation of calibration equation and

validation equation in which the entire sample population were chosen for calibration model and 20 different segments, each containing two or three randomly selected samples so that every sample was selected once, were used for validation purposes. Wavelengths with the highest regression coefficient were selected for inclusion in subsequent partial least square (PLS) analyses so that the overall proportion of variability described increased with iteration. Minor deviations in validation  $R^2$  values were noticed between different PLS analysis using the same wavelengths due to the random selection of the validation data set (data not shown). To take this into account, five PLS analyses were conducted using the same wavelength set and the mean  $R^2$  and standard deviation (SD) presented.

VIS and NIR spectroscopic data were analyzed separately. Also, for the NIR data, the effects of filtering (using “smooth” function) and the subtraction of “dark current” noise were tested by constructing data sets of VIS and NIR spectroscopy with or without the filtering, with different smoothing coefficients and also with or without the subtraction of dark current.

## **4.4. Results**

### **4.4.1 Color**

Minimums, maximums, means and standard deviations of  $L^*$ ,  $a^*$ ,  $b^*$  color component values of first and second block samples are presented in Table 4.1, third and fourth block samples are presented in Table 4.2, and all samples are presented in Table 4.3. These statistics showed that color varied significantly among the samples. However, color variation of the first two blocks (first and second) and last two blocks (third and fourth) showed similar characteristics.

Table 4.1: Minimums (min), maximums (max), means, and standard deviations (SD) for L\*, a\*, b\* color coordinate values of the first and second blocks of beef rib eye samples.

<b>First and second blocks (n=24)</b>	<b>Min</b>	<b>Max</b>	<b>Mean</b>	<b>SD</b>
<b>L*</b>	30.31	41.49	36.01	2.78
<b>a*</b>	14.65	26.39	21.20	3.70
<b>b*</b>	0.44	10.23	4.15	2.23

Table 4.2: Minimums (min), maximums (max), means, and standard deviations (SD) for L\*, a\*, b\* color coordinate values of the third and fourth blocks of beef rib eye samples.

<b>Third and fourth blocks (n=24)</b>	<b>Min</b>	<b>Max</b>	<b>Mean</b>	<b>SD</b>
<b>L*</b>	29.04	39.44	35.21	2.34
<b>a*</b>	18	27.24	22.28	2.10
<b>b*</b>	3.85	10.91	6.57	1.64

Table 4.3: Minimums (min), maximums (max), means, and standard deviations (SD) of L\*, a\*, b\* color coordinate values of all beef rib eye samples.

<b>All Samples (n=48)</b>	<b>Min</b>	<b>Max</b>	<b>Mean</b>	<b>SD</b>
<b>L*</b>	29.04	41.49	35.61	2.57
<b>a*</b>	14.65	27.24	21.74	3.027
<b>b*</b>	0.44	10.91	5.36	2.29

#### **4.4.2 Crude Fat and Image Processed Fat**

Minimums, maximums, means and standard deviations (SD) of crude fat, image processed fat (LARGE) and image processed fat (SMALL) for all samples are shown in Table 4.4 and are shown for different Canada quality grades in Table 4.5. As expected, Prime steaks had the most intramuscular fat, as this grade has the most visual fat. The SD of the Prime sample was higher than that of the other grades because it contained some samples with exceptionally high intramuscular fat.

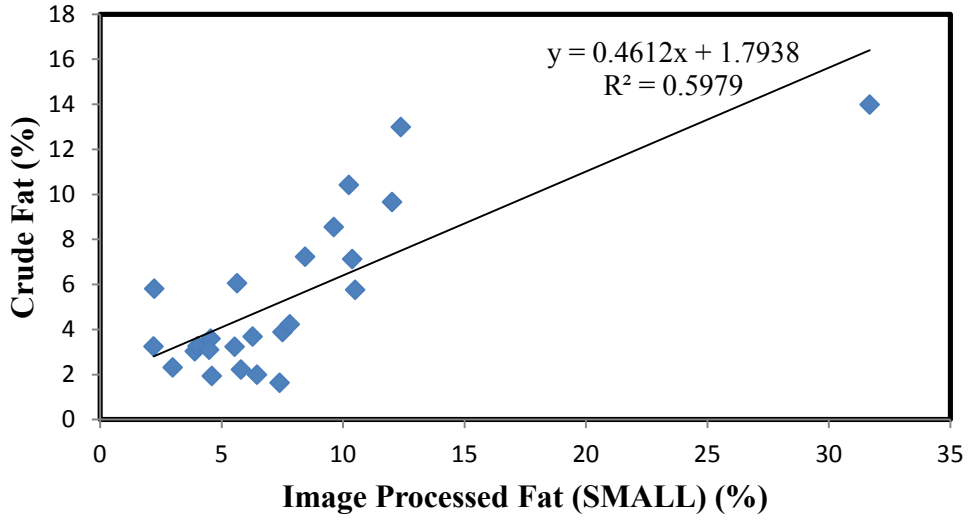
Scatter plots of crude fat regressed to the fat digitally quantified in the LARGE and SMALL image regions [Figure 4.12 (a), (b)] showed that the visual fat in these regions did not correlate well with total extractable fat, as extractable fat described only 69 and 59% of the variation visual fat in each respective region.

Table 4.4: Minimums (min), maximums (max), means, and standard deviations (SD) of intramuscular fat content using different methods for all beef rib eye samples. Crude fat was calculated for all (n=48) beef rib eye samples but image processed fat was calculated for only third and fourth block beef rib eye samples (n=24).

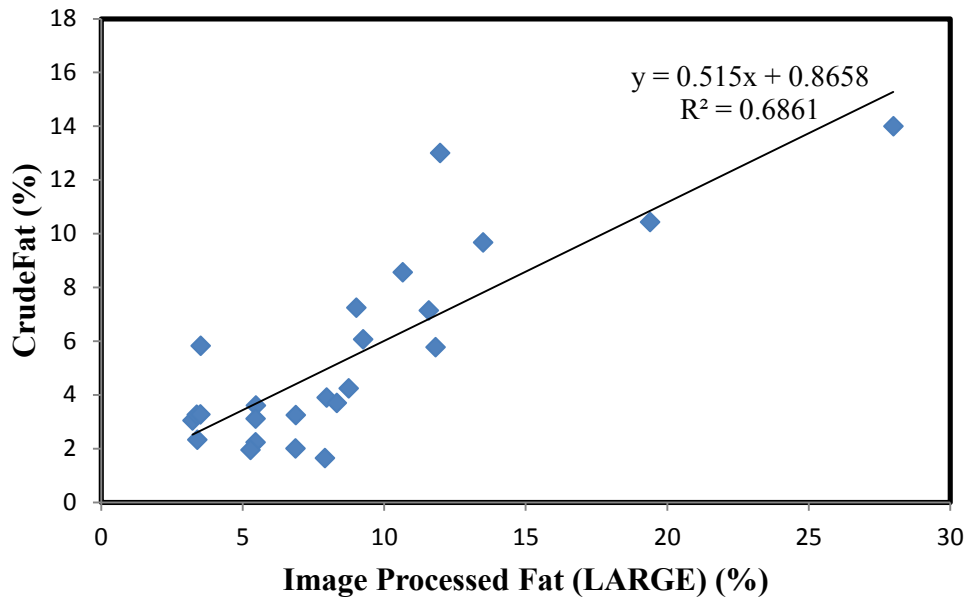
<b>Crude Fat (%) (n=48)</b>				<b>Image Processed Fat (%) (LARGE) (n=24)</b>				<b>Image Processed Fat (%) (SMALL) (n=24)</b>			
<b>min</b>	<b>max</b>	<b>mean</b>	<b>SD</b>	<b>min</b>	<b>max</b>	<b>mean</b>	<b>SD</b>	<b>min</b>	<b>max</b>	<b>mean</b>	<b>SD</b>
1.31	17.51	5.56	3.93	3.22	27.99	8.77	5.65	2.2	31.68	7.78	5.89

Table 4.5: Minimums (min), maximums (max), means, and standard deviations (SD) of intramuscular fat content using different methods for all beef rib eye samples according to quality grade. The crude fat was calculated for all (n=12 in each grade) beef rib eye samples but image processed fat was calculated for only third and fourth block beef rib eye samples (n=6 in each grade).

<b>Grade</b>	<b>Crude Fat (%) (n=12)</b>				<b>Image Processed Fat (%) (LARGE) (n=6)</b>				<b>Image Processed Fat (%) (SMALL) (n=6)</b>			
	<b>Min</b>	<b>Max</b>	<b>Mean</b>	<b>SD</b>	<b>Min</b>	<b>Max</b>	<b>Mean</b>	<b>SD</b>	<b>Min</b>	<b>Max</b>	<b>Mean</b>	<b>SD</b>
<b>A</b>	1.31	5.88	2.92	1.51	3.39	7.90	5.40	1.79	2.23	7.39	4.91	2.02
<b>AA</b>	1.68	3.89	3.11	0.62	3.22	7.96	5.06	2.03	2.20	7.51	4.61	1.79
<b>AAA</b>	3.60	7.14	4.63	1.15	5.46	11.81	9.19	2.34	4.55	10.50	7.53	2.49
<b>Prime</b>	7.24	17.51	11.58	2.73	9.01	27.99	15.42	7.12	8.44	31.68	14.06	8.76



(a)

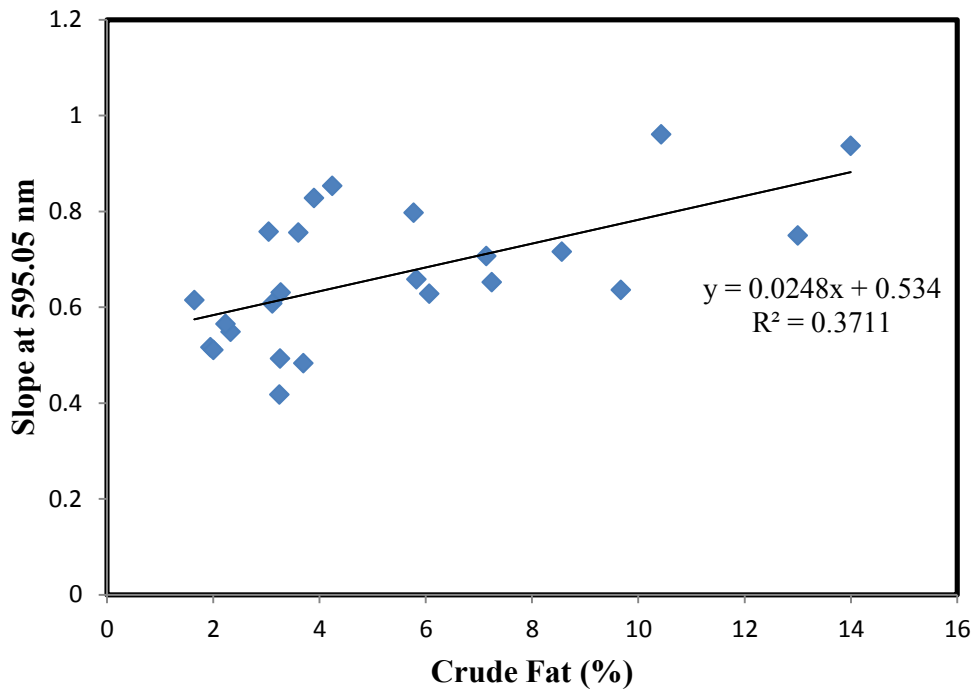


(b)

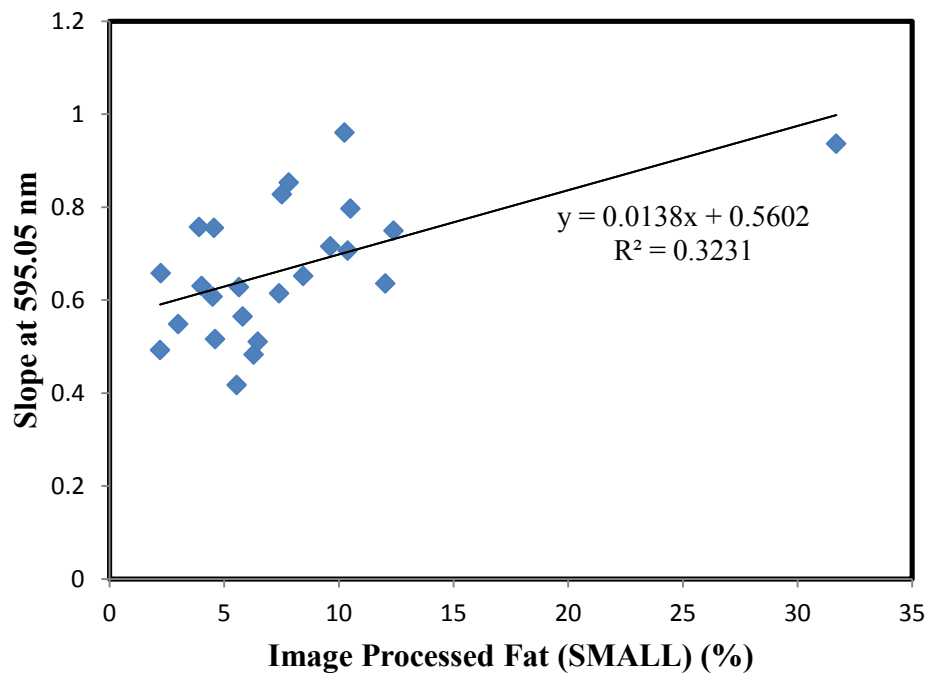
Figure 4.12: (a) Scatter plot of crude fat and image processed fat (SMALL), (b) Scatter plot of crude fat and image processed fat (SMALL).

### 4.4.3 Slope of Reflectivity

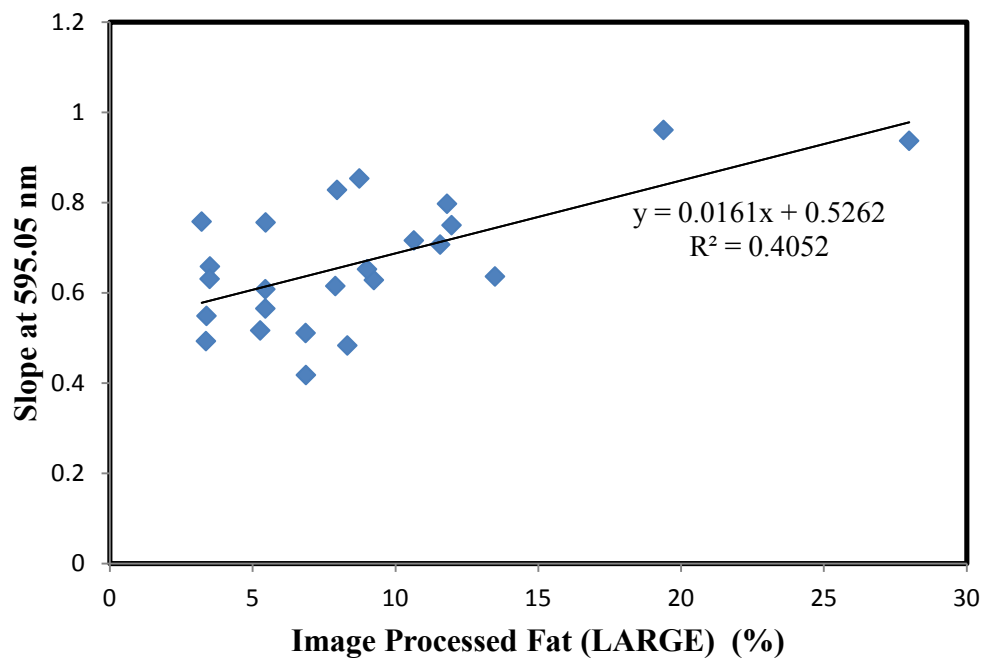
Scatter plots of slope of reflectivity at 595.05 nm from VIS light and 595 nm from LED light regressed with crude fat and image processed fat (LARGE and SMALL) for the third and fourth blocks are presented in Figure 4.13.  $R^2$  values from each regression indicated no strong linear relationships between slope of reflectivity and visual fat (Figure 4.13), with regressions being particularly poor between estimates of fat and the LED light source.



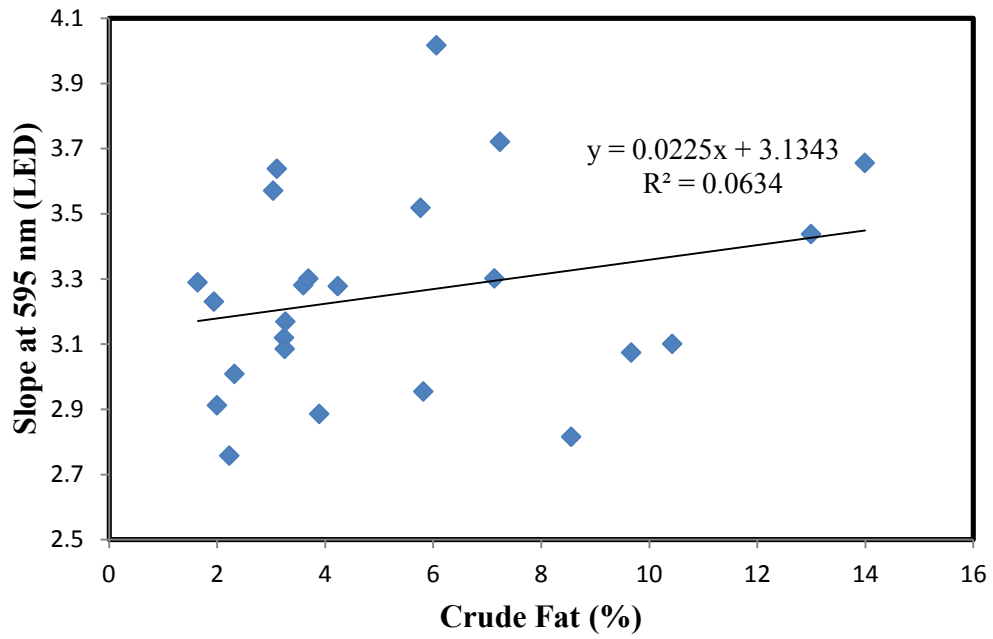
(a)



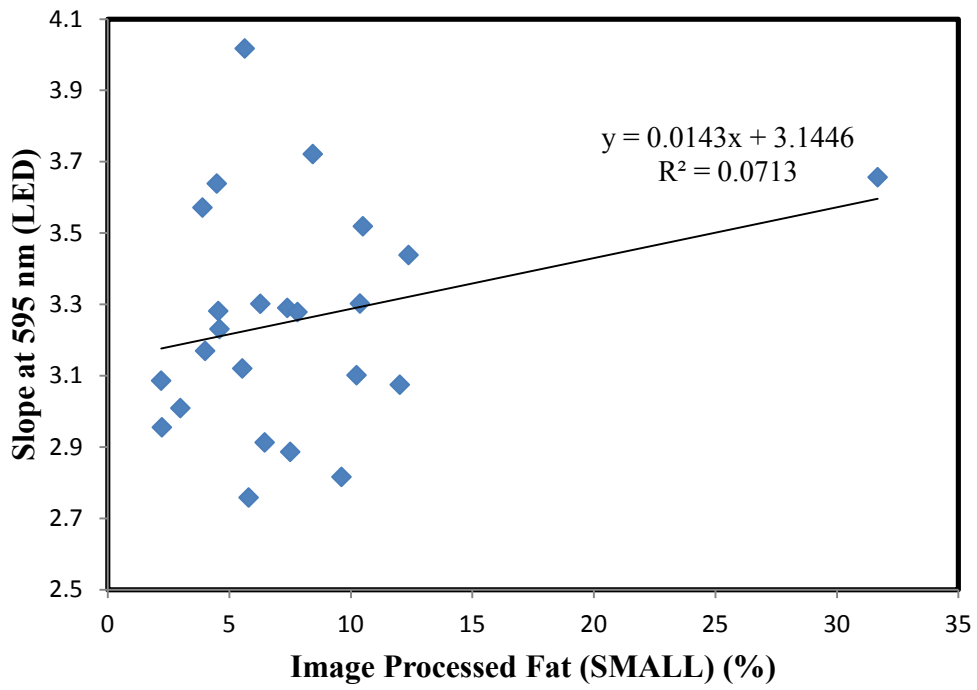
(b)



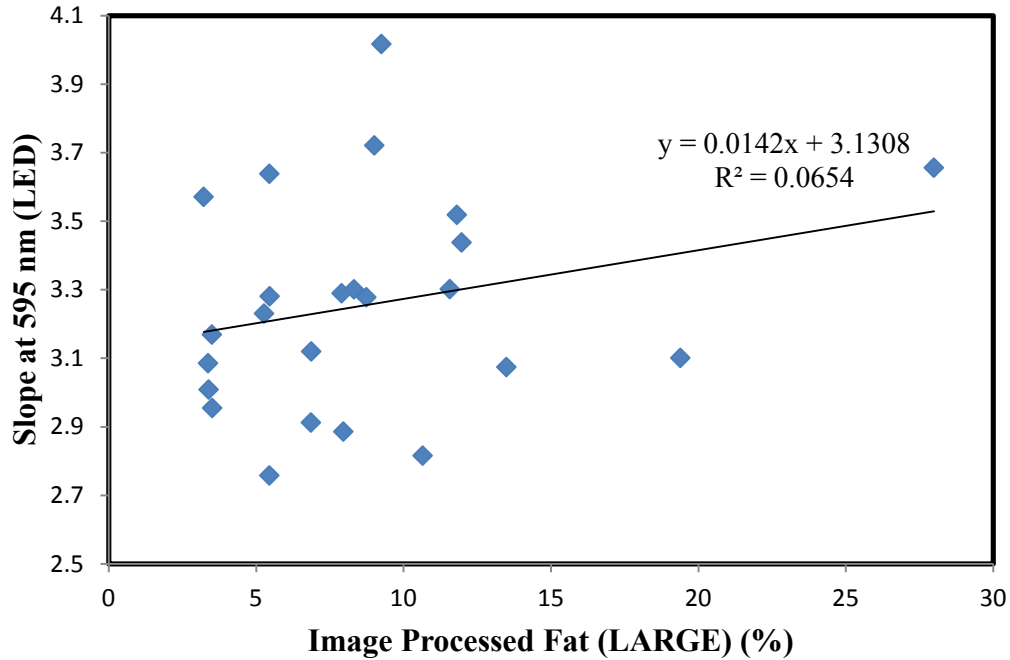
(c)



(d)



(e)



(f)

Figure 4.13: Plots of slope of reflectivity at 595 nm and percentage fat measured using different methods and different instruments from samples of the third and fourth block, (a) plots of slope of reflectivity at 595.05 nm wavelength of VIS spectroscopy using spectrometer with crude fat, (b) plots of slope of reflectivity at 595.05 nm wavelength of VIS spectroscopy using spectrometer with image processed fat (SMALL), (c) plots of slope of reflectivity at 595.05 nm wavelength of VIS spectroscopy using spectrometer with image processed fat (LARGE), (d) plots of slope of reflectivity at 595 nm wavelength of LED spectroscopy using handheld device with crude fat, (e) plots of slope of reflectivity at 595 nm wavelength of LED spectroscopy using handheld device with image processed fat (SMALL), (f) plots of slope of reflectivity at 595 nm wavelength of LED spectroscopy using handheld device with image processed fat (LARGE).

#### 4.4.4 Correlation Coefficients

The Pearson Correlation coefficient (r) values and probability (p) values are presented in Tables 4.6 and 4.7 respectively. Correlations were considered significant at  $p < 0.05$  and are highlighted in Table 4.7.

Table 4.6: Pearson Correlation coefficient (r) values among color, slope, and fat.

Variable	L*	a*	b*	Slope at 595.05 nm	Slope at 595 nm (LED)	Image Fat (%) (LARGE)	Image Fat (%) (SMALL)	Crude Fat (%)
n	24	24	24	24	24	24	24	24
L*	1.00	0.05	0.55	0.57	-0.15	0.32	0.26	0.42
a*		1.00	0.83	0.41	0.00	0.35	0.18	0.40
b*			1.00	0.58	-0.03	0.47	0.31	0.60
Slope at 595.05 nm				1.00	0.20	0.64	0.57	0.61
Slope at 595 nm (LED)					1.00	0.26	0.27	0.25
Image Fat (%) (LARGE)						1.00	0.93	0.83
Image Fat (%) (SMALL)							1.00	0.77
Crude Fat (%)								1.00

Table 4.7: Pearson Correlation probability (p) values among color, slope, and fat with highlighted in green for  $p < 0.05$ .

Variable	L*	a*	b*	Slope at 595.05 nm	Slope at 595 nm (LED)	Image Fat (%) (LARGE)	Image Fat (%) (SMALL)	Crude Fat (%)
n	24	24	24	24	24	24	24	24
L*	0.0000	0.8226	0.0059	0.0035	0.4862	0.1242	0.2120	0.0397
a*		0.0000	0.0000	0.0473	0.9891	0.0909	0.4134	0.0505
b*			0.0000	0.0027	0.8888	0.0194	0.1470	0.0019
Slope at 595.05 nm				0.0000	0.3399	0.0008	0.0038	0.0016
Slope at 595 nm (LED)					0.0000	0.2277	0.2071	0.2354
Image Fat (%) (LARGE)						0.0000	0.0000	0.0000
Image Fat (%) (SMALL)							0.0000	0.0000
Crude Fat (%)								0.0000

#### 4.4.5 Spectroscopic Data Analysis Using PLS Method

The effect of the various data transformations on the relationships between NIR reflectance and fat quantification methods as described by PLS analysis were estimated using  $R^2$  values (Table 4.8). Comparison of NIR spectroscopy data transformation showed that dark current noise subtraction and a smoothing coefficient higher or lower than 11 reduced  $R^2$  values from the PLS analysis. Application of a smoothing filter at different stages of the averaged reflectivity calculation process had limited effect on  $R^2$  values (Table 4.8). PLS analysis on reflectance data (without normalization) obtained marginally lower but comparatively similar  $R^2$  value ( $R^2 = 0.87$ ) compared to PLS analysis on normalized data (Table 4.8).

Table 4.9 shows the calibration and validation  $R^2$  values of VIS and NIR spectroscopy PLS analyses. Reflectivity data from VIS and NIR spectroscopy were capable of describing over 65% of the variation in crude fat and image processed fat using PLS analysis methods. NIR spectroscopy produced higher  $R^2$  values for most relationships with fat (Table 4.9) than VIS reflectance.

#### 4.5 Discussion

Crude fat percentage differences are limited between the Canada quality grades A, AA and AAA but a comparatively high difference in crude fat percentage was noticed between Canada AAA and Canada Prime (Table 4.5). These results support concerns regarding the efficacy of the current Canadian beef grading system and support the use of alternative technology in assessing intramuscular fat content. Estimation of intramuscular fat (IMF) by measurement of visible fat on the surface of LT muscle using digital image processing techniques is the current practice in beef grading and in this experiment showed a 60% to 70%  $R^2$  value between crude fat and image estimated fat.

Table 4.8: Effect of different data (NIR spectroscopy and crude fat) transformations (e.g. normalization, dark current subtraction, smoothing) on calibration and validation  $R^2$  means and standard deviations using PLS method.

	Test No.	Norm <sup>1</sup>	Dark Current	Smoothing	S.C. <sup>2</sup>	Calibration $R^2$			Validation $R^2$		
						n	mean	SD	n	mean	SD
First and Second Block	1	Yes	No	After average	11	5	0.96	0.0004	5	0.90	0.0094
	2	Yes	No	Before Normalization	11	5	0.96	0.0004	5	0.88	0.0171
	3	Yes	No	Before normalization	5	5	0.88	0.0072	5	0.77	0.0153
	4	Yes	No	Before normalization	21	5	0.94	3E-06	5	0.80	0.007
	5	Yes	No	After normalization but before average	11	5	0.96	0.0004	5	0.89	0.0148

	Test No.	Norm <sup>1</sup>	Dark Current	Smoothing	S.C. <sup>2</sup>	Calibration $R^2$			Validation $R^2$		
						n	mean	SD	n	mean	SD
Third and Fourth Block	1	Yes	Yes	Before Normalization	11	5	0.99	0.0091	5	0.60	0.0443
	2	Yes	No	After normalization but before average	11	5	0.99	0	5	0.90	0.0164
	3	Yes	No	Before Normalization	11	5	0.99	0	5	0.90	0.0136
	4	No	No	After normalization but before average	11	5	0.97	0.006	5	0.88	0.0084
	5	Yes	Yes	After normalization but before average	11	5	0.99	0.0018	5	0.72	0.0254
	6	Yes	No	After average	11	5	0.98	0.0033	5	0.90	0.0121
	7	Yes	Yes	After average	11	5	0.99	0.0018	5	0.73	0.0316

<sup>1</sup> Normalization

<sup>2</sup> Smoothing Coefficient

Table 4.9: Calibration and validation of PLS  $R^2$  means with standard deviations in parentheses of different spectroscopic analyses of beef rib eyes (N. A. = not analyzed).

VIS spectroscopy		First and second block		Third and Fourth block	
		Calibration $R^2$ mean(SD)	Validation $R^2$ mean(SD)	Calibration $R^2$ mean(SD)	Validation $R^2$ mean(SD)
Crude Fat	Dark Current subtracted	N.A.	N.A.	0.86(0)	0.65(0.0391)
	No dark current subtracted	0.95(0)	0.80(0.025)	0.85(0.036)	0.51(0.055)
Image Processed Fat	Large	N.A.	N.A.	0.95(0)	0.83(0.0223)
	Small	N.A.	N.A.	0.94(0.0034)	0.69(0.0263)
NIR spectroscopy					
Crude Fat	Dark Current subtracted	N.A.	N.A.	0.99(0.0018)	0.72(0.0254)
	No dark current subtracted	0.96(0.0004)	0.89(0.0148)	0.99(0)	0.90(0.0164)
Image Processed Fat	Large	N.A.	N.A.	0.94(0)	0.80(0.036)
	Small	N.A.	N.A.	0.96(0.0158)	0.65(0.0163)

These results indicated that visual fat is a moderate indicator of chemically extractable fat in beef, and the prediction ability of VIS light may be limited by the penetration depth of VIS light. Also, intramuscular fat may be concentrated on the surface of LD muscle more so than in the remainder of the LT muscle, skewing fat content prediction.

No significant correlation between the slope of reflectivity at 595 nm (LED) and fat percentage (crude fat and image estimated fat) was identified in this study. Slope of reflectivity at 595.05 nm VIS wavelength showed a slightly higher correlation than 595 nm (LED) with  $P < 0.05$  but was not sufficient to estimate percentage fat effectively. Slope of reflectivity of VIS light showed promising results in previous individual LT steak testing (Chapter 3) in estimating the amount of IMF in the muscle, but in the present study performed poorly to predict IMF. Why this occurred was not clear, but this discrepancy warrants further investigation. Myoglobin, a muscle protein responsible for the storage of oxygen in muscle, dominates the VIS light spectrum of meat and its state (deoxygenated, oxygenated or oxidized) determines meat color (Mancini and Hunt, 2005). Lean meat color varied dramatically within the steaks studied in the present experiment, possibly due to differences in bloom time or biologically variation in myoglobin concentration. The correlation coefficients and  $P$  values indicated that slope of reflectivity at 595.05 nm was significantly correlated with all three components of meat color and as well as with crude fat and image fat (LARGE and SMALL). Therefore, the influence of meat color on VIS light prediction of visible fat is worthy of examination.

PLS analysis on normalized whole spectrum NIR reflectance (reflectivity) achieved better linear relationships with and predictions of IMF than VIS reflectivity. Additional investigation into the effects of smoothing and subtraction of dark current were conducted because these data transformations could affect  $R^2$  values, but minimal effect was observed as long as data were normalized. Without normalization, results cannot be compared between samples and measurement times as data would not be adjusted to a fixed reference.

VIS spectroscopy predicted image processed fat LARGE and SMALL ( $R^2$  values = 0.83 and 0.69, respectively) better than it predicted crude fat ( $R^2 = 0.65$ ). This is not unexpected because

images were scanned using VIS light and as a result image processed fat was a true representation of the amount of surface fat concentration. Similarly, VIS spectroscopy only interacted with elements on the meat surface because of the low penetration depth of VIS light compare to NIR light (Section 4.1). In contrast, NIR spectroscopy described greater proportions of variation in crude fat ( $R^2 = 0.83$ ) and image processed fat [ $R^2 = 0.80$  (LARGE) and 0.65 (SMALL)] than VIS light. In the case of the LARGE area image processed fat a higher  $R^2$  value was obtained compared to the SMALL area image processed fat in both VIS and NIR spectroscopy. In the LARGE area image processing, the image processing region contained most of the muscle surface and illustrates the importance of image processing of the entire muscle surface for increased accuracy of prediction. Image processing on a small region could be affected by regional concentration of fat that may lead to erroneous over- or under-estimation of the fat on the entire LT muscle surface.

The highest validation  $R^2$  value obtained using VIS spectroscopy data was 0.80 for samples of the first and second blocks, while for NIR spectroscopy data a  $R^2$  value of 0.89 was obtained for the same blocks. NIR spectroscopy showed true potential in prediction of crude fat relative to VIS light. In the case of the third and fourth blocks, the highest validation  $R^2$  values for prediction of crude fat were  $R^2 = 0.65$  for VIS spectroscopy data and  $R^2 = 0.90$  for NIR spectroscopy. In the case of the VIS spectroscopy data PLS analysis, data with dark current subtracted produced a marginally higher  $R^2$  value ( $R^2 = 0.65$ ) than data without dark current subtraction ( $R^2 = 0.51$ ). In contrast, NIR spectroscopy data analysis repeatedly produced a lower  $R^2$  value with dark current subtraction. It was noticed that VIS light signal to noise ratio was much higher compare to signal to noise ration of NIR light and this could explain the increased  $R^2$  value when dark current was subtracted from VIS spectroscopy data. Further investigation of

the effect of dark current correction on the prediction capability of the data is worthwhile given that small changes in the meat surface may be changes that are important but smaller than the level of noise and may be obscured with dark current subtraction.

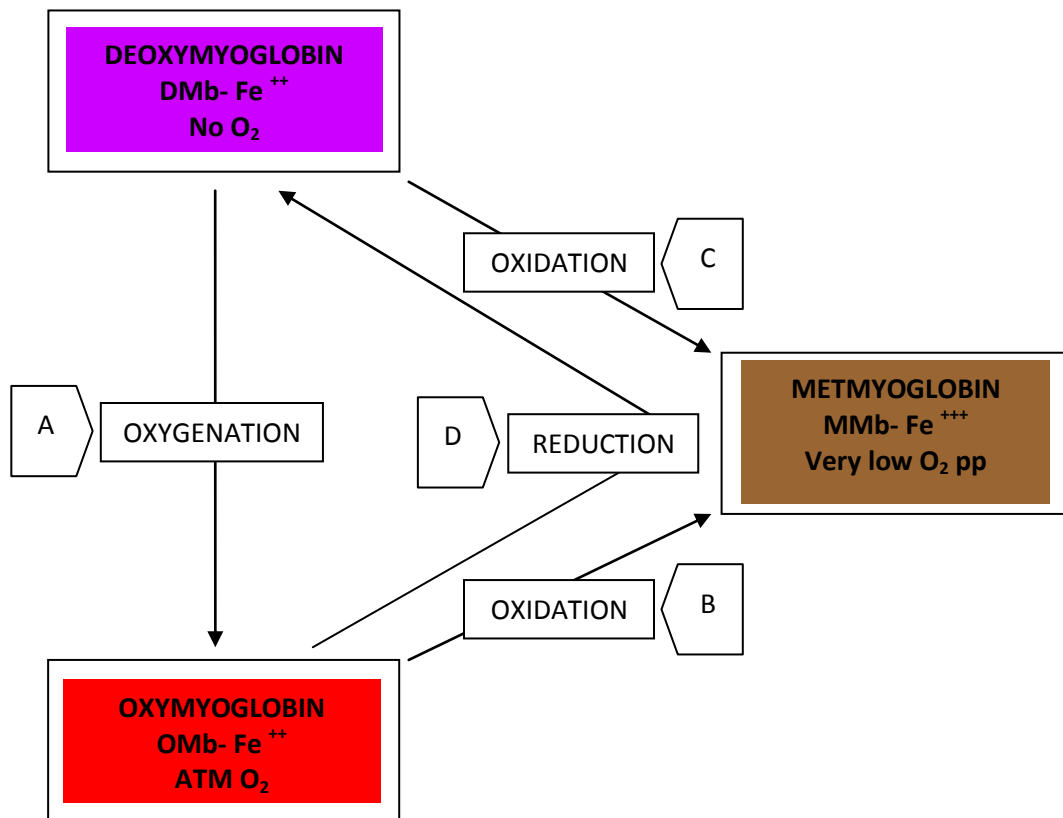
The present experiment was the first study to separate the relationship of VIS and NIR light with visual and chemical fat in meat, as most research to date has focused on both together (Shackelford et al., 2004; Prevolnik et al., 2005; Dian et al., 2008; Prieto et al., 2014) or just NIR (Rødbotten et al., 2000; Su et al., 2014). It is also the first study to use reflectivity rather than absorbance, complicating comparison of prediction results to those of other studies. Despite this, the present study achieved levels of prediction comparable to those observed using NIR (Su et al., 2014) and VIS-NIR (Prieto et al., 2014) absorbance and the results support continued investigation in this area.

## Chapter 5

# Modelling of Visible Light Reflectance and Surface Fat Content of Meat: A Paper Model Experiment

### 5.1 Introduction

Myoglobin is the principle protein responsible for meat color (Mancini and Hunt, 2005). There are three different myoglobin states found in meat: deoxymyoglobin; oxymyoglobin; and metmyoglobin (Figure 5.1).



Reaction A:  $DMb + O_2 \rightarrow OMb$

Reaction B:  $OMb + [\text{oxygen consumption or low } O_2 \text{ partial pressure}] - e^- \rightarrow MMb$

Reaction C:  $[DMb - \text{hydroxyl Ion} - \text{Hydrogen Ion Complex}] + O_2 \rightarrow MMb + O_2^-$

Reaction D:  $MMb + \text{Oxygen consumption} + \text{met myoglobin reducing activity} \rightarrow DMb$

Figure 5.1: Interactions between the three major myoglobin states and their associated colors.

Depending upon myoglobin state and concentration, meat color varies with time post mortem, muscle pH and temperature, oxygen partial pressure and muscle type (Brooks, 1935; Livingstone and Brown, 1982; Wallace et al., 1982; Mancini and Hunt, 2005).

Preliminary experiments (Chapter 3) indicated that wavelengths in the red region of the visible light spectrum were very effective at predicting the amount of fat on the surface of meat as long as the lean meat surface color was constant. In the visible light spectroscopic measurement it was observed that the surface reflectance or absorbance varied with the color of the lean of the meat, which would vary with myoglobin state (Mancini and Hunt 2005).

Deoxymyoglobin, the state in which myoglobin has no oxygen bound to the heme iron, is associated with very low oxygen partial pressure (<1.4 mm Hg; Brooks, 1935). In this state, the color of beef is purplish-red or purplish-pink. This state is usually found in vacuum packaged beef after cutting (Mancini and Hunt, 2005). Immediately after exposure to oxygen, myoglobin oxygenates and the color changes to a bright cherry-red, which is the color associated with the normal beef (Mancini and Hunt, 2005). The layer of oxymyoglobin extends beneath the surface of the meat with the highest oxygen concentration remaining at the meat surface. Oxygen partial pressure, meat's temperature, the pH of meat and the rate at which oxygen is consumed by other respiratory processes of the meat are the factors that determine the depth of oxygen penetration and oxymyoglobin thickness under the meat surface (Mancini and Hunt, 2005). The inside of the meat remains the purple color of deoxymyoglobin. Between the outer layer of red oxymyoglobin and inner layer of purple deoxymyoglobin a thin layer of brown oxidized myoglobin, called metmyoglobin, which exists because at low oxygen partial pressure oxidation is preferred over oxygenation (Brooks, 1929; George and Stratman, 1952). Metmyoglobin is transformed to deoxymyoglobin by enzymes inherent to the muscle tissue that have metmyoglobin reducing

activity (MRA) (Price and Schweigert, 1989). Myoglobin therefore continuously cycles through its three states and so the actual surface meat color is characterized by not just one myoglobin state but the relative concentrations of all three of the states. Opacity of the meat surface layer is also a key factor that influences the perception of each of the three myoglobin derivatives (Krzywicki, 1979).

The time required for the oxygenation of each surface myoglobin to oxymyoglobin from either one of the other two states is called the blooming time. The general blooming time is usually considered to be 30 to 45 min, and the minimum time as required by federal grading guidelines is 10 min after “knife-ribbed” (“knife-rib means to carcass between the 12<sup>th</sup> and 13<sup>th</sup> ribs by severing the vertebrae and cutting 15 cm or more beyond the *Longissimus* muscle in order to expose them for evaluation by a grader [Livestock and Poultry Carcass Grading Regulations (SOR/92-541), Government of Canada]. With the exposure of the meat to atmospheric oxygen, the meat color brightens with the exposure or “blooming” time. In the beef grading system grading is performed after a minimum of 10 minutes blooming time.

Prolonged exposure to oxygen also promotes oxidation of the myoglobin heme iron and causes the brown discoloration of meat (Livingston and Brown, 1982; Wallace et al., 1982). The rate of oxidation of myoglobin to metmyoglobin is affected by meat storage temperature, oxygen partial pressure, pH, activity of muscle reducing enzymes (NADH reductase) and microbial growth (Mancini and Hunt, 2005).

Current grading technology employs a digital camera image processed in computer, and there is agreement that this can be advantageous for the evaluation of meat surface color (Mancini and Hunt, 2005). O’Sullivan et al. (2003) mentioned that a JPEG image derived from a digital camera has several benefits over a colorimeter because only one measurement was needed for

the whole meat surface to be assessed for meat surface color and surface color variation, thus taking into account the different myoglobin states over the whole surface. Also, the color of a digital image can be described using multiple color measurement systems (Hunter, CIE, XYZ). According to Lu et al. (2000) meat color can be predicted using a combination of neural network or statistical model and digital image analysis. In the previous experiments (Chapter 4), scanning the meat surface with a digital scanner produced a picture more faithful to the original meat than that of a digital camera image. A digital camera image [Figure 5.2 (a)] included shadow and glare effects, which were mostly eliminated in the scanned image [Figure 5.2 (b)]. Using scanned images, the ranges of RGB (Red, Green and Blue) values associated with meat surface color can be characterized and used for quality control or detection of abnormal colors.

Despite the advantages of a scanned image, the use of reflectance offers the advantages of decreased detection and processing time and reduced computing and electronic storage requirements. The primary objective in the preliminary experiments (Chapters 3 and 4) was to predict the amount of surface fat (also known as marbling) in the beef *longissimus thoracis* (LT, rib eye) muscle using visible light spectroscopy. Prediction algorithms were developed (Chapter 3) for individual steaks using surface reflectance of certain wavelengths in visible light spectrum which were not transferable to other steaks, suggesting that the color of lean meat on the measurement surface needed to be constant. An added complication noted in Chapter 3 was that the spatial distribution of lean meat color was not constant over the surface of meat. With this, prediction of marbling in beef using one algorithm becomes almost impossible without considering the effect of lean meat color in reflectance of visible light spectrum. To consider the effect of lean meat color on VIS light reflectance and reflectivity, a paper model was used to test the hypothesis that the ability of VIS light wavelengths to predict the amount of white on a

surface varied with the non-white color of the surface. The objective in this paper model experiment was to find an equation that would model the effect of variation in lean meat color on marbling prediction.

In recent papers partial least square regression (PLS) analysis was found to be very useful for spectroscopic data analysis. PLS analysis is useful for finding fundamental relations (Martens and Næs, 1989) between two variables (amount of fat and spectral reflectivity of meat surface). Khatri et al. (2012) mentioned that PLS would model two variable spaces (amount of fat in Y space and spectral reflectivity in X space) that co-vary with each other in “multidimensional direction”. In the present study, the variable space of color was hypothesized to be a third variable factor that was affecting the prediction of fat using spectral method. Hence, partial least squares analysis was performed on the data collected from the present experiment to test the hypothesis.

What can be duplicated in modelling reflectance spectroscopy as a tool for estimating meat quality is that the reflectance of the meat surface will be measured by shining the light on to surface and the intensity of the reflected light measured from the surface using a spectrometer. What cannot be duplicated in modelling the use of reflectance in meat is that the light does not just reflect back from the topmost layer of the meat surface but also penetrates into the muscle tissue to a depth of 3 to 4 mm (Lawrie, 1964 cited by Krzywicki, 1979). A percentage of the light energy will be absorbed by the meat pigments as well due to refraction and reflections caused by colorless proteins of the muscle (Krzywicki, 1979). Modelling of this is not necessary, however, to examine the interaction of color and the use of VIS light reflectance to estimate the proportion of fat on a meat surface.



(a)

(b)

Figure 5.2: Digital JPEG image taken by (a) Logitech camera (webcam C905), and (b) EPSON PerfectionV33 flatbed scanner.

## 5.2. Materials and Methods

### 5.2.1 Materials

Commercially available laser printer paper (21.5 cm × 28 cm) was used for this experiment. The printing was performed using a laser color printer (WorkCenter™ 7545, Xerox, Norwalk, Connecticut, USA). Eight different color tones were used for this experiment (Figure 5.2.1.1). The color tones were labeled as CL1, CL2, CL3, CL4, CL5, SCL1, SCL2, and SCL3 (Figure 5.3). The RGB (0 to 255 scale) color coordinate values were chosen from averaged myoglobin color from scanned digital image of different real meat steak. The  $L^*a^*b^*$  color coordinate values (0 to 255 scale) were calculated from the RGB values using standard transformation functions available in MATLAB™ (Appendix D). Each different color tone was printed as a circle approximately 7.5 cm in diameter filled with same color tone to model a particular sample at a particular myoglobin (color) state. There were four different color tones (light to dark) that were close to brown (the color of metmyoglobin) and four different color tones (light to dark) which

were close to red or bright red (the color of oxymyoglobin). Representative pixel RGB values were chosen from the scanned images of the real meat (Chapter 4).

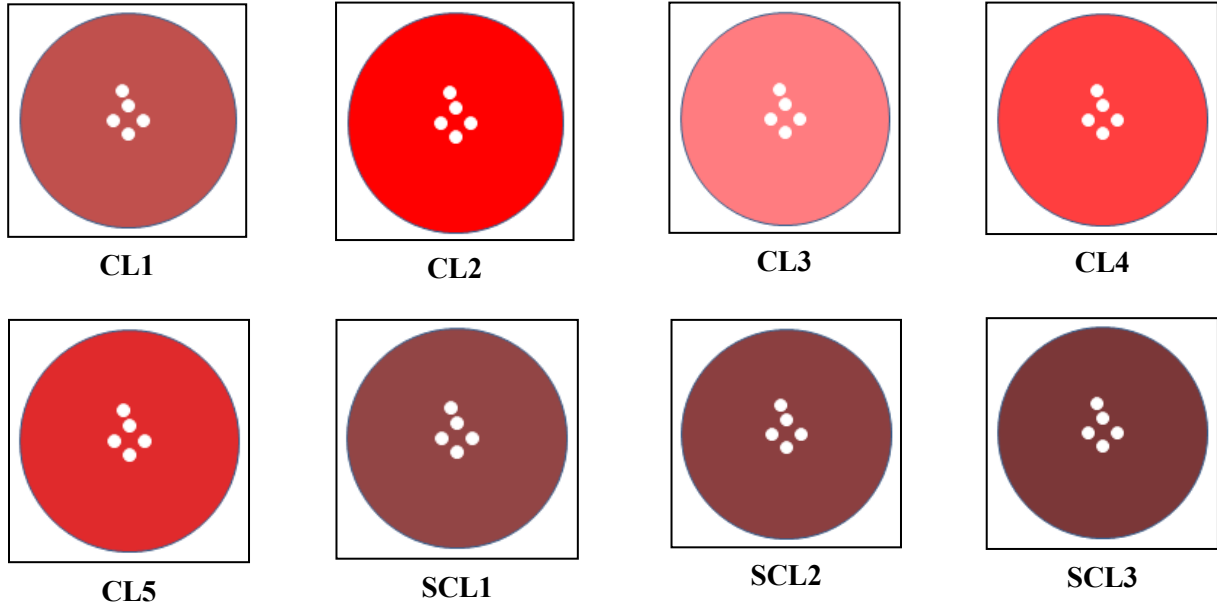


Figure 5.3: Eight different color circles used for the paper model experiment with white small circles simulating the surface fat or marbling on the beef.

Fat pieces on the meat surface were modeled using 5 mm diameter circles (Figure 5.4). In each particular color tone the number of fat pieces was increased from one to twenty-three with an interval of two to model different marbling grades within each particular color tone. One circle with zero fat pieces was created for modeling absolute lean sample. The same Teflon<sup>TM</sup> sheet described in Chapter 3 and Chapter 4 was used for normalization. There were five circles with the same number (five) of fat pieces (small white circles) each with white circles in a different configuration to test the light source for uniformity of detection over the incident surface as well as the consistency of the instrument over time (Figure 5.4).

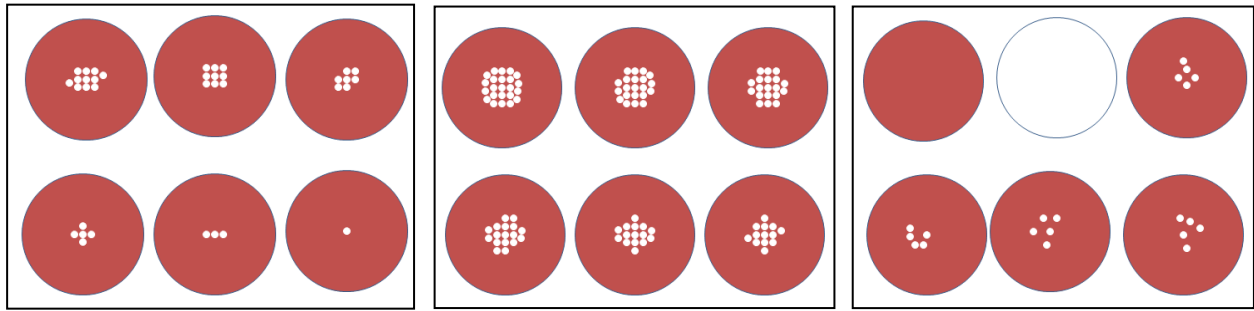


Figure 5.4: Illustration of paper models simulating different marbling grades and increments in surface fat content by varying the number and pattern of small white circles to test the use of VIS light for fat quantification, and for detection of uniformity and consistency of light source.

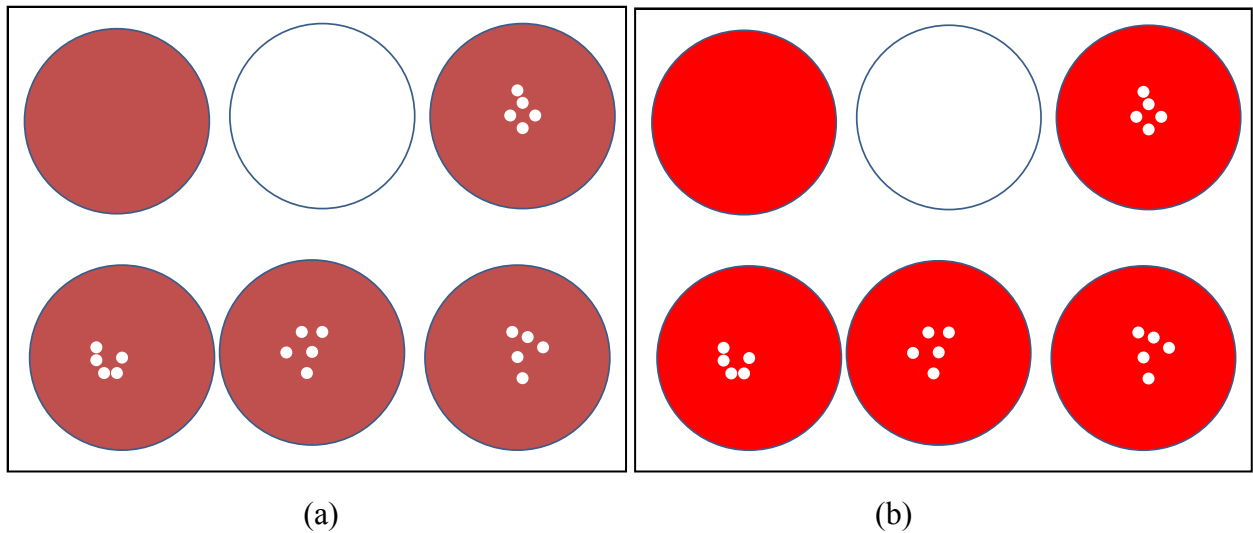


Figure 5.5: Illustrations of paper models used that simulated (a) metmyoglobin color and (b) oxymyoglobin color with white small circles representing the intramuscular fat in lean meat.

The reflectance intensity of the visible light spectrum was measured using a USB spectrometer (OceanOptics USB4000) as explained in Section 3.2.2 of Chapter 3. The light source (HL-2000) which was used during the experiments of Chapter 3 and Chapter 4 was identified to have non-uniform intensity over the measurement surface region (data not shown). A commercially available 100 watt incandescent light bulb (Soft White, 120V, 100W, Philips,

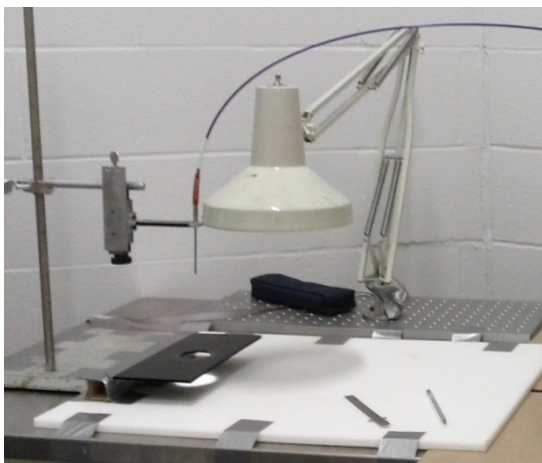
Canada) was used as this kind of bulb had a broad optical spectrum that extends well into the NIR region. The light source was tested for repeatability of measurement and stability over time (data not shown). Uniformity, stability and repeatability of the light source were tested using a paper model by varying the pattern of the same number of white dots on identically colored circles of a constant diameter (Figure 5.5). The reflectance light was collected using the bifurcated fiber optic cable (OceanOptics R600-7-VIS-125F) as explained in Section 3.2.2 of Chapter 3. Although it had multiple fiber channels surrounding the main collection fiber for carrying source light on to the measurement surface, the light coming through those fiber channels was closed. The collection fiber in the middle was used for collection of the reflected light. The height from the measurement surface to the end of the probe was kept constant during any measurement and its corresponding reference measurement for normalization [Figure 5.6 (a)].

The Teflon<sup>TM</sup> sheet was used as a reference measurement for normalization. The black mask cover (Section 3.2.2 of Chapter 3) was used to cover the regions on the measurement surface except the area to be measured [Figure 5.6 (b)]. This prevented interference from other surface regions of the sample that were not intended for measurement and it was used throughout the study.

### **5.2.2 Experimental Setup**

The entire experiment was performed in a dark lab room with no window. The light source (a commercial incandescent light bulb) was attached to a table lamp stand and the stand was placed on a table. A comparatively smaller stand with height adjustment feature was made for holding the fiber optic probe. Both stands were fixed to the table to confer positional stability [Figure 5.6 (a)]. The light source was placed over the probe at a fixed distance so that the measurement

surface had as uniform light intensity as possible and the relative position and height of the light source was monitored during the experiment to ensure that fiber optic probe height was constant. The lab temperature was constant (21 - 22 °C) over time. One end of the bifurcated fiber optic cable with one fiber channel for collecting reflected light was connected to spectrometer using a SMA905 connector. The other end of the cable with multiple fiber channels for carrying light from light source was kept closed as we did not use it for sourcing light. The USB spectrometer was connected to a Netbook Computer (Aspire one 532h-2630, Acer, China). The interface software (SpectraSuite™, Ocean Optics, Dunedin, Florida, USA), installed in the Netbook, was used to set different parameters of spectrometer and collecting measurement readings from spectrometer. The reflectance data of entire spectrum from spectrometer was saved in an Excel™ file for further processing. The reflectance data was then processed and analyzed in MATLAB™.



(a)



(b)

Figure 5.6: (a) The fiber optic probe is attached to a standard laboratory stand using a custom made height adjustment holder with light source, white cutting board and black mask attaché to table with tape. This experimental apparatus was used for VIS spectroscopic measurements; (b) measurement area on sample (beef rib eye steak or paper model) with black mask cover and white fat pieces (white small circles for paper model) in the measurement area.

### **5.2.3 Spectroscopic Measurement**

The integration time for the spectrometer was set at 100 ms and an option for dark current reduction in the interface software was set to ‘ON’ for all the spectroscopic measurement. Fiber optic probe height was set at 12 cm from the measurement surface. The black mask cover was attached to the table using tape so that the relative position between optical fiber probe, light source and the area to be measured was constant for all the samples. Each paper model sample was placed under the black mask and adjusted so that the center circle of the black mask stayed exactly on top of the intended measurement area [Figure 5.6 (b)]. Reflectance spectra readings were taken from each sample of each paper model and also from the white Teflon™ sheet for normalization. “Dark current” noise was measured by covering the probe with a cap (provided with the fiber optic cable).

### **5.2.4 Light Source Test Experiments**

Light sources need to be tested to confirm the repeatability of the spectroscopic measurement and to confirm that they can produce a uniform illumination over the area to be measured. Uniformity, stability and consistency of the light source were tested using a series of experiments. A set of five different colored paper models representing different “meat” samples with the same amount of model “fat” depicted by the same number of small white circles were created for this testing. Within each paper model color set, four circles had the same background color and each had five small white circles in different positions (Figure 5.5). Although the position of the fat circles were different, the amount of “fat” or percentage of the total white area in each sample of a given set was same. The objective of these tests was to confirm the repeatability of the spectroscopic measurement method used in this study. The first hypothesis

tested was that the light source produced uniform illumination over the entire measurement surface area. The second hypothesis considered was that the light source was consistent and stable over time. The measured data was then processed and analyzed in MATLAB<sup>TM</sup>. The first hypothesis would be accepted if each circle within a given color set produced identical results in spectroscopic analysis. The second hypothesis would be accepted if the results were consistent between each paper model replicate measurement.

### 5.2.5 Data Analysis

All reflectance spectroscopic data measured were saved in Excel<sup>TM</sup> (Microsoft Office) file. MATLAB<sup>TM</sup> was used to read the data from all Excel<sup>TM</sup> files and then analyze. Reflectivity at each wavelength was calculated using the following formula;

$$R = \frac{I_{\text{reflected}} - I_{\text{dark}}}{I_{\text{reference}} - I_{\text{dark}}} \times 100 \quad (5.1)$$

where R was the percentage reflectivity of each wavelength,  $I_{\text{reflected}}$  was the light intensity at each wavelength reflected back from the sample,  $I_{\text{reference}}$  was the light intensity at each wavelength reflected back from the white reference (Teflon<sup>TM</sup> sheet) and  $I_{\text{dark}}$  was the dark noise which was measured when there was no light (the probe was covered with a cap). During the recording of  $I_{\text{reflected}}$  and  $I_{\text{reference}}$  great care was taken to ensure that the experimental setup and all other measurement conditions remained constant. A substantial amount of noise was removed by subtracting the dark noise ( $I_{\text{dark}}$ ) from the  $I_{\text{reflected}}$  and  $I_{\text{reference}}$ ; however, a smoothing filter of moving average type with a smoothing coefficient of 51 (span =  $51 \times 0.22 = 11.22$  nm) was used to filter each individual reflectance spectra before calculation of reflectivity. After calculating the reflectivity at each wavelength, the slope of reflectivity was calculated to regress onto the

number of small circles or “amount of fat” in each sample. The slope of reflectivity data were also filtered using same smoothing filter and smoothing coefficients as used for reflectance data. The results were then plotted using the plot command in MATLAB™. A different smoothing coefficient of 91 (span = 91 × 0.22 = 20.02 nm) were also used in some special circumstances. Area covered by small white circles was converted to a proportional percentage of the total area of each color tone circle for percentage of fat. The percentage fat was calculated using the following equation;

$$\text{Percentage FAT} = \frac{\text{Area covered by white small circles (modeled as fat)}}{\text{Area covered by background color (modeled as myoglobin color)}} \times 100 \quad (5.2)$$

### 5.2.6 Statistical Analysis

The reflectivity spectrum data of paper model was normalized for PLS analysis using the following equation:

$$R = \frac{I_{\text{reflected}} - I_{\text{dark}}}{I_{\text{reference}} - I_{\text{dark}}} \quad (5.3)$$

The parameters of this equation are explained in Section 5.2.5 of this chapter. A smoothing filter was not applied on this paper model spectroscopic data, but certain boundary wavelengths were discarded from the data set due to presence of significant amount of noise. The effective wavelength range used in this analysis was from 410.1 to 700.1 nm. The dark current was subtracted as was done in other reflectivity calculations. PLS was analyzed using the statistical analysis software Unscrambler™ (Camo, Woodbridge, USA). For easy identification of modeled myoglobin colors, sample IDs were prefixed with color identifier such as B as Brown for color tone CL1, R as Red for color tone CL2, P as Pink for color tone CL3, RP as Reddish Pink for

color tone CL4, and BR as Brown Red for color tone CL5. A number identifier was used to indicate the number of fat pieces such as R5 for 5 pieces of fat (pieces of fat were modeled as small white circles) on red background. In this PLS analysis number of fat pieces (1 to 23 pieces of fat in odd sequence) or percentage fat (calculated using equation 5.2) was used as the dependent variable and reflectivity (using Equation 5.3 without smoothing) from 410.1 to 700.1 nm as this range had limited noise. The PLS analysis was performed using the NIPALS algorithm with a random cross validation method. Various trends in the data sets were denoted as factors and the default setting of seven factors was utilized. Wavelengths with higher regression coefficients at each factor were selected in order to improve the explained variance of each factor. This process was continued in an iterative manner until a maximum overall explained variance was achieved.

## **5.3. Results**

### **5.3.1 Light Source Test Results**

The paper model samples used for uniformity testing of the light source each had five small white circles (same amount of fat) and had same color tone (myoglobin color) but the small white circles were oriented in different locations in each sample. There were five samples with the same number (five) of small white circles in each color tone (Figure 5.4). Figure 5.7 is presented the plot of reflectivity as a function of wavelength of these five samples within one color tone (CL1). Here, the smoothing coefficient of 91 was used for ease of uniformity identification. The reflectivity plots (Figure 5.7) of five samples containing the same number of white circles were closely matched with each other regardless of the location of the white small circles, indicating that the light source illumination over the entire measurement area was uniform.

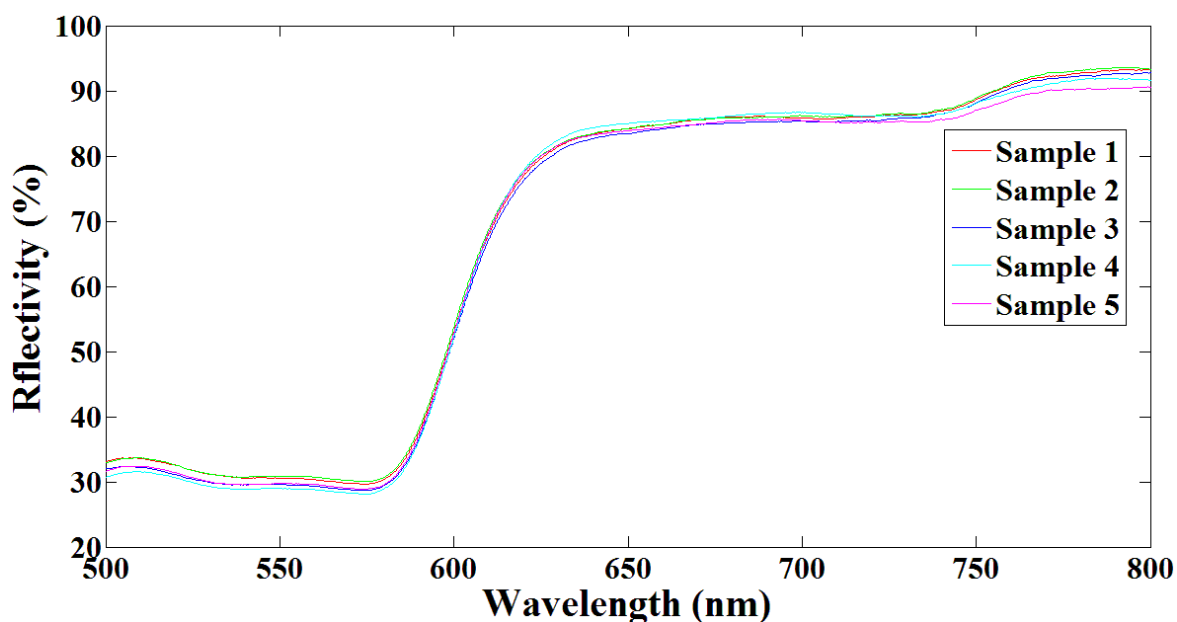


Figure 5.7: Reflectivity plots of five samples with same amount of model fat and same color tone (model myoglobin color tone of CL1) but different positioned fat pieces with smoothing coefficient of 91.

### 5.3.2 Spectroscopic Measurement Results

Reflectivity as a function of wavelength plot for the different numbers of fat pieces from the same color tone (CL1) showed that the results of the paper model were similar to our previous experiments with real meat samples in Chapter 3 (Figure 5.8). The results of the predictive algorithm (slope of reflectivity at specific wavelengths) for each color group were plotted against the percentage of FAT (Figure 5.9) as calculated using Equation 5.2. There was a linear relationship between the slopes of reflectivity at specific wavelengths and number of fat pieces or percentage of fat as observed in Chapter 3. Linear relationships were found to exist for each different background color tone (modeled myoglobin color) and each paper model regression had a linear relationship between slope and percentage fat with average  $R^2$  value of 0.99 (standard deviation (SD) = 0.009). Linear regression equations for each paper model color are presented in

Table 5.1, along with the corresponding R, G, B, L\*, a\*, b\*, Y intercept and slope of the regression equation (slope of slopes). Regression of the slopes of reflectivity for each color tone on to the percentage of fat together in one plot confirmed that as the background color changed, so too did the slope and amplitude (Y intercept) of the regression line (Figure 5.10).

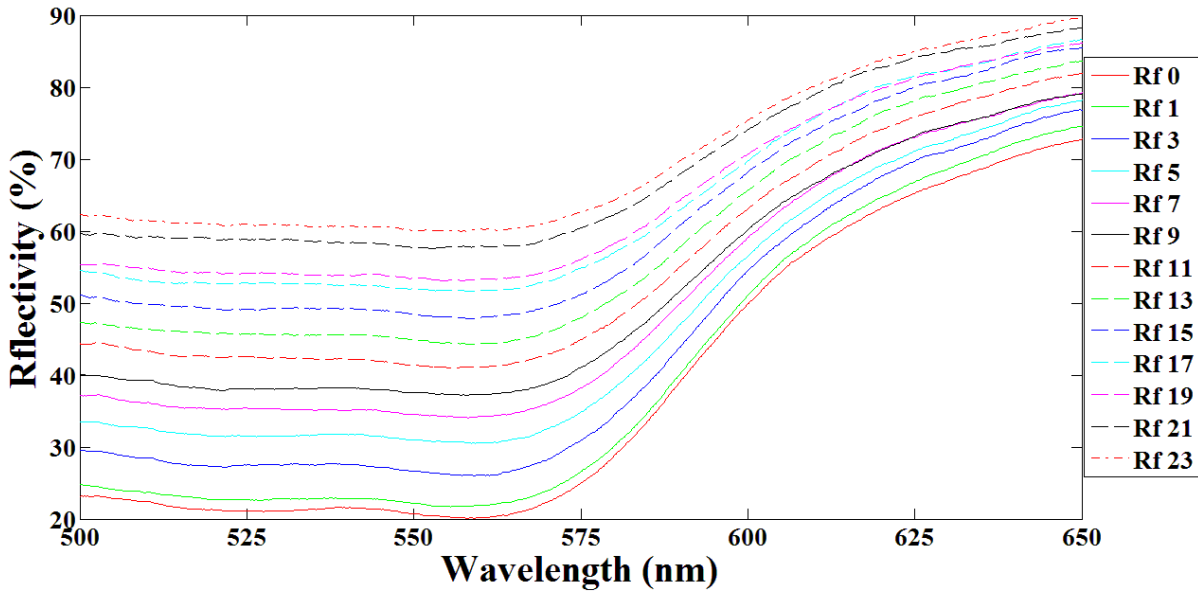


Figure 5.8: Reflectivity as a function of wavelength plot for varying number of small white circles from 0 to 23 on the same color tone (CL1) samples with smoothing coefficient 51.

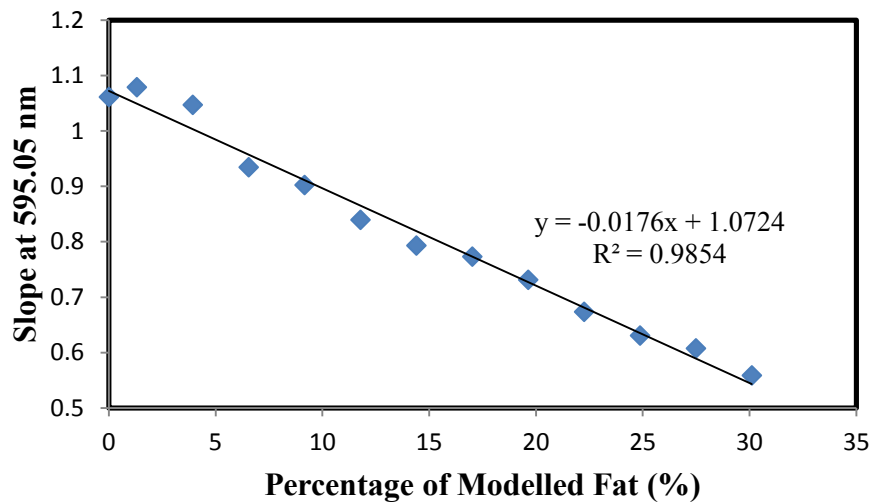


Figure 5.9: Slope of reflectivity at 595.05 nm as a function of the percentage of small white circle area from color tone CL1 samples.

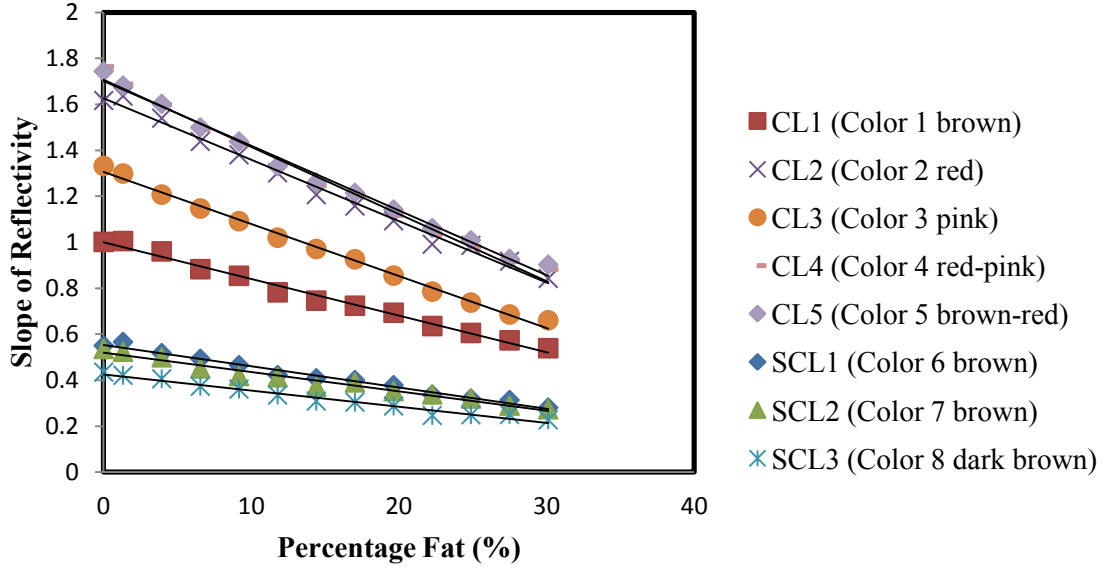


Figure 5.10: Slope of reflectivity (at 595.05 nm) as a function of percentage of fat for different background color tones (modeled as myoglobin color).

Table 5.1: Linear fit equations, R, G, B, L\*, a\*, b\*, Y intercept, Slope of slopes at 595.05 nm for each different myoglobin color model.

Color ID	Linear fit Equation	R	G	B	L*	a*	b*	Y intercept	Slope of slopes
CL1	$y = -0.0411x + 1.0561$	192	80	78	126	174	153	1.0006133	-0.0411
CL2	$y = -0.0687x + 1.7195$	254	0	2	138	209	197	1.61593862	-0.0687
CL3	$y = -0.0584x + 1.386$	255	124	129	174	179	150	1.33097361	-0.0584
CL4	$y = -0.0754x + 1.8111$	255	62	63	148	200	175	1.7618023	-0.0754
CL5	$y = -0.0726x + 1.8008$	224	42	44	128	196	175	1.74310341	-0.0726
SCL1	$y = -0.0239x + 0.5855$	146	69	69	101	161	143	0.54935174	-0.0239
SCL2	$y = -0.0217x + 0.5495$	139	63	64	95	161	143	0.53509916	-0.0217
SCL3	$y = -0.018x + 0.449$	123	55	56	84	158	142	0.4341367	-0.018

Regression of  $a^*$  (redness) values on to the Y intercepts of the regression equations indicated that  $a^*$  values described 91% of the variation in Y intercepts ( $R^2 = 0.91$ ), suggesting that background redness influenced slope of reflectivity (595.05 nm) amplitude when reflectance at 595.05 nm was used. This was confirmed by a  $R^2 = 0.99$  for a regression between the slope values of the regression of slope of reflectivity on to the proportion of white and the Y intercepts at this wavelength.

The influence of sample background color on the linear mathematical description of whiteness in the colored sample circles persisted at 525 nm, the isobestic wavelength of myoglobin, a wavelength that exhibits minimal differentiation of purple, red and brown (Krzywicki, 1979). At 525.12 nm, a linear relationship between reflectivity and percentage white circle was found (Figure 5.11) that was closely related ( $R^2 = 0.99$ ) to the amount of white on the sample circle.

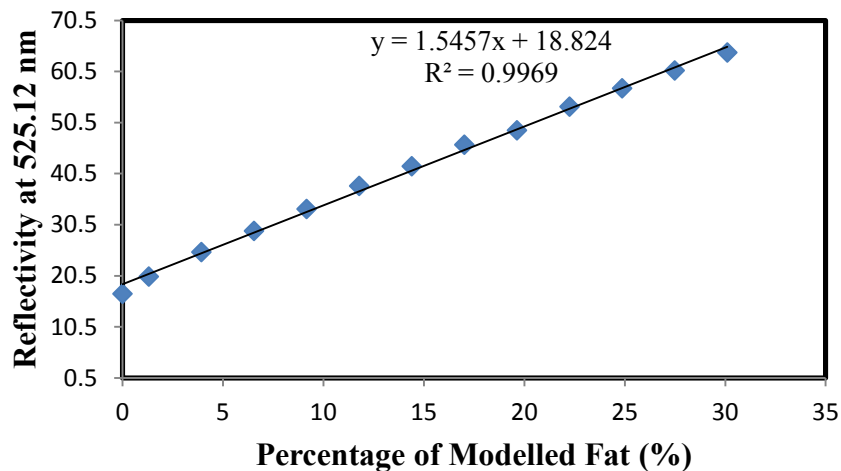


Figure 5.11: Reflectivity at 525.12 nm wavelength as a function of percentage of modeled fat (percentage white dot area) from color tone SCL1 samples.

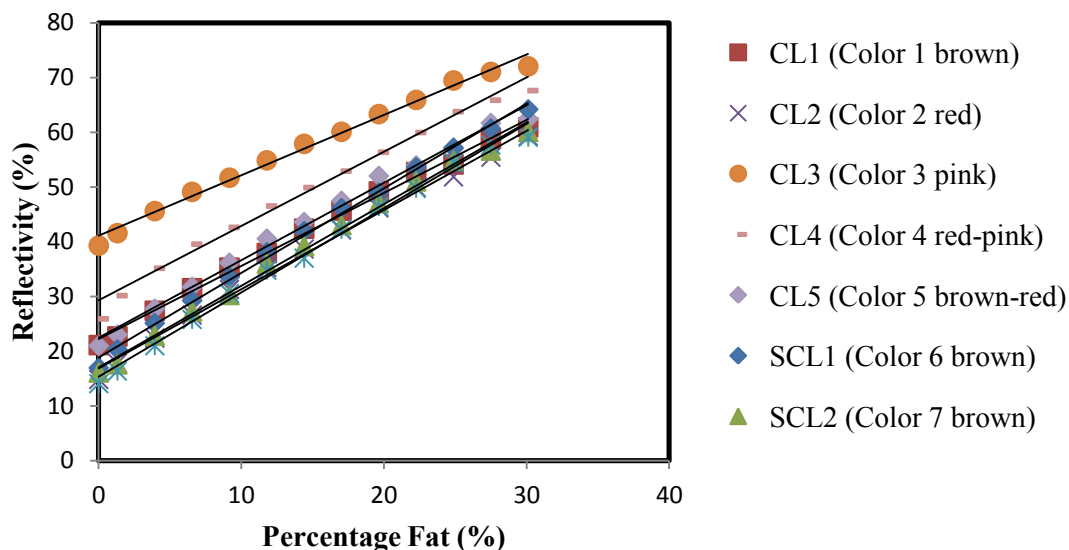


Figure 5.12: Reflectivity (at 525.12 nm) as a function of percentage of fat of different background color tone (modeled as myoglobin color).

The changes in reflectivity at 525.12 nm due to background color variation appeared to be one rather than two dimensional (Figure 5.12), however, with only a change in reflectivity amplitude (Y intercept). The changes in slope of reflectivity between different colors were significantly low (Table 5.2).

Table 5.2 shows the linear fit equations for each color set along with the corresponding R, G, B, L\*, a\*, b\*, Y intercept and Slope of reflectivity values at 525.12 nm. The linear relationship between reflectivity at 525.12 nm and percentage of modeled fat was found to have an average  $R^2$  of 0.99 (SD = 0.0027). Regression analysis showed a  $R^2 = 0.73$  between Y intercept and L\* values and a  $R^2 = 0.88$  between the Y intercept and the slope of reflectivity, indicating that lightness influenced the amplitude of the reflectivity and that amplitude and slope of reflectivity were confounded. However,  $R^2 = 0.09$  between the slope of reflectivity and a\* indicated that

redness did not affect the slope of reflectivity. As a result, limited variation was noted in the slope of reflectivity values among the color tones due to variation in redness.

Table 5.2: Linear fit equations, R, G, B, L\*, a\*, b\*, Y intercept, and slope of reflectivity regression for each different color model.

Color ID	Equation of linear fit	R	G	B	L*	a*	b*	Y intercept	Slope of reflectivity
CL1	$y = 1.3339x + 22.191$	192	80	78	126	174	153	22.191	1.3339
CL2	$y = 1.4468x + 16.858$	254	0	2	138	209	197	16.858	1.4468
CL3	$y = 1.1035x + 41.078$	255	124	129	174	179	150	41.078	1.1035
CL4	$y = 1.3582x + 29.261$	255	62	63	148	200	175	29.261	1.3582
CL5	$y = 1.4155x + 22.44$	224	42	44	128	196	175	22.44	1.4155
SCL1	$y = 1.5457x + 18.824$	146	69	69	101	161	143	18.824	1.5457
SCL2	$y = 1.49x + 17.022$	139	63	64	95	161	143	17.022	1.49
SCL3	$y = 1.5382x + 15.339$	123	55	56	84	158	142	15.339	1.5382

### 5.3.3 PLS Analysis Results

Partial least squares analysis of the reflectivity spectra associated with each color and each level of fat within each color separated samples based upon the amount of fat along the first factor, which accounted for 66% of X-variance (X variables = predictors or reflectivity spectra) and 63% of Y-variance (Y variables = responses or percentage of modeled fat) of the total data variation [Figure 5.13 (a)]. The second factor, which separated samples on the basis of color, accounted for 21% of X-variance and 14% of Y-variance of total data variation [Figure 5.13 (a)]. Factor 3 separated red and pink samples from brown and brown-red samples and described 6% X-variance and 4% Y-variance of the total variation [Figure 5.13 (b)], and finally Factor 4

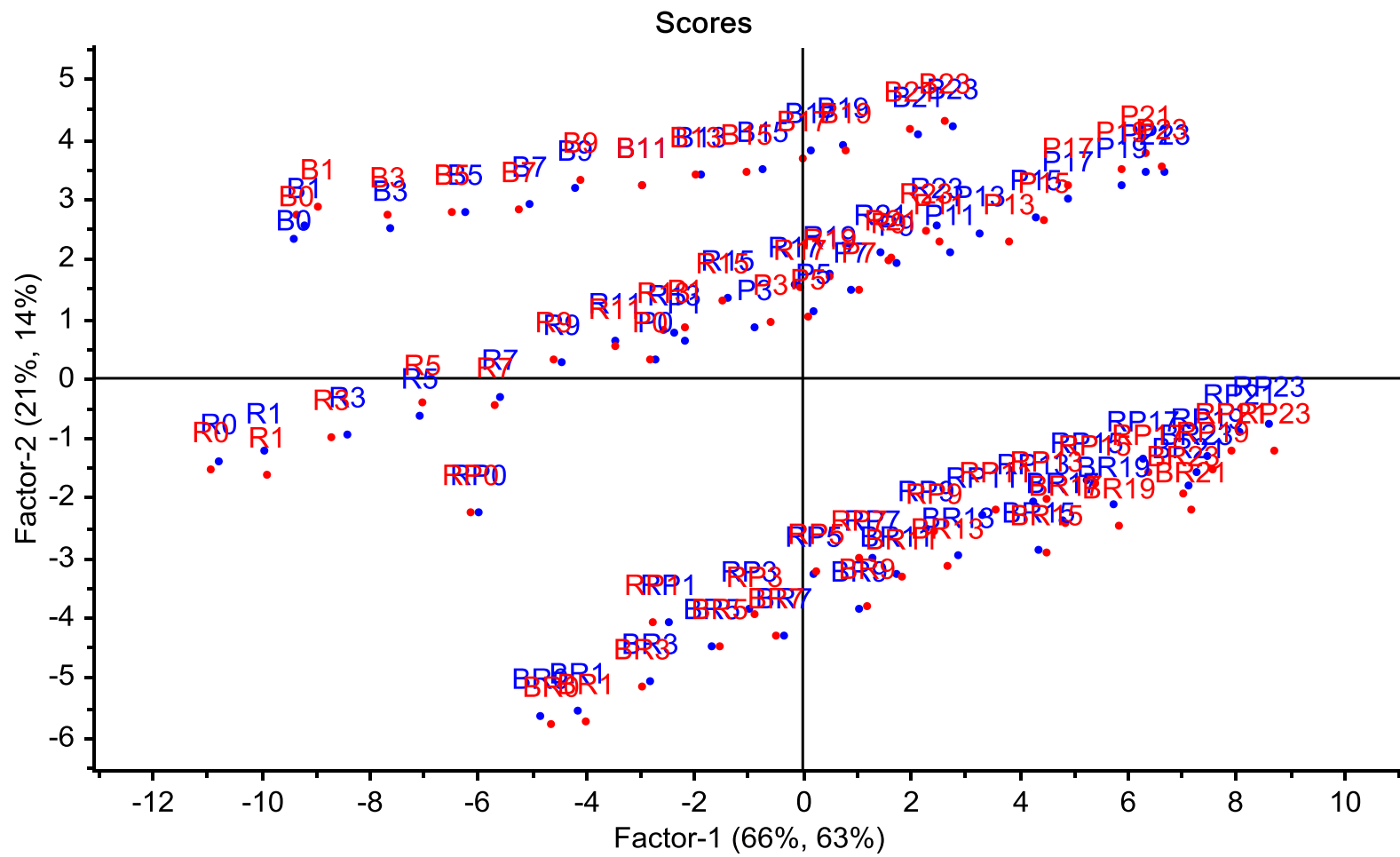
separated red samples from samples of all other color and accounted for 1% of X-variance and 15% of Y-variance of total variation [Figure 5.13 (c)]. Four wavelengths were identified which were used in the prediction equation. PLS analysis showed that these four wavelengths predicted visible fat with 94% accuracy using these 4 factors out of 7 factors. The model was cross validated with 93% accuracy. Fat pieces in the data set were changed to percentage of fat for the final model to be tested and accuracy of prediction remained identical ( $R^2 = 94\%$ ) as did the amount of variation described. In this model, the explained Y variation of calibration and validation at each factor were very close (Figure 5.14) and this model was also cross validated with 93% accuracy.

#### **5.3.4 Analysis Results of Data Obtained from Meat Sample**

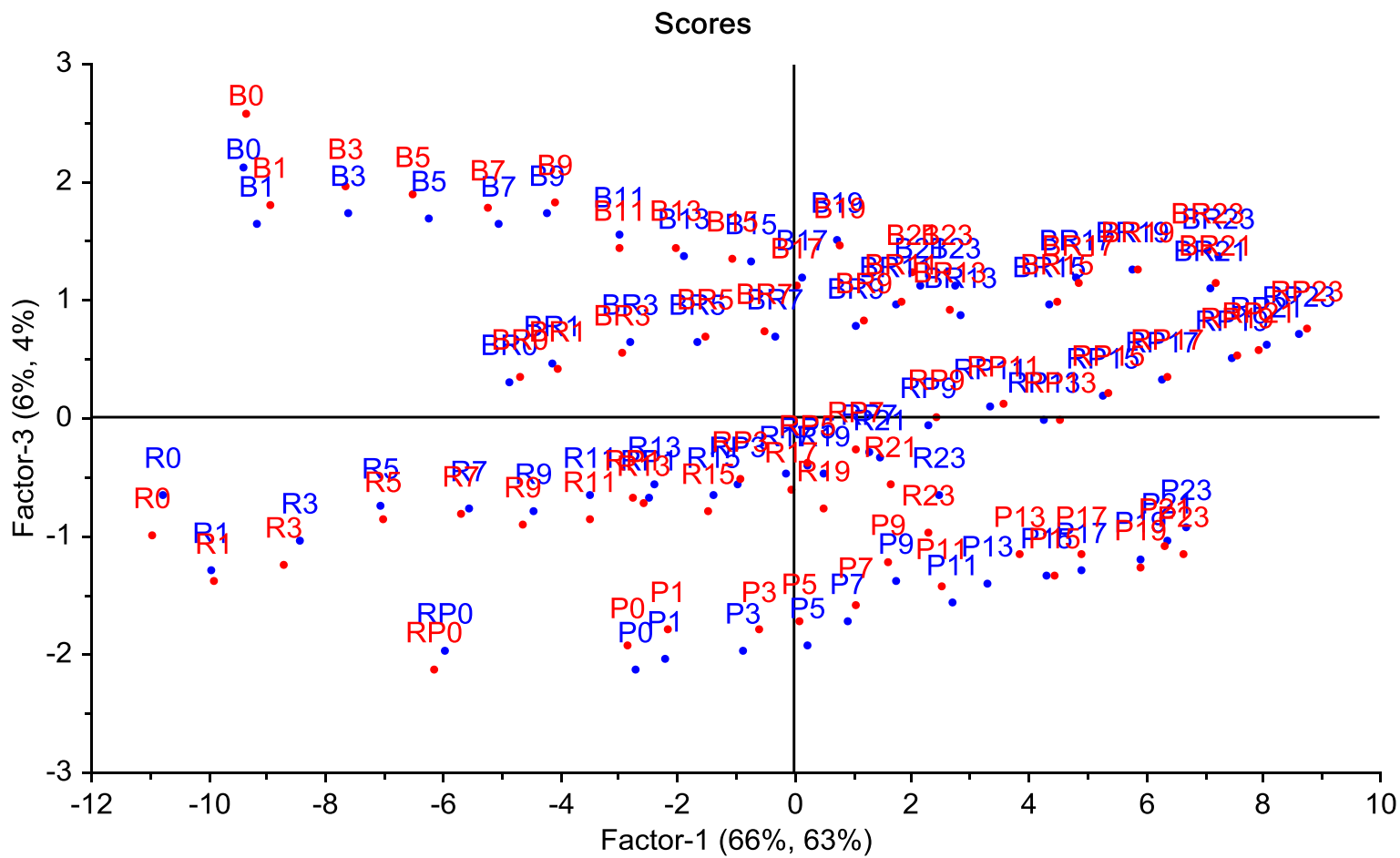
Slope of reflectivity at 595.05 nm data from three beef rib steaks that were collected during experimentation performed on 12/11/10, 25/11/10, and 6/4/11 (Section 3.2 of Chapter 3) were plotted together against number of fat pieces (Figure 5.15). This plot confirmed that a similar phenomenon occurred during the experiments reported in Chapter 3 to that noted with the paper model in the present study.

#### **5.4. Discussion**

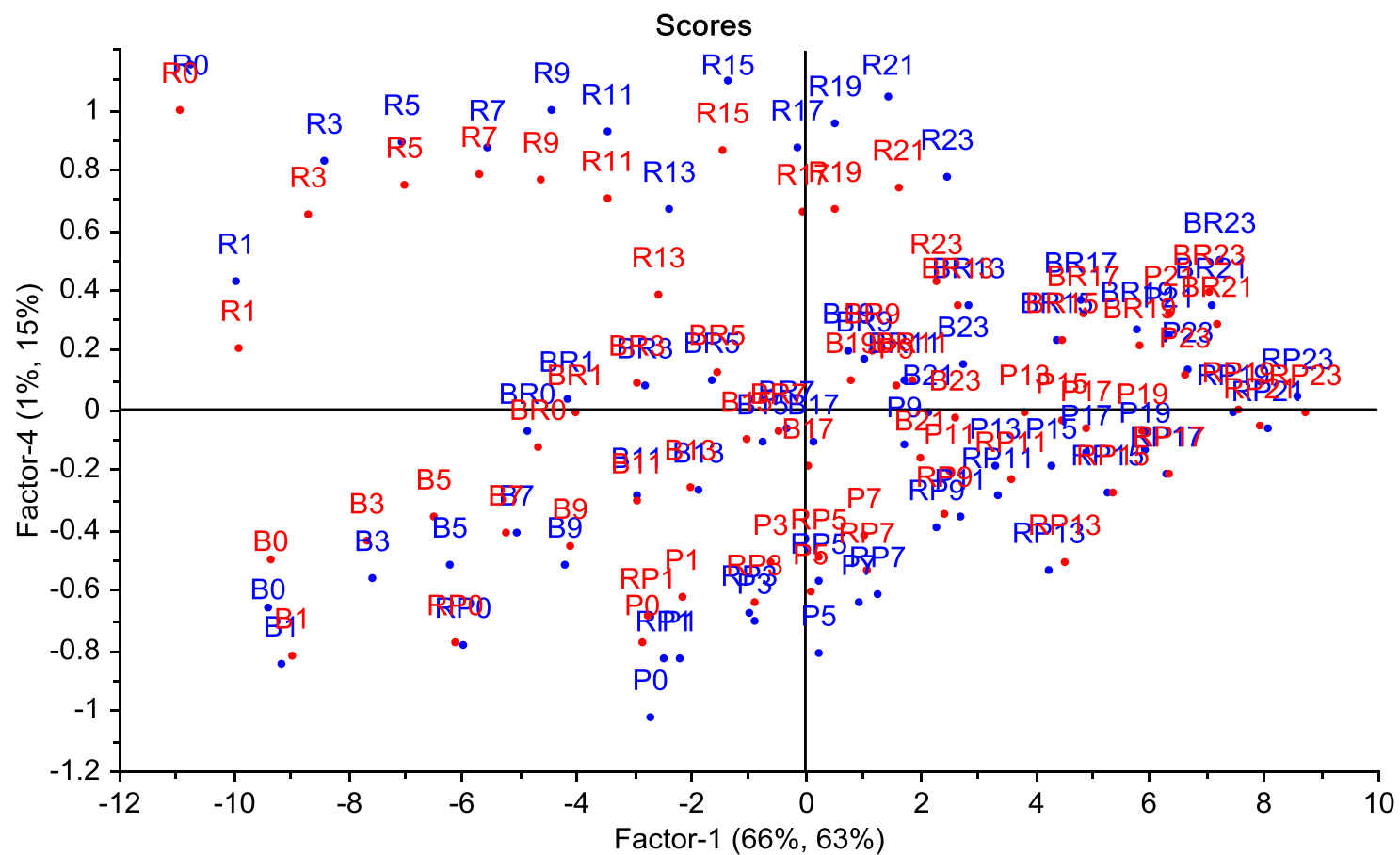
Creation of a model that imitated a meat surface color with both lean meat and intramuscular fat on white commercial paper enabled controlled experimentation of the effects of meat lean color on the detection of white fat using visible light and verification of uniformity and repeatability of the light source.



(a)



(b)



(C)

Figure 5.13: Scatter plots of X-variance and Y-variance explained by each PLS calculated factor in the PLS descriptive model (Blue: Calibration, Red: Validation). (a) X-variance and Y-variance explained by Factor 2, (b) X-variance and Y-variance explained by Factor 3, and (c) X-variance and Y-variance explained by Factor 4 relative to Factor 1.

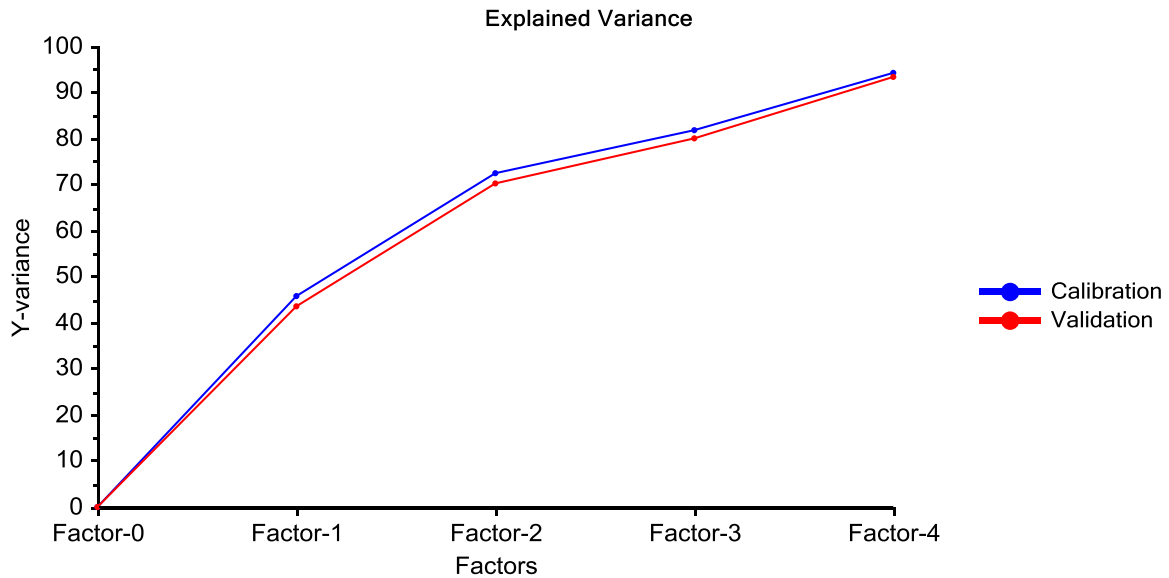


Figure 5.14: Y-variance explained by four factors using four wavelength model predicting percentage of visible fat.

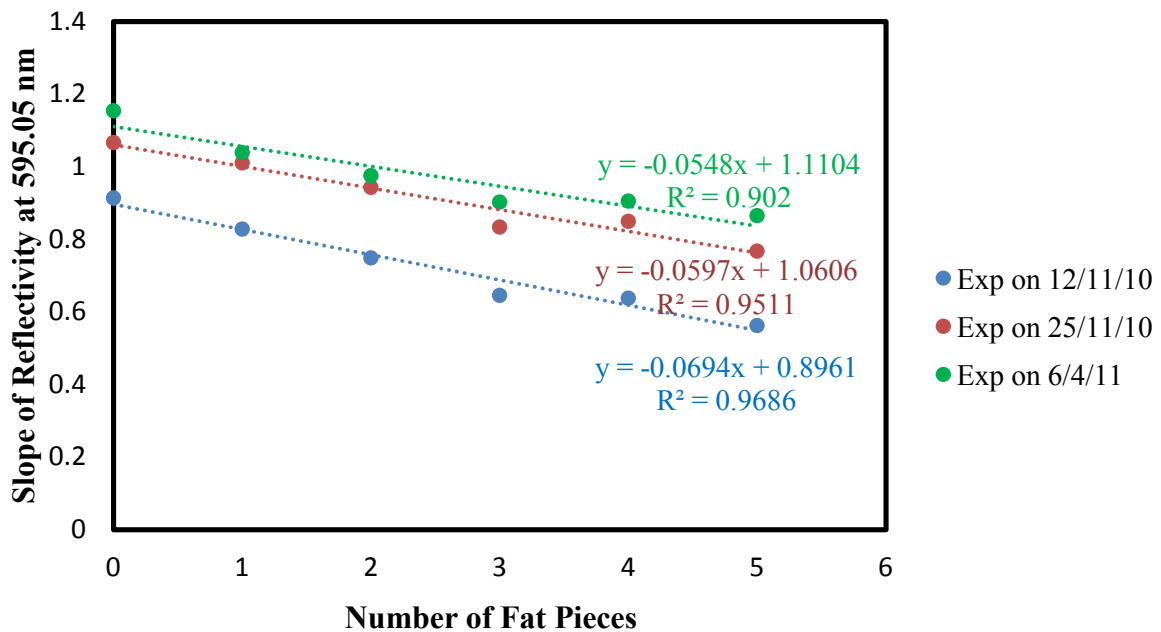


Figure 5.15: Relationships between slope of reflectivity at 595.05 nm and the number of fat pieces added to the surface of three beef rib steaks of experiments (Exp) performed on 12/11/10, 25/11/10, and 6/4/11.

#### **5.4.1 Light Source Test**

In this test the paper model samples that were used had the same number of white circles but positioned in different location of the measurement area detected by the spectrometer probe. All the samples used had the same background color tone (CL1). The reflectivity as a function of wavelength plots of these samples showed that reflectivity spectrum from each sample were almost identical regardless of the location of the white small circles in the measurement area. This substantiated that the scanned region had a uniform illumination from the light source. Similar results were found for each different background color, establishing that the uniformity of the light source was consistence and stable regardless of various uncontrollable factors such as electrical noise, ambient noise, and time varying anonymous factors. These tests were necessary to indicate the repeatability of experimental results and the validity of our experimental system. These results confirmed that results from various experiments of this study can be utilized for inter-experimental comparison. The uniformity of the light source was also necessary as the surface fat of multiple samples containing equal amount of fat can be oriented in any location inside the measurement area and it should produce identical result to estimate equal amount of fat for each sample.

#### **5.4.2 Spectral Data Analyses**

Reflectivity as a function of wavelength plot for different number of fat pieces showed similar trends in spectrum reflectivity found in previous experiments with real meat samples. Linear relationships found between the slope of reflectivity and the number of fat pieces or percentage of fat (here modeled fat) had an average  $R^2$  value of 0.99. This showed that similar analysis can be done on the paper model samples to obtain an equation which should describe the effect of

myoglobin color on fat prediction. Although the meat surface characteristics cannot be fully represented by printed color paper, the test was to find the effect of color variation on fat prediction as well to find a solution to describing the effect of the color variation.

Slope of reflectivity as a function of percentage of white circles plotted for different modeled myoglobin colors (Figure 5.10) clearly showed the effect of lean color variation on the accuracy of fat prediction. The linear fit of actual slope data had variation in amplitude and as well as in slope. The linear regressions between the Y intercept and  $a^*$  values and between the Y intercept and the slope of the regression of slopes of reflectivity on to fat theoretically could be used to calculate the amount of modeled fat by incorporating the effect of color variation. The equation that described the correlation between  $a^*$  and Y intercept could be used to obtain a Y intercept value depending on a particular value of  $a^*$  color component. A colorimeter could be used to obtain the  $a^*$  value for the lean muscle of a sample for use in this equation. This calculated Y intercept could then be used in the regression equation that describes the linear relationship between the Y intercept and the slope of reflectivity slopes to calculate a slope of reflectivity slopes value. Using the slope of slopes value and the previously calculated Y intercept value a geometric straight line equation (in the form of  $Y = mX + c$ ) could be used predict the percentage of fat for that particular  $a^*$  value. This equation would have a large amount of error, as the errors associated with each respective regression would add together and so a substantial error would be associated with any predicted value from this two-step calculation process.

Formulation of a marbling algorithm is complicated by the fact that the spatial distribution of color is not consistent at the surface of the beef steak; therefore, a wavelength was sought that would minimize the effect of myoglobin on reflectivity, which varies linearly with the amount of fat on the surface of meat. At the isobestic point of 525 nm the effect of color variation due to

various myoglobin states is reduced (Krzywicki, 1979). This study also indicated that the variation due to color was less than the analysis at 595 nm. It was observed that at 525 nm the reflectivity was directly correlated to the amount of fat at constant background color with average  $R^2$  of 0.99, but that background color still influenced prediction equation slope. The slope of the linear fit of reflectivity varied between 1.33 and 1.55, with the exception of the color pink, which had a slope of 1.1 (Table 5.2).

The paper model test indicated that the prediction algorithm using slope of reflectivity to predict fat was affected by the color (representative of myoglobin state). It was noticed that slope of reflectivity, which had linear relation with number and percentage of white circles in a constant color was varying linearly (linear correlation found between Y intercept and color component  $a^*$ ) with background color (modeled as meat color) of the paper model circles at constant amount of modeled fat. This signified that the prediction algorithm was actually correlated with amount of certain color pigments on the meat surface but not the amount of fat. Therefore the prediction algorithm was actually predicting the absence of color pigments on the meat surface but not the increase in fat percentage. The sensitivity of the prediction algorithm with lean meat color and two dimensional interactions of slope of reflectivity with varying color and fat suggested that the slope of reflectivity equation needed to be adjusted for the lean meat color in a multivariate analysis environment to predict fat accurately.

This conclusion was confirmed when partial least square analysis results showed that 96% of the variation could be described by four factors. PLS successfully separated the samples based on the amount of modeled fat (factor 1) and background color tones (factors 2 to 4). Examination of the weighted regression coefficient of reflectivity spectrum in the wavelength range of 430 to 626 nm indicated four key wavelengths described the total paper model data variation with 94%

accuracy, implying that a device with light emitting diodes of these wavelengths could with high success predict the proportion of white on a circles within the range of colors studied as the four wavelength model equation was cross validated to 93% accuracy.

### **5.4.3 Analyses Using Data Obtained from Meat Sample**

Data from three beef rib eye steaks, which were collected during the preliminary experiments with fat pieces (Chapter 3), were combined together for comparison with the paper model data analysis. Plotting of this data showed a similar pattern as that found during linear regression analysis of the paper model data. At 600 nm, the slope of reflectivity data from each steak linearly correlated with fat pieces with an average of 95% accuracy. The slope of each trend line varied however by steak even though the amount of fat (same number of fat pieces) was the same. Although not confirmed with measurement of  $L^*$ ,  $a^*$  and  $b^*$  coordinates, each individual steak most likely had different concentrations of each myoglobin state, hence changes in lean meat color between the steaks reflected the same effect as was observed with varying background color in the paper model. In fact, the slope of reflectivity was not correlated with the amount of white fat but was correlated with color indicators such as  $a^*$  values, supporting this conclusion.

## **5.5. Conclusion**

The results of this study supported the hypothesis that the variation in lean meat color was responsible for the failure of fat prediction using slope of reflectivity. This study indicated that the ability to predict the amount of fat across beef samples was obscured by the amplitude of the reflectivity varying with the color of the beef. This observation has not been reported in the literature and is most likely the reason that visible light has not been used successfully to predict

the amount of fat in whole meat pieces. In experiments with beef and the paper model, the amount of fat or white in each measurement area had a strong linear relationship with reflectivity in the visible light range, implying that the use of visible light to predict the fat in meat may be possible if the 'background' color of the myoglobin could be described and the variation captured in a predictive algorithm. The results were similar between the meat surface and the paper model indicated that the reflectance was not measuring any chemical aspects of the fat, but was in fact measuring the amount of color variation on the surface of the meat or paper. This substantiated the hypothesis that a similar analysis could be performed on an extensive paper model to obtain an equation that would describe the effect of myoglobin color on fat prediction. Also, that the position of the fat did not affect the reflectivity indicated that the method was repeatable and therefore valid because different experimental results could be compared to each other over time. The uniformity of the light source was also necessary as a surface containing a similar amount of fat in any configuration inside the scanned region should produce an identical result at any time for the technology to be applicable. The color of myoglobin in the paper model accounted for 33% of the variation in percentage of white circle area in the model, substantiating that PLS analysis of visible light reflectance not only detected the amount of white on the surface, but also the non-white color of the surface. Being able to describe the myoglobin state therefore was crucial to the success of using visible light to estimate marbling in whole steak pieces.

## **Chapter 6**

# **Comparison of NIR Prediction of Fat Content in Whole and Homogenize Beef**

### **6.1 Introduction**

Measurement of meat quality using chemical analysis techniques is time consuming, destructive and not suitable for the meat processing industry. A rapid method that could measure meat quality on a whole steak would be ideal for industrial meat processing environments. Previous experiments described in this thesis (Chapter 5) showed that measurement of fat concentration on whole steak using spectral analysis at visible light region (400 to 700 nm) was greatly affected by surface color of meat. Even if it could be assumed that the meat surface color is constant, there are other factors that can affect prediction accuracy.

The amount of fat or “marbling” on the surface of meat is the primary characteristic used to predict the amount of fat throughout the meat and is the basis of measurement for technologies such as digital image processing and spectral analysis. Spectral analysis using visible (VIS) light is mostly dependent on surface characteristics as the penetration strength of wavelengths at VIS region is comparatively less than that of near infrared (NIR) light (700 nm to 2500 nm). Previous experimentation (Chapters 3 to 5) showed that marbling was uneven over the whole surface of any meat steak and so spectral readings needed to be averaged over more than one region on the meat surface for accurate estimation of surface fat. Even with averaged readings from more than one region, the accuracy of fat prediction on the meat surface still depends on the representativeness of the selected regions. It was notable that this is not a problem using digital image processing because the whole meat surface is considered. A 2-D spectral scan (such as

hyper-spectral imaging) of the whole meat surface or the use of penetrating light such as NIR may resolve this shortcoming in spectral analysis.

Again, even with accurate characterization of the marbling visible on the surface of a steak, the amount of marbling and location of fat throughout the whole rib-eye muscle may be difficult to predict from just one location. Usually the intramuscular fat is concentrated near the blood vessels inside a muscle. It is important to verify the relationship between fat visible on the surface of muscle, and the amount of fat that is actually in the muscle that can be extracted chemically. This percentage of fat measured using chemical extraction is called 'crude fat'. The crude fat is then compared with the percentage of fat estimated using other techniques such as VIS-NIR spectral analysis and digital image analysis to verify the fat prediction accuracy and to search for any kind of relationship that may exist.

NIR spectroscopy is used in many aspects of sensory analysis and nutrient content estimation of food products (Osborne, 1981) and is successfully used for assessment of chemical components and their relative percentage in meat (Kruggel et al., 1981). NIR spectroscopy has the potential to measure and estimate different quality attributes in meat (Leroy et al., 2003) and research has shown that NIR spectroscopy has the ability to predict the amount of fat, moisture, protein in ground meat and ground meat products. NIR technology is calibrated for homogenized product (Ripoll et al., 2008; Sierra et al., 2008) and Togerson et al., (2003) showed the capability of NIR to predict fat, moisture and protein content of ground beef online in an industrial setting. This method to predict meat quality of homogenized product using NIR is not suitable for meat processing plants however because this technique is time consuming and destructive. A fast, non-invasive and non-destructive method of assessing fresh intact meat would be useful for an on-line prediction of technological and sensory qualities (Leroy et al., 2003). Although digital

image processing technology currently is available for this, spectral measurement offers an alternative technology that is less expensive, requires less computing power and storage and greater ease of use than digital imaging equipment. According to Rodbotten et al. (2000) amount of fat has been successfully predicted using VIS-NIR (400 to 1700 nm) in whole beef. Despite being mentioned in the literature, the most appropriate method, the prediction accuracy and the percentage of correlation to the amount of fat in whole meat associated with using NIR technology is still unclear. To further understand the relationship between meat surface spectra and intramuscular fat content, an experiment was conducted to test the hypothesis that marbling visible on the surface detected can be detected and described using NIR spectroscopy and is representative of that within the meat.

## **6.2 Materials and Methods**

### **6.2.1 Materials**

*Longissimus thoracis* muscle samples from 24 rib sections were collected from 24 different carcasses, with 6 carcasses from each of the four quality grades (A, AA, AAA and Prime). The rib eye steaks were cut from the remaining rib eye sections from a previous experiment (Chapter 4). These rib eye sections had been aged for 21 days and stored frozen at -20 °C under vacuum.

Sample color was measured from digital scanned images using digital image processing and from the meat sample by colorimeter (Konica Minolta Chroma Meter CR-400) as described in Section 4.2.1 of this thesis. The white calibration unit (CR-A43 Calibration Plate) (Section 4.2.1 of Chapter 4) was used for instrument calibration purposes. A digital color image scanner (EPSON PerfectionV33 Flatbed scanner) (Section 4.2.1 of Chapter 4) was used to scan the surface of the samples for digital image processing.

The reflectance intensity of the visible light spectrum was measured using a VIS spectrometer (Ocean Optics USB4000) as described in Section 3.2.2 of Chapter 3. The reflectance light was collected using a bifurcated fiber optic cable (Ocean Optics R600-7-VIS-125F) as described in Section 3.2.2 of Chapter 3. Although it had multiple fiber channels surrounding the main collection fiber for carrying source light to the measurement surface, the light coming through those fiber channels was not uniform (identified during experiments of Chapter 5) onto the measurement surface and so this light source was not used. Instead, a commercial incandescent light bulb (Soft White, 120V, 100W, Philips, Canada) as described in Section 5.2.1 of Chapter 5 was used as a broad spectrum light source. The collection fiber in the middle was used for the collection of the reflected light. The height from the measurement surface to the end of the probe was maintained constant during sample and reference measurement. Reflected light spectrum of the same Teflon<sup>TM</sup> sheet as described in Section 3.2.2 of Chapter 3 was used as a reference for normalization. The same black mask cover as described in Section 3.2.2 of Chapter 3 was used to cover regions on the measurement surface not intended to be measured.

The AQ6370C Optical Spectrum Analyzer (Section 3.2.3 of Chapter 3) was used for NIR spectrum measurement. During NIR measurements, the fiber optic cable used was the same cable (Ocean Optics R600-7-VIS-125F) as used in the visible spectroscopic measurements. The SMA905 to FC (PC type connector which is compatible with AQ6370C) converter adapter (Section 3.2.3 of Chapter 3) was used to attach the cable to the Yokogawa AQ6370C optical spectrum analyzer. The recorded spectrum data was stored directly in the AQ6370C's internal memory during the measurement. A USB flash drive was used to transfer the data from AQ6370C to computer for data analysis.

A commercially available 125 watt infrared heating lamp (125R40/1 (S4750), Satco, Brentwood, New York, USA) [Figure 6.1 (a)] with an optical filter was used as a light source. This type of infrared heating lamp has a wide light spectrum ranging from visible to infrared. This light source operates at 125 watt and 120 volts. It had a medium (E26) base and an average life of 5000 h. A high temperature (up to 200 °C) resistance electrical socket (Medium Base Socket –PLT 243201) [Figure 6.1 (b)] was used to power the lamp. A metal (steel) cover was used to cover the lamp to focus the infrared light only towards the measurement surface [Figure 6.1 (c)]. Aluminum foil sheets were used to cover gaps in the assembly to prevent light leakage. A standard laboratory stand was used to position the NIR light source onto the measurement surface.

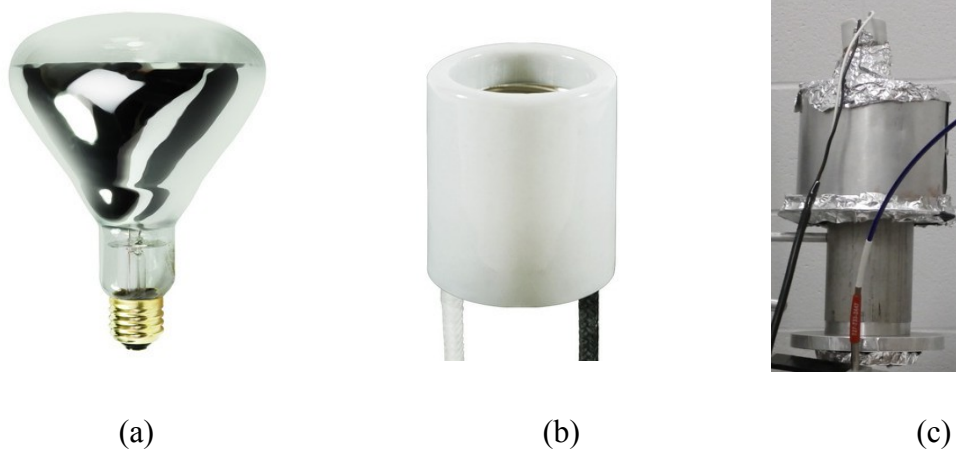


Figure 6.1: (a) Satco S4750-125 watt infrared heating lamp, (b) Medium Base Socket-PLT 243201, (c) Infrared heating lamp with cover and heat protection.

To prevent the overtone effect during measurement, an optical filter (FGL850S – 5.08 cm square RG 850 colored glass filter, 850 nm longpass, Thorlabs, Newton, New Jersey, USA) (Figure 6.2 (a)) was used. Figure 6.2 (b) presents a graph provided by the manufacturer (Thorlabs, Newton, New Jersey, USA) for the percentage transmission characteristics of the

filter (blue region) as a function of wavelength, indicating that the filter is able to block light wavelengths shorter than 800 nm, preventing overtones until 1600 nm ( $800 \text{ nm} \times 2$ ). A high thickness ( $\sim 1.5 \text{ cm}$ ) metal pipe and a circular high thickness ( $\sim 1.5 \text{ cm}$ ) metal ring plate in front the metal pipe was attached to the opening of the other metal cover that holds the infrared heating lamp to protect the filter from excess heat generated by the lamp assembly (Figure 6.1 (c)).

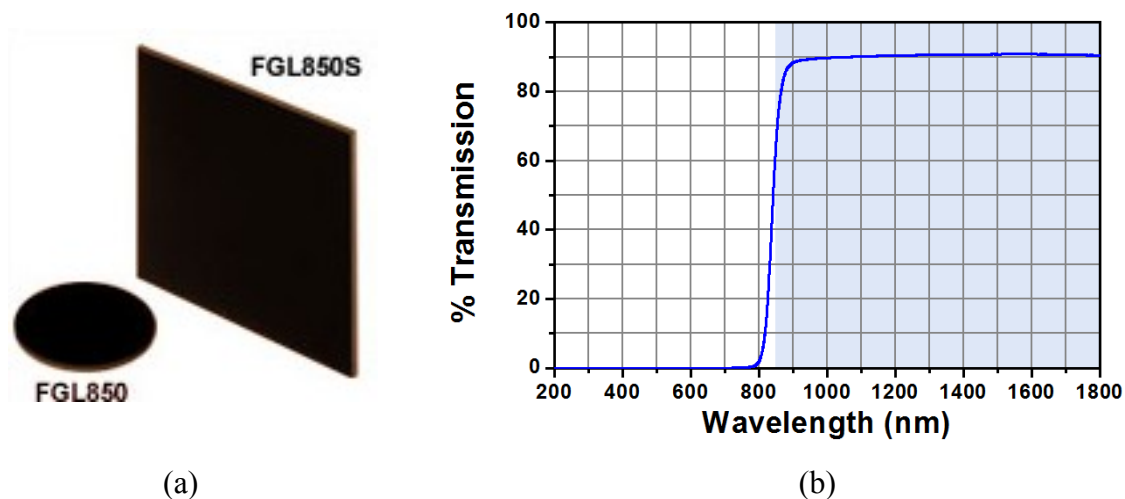


Figure 6.2: (a) FGL850S – 5.08 cm square RG 850 colored glass filter, (b) Transmission characteristics graph of FGL850S filter.

Fat content of the meat samples was determined after lyophilisation and grinding of the meat as previously described in Section 4.2.4 of Chapter 4.

### 6.2.2 Sample Preparation

The rib eye steaks of 2.5 cm thick were cut with a band saw from the frozen rib eye sections from a previous experiment (Chapter 4). Five rib sections were selected daily according to sequential sample ID for NIR spectral analysis. Samples were thawed in a laboratory cooler at 4 °C for 24 h prior to measurement. A rectangular portion of the *longissimus thoracis* (LT) muscle

[Figure 6.3 (a)] was separated from the subcutaneous fat and other muscles in the cut [Figure 6.3 (b)]. The sample was returned to 4 °C for one hour to oxygenate (“bloom”).



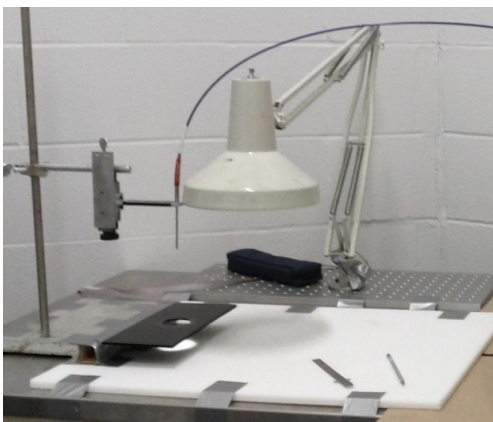
Figure 6.3: (a) Modified sample (rectangular portion of *longissimus* muscle removed from the whole rib eye steak), and (b) whole rib eye steak.

### 6.2.3 Measurement on Whole Sample

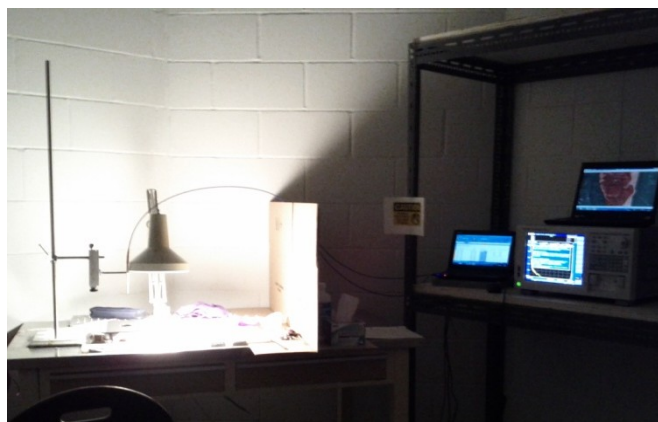
After one hour blooming, the  $L^*$ ,  $a^*$  and  $b^*$  color coordinates of the LT sample were measured using a colorimeter (CR-400, Konica-Minolta, Folio Instruments, Kitchener, Ontario) calibrated prior to measurement using the white calibration plate supplied by the manufacturer.  $L^*$ ,  $a^*$  and  $b^*$  color coordinate values were recorded from two different locations on the LT surface, with the two locations chosen to measure the color of lean muscle. The sample was scanned using the digital scanner (EPSON PerfectionV33 Flatbed) connected to a laptop computer (ThinkPad X220, Lenovo, China) and following scanning was positioned for VIS and NIR spectroscopic measurement.

The VIS light source was attached to a table lamp stand and the stand was placed on a table. A comparatively smaller stand with height adjustment capability held the fiber optic probe. Both stands were fixed to the table using good quality tape or bolts in order to confirm the positional stability [Figure 6.4 (a)]. The light source was placed over the probe at a fixed distance so that

the measurement surface had almost uniform light intensity. It was carefully monitored during the experiment that the position and height of the light source and the fiber optic probe were constant. The lab temperature was constant (21 to 22 °C). All spectroscopic measurements were performed in a darkened room. A cardboard partition was used to block the light from the computer and NIR spectrometer screens [Figure 6.4 (b)]. One end of the bifurcated fiber optic cable with one fiber channel for collecting reflected light was connected to spectrometer using SMA905 connector. The other end of the cable with multiple fiber channels for carrying light from light source was kept closed as we did not use it for sourcing light. The VIS spectrometer was connected to a Netbook Computer (Aspire one 532h-2630, Acer, China). The interface software (SpectraSuite™), installed in the Netbook, was used to set different parameters of the spectrometer and collecting measurement readings from the spectrometer. The integration time for the spectrometer was set at 100 ms and an option for dark current reduction in the interface software was set to 'ON' for all the VIS spectroscopic measurements.



(a)



(b)

Figure 6.4: (a) Experimental setup with VIS light source, fiber optic cable, optical probe, and (b) cardboard partition to prevent light from computer and NIR spectrometer screens.

For VIS spectroscopic measurements, each sample was placed under the black mask cover with the measurement surface facing up. A piece of waxed sheet was placed on the measurement surface and the white Teflon™ sheet was placed over each sample. Afterwards, the black mask cover was placed on top of the Teflon™ sheet. The fiber optic probe was positioned 10 cm above each sample. After completion of the reference reading for the VIS light spectroscopy, the waxed sheet was removed from the measurement surface of the sample and the black mask cover was placed over the sample surface. VIS spectroscopic reading of the sample was then recorded. A “dark current” spectroscopic reading was taken by covering the fiber optic probe using a cap for subsequent subtraction of “dark current” noise from sample spectroscopic readings. All reflectance data of entire spectrum from spectrometer were saved in Excel™ file for further processing. The reflectance data was then processed and analyzed in MATLAB™ and Unscrambler™ software (CAMO, Woodbridge, New Jersey).

The NIR spectrometer (Yokogawa AQ6370C) was allowed to equilibrate for one hour prior to use. An optical alignment and a wavelength calibration using the internal calibration light source were conducted prior to starting experimental measurements. The infrared light source with a metal cover and attached filter was connected to the stand after VIS spectroscopic measurements. The same stand was used to hold the fiber optic cable and the probe (Figure 6.5). The light source was placed over the fiber optic probe so that the measurement surface received the maximum amount of incident light. The height of the probe was set to 10 cm for all NIR spectroscopic measurements. The heights of the light source and the probe were kept constant for all NIR measurements to maintain measurement consistency.

The fiber optic cable connected to the visible light spectrometer (Ocean Optics USB4000) was disconnected and connected to the AQ6370C using SMA905 and FC converter adapter for NIR

measurements. The waxed sheet was again placed on the sample and the white Teflon™ reference placed over it with the black mask cover on top of the Teflon™ sheet. A “dark current” NIR spectroscopy reading was taken by covering the fiber optic probe with a cap and then the white Teflon™ sheet reading taken for normalization purposes. The NIR reading of the sample was taken after removing the Teflon™ sheet and the waxed sheet from the top of the sample measurement surface. The recorded data were stored in the AQ6370C’s internal memory as “CSV” file format and transferred to a computer using a USB flash drive for further analysis.

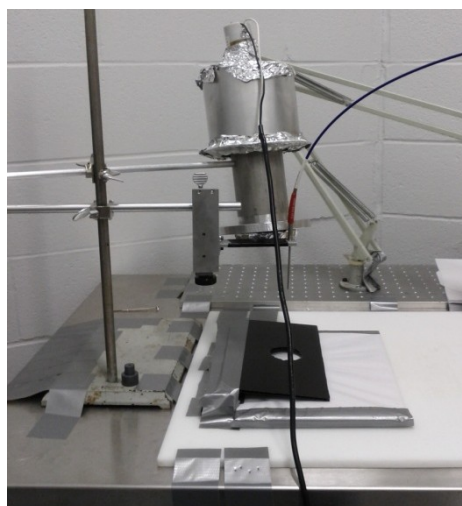


Figure 6.5: The fiber optic probe is attached to a standard laboratory stand using a custom made height adjustment holder with the NIR light source, white cutting board and black mask attached to table with tape. This experimental setup was used for NIR spectroscopic measurements.

After completion of all spectroscopic measurements, the sample remained under the black mask cover until marking of the sample’s digital image area that was used for spectroscopic measurement. Marking of that particular sample surface region used for spectroscopic measurements was done on a separate copy of the original scanned digital image [Figure 6.6 (a)] of the sample to identify the particular region for image processing purposes. The region was marked using a black circle with the help of Windows Paint™ [Figure 6.6 (b)]. The resolution of

original digital image taken by the scanner was reduced as described previously in Section 4.2.2.5 of Chapter 4.

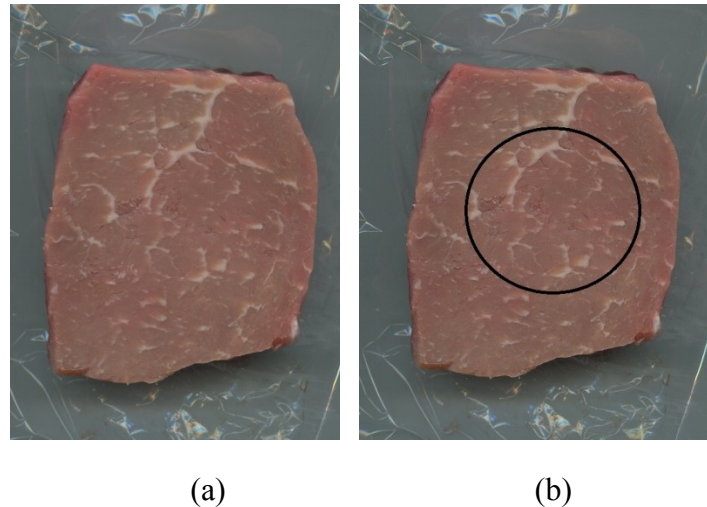


Figure 6.6: (a) Original scanned digital image (unmarked) of a sample (sample ID: 111YG), and (b) marking was done on a separate copy of the same digital image of the same sample.

#### 6.2.4 Preparation of Ground Beef Samples

Following VIS, NIR and digital characterization, the LT sample was ground in a food processor and pressed into a transparent plastic Petri dish (1.3 cm thickness, 8.6 cm diameter). The filled Petri Dish surface was pressed flat and uniform as much as possible by hand (Figure 6.7) and then immediately prepared for spectroscopic measurement.



Figure 6.7: Petri Dish filled with ground meat.

### **6.2.5 Measurements of Ground Beef Sample**

For VIS and NIR measurement of the ground samples, a piece of waxed paper was placed on top of the petri dish and the Teflon<sup>TM</sup> reference placed on top. The black mask cover was placed over the Teflon<sup>TM</sup> reference. The height of the fiber optic probe was set at 10 cm from the measurement surface, using a ruler. The VIS light source was placed over the fiber optic probe and the position was kept constant throughout the measurement of one sample and its corresponding reference measurement. No additional dark current measurement was taken as one dark current reading had already been obtained at the time of whole sample measurement. VIS light spectral data were recorded into an Excel<sup>TM</sup> (Microsoft Office) file and retained for further analysis.

After the VIS light spectroscopic measurement the NIR light source was substituted for the visible light source and its height and position adjusted using a ruler. The position of the NIR light source was kept constant throughout the measurement of one sample and its corresponding reference measurement. The fiber optic cable was connected to the NIR spectrometer using the SMA905 to FC converter adapter. A Teflon<sup>TM</sup> sheet reading was taken and the ground sample NIR reflectance spectrum was recorded. No additional dark current reading was taken. Recorded readings were saved as “CSV” files.

### **6.2.6 Crude Fat Sample Preparation**

Following spectroscopy, the ground meat sample was removed from the Petri dish and weighed. The weight was recorded and the ground meat was stored at -20 °C until lyophilization. The crude fat sample was prepared in a similar way as explained in Section 4.2.3 of Chapter 4.

## **6.2.7 Crude Fat Extraction**

The crude fat extraction was performed using the Goldfisch Fat Extraction Apparatus (Model 35001, Labconco Corp. 35181 Revision I, 1997). Crude fat extraction was performed as previously described in Section 4.2.4 of this thesis.

## **6.3. Data Analysis**

### **6.3.1 Digital Image Processing**

Digital image processing was done on both marked and unmarked images using two different image processing algorithms. The results from both (marked and unmarked image) image processing were then correlated with the spectroscopic readings of the corresponding sample. MATLAB™ software [MATLAB™ Version 7.9.0.529 (R2009b)] was used for image processing. The programming code was written in MATLAB™ programming language. In MATLAB™, images were represented in three color components: red (R); green (G); and blue (B) and each color component value was described in 8 bit color depth (scale: 0 to 255). The data type, “uint8” (8 bit) was used to allocate memory for each color component variables. Variables with binary (‘0’ and ‘1’) data type were used to describe black and white images.

The black circle marking [Figure 6.8 (a)] was considered the reference boundary for image processing of the marked images. The image was then loaded to MATLAB™ program memory using the “imread” function. The “imcrop” function was used to crop the image and remove unwanted regions from the image [Figure 6.8 (b)]. The MATLAB™ code for this image processing can be found in Appendix E. The reference boundary of the cropped image was identified using a simple thresholding of the image. It was observed that the reference boundary pixel’s RGB (R: red, G: green, B: blue) values were below 20 (scale: 0 to 255). Pixels with RGB

values below 20 were isolated from other image pixels and then replaced with green pixels (R=29, G=244, B=23). Thus the identified reference boundary was marked with green (Figure 6.9).

The inner region of the reference boundary was called the region of interest (ROI). The purpose of this image processing was to calculate the fat/lipid percentage of the ROI. In order to accomplish this purpose the ROI needed to be identified. The ROI boundary (also known as the reference boundary) pixels were isolated as white pixels [Figure 6.8 (a)] by transforming the image into black and white (B/W) image using the thresholding method. This was done to create a white circle on the ROI of the image using “imfill” function. The inner area of the ROI boundary was filled with white pixels using the “imfill” function [Figure 6.8 (b)]. This helped to differentiate the pixels in the ROI from other pixels of the image as the ROI pixels were white and other image pixels were black.

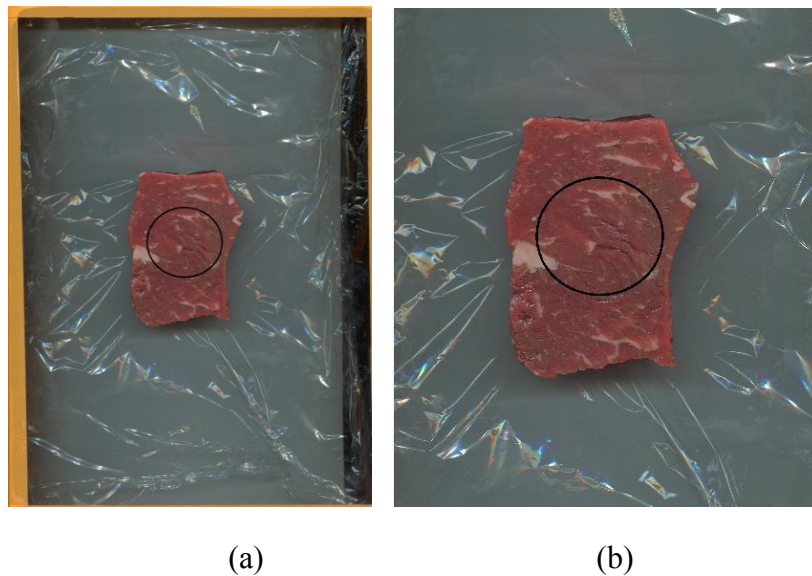


Figure 6.8: (a) A beef sample (sample ID: 132YG) image just after scanning and resolution reduction, and (b) a portion of the same scanned image that was cropped using MATLAB™ program for image processing purposes.

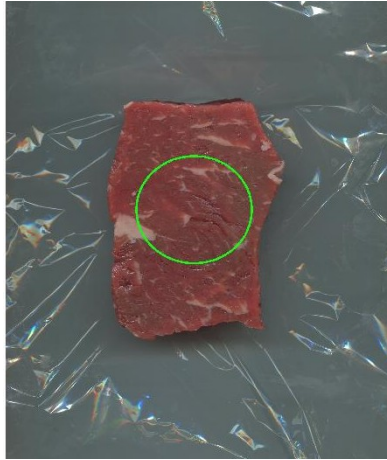


Figure 6.9: The same beef sample image with identified reference boundary and marked with green color using MATLAB™ image processing program.

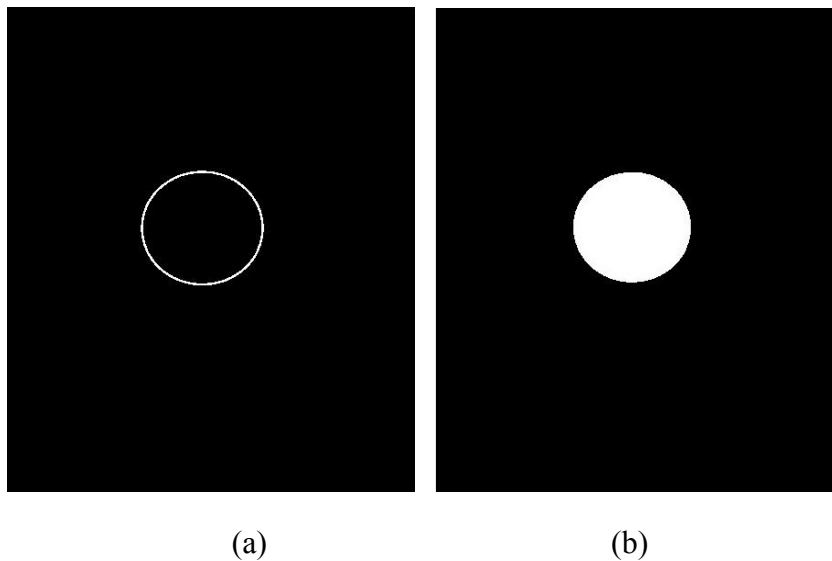


Figure 6.10: (a) The ROI boundary pixels were isolated as white pixels by transforming the sample image of Figure 6.9 into B/W image, and (b) the ROI was filled with white pixels using “imfill” function.

The ROI was cropped from the original image by pixel mapping technique. In this technique, the filled ROI was represented as an only white circle in the black and white sample image. Pixels of this white circle were mapped on to the original image to isolate the ROI of the original

image from the entire image. Thus ROI of original image was isolated from the original image (Figure 6.11).



Figure 6.11: Isolated ROI of original image.

The ROI pixels of the original image were passed through a thresholding setting that differentiated between fat and lean muscle regions on the meat surface. In this thresholding method, a range of RGB values were set to isolate the pixels representing lean muscle region from the entire image. It was observed that the uneven meat surface had some bright regions (effect of uneven surface glare) and some dark regions (due to shadows formed by uneven surface). These bright and dark regions on meat surface were very difficult to identify as fat or lean muscle. These regions were identified and isolated from the ROI of original image using image thresholding described in Section 4.3.1 of Chapter 4. The remaining ROI regions were then processed to evaluate the percentage of fat region in the lean meat. A similar thresholding method described in Section 4.3.1 of Chapter 4 was utilized in this image processing. However, minor changes in the RGB values were required for the thresholding conditions, applied in this image processing. The MATLAB<sup>TM</sup> program used for this image processing can be found in Appendix E.

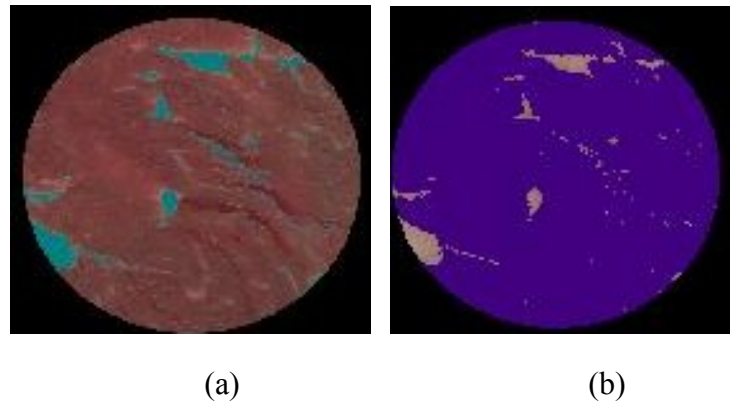


Figure 6.12: Identification of the fat and lean muscle regions of ROI of the original beef sample image. (a) Identified fat regions (marked with green), and (b) identified lean muscle regions (marked with blue).

After application of this thresholding, the fat regions were identified and isolated from the ROI of original image. Figure 6.12 (a) illustrated that the fat regions were identified and marked with green in the original image ROI and the lean muscle regions were selected and marked with blue in Figure 6.12 (b). The percentage fat of original sample ROI was calculated using equation (4.4) as described in Section 4.3.1 of Chapter 4.

The unmarked images were processed using a different algorithm to take into consideration the entire meat sample surface and so the entire sample surface boundary of the meat sample needed to be accurately identified. The image was processed to calculate the percentage of fat coverage over the entire sample surface. Image thresholding with appropriate RGB value conditions were applied to accomplish this objective. The MATLAB™ code for this image processing can be found in Appendix E.

Using similar methods as described in the image processing of marked images, the unmarked images were cropped from the original scanned images in order to remove unwanted image regions and decrease the image size for ease of processing (Figure 6.8). The cropped image was

processed to identify the sample boundary from the entire scanned image and isolate the sample from background.

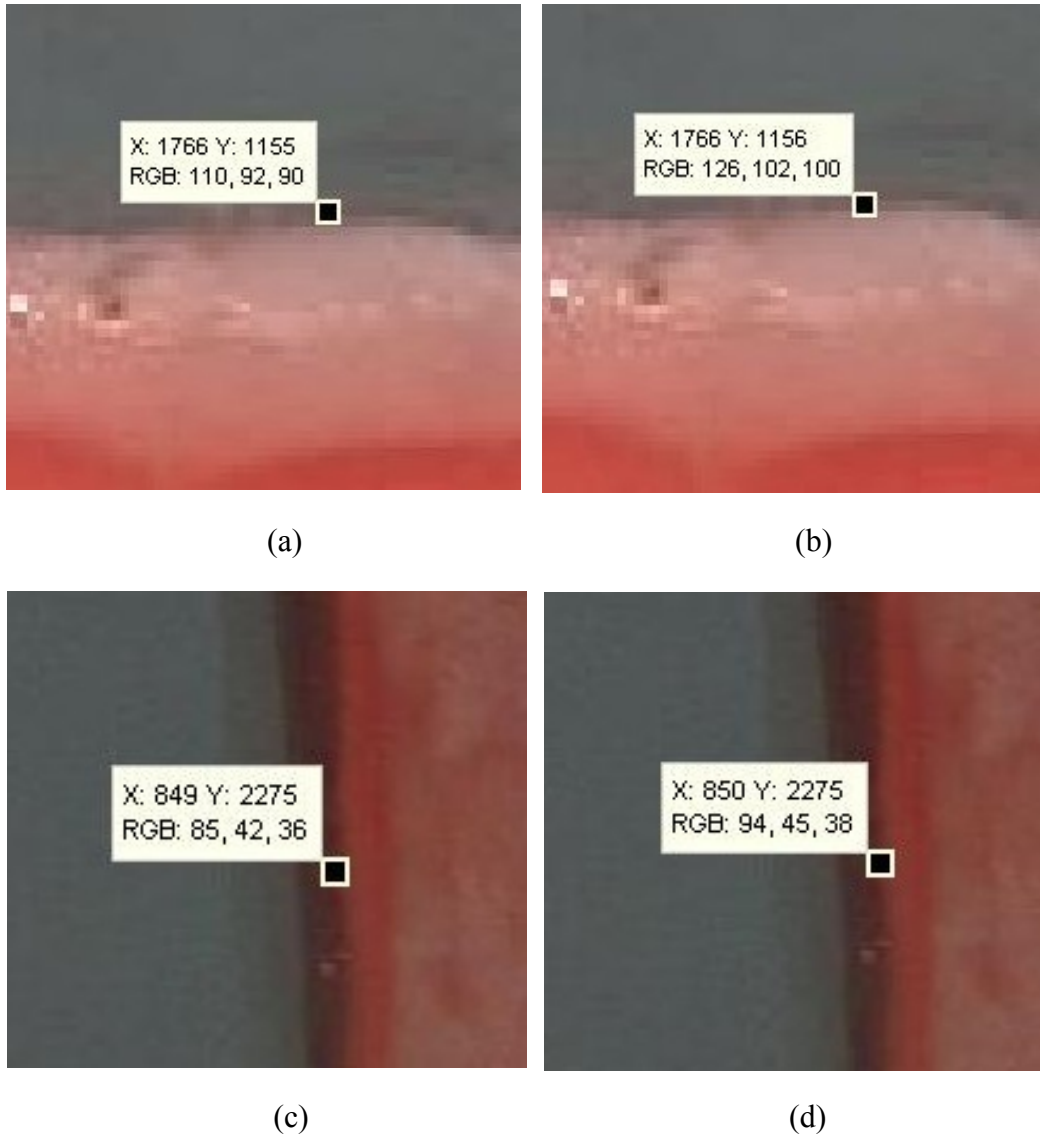


Figure 6.13: RGB values of different pixels of the sample, (a) selected pixel outside sample boundary, (b) selected pixel correspond to the sample and located at the brighter boundary of sample surface, (c) selected pixel outside sample boundary, (d) selected pixel correspond to the sample and located at the darker boundary of sample surface.

Using visual inspection, two RGB value conditions were identified to be sufficient to identify the sample boundary. There were two different conditions found in two different cases at a sample boundary location. In one case the sample boundary was comparatively brighter as shown in Figure 6.13 (a) and (b). In Figure 6.13 (a) the RGB values of the selected pixel, which was located outside the sample boundary, were R=110, G=92, B=90. The pixel selected in Figure 6.13 (b) corresponds to the sample and was located at the sample boundary. The RGB values of this pixel were R=126, G=102, B=100. There was another case where the sample boundary pixels were comparatively darker as shown in Figure 6.13 (c) and (d). In Figure 6.13 (c) the RGB values of the selected pixel that was located outside the sample boundary were R=85, G=42, B=36. The pixel selected in Figure 6.13 (d) was located at the sample boundary and its RGB values were R=94, G=45, B=38.

It was observed that at the bright sample boundary, the pixel values were comparatively higher than the dark sample boundary. The R value of 120 was found to be important in this case to meet the objective of this image processing. Inside the sample boundary the pixel R values were higher ( $R > 120$ ) in comparison to pixels that were located outside the sample boundary, so the condition for the R value was that it must be higher than 120. In some cases it was noticed that a glare region might exist at the boundary. It was nearly impossible to identify a glare region as a fat or lean muscle region and so these regions were eliminated. To eliminate a glare region the G and B values were restricted to 140 and 130 respectively. It was also noticed that a shadow region might also exist near sample boundary but the pixel R values in this region were much lower than 120, so the R value condition, which was already set to higher than 120, eliminated the shadow regions from sample boundary.

In the case of a comparatively dark sample boundary, RGB values of the pixels were lower than those of pixels that were located near a bright sample boundary. Using visual inspection, the R value 90 was found to be important in this case to meet the objective of this image processing. It was observed that in this case the pixel that corresponded to the sample boundary had an R value higher than 90, so the R value condition was set to be higher than 90. In some cases it was noticed that bright pixels outside the sample boundary had R values between 90 and 120 but had higher G and B values in comparison with pixels that were located inside sample boundary. Using visual inspection it was determined that G and B values should be below 70 for pixels located at a dark sample boundary. The glare regions and shadow regions were similarly eliminated.

The sample boundary of the cropped image [Figure 6.14 (a)] was identified using previous two RGB value conditions. Identified sample boundary pixels were marked with white and the remaining pixels were marked with black. The result of this thresholding method was a black and white image with an identified sample boundary. The inner region of the sample boundary was filled with white pixels using the “imfill” MATLAB<sup>TM</sup> function. As a result of this the entire sample surface was identified as a white object [Figure 6.14 (b)]. The entire sample surface was isolated [Figure 6.14 (c)] from the original cropped image [Figure 6.14 (a)] using pixel mapping technique similar to that described in Section 4.3.1 of Chapter 4.

The fat regions [Figure 6.15 (a)] and lean muscle regions [Figure 6.15 (b)] of the entire sample surface were identified and marked with green and blue, respectively. This identification and isolation was done using similar thresholding method and same RGB value conditions as used previously in the image processing of the marked images. The percentage of fat coverage of the entire sample surface (WHOLE region) was calculated using a method and Equation 4.4 as

described before in the image processing of marked images. The MATLAB™ program for the image processing of unmarked images is given in Appendix E.

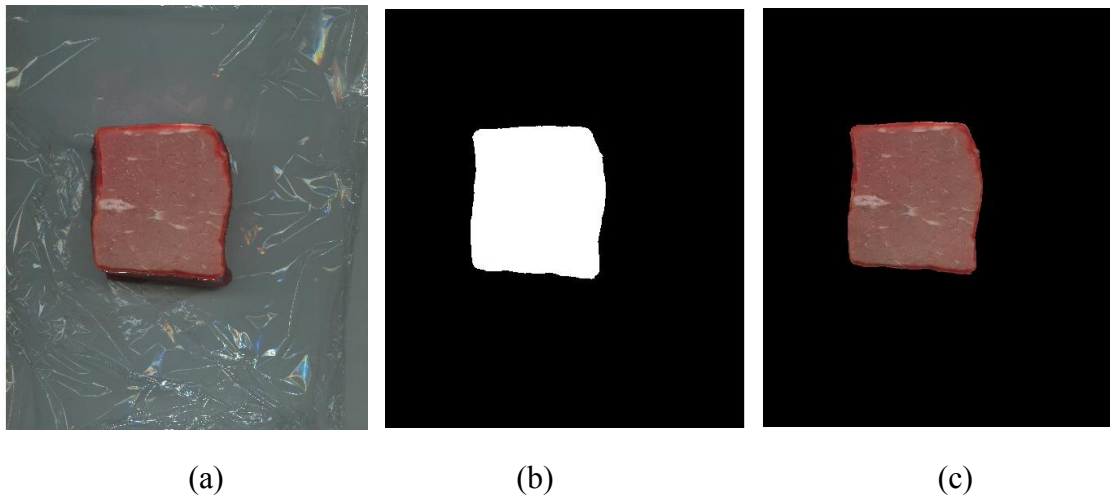


Figure 6.14: Identification of the entire sample surface, (a) cropped image of the original sample, (b) identified sample surface (marked with white), and (c) isolated sample surface from the original cropped image.

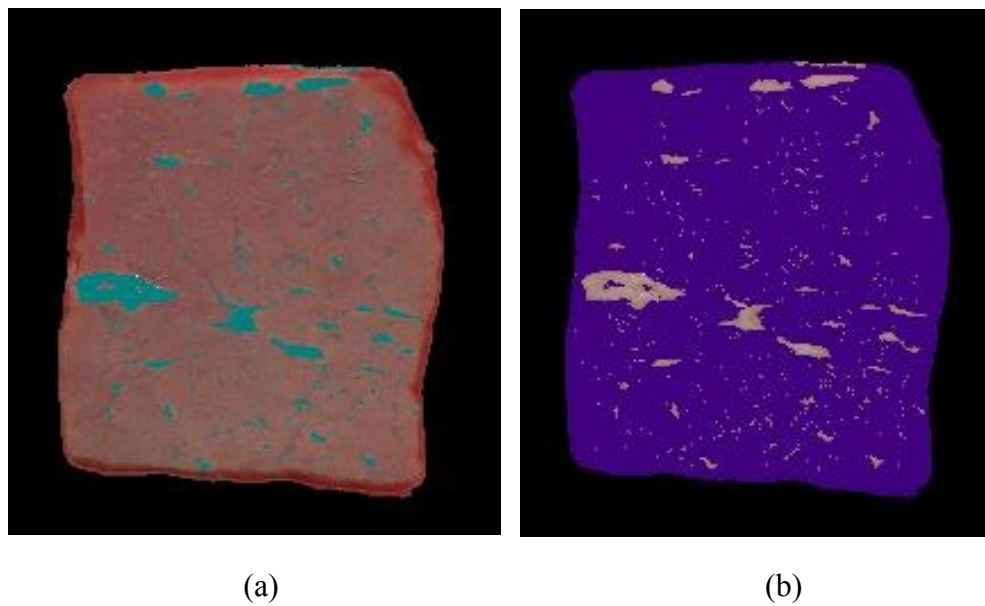


Figure 6.15: Identification of the fat and lean muscle region over entire sample surface, (a) identified fat regions (marked with green), (b) identified lean muscle regions (marked with blue).

### 6.3.2 Spectroscopy

All recorded data of VIS spectroscopy were stored in Excel<sup>TM</sup> (Microsoft Office) files. The Excel<sup>TM</sup> files were then loaded in MATLAB<sup>TM</sup> and processed using MATLAB<sup>TM</sup> program. The MATLAB<sup>TM</sup> code can be found in Appendix C.

The “dark current” noise reading was subtracted from the each reflected intensity spectrum data [equation (6.1)]. Due to the small sample size, only one spectrum reading per sample was recorded in this experiment so no averaging was required. After “dark current” subtraction the reflectance spectrum data were normalized using the reference spectra collected from the Teflon<sup>TM</sup> sheet [equation (6.2)]. These normalized reflectance spectra (reflectivity spectra) were filtered using MATLAB<sup>TM</sup> library function “smooth” with a smoothing coefficient of 50 (span =  $50 \times 0.22 = 11$  nm). There was a significant amount of noise present in the wavelengths near either end of the entire spectrum range of the VIS spectrometer. This noise would interfere with entire spectrum data after application of smoothing, so the noisy wavelengths were removed from the entire spectrum data before application of the smoothing filter. After removing the noisy wavelengths, the effective range of the VIS spectrum was 425.06 to 985.01 nm. The following equations were used to calculate the VIS reflectivity spectra of each sample.

$$\text{Reflectance} = I_{\text{reflected}} - I_{\text{dark}} \quad (6.1)$$

$$R = \frac{I_{\text{reflected}} - I_{\text{dark}}}{I_{\text{reference}} - I_{\text{dark}}} \quad (6.2)$$

Where R is the reflectivity of each wavelength,  $I_{\text{reflected}}$  is the light intensity of each wavelength reflected from the sample,  $I_{\text{reference}}$  is the light intensity of each wavelength reflected from the white reference (Teflon<sup>TM</sup> sheet) and  $I_{\text{dark}}$  is the “dark current” noise, measured by covering the probe with a cap and taking a spectra reading. MATLAB<sup>TM</sup> was used to calculate the reflectivity

data and these data were stored in another Excel<sup>TM</sup> file along with fat quantification data (e.g. crude fat data and image processed fat data).

In this data analysis the effect of “dark current” noise subtraction on the regression coefficient was also tested and compared with the results of previous experiment of Chapter 4. So, two separate data sets were created for each regression analysis; one with “dark current” subtraction and another one without “dark current subtraction”.

NIR reflectivity data were calculated using similar method as was used for VIS reflectivity data calculation. The recorded NIR reflectance spectra had a resolution of 0.1 nm and it was changed to 1 nm in MATLAB<sup>TM</sup> program. There were significant amount of noise in the wavelengths at either end of the entire spectra range of the spectrometer. These wavelengths were identified through visual inspection and removed before reflectivity calculation. The effective wavelength range of 920 to 1659 nm was utilized for the PLS analysis. Effect of “dark current noise” in the regression coefficients was also tested in NIR spectroscopy data analysis using PLS method. Similarly, two separate data sets, with and without “dark current” subtraction were created as was done for the VIS spectroscopy data sets.

### **6.3.3 Statistical Analysis**

Correlations were calculated in MATLAB<sup>TM</sup> using MATLAB<sup>TM</sup> library functions. In these calculations MATLAB<sup>TM</sup> function “corr” was used to calculate r values and p values as described in Section 4.3.5 of Chapter 4.

Multivariate statistical analysis was performed in Unscrambler X (Version 10.2, Camo Scientific Inc., Woodbridge, CA) software. Partial least squares (PLS) method was used as described previously in Section 4.3.5 of Chapter 4 to relate VIS and NIR reflectivity spectra to fat quantification measurements.

## 6.4. Results

### 6.4.1 Color

Minimums, maximums, means and standard deviations of L\*, a\*, b\* color coordinate values of all 48 samples are presented in Table 6.1. Sufficient variation in the lean muscle color was present for regression purposes. The color coordinate values were slightly higher than what was measured during the experiment reported in Chapter 4, even though the samples of present study and samples used in experiment of Chapter 4 were from the same rib eye sections.

Table 6.1: Minimums (Min), maximums (Max), means, and standard deviations (SD) of L\*, a\*, b\* color component values of all beef samples (n=48).

All samples (n=48)	Min	Max	Mean	SD
L*	39.67	56.03	48.48	3.69
a*	23.71	34.02	29.42	2.35
b*	11.45	17.73	15.04	1.27

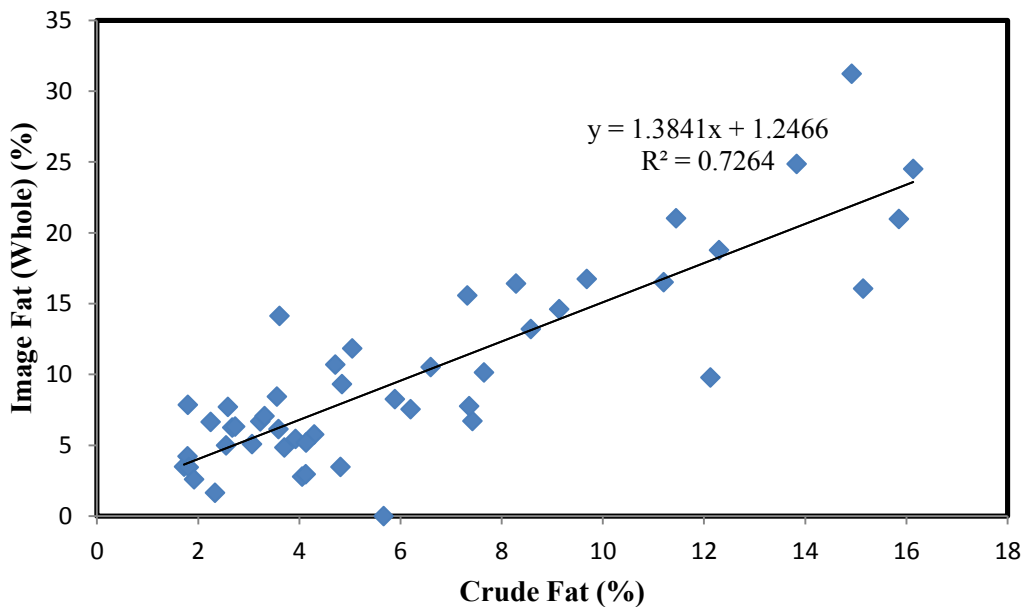
### 6.4.2 Crude Fat and Image Processed Fat

Regression of image processed fat WHOLE and CIRCLED [Figure 6.16 (a) and (b)] showed that image processed fat captured about 72% of the crude fat variation. Comparison of crude fat data from the same rib sections measured in a previous experiment (first rib eye crude fat) (Chapter 4) and in this experiment (ground meat experiment crude fat) showed 84% agreement between the measurements, indicating that position of sampling within the rib section was a source of variation [Figure 6.16 (c)]. Results of crude fat extraction indicated that Prime beef had

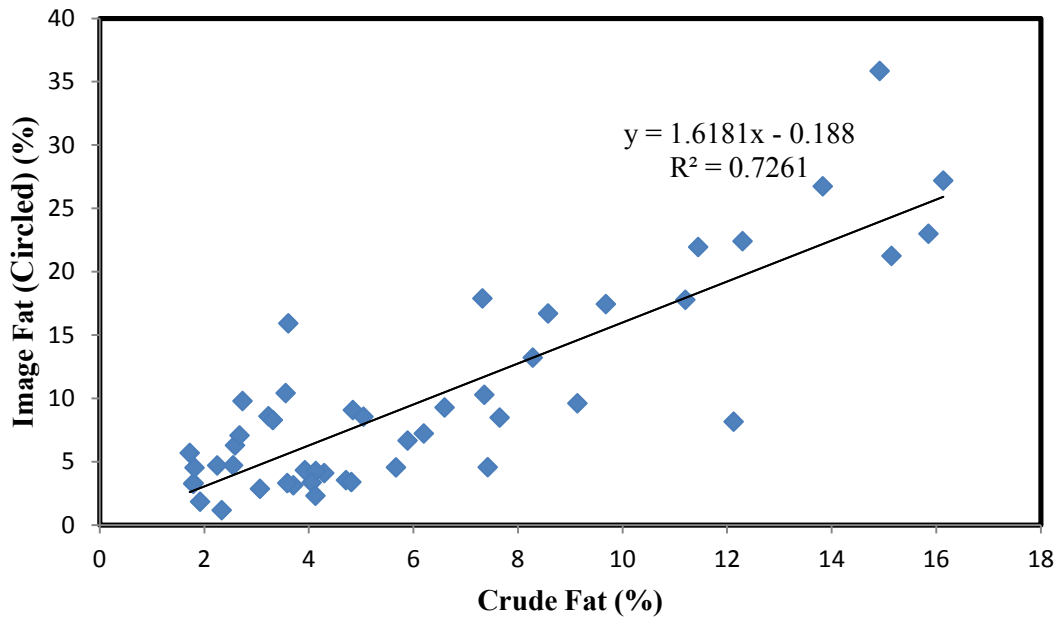
the most and Canada A beef had the least extractable crude fat. Fat detected by image processing appeared to over-estimate the overall fat content of the beef, as the estimated percentage fat was numerically higher for both whole and circled images than the crude fat measurement (Table 6.2).

### 6.4.3 Correlation Coefficients

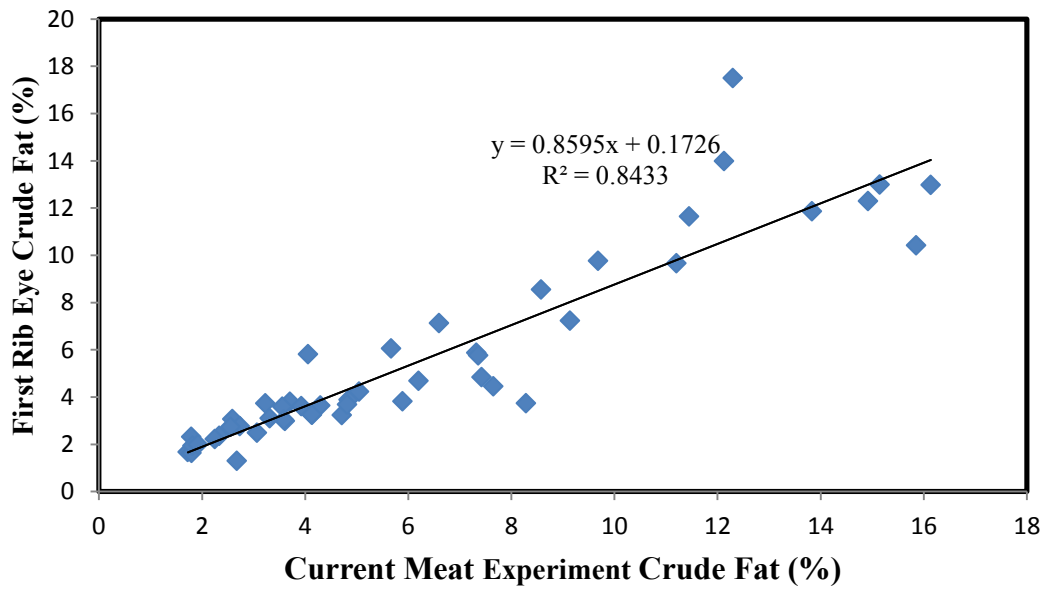
The Pearson Correlation coefficient ( $r$ ) values and their probability ( $p$ ) values are presented in Table 6.3 and 6.4 respectively. Correlations with  $p < 0.05$  are highlighted in Table 6.4. All the color coordinate ( $L^*a^*b^*$ ) values were significantly correlated to each other. Crude fat was significantly correlated to  $L^*$  and  $b^*$ . Image processed fat (WHOLE) was significantly correlated to  $L^*$  and  $b^*$ . Image processed fat (CIRCLED) was significantly correlated to all color components. Crude fat was significantly correlated with image processed fat (WHOLE and CIRCLED). The coordinate  $a^*$  value was negatively correlated to  $L^*$ , crude fat, and image processed fat (WHOLE and CIRCLED).



(a)



(b)



(c)

Figure 6.16: Relationships between percentage crude fat as predicted using WHOLE and CIRCLED images and crude fat then extracted chemically. (a) Crude fat and image processed fat (WHOLE), (b) crude fat and image processed fat (CIRCLED), and (c) crude fat measured in the current experiment and crude fat measured from first rib eye measured during experiment reported in Chapter 4.

Table 6.2: Means and standard deviations (SD) of fat detected chemically and with surface image processing for each Canada beef grade.

Grade	Crude Fat (n=12)		Image Processed Fat (WHOLE) (n=12)		Image Processed Fat (CIRCLED) (n=12)	
	Mean	SD	Mean	SD	Mean	SD
A	2.87	1.55	5.98	3.69	5.98	4.57
AA	3.77	1.10	6.85	3.25	5.81	3.85
AAA	5.90	1.59	8.55	3.57	7.36	3.16
Prime	12.53	2.64	19.02	5.88	20.67	7.59

#### 6.4.4 VIS Spectroscopy

Individual weighted regression coefficients plots (data not shown) indicated that regression coefficients from 465 to 970 nm had the least noise as characterized by dramatic fluctuations in coefficient values. As a result, this range of spectra was used in each sample for PLS analyses.

PLS regression coefficient results for VIS (white) light spectroscopy are shown in Table 6.5. VIS spectroscopy of the whole beef had a prediction accuracy of about 74% for chemically-extractable crude fat, while it has a prediction accuracy of about 69% for crude fat in the homogenized product. The poorest predictions of fat content were observed for image processed fat, with  $R^2$  values ranging from 0.58 to 0.65 (Table 6.5). Subtraction of dark current appeared to increase the accuracy of predicting the amount of crude fat and visible fat (image processed fat), suggesting that dark current noise interfered with important wavelengths.

Table 6.3: Pearson Correlation coefficient (r) values among color, crude fat, and image processed fat.

Variable	L*	a*	b*	Crude Fat (%)	Image Fat (%) (WHOLE)	Image Fat (%) (CIRCLED)
n	48	48	48	48	48	48
L*	1.00	-0.45	0.52	0.79	0.69	0.69
a*		1.00	0.39	-0.18	-0.26	-0.29
b*			1.00	0.56	0.38	0.31
Crude Fat (%)				1.00	0.87	0.85
Image Fat (%) (WHOLE)					1.00	0.96
Image Fat (%) (CIRCLED)						1.00

Table 6.4: Pearson Correlation probability (p) values among color, crude fat, and image processed fat with correlations highlighted in green for  $p < 0.05$ .

Variable	L*	a*	b*	Crude Fat (%)	Image Fat (%) (WHOLE)	Image Fat (%) (CIRCLED)
n	48	48	48	48	48	48
L*	0.0000	0.0012	0.0002	0.0000	0.0000	0.0000
a*		0.0000	0.0061	0.2263	0.0733	0.0485
b*			0.0000	0.0000	0.0071	0.0301
Crude Fat (%)				0.0000	0.0000	0.0000
Image Fat (%) (WHOLE)					0.0000	0.0000
Image Fat (%) (CIRCLED)						0.0000

Table 6.5: Calibration and validation  $R^2$  for VIS spectroscopic prediction of crude and image identified (WHOLE and CIRCLED) fat.

VIS Spectroscopy		Calibration $R^2$ mean (SD) n=5	Validation $R^2$ mean (SD) n=5
<b>Prediction of Crude Fat in Whole Beef</b>	<b>Dark current subtracted</b>	0.83 (0.02)	0.75 (0.01)
	<b>No dark current subtracted</b>	0.85 (0.00)	0.70 (0.02)
<b>Prediction of Crude Fat in Homogenized Beef</b>	<b>Dark current subtracted</b>	0.83 (0.01)	0.70 (0.02)
	<b>No dark current subtracted</b>	0.79 (0.01)	0.64 (0.02)
<b>Prediction of Image Fat in Whole Beef</b>	<b>WHOLE (dark current subtracted)</b>	0.78 (0.00)	0.63 (0.02)
	<b>WHOLE (no dark current subtracted)</b>	0.75 (0.02)	0.59 (0.02)
	<b>CIRCLED (dark current subtracted)</b>	0.79 (0.01)	0.65 (0.03)
	<b>CIRCLED (no dark current subtracted)</b>	0.74 (0.01)	0.58 (0.02)

#### 6.4.5 NIR Spectroscopy

The highest correlation was identified by searching for the lowest P values among the partial correlation coefficients for all wavelengths. The accuracy of predicting crude and image processed fat are shown in Table 6.6, with validation  $R^2$  taken as the measure of prediction accuracy. Prediction accuracies using NIR for whole and homogenized beef were about 76 and 83% with dark current subtracted and 77 and 87% without dark current subtracted. Prediction accuracy for whole and homogenized beef was higher than that for image processing and was

55% for the large (WHOLE) and 60% for the small (CIRCLED) area of the LT steak image with dark current subtracted. Not subtracting dark current appeared to increase the amount of variation predicted for most of the measurements, suggesting that some important wavelengths may have very low reflectance that is removed by subtraction of dark noise.

## **6.5. Discussion**

NIR technology and different methods utilizing NIR spectrum have been successfully used and commercialized for homogenized meat (Togerson et al., 2003; Leroy et al., 2003; Anderson, 2007; Prieto et al., 2009). However, despite many studies with NIR technology, NIR has not been used effectively in the commercial arena for whole intact meat (De Marchi et al., 2013). VIS light has often been included with NIR in the prediction of meat quality attributes (De Marchi et al., 2013), most likely because the optical spectrum is affected by overtones of fundamental wavelengths which are multiplied with increased wavelength range. For example, the overtone of wavelength  $\lambda$  can be found at wavelength at  $\lambda/2$ ,  $\lambda/3$  and so on (Osborne, 1981). In this study, an optical filter was used to block wavelengths below 850 nm to reduce the overtone effects in the spectral range of measurement, which was 600 nm to 1700 nm.

Similar to Kandaswamy et al. (2005), VIS and NIR light were measured and analyzed separately to test the prediction accuracy of each and the dark noise was subtracted from the sample data. Dark noise occurs randomly throughout the wavelengths and so subtracting the dark noise randomly increases or decreases the amount of correlation. The signal to noise ratio was found to be low in this experimental setup for NIR light, most likely because the scanning surface area was maximized by increasing the probe height at the expense of signal intensity. This low signal to noise ratio can be improved in the future experiments by increasing the intensity of the light source or by decreasing the height of the optical probe.

Table 6.6: Calibration and validation  $R^2$  for NIR spectroscopic prediction of crude and image identified (WHOLE and CIRCLED) fat.

NIR Spectroscopy		Calibration $R^2$ mean (SD) n=5	Validation $R^2$ mean (SD) n=5
Prediction of Crude Fat in Whole Beef	Dark current subtracted	0.90 (0.00)	0.76 (0.02)
	No dark current subtracted	0.91 (0.00)	0.78 (0.01)
Prediction of Crude Fat in Homogenized Beef	Dark current subtracted	0.91 (0.05)	0.84 (0.02)
	No dark current subtracted	0.97 (0.01)	0.87 (0.01)
Prediction of Image Fat in Whole Beef	WHOLE (dark current subtracted)	0.78 (0.08)	0.56 (0.03)
	WHOLE (no dark current subtracted)	0.77 (0.02)	0.53 (0.01)
	CIRCLED (dark current subtracted)	0.77 (0.00)	0.61 (0.02)
	CIRCLED (no dark current subtracted)	0.88 (0.00)	0.67 (0.03)

In the case of digital image processing technology, it may be possible to predict the chemical fat in a whole rib-eye steak using digital image processing methods with 60% to 70% accuracy ( $R^2 = 0.73$ ). The performance of Video Image Analysis-Computer Vision System (VIA-CVS, Research Management Systems Inc., Fort Collins, Colorado, USA) was investigated by Moore et al. (2010). The correlation coefficient ( $r$ ) values between chemically extracted (ether extracted) fat and marbling score by VIA-CVS were between 0.64 ( $R^2 = 0.41$ ) and 0.19 ( $R^2 = 0.04$ ) at different USDA (United States Department of Agriculture) marbling grades and an overall  $r$

value was 0.87 ( $R^2 = 0.76$ ) (Moore et al., 2010). This agrees with the  $R^2 = 0.73$  obtained in linear regression between surface marbling and crude fat (chemically processed fat) in the meat in the present study. The fat content of beef can vary dramatically between the surface and the interior, and this was shown by the differences in chemically processed fat noted between the measurement of the crude fat of the rib section in this study and by Zamarripa (2014), who analyzed the same rib sections for crude fat. A  $R^2 = 0.84$  was found when the crude fat measured in each rib section in the present study and by Zamarripa (2014) were regressed on each other.

The present study showed that fat content prediction correlations using VIS light had  $R^2$  values that varied between 0.58 and 0.74. The accuracy of predicting chemically extractable fat was comparatively higher in whole meat than in homogenized meat and higher than the prediction of digitally detected fat in both whole and circled image fat. Both digitally detected fat images were estimations of the surface intramuscular fat of the sample and interestingly the  $R^2$  validation values of VIS to predict the percentage of surface fat these two different image estimations (whole image and circled images) were similar.

This contradicted the results found in previous experiments (Chapter 4), which showed that the large area image processing was better predicted using VIS light than the small area image. During the previous experiments (Chapter 4) the small area was selected after the experiment by guessing the region where the optical measurement took place. However during this experiment the circled region was marked during the experiment exactly where the optical measurement took place, so the circled region was more accurately defined than the small region. Another aspect was the size of the image processed region in this experiment was smaller than that used the previous experiment (Chapter 4). This resulted in the surface area difference between the

whole image and the circled image in the present experiment was comparatively less than that of the surface area difference between the large and small images of the previous experiment.

For NIR light the prediction  $R^2$  values were between 0.53 and 0.87. In this experiment, however, NIR light showed higher  $R^2$  values for homogenized meat (i.e. minced sample) than for whole sample or intact meat, which is similar to that reported in literatures (Rodbotten et al., 2000; Prieto et al., 2009). Unexpectedly, VIS and NIR light predictions of crude fat in the whole sample was comparatively higher than prediction of image detected fat in the whole sample. This may be an indication that both VIS and NIR light penetrate the surface of the beef and detected the fat underneath, but this hypothesis was not investigated. In the case of homogenized meat, the prediction of fat content using NIR light was much better than using VIS light and this agreed with the findings of Kandaswamy et al. (2005); however, the prediction accuracies of both NIR and VIS light for crude fat in intact whole meat were similar. Rodbotten et al. (2000) found correlation coefficients between 0.76 to 0.84 and Root Mean Square Errors of Prediction (RMSEP) between 1.0 to 1.5% for NIR spectroscopy for prediction of fat content (range 1100 to 2500 nm) of intact meat. These results agreed with the results of the current study. Also, in the present study, the NIR light showed better  $R^2$  values with circled image fat than whole image fat, and this would be expected given that the circled area was the precise area measured.

Spectroscopy results for the homogenized beef showed that the accuracy of predicting crude fat using VIS light was lower than that of NIR light and the accuracy of prediction using VIS was also less for homogenized than for whole beef, which was unexpected. This may have been due to the color of the lean meat being changed with homogenization. In homogenized meat, the lean meat color changed and became lighter and so differentiation between fat and lean would have become increasingly difficult. Prediction of crude fat using NIR light was unaffected by

homogenization, suggesting that NIR detection was not affected by lean meat color. The significant correlations with  $P < 0.05$  among lean meat color components, especially  $L^*$  and different percentage fat (crude fat and image processed fat) indicated that variation of color was affecting the VIS light's ability to predict amount of fat.

NIR light showed better prediction accuracy for crude fat for the homogenize sample than for whole sample. This was because the chemical composition of the unit area sample surface was uniform and a true representation of the entire sample chemical composition was achieved after homogenization. With the whole beef sample, the NIR light was reflected back from the surface of the meat sample and accuracy depended on the penetration depth of the NIR light and surface fat distribution. According to the results, this introduced 30% error in the correlation analysis of whole sample data and 20% error in the correlation analysis of the homogenized sample data. Togerson et al. (2003) reported that the fine particle size in the homogenized sample will increase the correlation, and this is clearly understandable as a fine particle will increase the uniformity or homogeneity of the sample surface. However, Prieto et al. (2009) explained this phenomenon in terms of reduction in internal reflections within the muscle fiber, which would act as an optical fiber and both absorb and scatter light. This would not occur in homogenized meat as homogenization completely disrupts the fiber structure of intact meat. Thus NIR spectroscopy on homogenized meat produced better prediction efficiency of meat quality attributes and this has been noted by others (Barlocco et al., 2006; Prevolnik et al., 2005).

Using the prediction equations found in this study the percentage crude fat can be estimated with 70% to 75% using NIR light on whole meat and with 80% to 85% accuracy using NIR light on the homogenized meat. However Togerson et al. (2003) found better results (correlation coefficients 0.96 to 0.99) from NIR spectroscopy on homogenized meat. Noticeable differences

in their study were that great care was given to keeping the temperature constant on the sample surface, selecting an optical filter to avoid wavelengths that were affected by the different states and temperature of water, and use of a greater NIR range (1100 to 2500 nm) than in the 600 to 1700 nm used in the present study, which was further shortened due to the noise presence at the extreme wavelengths (Leroy et al. 2003). In the present study, each sample was removed from refrigeration at an equal interval and this effectively reduced the chances of varying temperature on the sample surface. However, depending on the sample mass, variations of the surrounding temperature can affect the sample surface temperature which may not be constant for each sample. In this study, the NIR readings from the spectrometer were calculated as reflectivity by normalizing the reflectance using a standard reference and finally filtering the reflectance using a zero order interpolation filter (smoothing filter). Normalization or standardization of the raw reflectance data from the instrument is common in optical physics because it standardizes the raw reflectance data against a known or common standard reference. Another benefit of normalization is that it also reduces the instrumental effects such as time drift of electronic components and effects of varying nature of surrounding environment (i.e. temperature, relative humidity, and other sources of lights).

In meat science, most VIS and NIR data is presented as absorbance values for comparative purposes. Calculation of absorbance data as  $\log(1/R)$  using raw reflectance data  $R$  from the instrument is not standardized NIR data. Furthermore, this absorbance data contains a great deal of unforeseeable noises and instrumental effects which can randomly affect the results. In many studies (Su et al., 2014; Prieto et al., 2014) no such standardization or normalization technique was mentioned or, if mentioned briefly (Khatri et al., 2012), is not explained in detail. Osborne (1981) reported that signals from the detector are amplified using an logarithmic amplifier and

data are recorded as  $\log (R/R_1)$ , where  $R$  is the reflectance of the reference and  $R_1$  is the reflectance of the sample. Osborne (1981) also mentioned that  $\log (R)$  is constant as the chosen reference does not change its reflectance with wavelength. However, unavoidable instrument effects and time drift of instrument response will generate varying  $R$  with time and surrounding environments even if the reference is constant. This raises serious concerns about the results that have been published to date in the meat science literature.

Further research is needed to increase the prediction efficiency and accuracy of VIS and NIR algorithms. Potential areas for additional investigation are increasing the range of the NIR wavelengths, considering the effect of temperature and increasing the signal intensity to improve the signal to noise ratio of the NIR reflectivity data.

## Chapter 7

### Estimation of Beef Toughness Using NIR

#### 7.1 Introduction

Tenderness is considered to be the most significant among meat eating qualities (Morgan et al., 1991; Savell and Cross, 1992). Park et al. (2001), Morgan et al. (1991) and Savell and Cross (1992) raised concern about the inconsistency of meat tenderness as a major challenge to beef industry. This makes the objective assessment of meat tenderness at processor and at retailer levels to be an absolute necessity. The different tenderness measurement techniques available, such as taste panel, slice shear force (SSF) (Shackelford et al., 2011) and the popular Warner-Bratzler shear force (WBSF) (Derington et al., 2011) are time consuming and require the destruction of a sample of meat to be used for the measurement purpose. However, optical spectroscopic measurement of meat tenderness has several benefits over other techniques. It is quick and can be measured online in an industrial environment without destroying any valuable meat product. Optical spectroscopic techniques were successfully utilized and commercialized [Togerson et al., 2003; Leroy et al., 2003; Anderson, 2007; Prieto et al., 2009 (review)] for determining the chemical composition (protein, fat and water) in emulsified or homogenize meat samples (Kruggel et al., 1981; Iwamoto et al., 1981; Lanza, 1983). Many studies have been conducted to measure meat tenderness using optical spectroscopic techniques (Park et al., 2001; Ripoll et al., 2008; Mitsumoto et al., 1991 and Shackelford et al., 2011). Optical spectroscopy using near-infrared (NIR) light has been investigated and it has the potential to assess meat tenderness (Park et al., 1998a; Park et al., 1998b, Shackelford et al. 2011; Park et al. 2001; Ripoll et al., 2008; Mitsumoto et al., 1991). Using NIR spectroscopy, Ripoll et al., (2008) found better correlations with sensory tenderness [ $R_p^2$  (coefficient of determination of prediction) = 0.981]

than correlation with WBSF [ $R_p^2$  (coefficient of determination of prediction) = 0.743]. This showed that NIR spectroscopy may predict tenderness in such a way that is best related to consumer taste. The hypothesis of this study was that polarized and non-polarized NIR reflectance spectroscopy can predict WBSF values of beef at 3 and 14 days post mortem. The objective of this study was to investigate and verify the potential of the NIR technology to predict beef tenderness and formulate an equation that is to be implemented in a handheld device (Chapter 2) for beef quality measurement purposes.

## **7.2 Materials and Methods**

### **7.2.1 Experimental Design**

This experiment was designed to investigate the effects of post mortem carcass temperature, electrical stimulation, and ageing on various beef qualities in another study (Zamarripa, 2014). This helped achieve a significant amount of variation in beef toughness. This was important for the statistical analysis to produce meaningful results in the analysis of toughness estimation using NIR spectroscopy. This experiment was a split-split-plot design (Figure 7.1). Various treatments that were utilized in this experimental design were as follows; (a) two different chilling temperature (warm and cold), (b) two electrical stimulation treatments (control and stimulated), and (c) two ageing treatments (3 and 14 days). In the split-split-plot design the main plot consisted of the two different chilling temperature treatments, the sub-plot consisted of the two electrical stimulation treatments, and finally, the sub-sub-plot consisted of the two ageing treatments.

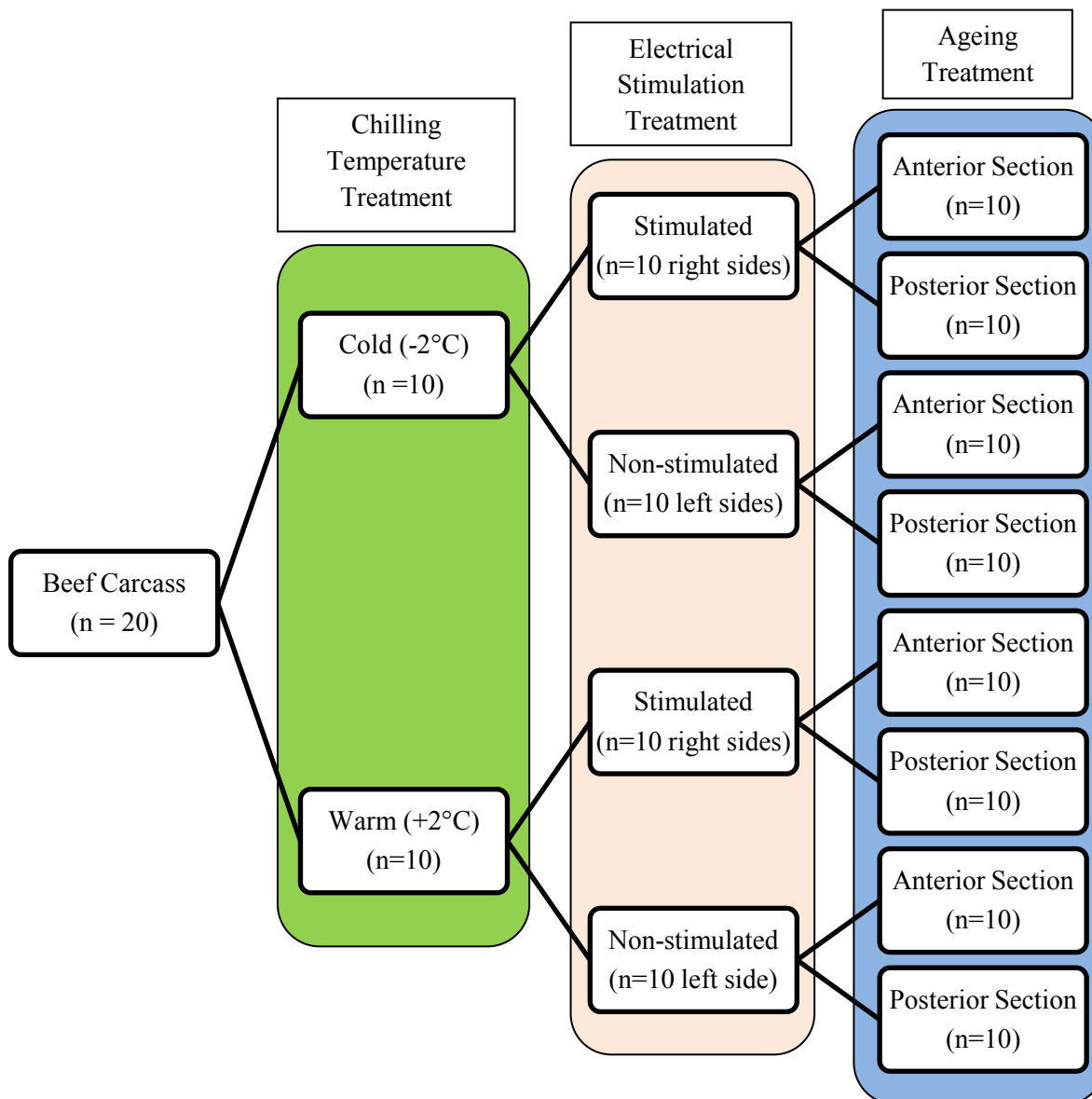


Figure 7.1: Split-split-plot experimental design to achieve sufficient variation of beef tenderness to obtain a robust statistical model for tenderness estimation using NIR spectroscopy.

### 7.2.2 Sample Preparation

Twenty cattle from the University of Alberta Kinsella Ranch were slaughtered at the Agriculture and Agri-Food Canada Meat Research Center at Lacombe, Alberta, on two slaughter dates with 10 cattle processed each day. Cattle were shipped to the Meat Research Center on the

same day of slaughter. Live weights were recorded prior to slaughter, and cattle carcasses processed in a manner simulating commercial practices. Weights of the trimmed hot carcass sides were recorded and the right side of each carcass was electrically stimulated (Koch-Britton Stimulator Model 350) with two cycles resulting in each carcass receiving 450 volts for 90 sec (Figure 7.2).

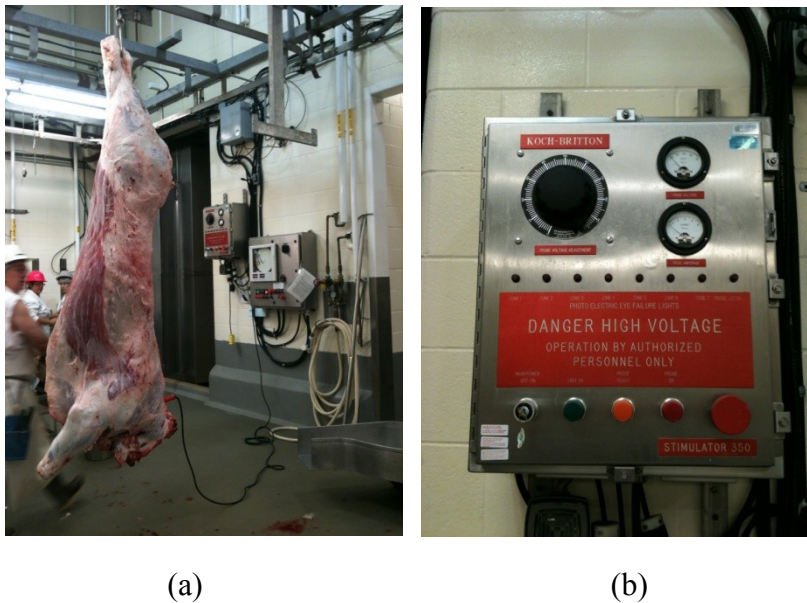


Figure 7.2: Electrical stimulation of a beef carcass side; (a) a beef carcass side, hanged from the roof rails was connected to the electrodes of the electrical stimulator; (b) electrical stimulator control panel to set the voltage and current that was conducted through the beef carcass side.

All carcass sides from each slaughter day (n=10) were pasteurized (Figure 7.3) and 5 carcass sides (left and right sides) among the total 10 carcass sides were sent to a 2°C cooler and remaining 5 carcass sides were sent to a -1.5°C cooler with wind speed of 0.5 meter/seconds in each cooler. The carcass sides were randomized and sorted among warm and cold cooler after weight balancing between the treatments (hot and cold) in order to achieve similar mean live weights in each treatment. Hot and cold gel-packs (Large Cryopak Soft ice-pack, Canadian Tire,

Canada) were used to accelerate the temperature treatment by increasing or slowing the rate of temperature change of each carcass (Figure 7.4). Frozen gel-packs were used for the carcass sides that were placed in the -1.5 °C cooler to accelerate the temperature decline. Warmed (35 °C) gel-packs were used for the carcass sides that were placed in the 2 °C cooler to slow the temperature decline. These gel-packs were attached to the loin area of each carcass sides for 2 h (Figure 7.4). After the gel-pack treatment, carcass sides kept in each cooler for 24 h and then were moved to the 2 °C cooler until fabrication. This modification of rate of temperature change using gel-packs enhanced the temperature treatment, which was designed to create differences in *longissimus thoracis* (LT) muscle toughness.

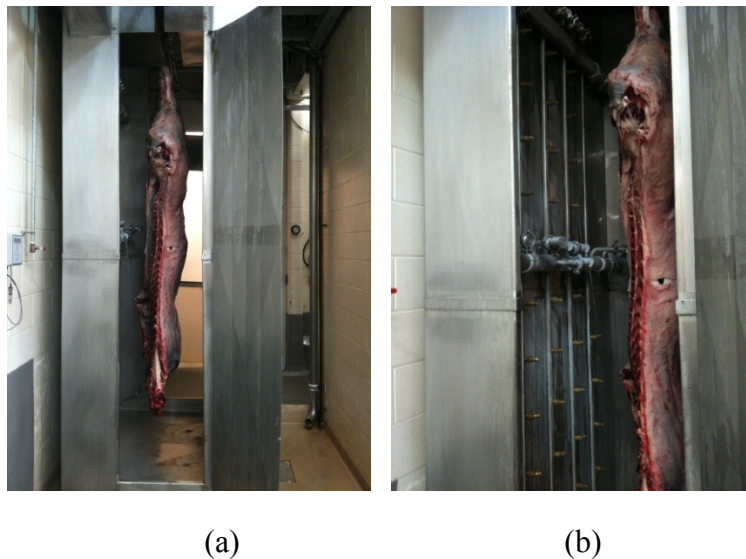


Figure 7.3: Image of the carcass pasteurization unit; (a) front view; (b) side view.

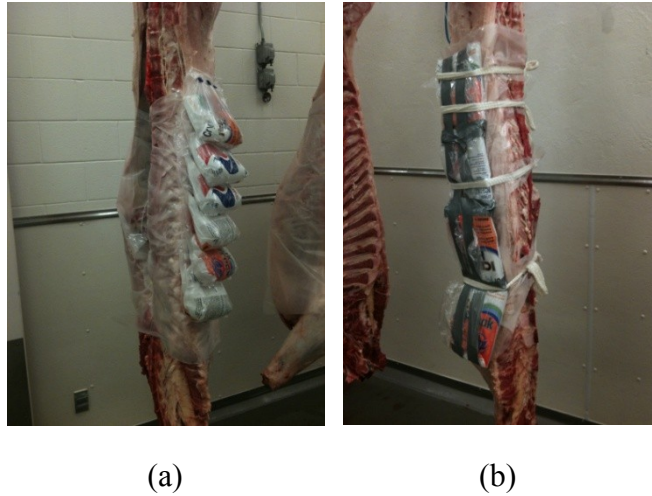


Figure 7.4: Hot and cold gel-packs on the carcass surface; (a) hot gel-packs; (b) cold gel-packs.

After fabrication of all carcass sides, one rib section was removed from each carcass side and divided into two sections as anterior and posterior. These two sections (anterior and posterior) were randomized between two ageing treatment groups, non-aged (3 days post mortem) and aged (14 days post mortem). NIR spectroscopic measurements were taken at 3 and 14 days post mortem from all sample sections (anterior and posterior). Three rib eye steaks of thickness 2.5 cm were cut from the posterior of section, with the first steak used for color and spectroscopic measurement, the second steak used for cooking loss and shear force (WBSF) measurement and the third steak used for pH and drip loss measurement (Figure 7.5). The color, cooking loss, pH, and drip loss measurements were taken for another study (Zamarripa, 2014). Samples were randomized by ageing group for spectroscopic measurements. Each sample was cut according to the randomization sequence and kept at 4 °C for 30 min for blooming. After 30 min, samples were brought out of the cooler for spectroscopic measurements.

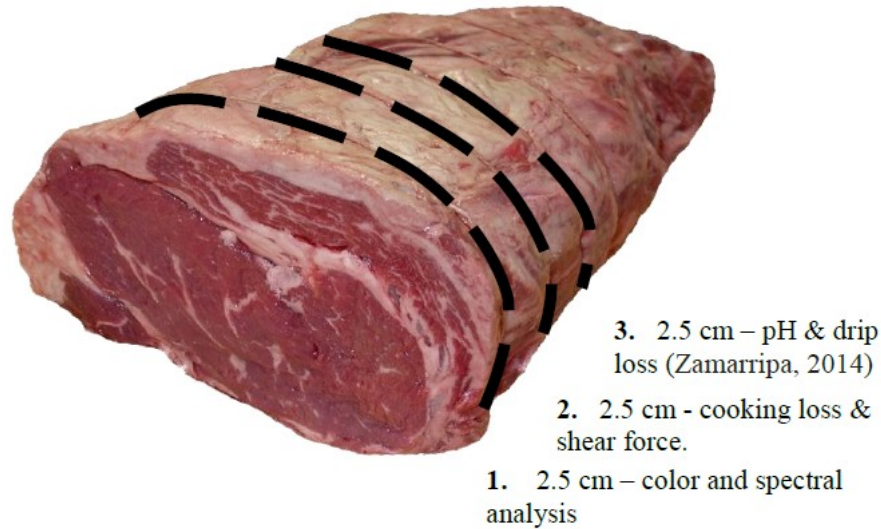


Figure 7.5: Distribution of rib eye steaks for different measurements.

### 7.2.3 NIR Spectroscopy

A Yokogawa AQ6370C Optical Spectrum Analyzer (Section 3.2.3 of Chapter 3) was used for spectroscopic measurement. According to specification, an optical alignment and wavelength calibration using the internal calibration light source was performed after an hour of recommended warm up time.

NIR readings were recorded for the full wavelength range of 600 to 1700 nm. The NIR light source, a commercially available 125 watt, 120 volt infrared heating lamp (Satco S4750) with an optical filter (FGL850S) was described in Section 6.2.1, was used. To prevent the overtone effect during measurement, the optical filter (FGL850S) was used.

The reflectance light was collected using a bifurcated fiber optic cable (Ocean Optics R600-7-VIS-125F) along with the SMA905 to FC converter adapter (Section 3.2.3 of Chapter 3). The converter adapter was used to attach the cable to the Yokogawa AQ6370C optical spectrum analyzer. The multiple fiber channels surrounding the main collection fiber for carrying source light on to measurement surface were closed but the collection fiber in the middle was used for

the collection of the reflected light. The height from the measurement surface to the end of the probe was held constant at 10 cm during any measurement and its corresponding reference measurement.

An optical polarizer (LPIRE050-C linear polarizer, Thorlabs, Newton, New Jersey, USA) of diameter 1.27 cm (Section 4.2.1 of Chapter 4) was used for polarized light spectroscopy. The reflected light was passed through the polarizer before being sent to the spectrometer. For this purpose a polarizer holder adapter (Figure 7.6) was designed and fabricated in the Electrical Engineering department workshop of the University of Alberta. This was designed to hold the polarizer perpendicularly at the end of the fiber optic probe. This adapter had two parts; one part was a small cylinder (Diameter = 12.82 mm and Length = 23.57 mm) to attach to the fiber optic probe and the other one was a large cylinder (Diameter = 21.49 mm and Length = 15.36 mm) to hold the polarizer inside. The small cylinder had a small cylindrical hole of diameter 3.19 mm at the center to pass the fiber optic probe inside the small cylinder and hold on to the probe. On one side of the large cylinder had a large cylindrical opening of diameter 12.81 mm at the center to keep the polarizer inside and hold on to the small cylinder by passing it inside the large cylinder. There was a small circular opening of diameter 3.2 mm on the other side of the large cylinder to pass the reflected light inside the large cylinder. The reflected light from measurement surface was passed through the polarizer and carried to the spectrometer via the fiber optic probe and fiber optic cable. Thus, polarized reflected light was sent to the spectrometer for spectroscopic measurements of polarized light.

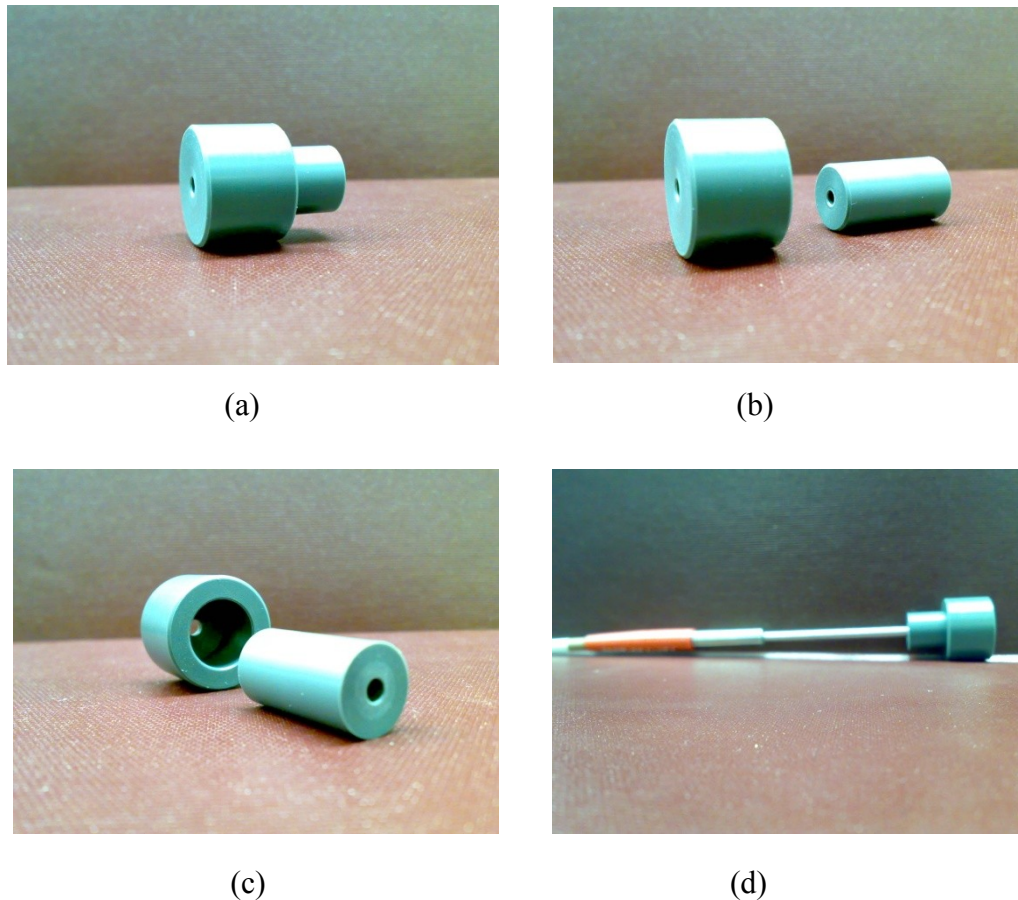


Figure 7.6: (a) Polarizer holder adapter assembly; (b) Front view of unassembled small and large cylinder; (c) Back view of unassembled small and large cylinder; (d) Polarizer holder adapter assembly attached to the fiber optic probe.

During this experiment a 2.53 cm thick Teflon<sup>TM</sup> sheet was used as a reference measurement for normalization. The Teflon<sup>TM</sup> sheet had a uniform distribution of spectral intensity and was therefore suitable as a reference for normalization. The same plastic black cover with a hole in the center of diameter approx. 4.5 cm as described in Section 3.2.2 was used to cover the entire region on the measurement surface except the area intended to be measured. A standard laboratory stand was used to attach and hold the NIR light source. The recorded spectrum data was stored directly in the AQ6370C's internal memory during the measurement. A USB flash drive was used to transfer the data from AQ6370C to computer for data analysis.

#### **7.2.4 Experimental Setup**

The entire experiment was performed in a darkened room. A thick card board sheet was used to separate the instruments and computers from the measurement area to prevent light contamination from computer and instruments screens (e.g. AQ6370C LCD panel). The infrared light source with the metal cover and attached filter was connected to a standard lab stand. This same stand was used to hold the fiber optic probe. The experimental setup was as described in previous experiment reported in Section 6.2.3 of Chapter 6.

#### **7.2.5 NIR Spectroscopic Measurement**

After 30 min blooming the sample was prepared for the spectroscopic measurement. The appropriate end of the fiber optic cable was then connected to the AQ6370C using SMA905 and FC converter adapter. A dark current reading was taken by covering the fiber optic probe with a cap followed by a reading of the Teflon<sup>TM</sup> reference as previously described in Section 6.2.3 of Chapter 6. An NIR reading was then taken from the measurement surface of the sample after that of the Teflon<sup>TM</sup> reference. Three readings were taken: one without the polarizer and two with the polarizer. The two readings with the polarizer included one with the polarizer axis oriented parallel to the muscle fiber direction and another with the polarizer axis oriented perpendicular (90°) to the muscle fiber direction. All readings were stored as “CSV” file in the internal memory of AQ6370C using proper labeling according to the sample Identification number. The data was then transferred to a computer using a USB flash drive for further data analysis.

#### **7.2.6 Warner-Bratzler Shear Force (WBSF)**

The Warner–Bratzler Shear Force (WBSF) measurement was performed according to the AMSA method (AMSA, 1995). The steaks were trimmed of subcutaneous fat and cooked on an electric grill (General Electric 4 in 1 Grill/ Griddle, China) heated to 176 °C. A stainless steel

thermocouple was placed into the geometric center of each steak to monitor and record the internal temperature of the steak (Tinytag View 2s, Gemini Data Loggers, Chichester, West Sussex, UK). Steaks were cooked until the internal temperature reached at 71 °C. Cooked steaks were removed from the grill, placed into a plastic bag and cooled to 10 °C in an ice water bath. Steaks were equilibrated at 4 °C overnight and allowed to reach room temperature the following day prior to shear force analysis. Six cores of 1.27 cm diameter and 2 cm long parallel to the muscle fibers were removed from each steak using a cork borer. Each core was sheared once perpendicular to the fiber direction using a materials testing machine (AMETEK, Inc. Lloyd Instrument LRX plus, Digital Metrology Measurements, West Sussex, UK) fitted with a Warner–Bratzler type shear blade travelling at 225 mm/min. The WBSF values were recorded in newtons (N) and values were averaged to get an average estimate of WBSF value of the steak. The WBSF measurements were performed in collaboration with José Angel Puente Zamarripa.

### **7.3. Data and Statistical Analyses**

#### **7.3.1 NIR Spectroscopy**

Reflectivity is a ratio of two reflected light intensities and the denominator was the reflected light from the Teflon<sup>TM</sup> sheet (Equation 7.1).

$$R = \frac{I_{reflected}}{I_{reference}} \quad (7.1)$$

Where R is the reflectivity of each wavelength,  $I_{reflected}$  is the reflected light intensity from the sample;  $I_{reference}$  is the reflected light intensity from the white reference (Teflon<sup>TM</sup> sheet). In this data analysis the “dark current” was not subtracted because it was identified in previous data analyses results of Chapter 4 (Section 4.4.3) and Chapter 6 (Section 6.4.3) that subtraction of

dark current may cause adverse effect on statistical data analysis. Furthermore, if the dark current noise is as high as the actual intensity data, essential information can be eliminated through subtraction of dark current. Considering these factors dark current was not subtracted in this data analysis.

Reflectivity should always be less than one; therefore, the reflectivity reading of any wavelength that was higher than one was identified as contaminated with noise. Identification and removal of this noise was necessary because it would contaminate the neighboring wavelength readings after application of the smoothing filter to the entire NIR data. These wavelengths (600 to 929 nm and 1651 to 1700 nm) were removed from the entire NIR wavelength range (600 to 1700 nm). The recorded NIR spectra had resolution of 0.1 nm. This resolution was reduced to 1 nm using MATLAB™ program for ease of data analysis. The final reflectivity data were calculated after filtering the reflected light intensity of remaining wavelengths (930 to 1650 nm) using the MATLAB™ library function “smooth”. This library function was a moving average filter with smoothing coefficient of 11 (span =  $11 \times 1 = 11$  nm). Calculated reflectivity data were stored in another Excel file along with WBSF data for statistical analysis. Table 7.1 listed the various data sets that were calculated for statistical analysis. Unscrambler X (Version: 10.2 ) (64-bit) software was used for statistical analysis of the NIR reflectivity data sets using Partial Least Square (PLS) method. Wavelengths with higher regression coefficients were selected in the next consecutive partial least square (PLS) analysis to improve the overall result at every PLS analysis. Weighted regression coefficient plot from 930 to 1650 nm showed that boundary wavelength values were changing rapidly with closely spaced wavelengths due to the noise present in the actual data. These regions were also deleted to improve the overall result. After achieving highest possible  $R^2$  value the selected wavelengths

were used to generate five more PLS analysis using the same wavelengths. This was performed for each data set and the results were averaged. The mean and standard deviation of each data analysis are presented in result section of this chapter.

Table 7.1: various data sets calculated for PLS analysis.

<b>Data Set</b>	<b>NIR Data Type</b>	<b>Day of NIR Measurement</b>	<b>Day of WBSF Measurement</b>
1	NP <sup>1</sup>	Day 3	Day 3
2	P <sup>2</sup>	Day 3	Day 3
3	P90 <sup>3</sup>	Day 3	Day 3
4	NP	Day 3	Day 14
5	P	Day 3	Day 14
6	P90	Day 3	Day 14
7	NP	Day 14	Day 3
8	P	Day 14	Day 3
9	P90	Day 14	Day 3
10	NP	Day 14	Day 14
11	P	Day 14	Day 14
12	P90	Day 14	Day 14

<sup>1</sup> Non-polarized

<sup>2</sup> Polarizer grating perpendicular with the muscle fiber direction

<sup>3</sup> Polarizer grating perpendicular with muscle fiber direction

## 7.4 Results

Minimum, maximum, mean and standard deviation values for WBSF are shown in Tables 7.2 and 7.3. The treatments applied to the carcass sides introduced sufficient variation and range of WBSF values for regression analyses.

NIR measured on day 3 characterized 86% of the day 3 WBSF data used for calibration and predicted day 3 WBSF with 65% accuracy (calibration  $R^2=0.86$ , validation  $R^2=0.65$ ) using non-polarized NIR light. Polarization parallel to the muscle fiber direction improved prediction of day 3 WBSF, with calibration  $R^2=0.96$  and validation  $R^2=0.83$ . Polarization perpendicular to the

muscle fiber direction produced similar results to parallel polarization, with calibration  $R^2=0.98$  and validation  $R^2=0.83$  for the day 3 WBSF data.

Table 7.2: Minimum (Min), maximum (Max), mean and standard deviation (SD) values of WBSF measured after 3 days of storage of beef samples with different treatments (n=10).

Treatments	Stimulated				Non-stimulated			
	Min	Max	Mean	SD	Min	Max	Mean	SD
<b>Warm</b>	26.25	44.98	35.81	7.11	28.17	60.17	42.01	9.51
<b>Cold</b>	22.82	39.24	33.41	6.50	28.45	66.76	47.55	10.70

Table 7.3: Minimum (Min), maximum (Max), mean and standard deviation (SD) values of WBSF measured after 3 and 14 days of storage (ageing treatment) of beef samples (n=40).

Days post mortem	Minimum	Maximum	Mean	SD
3	22.8	66.7	39.7	10.0
14	16.0	34.5	26.8	4.6

Non-polarized NIR measured on day 14 predicted the WBSF measured on day 14 poorly, with a calibration  $R^2=0.84$  and a validation  $R^2=0.51$ . Parallel polarized NIR light described more WBSF variation than non-polarized NIR, with a calibration  $R^2=0.95$  and validation  $R^2=0.75$ . Perpendicular polarized NIR predicted WBSF similarly to parallel polarized NIR, with a calibration  $R^2=0.95$  and a validation  $R^2=0.77$ .

NIR measured on day 3 prediction of WBSF measured on day 14 resulted in a calibration  $R^2=0.93$  and a validation  $R^2=0.66$  using non-polarized NIR light. Parallel polarized NIR light on day 3 prediction of WBSF on day 14 produced a calibration  $R^2=0.92$  and a validation  $R^2=0.41$  while perpendicular polarization for the same samples produced a calibration  $R^2=0.91$  and a validation  $R^2=0.74$ .

Table 7.4: Calibration and validation regression coefficient ( $R^2$ ) values of various PLS analysis.

	<b>NIR on Day 3</b>	<b>Calibration <math>R^2</math> mean (SD)</b>	<b>Validation <math>R^2</math> mean (SD)</b>
<b>WBSF on Day 3</b>	NP <sup>1</sup>	0.86 (0.01)	0.65 (0.02)
	P <sup>2</sup>	0.96 (0.01)	0.83 (0.00)
	P90 <sup>3</sup>	0.98 (0.00)	0.83 (0.02)
	<b>NIR on Day 14</b>	<b>Calibration <math>R^2</math> mean (SD)</b>	<b>Validation <math>R^2</math> mean (SD)</b>
<b>WBSF on Day 14</b>	NP	0.84 (0.00)	0.51 (0.02)
	P	0.95 (0.00)	0.75 (0.01)
	P90	0.95 (0.00)	0.76 (0.01)
	<b>NIR on Day 3</b>	<b>Calibration <math>R^2</math> mean (SD)</b>	<b>Validation <math>R^2</math> mean (SD)</b>
<b>WBSF on Day 14</b>	NP	0.93 (0.01)	0.66 (0.03)
	P	0.92 (0.00)	0.41 (0.02)
	P90	0.91 (0.01)	0.74 (0.01)

<sup>1</sup> Non-polarized

<sup>2</sup> Polarizer grating parallel with the muscle fiber direction

<sup>3</sup> Polarizer grating perpendicular with muscle fiber direction

## 7.5 Discussion

Electrical stimulation and different cooling treatments to vary the rate of temperature change early post-mortem of beef carcasses were used to achieve a wide range of WBSF values. WBSF varies with the rates of early post mortem temperature and pH decline (Bruce and Ball 1990; Bruce et al., 2001). Electrical stimulation helps to reduce muscle pH rapidly early post mortem and hasten rigor mortis which as a result produces tender beef (Ducastaing et al., 1985; Etherington 1984; Bruce et al., 2004). Electrical stimulation in this study affected WBSF as predicted, with the highest variation observed in WBSF achieved in beef samples that were treated with cold chiller temperature and electrical stimulation (Table 7.2). The detailed analysis of different treatments and their effects on beef tenderness were reported in the study by Zamarripa (2014).

NIR spectroscopic technology has been very promising for determination of different quality attributes in meat and has been used commercially for this purpose for homogenized meat, but has not been effectively commercialized to be applicable on whole or intact meat. NIR spectroscopy (NIRS) on homogenized, minced or freeze-dried meat to predict WBSF and this has produced varied results. De Marchi et al. (2007) performed NIRS on fresh minced meat to predict WBSF ( $\text{kg}\cdot\text{cm}^{-2}$ ) and found a very low calibration  $R^2$  value of 0.08. The same authors performed NIRS on freeze-dried meat and produced a prediction model for WBSF ( $\text{kg}\cdot\text{cm}^{-2}$ ) with a calibration  $R^2$  value of 0.20. Prieto et al. (2008) performed NIRS on homogenized meat and predicted WBSF (kg) with calibration  $R^2$  values of 0.17 for beef from mature steers and 0.45 for beef from young cattle, suggesting that connective tissue may be an influence. Ripoll et al. (2008) in a similar study to the present study obtained a calibration  $R^2$  value of 0.74. These results indicated that an algorithm for WBSF value of beef cannot be predicted reliably using

NIRS on homogenized, minced or freeze-dried meat. Some literature has shown that visible light was added to the NIR light (VISNIR) for prediction of intact beef tenderness. Shackleford et al. (2011) indicated that the ability of the VISNIR system to predict beef tenderness was affected by bloom time. Shackleford et al. (2011) also described a VISNIR technique that would be unbiased by bloom time. This study was conducted to find the potential of the NIR reflectance and polarized NIR reflectance spectroscopy to predict beef tenderness on whole or intact meat. NIR light is not affected by visible color (Chapter 6) and this makes it immune to bloom time. However, NIR light spectroscopy can be affected by sample temperature (Togerson et al., 2003). To maintain a constant temperature a constant time gap between removal of the sample from the cooler and NIR spectroscopic measurement was maintained.

In the present study, confounding effects such as overtones and day to day machine variation were eliminated so that the relationship between NIR reflectance and beef tenderness could be understood. To do this, an optical filter with a cut-off wavelength below 850 nm was also used to reduce the overtone effect in the reflected spectrum (Osborne, 1981) and reflected light was normalized using a reference reflectance reading from a white Teflon<sup>TM</sup> sheet. Ripoll et al. (2008), Park et al. (2001) and Mitsumoto et al. (1991) also used a reference value from a ceramic disk; however it was unclear how the reference value was used to calculate the log (1/R). Unlike these previous researchers, reflectivity rather than absorbance was calculated and used in the statistical analysis in the present study.

Polarization appeared to improve prediction of cooked beef toughness using NIR reflectance. Swatland (2012) mentioned that the polarizing microscope was able to detect two different bands along the myofibril, the anisotropic A-band and isotropic I-band and also he mentioned that the A-band of the sarcomere transmitted more light than the I-band which is the opposite to the

stained myofibril viewed from an ordinary microscope. Furthermore, he indicated that most certainly polarized light microscopy might be used to measure the differences between two different refractive indices of the myofibril. Luc et al., (2008) mentioned that many materials produce fluorescence polarized emission when excited with polarized light and these authors used fluorescence polarization technique to estimate sarcomere length. Visible fluorescence polarization measurement has been used to obtain information about the structure and structural modification of beef caused by ageing (Clerjon et al., 2011). In this study it was assumed that meat muscle fibers had similar polarization effect on NIR light that were related to tenderness and the results of the present study are in agreement.

In statistical analysis it was important to have a wide range of variation in the controllable variables (tenderness). To achieve a wide range of tenderness in the entire sample set of this experiment, various techniques such as electrical stimulation, early post mortem heating and cooling and ageing were applied (Jeremiah et al., 1985; Aalhus et al., 2001; George et al., 1980; Aalhus et al., 1992; Ducastaing et al., 1985; Etherington 1984; Bruce and Ball 1990; Bruce et al., 2001; Bruce et al., 2004). A wide range of WBSF values were obtained through post mortem treatments for the different measurement days (3 days of post mortem and 14 days of post mortem), with a range of 43.94 (N) between minimum and maximum tenderness for day 3 and a range of 18.56 (N) between minimum and maximum tenderness for day 14.

Non-polarized NIR spectroscopy predicted WBSF measured on day 3 with 65% accuracy but had a calibration  $R^2 = 0.86$ . This indicated that some of the sample used in validation segment of PLS analysis had WBSF values which were not predicted by the calibration model. The validation  $R^2$  value was in agreement with findings of many other studies. Results from the literature suggest that fitting a comprehensive model to NIR data is difficult. Byrne et al. (1998)

conducted NIR spectroscopy (NIRS) on intact beef to predict WBSF (kg) and found calibration  $R^2$  values between 0.37 and 0.67, while Park et al. (1998a) conducted a similar study and found calibration  $R^2$  value of 0.67. Rodbotten et al. (2001) performed NIRS on intact beef and predicted WBSF ( $\text{kg}\cdot\text{cm}^{-2}$ ) at 2 days post mortem with a calibration  $R^2$  value of 0.69, and Venel et al. (2001) performed NIRS on intact beef and predicted WBSF (N) with a calibration  $R^2$  value of 0.58. Prediction of fatness in whole meat has also been inconsistent in previous research, as Leroy et al. (2003) performed a similar study and found validation  $R^2$  values between 0.12 and 0.41, while Liu et al. (2003) in a similar study found calibration  $R^2$  values between 0.17 and 0.72. Of the published research, the results of Andres et al. (2008) predicted WBSF ( $\text{kg}\cdot\text{cm}^{-2}$ ) on whole meat were similar to those of the current study, as these authors obtained a calibration  $R^2$  value of 0.65, exactly matching the validation  $R^2$  value of the present study.

Non-polarized NIRS measured on day 14 predicted WBSF measured on day 14 with calibration  $R^2$  value of 0.84 and validation  $R^2$  value of 0.50. This signified that prediction accuracy of day 14 measurement was reduced over prediction accuracy day 3 measurements. These results agreed with the results of Rodbotten et al. (2001) who found a calibration  $R^2$  value of 0.62 at 9 days post mortem and 0.36 at 21 days post mortem for absorbance. This clearly indicated that prediction accuracy decreases with ageing of beef. An interesting finding of the present study was that non-polarized NIRS measured on day 3 produced a similar prediction accuracy for WBSF aged 14 days of 65.8% (validation  $R^2=0.658$ ) almost identical to the accuracy obtained for the prediction of WBSF measured on day 3, suggesting that NIRS on day 3 could predict WBSF at both day 3 and day 14 with equal accuracy.

There were few studies performed using polarized NIR light spectroscopy in a similar fashion to that performed in the present study. Polarized (P) NIRS measured on day 3 predicted WBSF

measured on day 3 with calibration  $R^2$  of 0.96 and validation  $R^2$  of 0.83. Polarized NIRS perpendicular to the muscle fibers (P90) measured on day 3 predicted WBSF measured on day 3 with calibration  $R^2$  of 0.98 and validation  $R^2$  of 0.83. These results indicated that polarized NIRS can predict WBSF at 3 days postmortem with higher accuracy than non-polarized. Polarized (P) NIRS measured on day 14 predicted WBSF measured on day 14 with calibration  $R^2$  of 0.95 and validation  $R^2$  of 0.75. Polarized (P90) NIRS measured on day 14 predicted WBSF measured on day 14 with calibration  $R^2$  of 0.95 and validation  $R^2$  of 0.77. This was a significant improvement in comparison to prediction accuracy of non-polarized NIRS at 14 days post mortem. The notable point in these results was that polarized (P) NIRS and 90° polarized (P90) NIRS had similar prediction capability in both day 3 post mortem measurements and day 14 post mortem measurements. However analysis of the results of the prediction of WBSF measured on day 14 using NIRS measured on day 3 presented a slightly different picture. Polarized (P) NIRS measured on day 3 predicted WBSF measured on day 14 with calibration  $R^2$  of 0.92 and validation  $R^2$  of 0.41. Polarized (P90) NIRS measured on day 3 predicted WBSF measured on day 14 with calibration  $R^2$  of 0.91 and validation  $R^2$  of 0.74. In this case the prediction accuracy of polarized (P90) NIRS was greater than polarized (P) NIRS parallel to the muscle fibers and slightly improved prediction than non-polarized NIRS. These results clearly indicated that NIRS technology to predict WBSF can be improved by polarization. Luc et al. (2008) concluded that fluorescence polarization can be used to investigate the alignment of muscle fiber structure and can be used to identify cold shortening. Muscle fiber structure and cold shortening are among the most important factors affecting meat tenderness (Locker and Hagyard, 1963). Luc et al. (2008) used another polarizer as an analyzer and Swatland (2012) also suggested a similar optical arrangement with a polarizer used as an analyzer in the receiving end of the reflected light before

going to the spectrophotometer. Implications of such an optical arrangement can be tested in future experimentation to improve prediction accuracy. The equation formulated (not shown, commercially confidential) in this study can be integrated in the handheld device and the wavelengths that were used in the equation to predict WBSF can be obtained using infrared LED and optical filters for an anticipate prediction success of about 80% if polarization is used. In order to understand the physiological causes of these results and find out the full potential of polarized NIRS, further research on this field is required.

## **7.6 Conclusion**

The NIR spectroscopy can predict tenderness of beef in terms of WBSF with moderate accuracy. Further research is needed to improve the prediction accuracy over that obtained in this study and also to better understand the effect of polarization NIR spectroscopy. Improvement of correlation coefficients to predict beef tenderness by introducing polarizer to NIR spectroscopy was a significant achievement of this study. This study opened a new way to improve instrument assessment of beef tenderness in future research.

## **Chapter 8**

# **Visible Light and Near-infrared Spectroscopy on Whole Beef Rib Eye Steaks**

### **8.1 Introduction**

Previously we completed experiments with visible light and NIR (near-infrared) spectroscopy on whole beef rib eye steaks (Chapter 4), in a paper model experiment (Chapter 5), a ground meat (Chapter 6), and NIR spectroscopy with polarization (Chapter 7). The enormous amount of data collected and experienced gained from these experiments has assisted to build statistical models related to beef intramuscular fat content and toughness. These statistical models were based on highest possible correlations, which can be found through statistical analysis, between different wavelengths and meat quality attributes. The primary objective of this experiment was to validate those statistical models using data sets measured in similar way as done in previous experiments. Successful validation of the discovered statistical models ensured consistency and repeatability of the model regardless of any changes in environmental parameters and other measurement variables. The hypothesis of this experiment was that the correlation found in the previous experiments between light spectroscopy and amount of fat content in beef can be repeated with a similar experiment.

### **8.2 Materials and Methods**

#### **8.2.1 Materials**

Samples of rib eye steak from rib loin were removed from 48 different animals with 12 samples in each marbling grade (A, AA, AAA, Prime) at 3 to 4 days post mortem. The surface of the *m. longissimus thoracis* (LT) muscle between the 12th and 13th rib was used for grading. The

grading was done by certified meat graders of the Canadian Beef Grading Agency. The samples were acquired from a large Alberta abattoir in groups of 12 samples over one month period with 3 samples from each grade at each sampling time. Samples were then randomized prior to spectroscopic and other measurements to eliminate any possible effect of instruments or environment in the statistical analysis. Samples were stored in a laboratory cooler at 4°C and not frozen before measurement.

Sample color was measured using the colorimeter (Konica Minolta Chroma Meter CR-400) with aperture size 8 mm (diameter) that uses silicon photocell sensors as detector and pulsed xenon lamp as light source. Measurement time was about 1 second and minimum measurement interval was about 3 sec. The white calibration unit (CR-A43 Calibration Plate) was used for instrument calibration purposes.

A digital color image scanner (EPSON PerfectionV33 Flatbed scanner) was used to scan surface of the samples for digital image processing (Section 4.2.1 of Chapter 4). The reflected light intensity of the visible light spectrum was measured using the VIS spectrometer (Ocean Optics USB4000) and has been described previously (Section 3.2.2 of Chapter 3). For VIS light measurements, a commercially available 100 watt incandescent bulb (Section 5.2.1 of Chapter 5) was used as a broad spectrum light source. For NIR measurements, a commercially available 125 watt infrared heating lamp (Satco S4750) with an optical filter (FGL850S) was used as a light source (Section 6.2.1 of Chapter 6). This type of infrared heating lamp had very wide range of spectrum from visible to infrared. The reflectance light was collected using a bifurcated fiber optic cable (Ocean Optics R600-7-VIS-125F), previously described in Section 3.2.2 of Chapter 3. The height from the measurement surface to the end of the probe was maintained at 10 cm during any measurement and its corresponding reference measurement for normalization. The

Teflon<sup>TM</sup> sheet of 2.53 cm thick (Section 7.2.3 of Chapter 7) was used as a reference measurement for both VIS and NIR spectroscopy. A plastic black cover with a hole in the center of diameter (approx. 4.5 cm, termed black mask) was used to cover the entire region on the measurement surface except the area intended for measurement as described previously (Section 3.2.2 of Chapter 3). The Yokogawa AQ6370C Optical Spectrum Analyzer was used for NIR Spectrum measurement and its configuration and use were similar to that described previously in Section 3.2.3 of Chapter 3. The fiber optic cable was the same cable (Ocean Optics R600-7-VIS-125F Bifurcated fiber optic cable) as used in the visible spectroscopic analysis. The SMA905 to FC (PC type connector which is compatible with AQ6370C) converter adapter (Section 3.2.3 of Chapter 3) was used to attach the cable to the Yokogawa AQ6370C optical spectrum analyzer. The recorded spectrum data was stored directly in the AQ6370C's internal memory during the measurement. A USB flash drive was used to transfer the data from AQ6370C to computer for data analysis. MATLAB<sup>TM</sup> computing software and statistical analysis software Unscrambler<sup>TM</sup> (CAMO, Woodbridge, New Jersey) were used for data analysis.

## **8.2.2 Experimental Setup**

The entire experiment was performed in a darkened room. A thick cardboard sheet was used to prevent stray light from the spectrometer and computer screens from penetrating the measurement area. The lab temperature was held constant (21 - 22 °C). One end of the bifurcated fiber optic cable with one fiber channel for collecting reflected light was connected to spectrometer using SMA905 connector. The other end of the cable with multiple fiber channels for carrying light from light source was kept closed as it was not used for sourcing light. The VIS spectrometer was connected to a Netbook Computer (Aspire one 532h-2630, Acer, China). The interface software (SpectraSuite<sup>TM</sup>), installed in the Netbook, was used for setting various

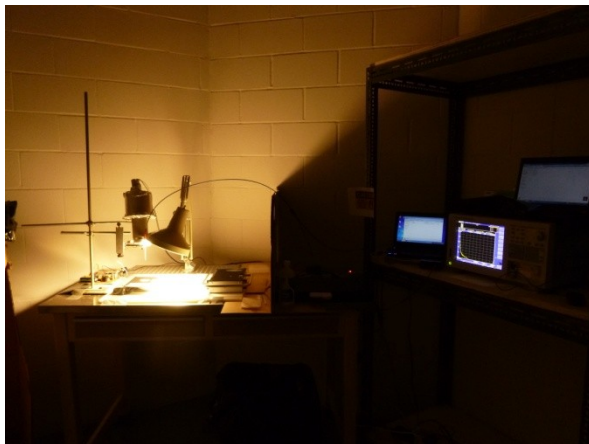
parameters (Section 6.2.3 of Chapter 6) of the spectrometer and collecting measurement readings from spectrometer. The reflectance data of entire spectrum from spectrometer was saved in Excel™ files for further processing. Figure 8.1 is illustrated the complete experimental setup in normal room light [(a) and (b)] and in darkened room [(c) and (d)].



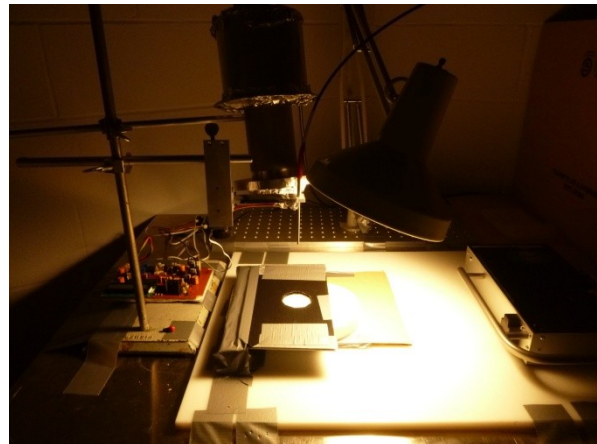
(a)



(b)



(c)



(d)

Figure 8.1: Images are illustrating the experimental setup with light source, fiber optic cable, optical probe and card board partition; (a) experimental setup in normal room light; (b) close up of experimental setup in normal room light; (c) experimental setup in dark room with light source on; (d) close up of experimental setup in dark room with light source on.

### **8.2.3 Sample Preparation**

Rib eye steaks 2.5 cm thick were removed from the posterior of each rib section just prior to measurement. Each sample was removed from the 4°C cooler randomly in a manner balanced for grade and equilibrated at room temperature (20-22 °C) for approximately 10 minutes in order to allow the samples to bloom.

### **8.2.4 Measurement on Whole Sample**

After blooming, the CIE L\*, a\* and b\* color of the samples was measured using the colorimeter (CR-400, Konica-Minolta, Japan). L\*, a\* and b\* color component values for the lean portion of the beef were recorded at three different position. Each sample was then scanned using the scanner (EPSON PerfectionV33 Flatbed, Epson, China) connected to a laptop computer (ThinkPad X220, Lenovo, China) to acquire a digital image of the sample measurement surface. Each sample was then prepared for VIS and NIR spectroscopic measurement and the white Teflon™ reference was measured just prior to each sample measurement for normalization. Fiber optic probe height was fixed at 10 cm. All VIS spectroscopic measurements were recorded in Excel™ files. All NIR readings were stored as “CSV” files in the internal memory of AQ6370C until transferred to a personal computer for analysis. Both references and samples were covered using the black mask cover to exclude areas not to be measured. A dark current spectroscopic reading was taken for both VIS and NIR spectroscopic measurements by covering the fiber optic probe with a cap. In this experiment two spectroscopic readings each from two different locations on the sample surface were recorded for each sample. After completion of all spectroscopic measurements, the sample was kept under the black mask cover in order to mark

the digital image of the sample with specific surface region where VIS and NIR spectroscopic measurements were performed for that sample (Figure 8.2). Marking was done on a separate copy of digital image of the sample taken by the digital image scanner. Identification of the location for marking was performed by visual inspection of that specific sample surface region used for spectral measurements. This was performed to identify the specific region for image processing purposes. The region was marked using a black circle with the help of Windows Paint™ program. The resolution of original digital image taken by the scanner was reduced as described previously in Section 4.2.2.5 of Chapter 4.

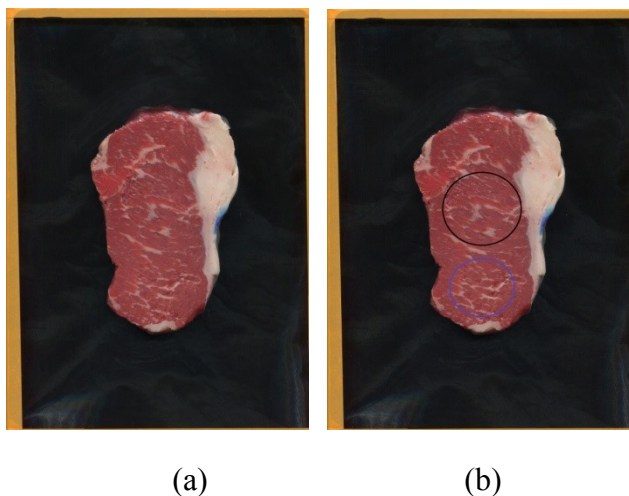


Figure 8.2 (a) Digital image of a sample (sample ID: 843N); (b) Marked digital image of the same sample.

### 8.2.5 Crude Fat Extraction

The crude fat extraction was performed using the Goldfish Fat Extraction Apparatus (Model 35001, Labconco Corp. 35181 Revision I, 1997). Crude fat extraction was performed as previously described in Section 4.2.4 of Chapter 4.

## 8.3 Data Analysis

### 8.3.1 Digital Image Processing

Digital image processing was performed only on marked (CIRCLED regions) images using an image processing algorithm described in Section 6.3.1 of Chapter 6. The results from image processing were then correlated with the spectroscopic readings of the corresponding sample in Unscrambler™ software. MATLAB™ software [MATLAB™ Version 7.9.0.529 (R2009b)] was used for image processing and the programming code was written in MATLAB™ programming language (Appendix E).

### 8.3.2 VIS and NIR Spectroscopy

All recorded data of VIS and NIR spectroscopy was stored in Excel™ files. The Excel™ files were named according to each sample ID number. The Excel™ data files were loaded in MATLAB™ and processed using MATLAB™ program similar to that described in previous chapters (Section 6.3.2 of Chapter 6). The MATLAB™ code can be found in Appendix C.

The NIR spectrum resolution was reduced to 1 nm from 0.1 nm. After removing the noisy wavelengths, the effective range of the VIS spectrum was 425.06 to 985.01 nm and of the NIR spectrum was 920 to 1659 nm. The reflectance data were first normalized using the reference readings taken from the Teflon™ sheet. The normalized reflectance or reflectivity was filtered using the MATLAB™ library function “smooth”, which was a moving average filter. The smoothing coefficients of this filter was set to 50 (span = 50 × 0.22 = 11 nm) for VIS spectroscopy data and 11 (span = 11 × 1 = 11 nm) for NIR spectroscopy data. Reflectivity data were calculated using the following formulae.

$$R = \frac{I_{\text{reflected}}}{I_{\text{reference}}} \quad (8.1)$$

Where  $R$  was the reflectivity of each wavelength,  $I_{\text{reflected}}$  was the light intensity of each wavelength reflected back from the sample, and  $I_{\text{reference}}$  was the light intensity of each wavelength reflected back from the white reference (Teflon™ sheet). Reflectivity was calculated with dark current noise included. Previous experiments of Chapter 4 and Chapter 6 indicated that dark current noise subtraction had a random effect on the correlation. Because of this reason analysis of the results without subtracting the dark current noise was performed. MATLAB™ generated reflectivity data were stored in Excel™ along with crude fat and image processed fat data and imported into Unscrambler™ software for Partial Least Square analysis.

Correlations were calculated in MATLAB™ using MATLAB™ library functions. In these calculations MATLAB™ function “corr” was used to calculate  $r$  values and  $p$  values as described in Section 4.3.5 of Chapter 4.

## **8.4 Results**

The wavelength range of 425 to 985 nm was selected after visual inspection of the data set as this range had the least noise as indicated by having the fewest fluctuations in PLS partial correlation coefficients. Meat quality data ranges indicated that sufficient variation existed in the data for regression analyses (Tables 8.1 to 8.3). The correlation plot between image processed fat and crude fat showed an  $R^2$  value of 0.57 (Figure 8.3), indicating that the two were moderately related. The Pearson Correlation coefficient ( $r$ ) values and probability ( $p$ ) values are presented in Table 8.4 and Table 8.5 respectively. Correlations with  $p < 0.05$  are highlighted in Table 8.5.

Table 8.1: Descriptive statistics of image detected and chemically extracted crude fat.

<b>Characteristic</b>	<b>n</b>	<b>Minimum</b>	<b>Maximum</b>	<b>Mean</b>	<b>Standard Deviation</b>
<b>Image fat (%) (CIRCLED)</b>	48	1.68	23.87	6.78	4.99
<b>Crude fat (%)</b>	48	0.99	15.95	5.34	3.99

Table 8.2: Descriptive statistics (minimum (min), maximum (max), mean and standard deviation (SD)) of image and crude fat (%) within each grade category (n = 12 /grade).

<b>Grade</b>	<b>Image FAT (CIRCLED)</b>				<b>Crude FAT</b>			
	<b>Min</b>	<b>Max</b>	<b>Mean</b>	<b>SD</b>	<b>Min</b>	<b>Max</b>	<b>Mean</b>	<b>SD</b>
A	1.68	13.05	4.64	3.28	0.99	3.83	2.27	0.95
AA	2.16	5.51	3.62	1.12	1.17	3.94	2.51	0.89
AAA	3.07	7.95	5.77	1.68	2.45	7.07	4.93	1.41
Prime	3.95	23.87	12.57	5.99	7.82	15.95	11.19	2.52

Table 8.3: Descriptive statistics for L\*, a\* and b\* color coordinate values.

<b>Color Coordinate</b>	<b>Minimum</b>	<b>Maximum</b>	<b>Mean</b>	<b>Standard Deviation</b>
L*	31.66	43.85	37.43	2.40
a*	17.31	27.89	23.17	2.35
b*	2.89	9.68	6.56	1.27

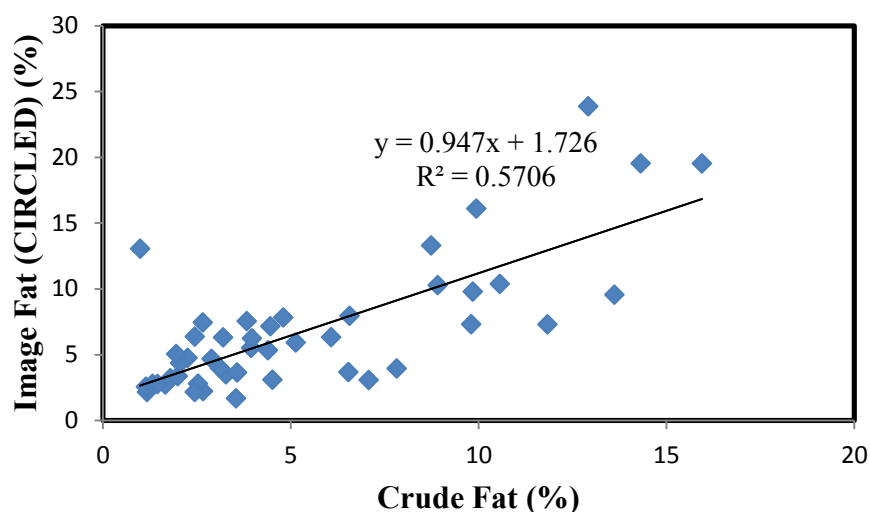


Figure 8.3: Linear relationship between image processed fat (CIRCLED) and crude fat percentages.

VIS spectroscopy obtained a mean regression coefficient calibration  $R^2$  value of 0.93 and a mean validation  $R^2$  value of 0.87 for crude fat prediction. Similarly, VIS spectroscopy produced a regression coefficient calibration  $R^2$  value of 0.86 and validation  $R^2$  value of 0.69 for image processed fat prediction. NIR spectroscopy produced a regression coefficient calibration  $R^2$  value of 0.97 and validation  $R^2$  value of 0.90 for crude fat prediction and a regression coefficient calibration  $R^2$  value of 0.97 and validation  $R^2$  value of 0.86 for image processed fat prediction (Table 8.6).

Table 8.4: Pearson Correlation coefficient (r) values among color and percentage fat (crude fat and image processed fat).

Variable	L*	a*	b*	Crude Fat (%)	Image Fat (%) (CIRCLED)
<b>n</b>	46	46	46	46	46
<b>L*</b>	1.00	-0.24	0.34	0.07	0.44
<b>a*</b>		1.00	0.73	0.68	0.26
<b>b</b>			1.00	0.57	0.41
<b>Crude Fat (%)</b>				1.00	0.76
<b>Image Fat (%) (CIRCLED)</b>					1.00

Table 8.5: Pearson Correlation probability (p) values among color and percentage fat (crude fat and image processed fat) with correlations highlighted in green for  $p < 0.05$ .

Variable	L*	a*	b*	Crude Fat (%)	Image Fat (%) (CIRCLED)
n	46	46	46	46	46
L*	0.0000	0.1016	0.0218	0.6439	0.0024
a*		0.0000	0.0000	0.0000	0.0816
b*			0.0000	0.0000	0.0052
Crude Fat (%)				0.0000	0.0000
Image Fat (%) (CIRCLED)					0.0000

Table 8.6: Mean calibration and validation  $R^2$  values with standard deviations (in parentheses) for prediction of image processed and chemically extracted crude fat for VIS and NIR reflectance.

VIS Spectroscopy		
Measurement	Calibration $R^2$ mean (SD)	Validation $R^2$ mean (SD)
Crude Fat	0.93 (0.00)	0.87 (0.01)
Image Processed Fat (CIRCLED)	0.86 (0.00)	0.69 (0.02)
NIR Spectroscopy		
Measurement	Calibration $R^2$ mean (SD)	Validation $R^2$ mean (SD)
Crude Fat	0.97 (0.00)	0.90 (0.01)
Image Processed Fat (CIRCLED)	0.97 (0.00)	0.86 (0.00)

## 8.5 Discussion

Image processed fat and crude fat percentage data had a wide range (Table 8.2) of values which strengthens  $R^2$  in PLS (reference). Although the focus of this study was to estimate image fat using VIS and NIR spectroscopy, image processed fat was only moderately related to the total extractable fat in the samples. For example, in a Canada A sample, the calculated image processed fat was 13.05% which was well above the mean crude fat content of the Canada A grade beef. After visual inspection of that sample surface, it was identified that the scanned area had a large piece of fat that increased the calculated fat using digital image processing. But the crude fat percentage of that same sample had normal fat percentage (close to the average crude fat percentage of Canada A samples). This clearly showed the potential for problems with the image processed fat calculation method.

Similarly, there appeared to be little discrimination chemically between Canada AA and AAA beef rib samples. Canada AAA samples had relatively higher crude fat percentage than Canada A and AA samples and Canada Prime samples had higher crude fat percentage range than Canada AAA samples which was as expected. However the Canada AAA and Canada Prime samples possessed the largest range of crude fat percentage (from 2.5% to 7% and 8% to 16%, respectively). These results provided evidence of the problem that the crude fat is not evenly distributed within the Canada beef grades or the grading assessment system used in the industry is not estimating crude fat accurately. The low correlation resulting from the regression of image fat on to crude fat would tend to support the latter conclusion.

In this experiment, VIS spectroscopy predicted crude fat with a mean calibration  $R^2$  of 0.93 and a mean validation  $R^2$  of 0.87 when dark current was not subtracted during data analysis. These results agreed with the results of our previous experiments (Section 4.4.5) where VIS

spectroscopy predicted crude fat with accuracy between 80 to 50% (calibration  $R^2$  of 0.95 to 0.85, validation  $R^2$  of 0.80 to 0.51). Results from experimentation in Section 6.4.4 showed that VIS spectroscopy predicted crude fat with 70% accuracy (calibration  $R^2$  of 0.85 and validation  $R^2$  of 0.70), but this beef had been frozen and thawed prior to measurement unlike the beef in this study. Freezing and thawing may have caused chemical and/or structural changes in the meat sample, as have been noted for Raman spectroscopy, the prediction power of which is improved by freezing and thawing (Fowler et al., 2014).

VIS spectroscopy predicted image processed fat within the precise region of measurement with calibration  $R^2$  values of 0.86 and validation  $R^2$  values of 0.69 in this experiment and results were very similar to those obtained in the first experiment (Section 4.4.5 of Chapter 4), which produced a mean calibration  $R^2$  value of 0.94 and a mean validation  $R^2$  value of 0.69. Again, freezing and thawing may have had an effect on the results from the experiment conducted in Section 6.4.4 of Chapter 6, as the CIRCLED image processed fat prediction produced a mean calibration  $R^2$  value of 0.74 and a mean validation  $R^2$  value of 0.58.

In the current study, NIR spectroscopy predicted crude fat with a mean calibration  $R^2$  value of 0.97 and a mean validation  $R^2$  values of 0.90. In NIR spectroscopy the dark current was not subtracted. Comparison of current results to previous NIR spectroscopy results without dark current subtracted showed that results of the present study were in agreement with those previous studies. The first experiment (Section 4.4.5 of Chapter 4) PLS analysis for crude fat obtained calibration  $R^2$  values of 0.96 and 0.99 and validation  $R^2$  values of 0.89 and 0.90. In experimentation with beef that had been frozen and then thawed (Section 6.4.4 of Chapter 6), crude fat prediction using PLS produced a mean calibration  $R^2$  value of 0.91 and a mean

validation  $R^2$  value of 0.78, suggesting that freezing and thawing may change the muscle elements detected by NIR spectroscopy as well.

For image processed fat, NIR spectroscopy produced unexpectedly high  $R^2$  values, as a mean calibration  $R^2$  value of 0.97 and mean validation  $R^2$  value of 0.86 were obtained in the present study. Previous experimentation (Section 4.4.5 of Chapter 4, first experiment) with NIR spectroscopy (no dark current subtracted) predicted image fat in the small measured region with a mean calibration  $R^2$  value of 0.96 and a mean validation  $R^2$  value of 0.65. The NIR spectroscopy (no dark current subtracted) predicted circled image processed fat in experimentation of Chapter 6, with a mean calibration  $R^2$  value of 0.87 and a mean validation  $R^2$  value of 0.68. Interestingly, the validation  $R^2$  value of the first experiment was close to the validation  $R^2$  value of frozen and thawed beef experiment, suggesting that freezing and thawing may not have a large impact on prediction of visible surface fat.

Why VIS spectroscopy predicted crude fat with greater accuracy than image fat is unclear, given the low penetration depth of the VIS light (Section 4.1 of Chapter 4). Interference of lean meat color should not be an issue in this difference, as the same meat samples were compared. The difference in prediction would only exist if the VIS light was detecting fat below the surface, because the relationship between image fat and crude fat was moderate at best, or if the image processing algorithm did not adequately capture all the visible fat on the surface of the beef. However, in this experiment the correlation between crude fat and  $L^*$  was not significant which was opposite to that found in experiments of Chapter 4 and Chapter 6. Similarly, a significant correlation existed between image processed fat and  $L^*$  value but this was the opposite to that found during experiment of Chapter 4. These results indicated that color affected the estimation of fat using VIS light spectroscopy more than we expected. As a result of this even multivariate

analysis was not able to predict fat contents at a consistent accuracy and reliably using VIS spectroscopy. The dramatic effect of color variation on VIS spectroscopy was not completely described by the multivariate PLS analysis. NIR spectroscopy on the other hand was not affected by meat color and was also expected to have a greater penetration capability than VIS light (Section 4.1 of Chapter 4). That NIR light had similar values for crude and image fat supported this expectation, and the high regression coefficient substantiates the development of NIR rather than VIS light technology for surface fat prediction in beef.

## **8.6 Conclusion**

VIS spectroscopy and NIR spectroscopy predicted crude fat with moderate  $R^2$  values and the prediction results were repeatable when compared to previous experiments with similar experimental designs. NIR spectroscopy was not affected by color of meat and predicted both crude and image fat similarly. NIR showed potential and needs to be investigated further for improved accuracy and formulation of a robust algorithm. Future analysis should combine all data collected from the current and previous experiments for greater statistical and predictive power than present in the current study.

## Chapter 9

### General Summary

The main objective of this research was to develop a system to predict beef quality attributes using light spectroscopy and image processing techniques. Simultaneously, a comparative study of various techniques used to assess beef quality, was conducted. Two major beef quality attributes that were taken into account in this study were beef marbling and/or fat content and cooked beef tenderness. In the beginning, eight preliminary experiments were conducted with eight different beef rib-eye steak purchased from local store. These experiments provided important experience and identified factors related to light spectroscopy that needed to be considered to predict fat content on the surface of beef. These experiments also provided the basic knowledge for the design, testing and validation of a handheld device to estimate fat content in beef. VIS light spectroscopy was used during these experiments. The increment of fat content on the meat surface was simulated using fat pieces cut from the inter-muscular fat that was attached to the purchased beef steaks. Results from these experiments showed a clear indication of linear correlation with slope of reflectivity at wavelengths ranging from 590 nm to 605 nm.

The design of a handheld device that would be able to use VIS light spectroscopy to predict fat content in meat was formulated. A prototype was built on a bread board and custom made microcontroller board was used in conjunction to test the design. The important subdivisions of the entire system were sensor unit, analog signal processing unit and digital processing and display unit. The prototype was tested during the experiments mentioned above and afterwards necessary up-grades were made to improve the performance of the system. The device sensor unit comprises of specifically selected LEDs for the wavelengths which were significant in

predicting fat and a photodiode. The analog unit was a multistage signal amplifier and a lock-in amplifier was used to reduce background noise and increase signal to noise ratio of the signal collected from the photodiode. The analog signal from the output stage of analog unit was converted to a digital signal using an 8 bit analog to digital converter and was processed by microcontroller of the digital processing unit. The results were displayed in the 16 x 2 segment LCD display. During the preliminary experiments with fat pieces, the results obtained from the handheld device were closely matched with the results obtained from the VIS light spectrometer.

An experiment was conducted using 48 samples comprised of 12 Canada A, 12 Canada AA, 12 Canada AAA and 12 Canada Prime grade beef rib muscles from a large Alberta abattoir to validate the algorithm formulated during preliminary experiment with fat pieces. Results of this experiment indicated that the algorithm failed to predict fat with significant correlation between crude fat or image processed fat. A possible cause for this failure was hypothesized to be that the lean meat color was the reason behind this failure. However, in the search for a new algorithm, partial least squares analysis was utilized to perform a regression analysis on the spectroscopic data in an attempt to predict crude fat. In this experiment, NIR light was used separately to check for the ability of NIR light spectroscopy in order to predict crude fat. VIS and NIR spectroscopy both predicted crude fat and image processed fat with moderate to high  $R^2$  values, however, NIR spectroscopy showed better potential than VIS light, most likely because NIR light was unaffected by meat color. A data transformation test using NIR spectroscopic data showed that dark current and smoothing coefficient higher or lower than 11 reduced the  $R^2$  values.

A paper model experiment was performed to investigate the failure of the previously found algorithm to predict fat content in meat using slope of reflectivity of VIS light spectroscopy. Meat surface characteristics cannot be fully simulated using the paper model but this study was

conducted to investigate the effect of color on VIS spectroscopy. This study also validated the experimental setup including the light source and the arrangement of the spectroscopic measurement and repeatability of the results. The hypothesis that the VIS light spectroscopy was affected by lean meat color was accepted, as the results identified that the VIS light spectroscopy actually interacted two dimensionally with various colored pigment on the meat surface and was measuring the absence of the colored pigment rather than the amount of surface fat. This needed to be addressed by a multivariate analysis in order to obtain an equation to predict fat that considered lean color and partial least square (PLS) regression analysis was able to explain 96% of the variation using the entire range of wavelengths. A four wavelength model was obtained which explained variation with 94% accuracy and the model was validated with 93% accuracy. The PLS analysis of VIS light spectroscopy was not only able to describe the amount of white in the paper model, but was able to describe the non-white region of the surface. This was crucial for the development of the prediction equation to estimate fat content in whole meat using visible light spectroscopy.

Spectroscopic technology to estimate chemical composition of meat has already been successfully commercialized for homogenized meat. An experiment was performed with the beef remaining from a previous experiment to reproduce results similar to other published results in the literature using homogenized meat. A comparative study between whole and homogenize meat was conducted during this experiment. The meat samples used in this study were frozen and thawed before the experiment. Because of this, the results obtained in this experiment cannot be fully compared with results obtained from fresh meat but a comparison between whole and homogenize meat were enough to validate the method. It was published that optical spectroscopy on homogenized meat had better prediction accuracy than whole meat and this was attempted to

be validated in this experiment. Optical spectroscopy was affected by overtone effect, so an optical filter was used to filter the light in order to avoid the overtone effect. VIS spectroscopy produced better results with whole meat but NIR spectroscopy produced better results with homogenized meat which was in accordance with the published results in literature. An interesting finding of this experiment was that two different rib-eye steaks from different position of same rib loin had crude fat that were 84% correlated. Image processed fat was also analyzed with VIS and NIR spectroscopic data. VIS light spectroscopy had higher  $R^2$  value with circled image region and NIR light had higher  $R^2$  value with whole image region. Another interesting finding was that dark current subtraction had random effect on the statistical analysis. Dark current subtraction could increase or decrease the  $R^2$  values randomly.

Prediction ability of NIR light spectroscopy with and without a polarizer was tested in order to predict meat tenderness was investigated in the next experiment. Various temperature treatment and electrical stimulation was applied to achieve tenderness variation in the samples. PLS analysis results indicated that polarized light with a polarizer grating parallel to muscle fiber direction and polarized light with polarizer grating perpendicular to muscle fiber had better prediction accuracy than non-polarized light for days 3 and 14 post mortem measurements. Day 3 postmortem NIR measurement predicted day 14 postmortem shear force with better accuracy using polarized light of polarizer grating perpendicular to muscle fiber than polarized light of polarizer grating parallel to muscle fiber. Increased prediction accuracy of NIR spectroscopy to predict shear force by introducing polarizer was an important discovery of this study.

A validation experiment was conducted with similar experimental setup that was used in the first experiment. The results from this experiment suggested that the VIS light prediction accuracy in order to predict fat content in whole meat was affected by meat color and may pose

some reliability issue. NIR light spectroscopy achieved identical results compare to results found in the first experiment. It was also realized that image processing was a better choice to predict fat content in whole meat in compare to VIS light spectroscopy but NIR light spectroscopy produced even better results than image processing. Being immune to meat color and having greater penetration depth than visible light, the NIR light spectroscopy showed true potential in order to predict fat content in whole meat.

Estimation of meat quality using optical spectroscopy is widely used in commercial equipment and much research has been conducted on this. However there were important differences in the experimental setups and methods among published studies and the work described in this thesis. The uniqueness of this thesis is that reflectivity or normalized reflectance was used instead of absorbance which was commonly used in most meat spectroscopy research. Normalization is important as this referenced the collected reflectance to a fixed standard and this help to reduce that effect of instrumental changes and environmental changes over time. In some literature this was either not mentioned or not explained properly as to how the normalization or referencing was performed. In this study normalization was performed using reflectance data from a white Teflon<sup>TM</sup> disk as a reference for the reflectance data from the actual sample. An experiment using paper models to investigate the effect of meat color on VIS spectroscopy was unique to this study. Statistical analysis in order to predict image processed fat using optical spectroscopy was not performed in previous published studies and this was unique to this study. Increased prediction accuracy in order to predict meat tenderness using polarizer was an important and unique discovery. Polarization had not been utilized in previous studies as in this study. Utilization of an optical filter in an effort to reduce overtone effect in the optical spectroscopy was not utilized in previous studies. Finally, the concept and design of the handheld

device to estimate various meat qualities attributes utilizing the principle of optical spectroscopy was a novel idea of this research.

In the course of the entire thesis, a cycle consisting of understanding the experimental system and improvement over the previous system was constantly followed at each step in a constantly evolving process. The objective being to achieve a most possible accuracy and optimum performance of the experimental system such an approach was taken. However it was given great importance that certain fundamental parameters and experimental setup remains constant in order to compare the experimental results to each other.

There were areas that can be improved in the future continuation of this study. A more robust and more complex lock-in amplifier or a DSP based digital lock-in amplifier should be used in the next design of the handheld device. This would be able to improve the noise immunity of the device and also increase the signal to noise ratio. The digital to analog converter used in this design had 10 bit resolution and that should be increased to at least 16 bit. Higher intensity LED or a high intensity wide band light combined with specific band pass optical filter combination can be utilized in the sensor unit for better performance of the device. Lithium ion battery instead of rechargeable metal-hydride battery would help extend the operation time and simultaneously lower the weight of the device. A high precision distance measuring sensor need to be used in order to achieve a constant optical height from the measurement surface. This would greatly improve the accuracy of the measurement both the device and the spectrometer. A spectrometer with entire range would be helpful to find other wavelengths that may improve the prediction accuracy. Increased number of samples could help make a robust prediction equation. In the PLS analysis each wavelength was selected manually based on higher correlation coefficients. This can be done using a computer program more effectively and quickly. Various noise reduction

techniques mentioned in the literature should be tested in an attempt to improve the  $R^2$  values. Also, a ceramic disk can also be tested as a reference for normalization instead of Teflon<sup>TM</sup> sheet to check for any performance improvement of the entire system.



```

#define ADC_VREF_TYPE 0x40

// Read the ADC conversion result
unsigned int read_adc(unsigned char adc_input)
{
    ADMUX=adc_input | (ADC_VREF_TYPE & 0xff);
    // Delay needed for the stabilization of the ADC input voltage
    delay_us(10);
    // Start the AD conversion
    ADCSRA|=0x40;
    // Wait for the AD conversion to complete
    while ((ADCSRA & 0x10)==0);
    ADCSRA|=0x10;
    return ADCW;
}

// Declare your global variables here
char buf[10];
unsigned int interval=0,counter=0,ch_adc=6;
float Refl_L1=0.0,Refl_L2=0.0,Refl_L3=0.0,Refl_L4=0.0,Refl_L5=0.0,data_adc=0.0;

void main(void)
{
    // Declare your local variables here
    interval=100;
    SW_ent=1;

    // Input/Output Ports initialization
    // Port A initialization
    // Func7=In Func6=In Func5=In Func4=Out Func3=Out Func2=Out Func1=Out Func0=Out
    // State7=T State6=T State5=T State4=0 State3=0 State2=0 State1=0 State0=0
    PORTA=0x00;
    DDRA=0x1F;

    // Port B initialization
    // Func7=In Func6=In Func5=In Func4=In Func3=In Func2=In Func1=In Func0=In
    // State7=T State6=T State5=T State4=T State3=T State2=T State1=T State0=T
    PORTB=0x00;
    DDRB=0x00;

    // Port C initialization
    // Func7=In Func6=In Func5=In Func4=In Func3=In Func2=In Func1=In Func0=In
    // State7=P State6=T State5=T State4=T State3=T State2=T State1=T State0=T
    PORTC=0x80;
    DDRC=0x00;
}

```

```

// Port D initialization
// Func7=Out Func6=In Func5=In Func4=Out Func3=In Func2=In Func1=In Func0=In
// State7=0 State6=T State5=T State4=0 State3=T State2=T State1=T State0=T
PORTD=0x00;
DDRD=0x90;

// Timer/Counter 0 initialization
// Clock source: System Clock
// Clock value: Timer 0 Stopped
// Mode: Normal top=FFh
// OC0 output: Disconnected
TCCR0=0x00;
TCNT0=0x00;
OCR0=0x00;

// Timer/Counter 1 initialization
// Clock source: System Clock
// Clock value: 2000.000 kHz
// Mode: Fast PWM top=ICR1
// OC1A output: Discon.
// OC1B output: Non-Inv.
// Noise Canceler: Off
// Input Capture on Falling Edge
// Timer1 Overflow Interrupt: Off
// Input Capture Interrupt: Off
// Compare A Match Interrupt: Off
// Compare B Match Interrupt: Off
TCCR1A=0x22;
TCCR1B=0x1A;
TCNT1H=0x00;
TCNT1L=0x00;
ICR1H=0x7F;
ICR1L=0xFF;
OCR1AH=0x00;
OCR1AL=0x00;
OCR1BH=0x11;
OCR1BL=0x68;

// Timer/Counter 2 initialization
// Clock source: System Clock
// Clock value: 500.000 kHz
// Mode: Phase correct PWM top=FFh
// OC2 output: Non-Inverted PWM
ASSR=0x00;
TCCR2=0x63;

```

```

TCNT2=0x00;
OCR2=0x7F;

// External Interrupt(s) initialization
// INT0: Off
// INT1: Off
// INT2: Off
MCUCR=0x00;
MCUCSR=0x00;

// Timer(s)/Counter(s) Interrupt(s) initialization
TIMSK=0x00;

// Analog Comparator initialization
// Analog Comparator: Off
// Analog Comparator Input Capture by Timer/Counter 1: Off
ACSR=0x80;
SFIOR=0x00;

// ADC initialization
// ADC Clock frequency: 1000.000 kHz
// ADC Voltage Reference: AVCC pin
ADMUX=ADC_VREF_TYPE & 0xff;
ADCSRA=0x84;

// LCD module initialization
lcd_init(20);

while (1)
{
// Place your code here
//Set servo position to bring LED_L1 in front of photodiode
LED_L1=0;
LED_L2=0;
LED_L3=0;
LED_L4=0;
LED_L5=0;
OCR1B=4192;
delay_ms(200);
// Switch On LED_L1, print LED wavelength and acquire data from ADC
LED_L1=1;
LED_L2=0;
LED_L3=0;
LED_L4=0;
LED_L5=0;
lcd_gotoxy(0,3);
}

```

```

lcd_putsf("L1 592nm  ");
delay_ms(interval);
for(counter=0;counter<2000;counter++)
{
    data_adc=read_adc(ch_adc);
    Refl_L1=Refl_L1+data_adc;
}
Refl_L1=Refl_L1/counter;

//If SW-ent is pressed the program will pause until release
if(SW_ent==0)while(SW_ent==0);

// Set servo position to bring LED_L2 in front of photodiode
LED_L1=0;
LED_L2=0;
LED_L3=0;
LED_L4=0;
LED_L5=0;
OCR1B=3640;
delay_ms(50);
// Switch On LED_L2, print LED wavelength and acquire data from ADC
LED_L1=0;
LED_L2=1;
LED_L3=0;
LED_L4=0;
LED_L5=0;
lcd_gotoxy(0,3);
lcd_putsf("L2 593nm  ");
delay_ms(interval);
for(counter=0;counter<2000;counter++)
{
    data_adc=read_adc(ch_adc);
    Refl_L2=Refl_L2+data_adc;
}
Refl_L2=Refl_L2/counter;
if(SW_ent==0)while(SW_ent==0);

// Set servo position to bring LED_L3 in front of photodiode
LED_L1=0;
LED_L2=0;
LED_L3=0;
LED_L4=0;
LED_L5=0;
OCR1B=3073;
delay_ms(50);

```

```

// Switch On LED_L3, print LED wavelength and acquire data from ADC
LED_L1=0;
LED_L2=0;
LED_L3=1;
LED_L4=0;
LED_L5=0;
lcd_gotoxy(0,3);
lcd_putsf("L3 595nm... ");
delay_ms(interval);
for(counter=0;counter<2000;counter++)
{
    data_adc=read_adc(ch_adc);
    Refl_L3=Refl_L3+data_adc;
}
Refl_L3=Refl_L3/counter;
if(SW_ent==0)while(SW_ent==0);

// Set servo position to bring LED_L4 in front of photodiode
LED_L1=0;
LED_L2=0;
LED_L3=0;
LED_L4=1;
LED_L5=0;
OCR1B=2515;
delay_ms(50);
// Switch On LED_L4, print LED wavelength and acquire data from ADC
LED_L1=0;
LED_L2=0;
LED_L3=0;
LED_L4=1;
LED_L5=0;
lcd_gotoxy(0,3);
lcd_putsf("L4 601nm ");
delay_ms(interval);
for(counter=0;counter<2000;counter++)
{
    data_adc=read_adc(ch_adc);
    Refl_L4=Refl_L4+data_adc;
}
Refl_L4=Refl_L4/counter;
if(SW_ent==0)while(SW_ent==0);

// Set servo position to bring LED_L5 in front of photodiode
LED_L1=0;

```

```

LED_L2=0;
LED_L3=0;
LED_L4=0;
LED_L5=0;
OCR1B=1940;
delay_ms(50);
// Switch On LED_L5, print LED wavelength and acquire data from ADC
LED_L1=0;
LED_L2=0;
LED_L3=0;
LED_L4=0;
LED_L5=1;
lcd_gotoxy(0,3);
lcd_putsf("L5 605nm  ");
delay_ms(interval);
for(counter=0;counter<2000;counter++)
{
    data_adc=read_adc(ch_adc);
    Refl_L5=Refl_L5+data_adc;
}
Refl_L5=Refl_L5/counter;
if(SW_ent==0)while(SW_ent==0);

```

```

lcd_gotoxy(0,0);
lcd_clear();
lcd_putsf("L1=");
Refl_L1=(Refl_L1);
ftoa(Refl_L1,2,buf);
lcd_puts(buf);

```

```

lcd_putsf(" L2=");
Refl_L2=(Refl_L2);
ftoa(Refl_L2,2,buf);
lcd_puts(buf);

```

```

lcd_gotoxy(0,1);
lcd_putsf("L3=");
Refl_L3=(Refl_L3);
ftoa(Refl_L3,2,buf);
lcd_puts(buf);

```

```

lcd_putsf(" L4=");
Refl_L4=(Refl_L4);
ftoa(Refl_L4,2,buf);
lcd_puts(buf);

```

```
    lcd_gotoxy(0,2);  
    lcd_putsf("L5=");  
    Refl_L5=(Refl_L5);  
    ftoa(Refl_L5,2,buf);  
    lcd_puts(buf);  
  
};  
}
```

## Appendix B: Programs for VIS, NIR, and LED Spectroscopy

```
% program to calculate and plot VIS spectroscopy data%

%Clear MATLAB program memory and clear output window
clear;
clc;

%Acquire VIS reflectance data from Excel files
lamda = xlsread('experiment 25_11_10.xlsx', 1, 'A4:A3651');
I_dark = xlsread('experiment 25_11_10.xlsx', 1, 'B4:B3651');
I_white = xlsread('experiment 25_11_10.xlsx', 1, 'AL4:AL3651');
I_fat0pc = xlsread('experiment 25_11_10.xlsx', 1, 'E4:E3651');
I_fat1pc = xlsread('experiment 25_11_10.xlsx', 1, 'H4:H3651');
I_fat2pc = xlsread('experiment 25_11_10.xlsx', 1, 'K4:K3651');
I_fat3pc = xlsread('experiment 25_11_10.xlsx', 1, 'N4:N3651');
I_fat4pc = xlsread('experiment 25_11_10.xlsx', 1, 'Q4:Q3651');
I_fat5pc = xlsread('experiment 25_11_10.xlsx', 1, 'T4:T3651');

%Set smoothing coefficient value
smoothing_coef=51;

%Apply smoothing on the reflectance data
I_darkf = smooth(I_dark,smoothing_coef);
I_whitef = smooth(I_white,smoothing_coef);
I_fat0pcf = smooth(I_fat0pc,smoothing_coef);
I_fat1pcf = smooth(I_fat1pc,smoothing_coef);
I_fat2pcf = smooth(I_fat2pc,smoothing_coef);
I_fat3pcf = smooth(I_fat3pc,smoothing_coef);
I_fat4pcf = smooth(I_fat4pc,smoothing_coef);
I_fat5pcf = smooth(I_fat5pc,smoothing_coef);

%Calculate reflectivity after subtraction of dark current and multiply with
%100 to obtain percentage reflectivity.
Rf0 = ((I_fat0pcf-I_darkf)./(I_whitef-I_darkf))*100;
Rf1 = ((I_fat1pcf-I_darkf)./(I_whitef-I_darkf))*100;
Rf2 = ((I_fat2pcf-I_darkf)./(I_whitef-I_darkf))*100;
Rf3 = ((I_fat3pcf-I_darkf)./(I_whitef-I_darkf))*100;
Rf4 = ((I_fat4pcf-I_darkf)./(I_whitef-I_darkf))*100;
Rf5 = ((I_fat5pcf-I_darkf)./(I_whitef-I_darkf))*100;

%Plot reflectivity as a function of wavelength
plot
(lamda,Rf0,'r',lamda,Rf1,'g',lamda,Rf2,'b',lamda,Rf3,'c',lamda,Rf4,'m',lamda,
Rf5,'k');
xlim([450 800]);
xlabel('Wavelength (nm)','fontsize',30,'fontweight','b','fontname','Times New
Roman');
ylabel('Reflectivity (%)','fontsize',30,'fontweight','b','fontname','Times
New Roman');
legend('Rf 0','Rf 1','Rf 2','Rf 3','Rf 4','Rf 5');
```

```

set(gca, 'XTick', 450:50:800, 'fontsize', 24, 'fontweight', 'b', 'fontname', 'Times
New Roman');
grid off;

%Calculate slope of reflectivity by using dR/dlamda
m0 = diff(Rf0)./diff(lamda);
m1 = diff(Rf1)./diff(lamda);
m2 = diff(Rf2)./diff(lamda);
m3 = diff(Rf3)./diff(lamda);
m4 = diff(Rf4)./diff(lamda);
m5 = diff(Rf5)./diff(lamda);

%Apply smoothing on slope of reflectivity
mf0 = smooth(m0, smoothing_coef);
mf1 = smooth(m1, smoothing_coef);
mf2 = smooth(m2, smoothing_coef);
mf3 = smooth(m3, smoothing_coef);
mf4 = smooth(m4, smoothing_coef);
mf5 = smooth(m5, smoothing_coef);

%Obtain new wavelength range for slope of reflectivity data
lamda1 = ones(3647,1);
for i=1:1:3647
    lamda1(i) = lamda(i);
end

%Plot slope of reflectivity as a function of wavelength
plot(lamda1, mf0, 'r');
hold on
plot(lamda1, mf1, 'g');
plot(lamda1, mf2, 'b');
plot(lamda1, mf3, 'c');
plot(lamda1, mf4, 'm');
plot(lamda1, mf5, 'k');
hold off
xlim([585 615]);
ylim([0 1.2]);
xlabel('Wavelength (nm)', 'fontsize', 30, 'fontweight', 'b', 'fontname', 'Times New
Roman');
ylabel('Slope of
Reflectivity', 'fontsize', 30, 'fontweight', 'b', 'fontname', 'Times New Roman');
legend('m 0', 'm 1', 'm 2', 'm 3', 'm 4', 'm 5');
set(gca, 'XTick', 585:5:615, 'fontsize', 24, 'fontweight', 'b', 'fontname', 'Times
New Roman');
set(gca, 'YTick', 0:0.2:1.2, 'fontsize', 24, 'fontweight', 'b', 'fontname', 'Times
New Roman');

%Create a temporary matrix of important wavelengths and there corresponding
%indexes
lamda_val_mat = [588.09 590.14 592.19 593.01 595.05 597.09 600.16 601.99
603.01 605.05 607.08 610.13 612.17];
axis_value_mat = [1139 1149 1159 1163 1173 1183 1198 1207 1212 1222 1232 1247
1257];

%Select important wavelength to plot using "switch case" method
set_lamda = 605.05;

```

```

switch set_lamda
    case 588.09
        axis_value = 1;
    case 590.14
        axis_value = 2;
    case 592.19
        axis_value = 3;
    case 593.01
        axis_value = 4;
    case 595.05
        axis_value = 5;
    case 597.09
        axis_value = 6;
    case 600.16
        axis_value = 7;
    case 601.99
        axis_value = 8;
    case 603.01
        axis_value = 9;
    case 605.05
        axis_value = 10;
    case 607.08
        axis_value = 11;
    case 610.13
        axis_value = 12;
    case 612.17
        axis_value = 13;
    otherwise
        axis_value = 4;
        set_lamda = 593.01;
end

%Obtain slope of reflectivity values of different pieces of fat at the
%selected wavelength
m_fat(1) = mf0(axis_value_mat(axis_value));
m_fat(2) = mf1(axis_value_mat(axis_value));
m_fat(3) = mf2(axis_value_mat(axis_value));
m_fat(4) = mf3(axis_value_mat(axis_value));
m_fat(5) = mf4(axis_value_mat(axis_value));
m_fat(6) = mf5(axis_value_mat(axis_value));

%Create a matrix of different number of fat pieces
fat(1)= 0;
fat(2)= 1;
fat(3)= 2;
fat(4)= 3;
fat(5)= 4;
fat(6)= 5;

%Linear regression analysis of slope of reflectivity and number of fat pieces
stats = regstats(m_fat,fat,'linear');
yhat = stats.yhat;
strrsqr = num2str(stats.rsquare);

```

```

%Plot slope of reflectivity as a function of number of fat pieces along
%with linear regression line plot
plot(fat,m_fat,'o', fat,yhat,'--k');
hold on;
xlabel('Number of Fat Pcs.','fontsize',30,'fontweight','b','fontname','Times
New Roman');
ylabel('Slope of
Reflectivity','fontsize',30,'fontweight','b','fontname','Times New Roman');
legend('Slope of Reflectivity at 605.05 nm');
set(gca,'XTick',-1:1:6,'fontsize',30,'fontweight','b','fontname','Times New
Roman');
set(gca,'YTick',0.3:0.1:0.7,'fontsize',30,'fontweight','b','fontname','Times
New Roman');
text(3,m_fat(3),['\bf\fontsize{30}\fontname{Times New Roman} R^2 = '
strrsqr],'HorizontalAlignment','left');
xlim([-1 6]);
ylim([0.3 0.7]);
hold off;
%End of program

```

```

%MATLAB program to calculate and plot LED spectroscopy data%

%Clear MATLAB program memory and clear output window
Clear;
CLC;

%Acquire LED reflectance data from Excel files
lamda_led = xlsread('experiment 25_11_10.xlsx', 1, 'AN4:AN6');
I_white = xlsread('experiment 25_11_10.xlsx', 1, 'AM4:AM6');
I_fat0pc = xlsread('experiment 25_11_10.xlsx', 1, 'F4:F6');
I_fat1pc = xlsread('experiment 25_11_10.xlsx', 1, 'I4:I6');
I_fat2pc = xlsread('experiment 25_11_10.xlsx', 1, 'L4:L6');
I_fat3pc = xlsread('experiment 25_11_10.xlsx', 1, 'O4:O6');
I_fat4pc = xlsread('experiment 25_11_10.xlsx', 1, 'R4:R6');
I_fat5pc = xlsread('experiment 25_11_10.xlsx', 1, 'U4:U6');

%Calculate reflectivity and multiply with 100 to obtain percentage
%reflectivity.
Rf0 = (I_fat0pc./I_white)*100;
Rf1 = (I_fat1pc./I_white)*100;
Rf2 = (I_fat2pc./I_white)*100;
Rf3 = (I_fat3pc./I_white)*100;
Rf4 = (I_fat4pc./I_white)*100;
Rf5 = (I_fat5pc./I_white)*100;

%Plot reflectivity as a function of wavelength
plot
(lamda_led,Rf0,'r',lamda_led,Rf1,'g',lamda_led,Rf2,'b',lamda_led,Rf3,'c',lamda_led,Rf4,'m',lamda_led,Rf5,'y');
xlim([585 610]);
xlabel('lamda LED'), ylabel('Reflectivity');
legend('Rf0','Rf1','Rf2','Rf3','Rf4','Rf5');
grid on;

%Calculate slope of reflectivity by using dR/dlamda
m0 = diff(Rf0)./diff(lamda_led);
m1 = diff(Rf1)./diff(lamda_led);
m2 = diff(Rf2)./diff(lamda_led);
m3 = diff(Rf3)./diff(lamda_led);
m4 = diff(Rf4)./diff(lamda_led);
m5 = diff(Rf5)./diff(lamda_led);

%Obtain new wavelength range for slope of reflectivity data
lamda_led1 = ones(2,1);
for i=1:1:2
    lamda_led1(i)= lamda_led(i);
end

%Plot slope of reflectivity as a function of wavelength
plot(lamda_led1,m0,'r');
hold on
plot(lamda_led1,m1,'g');
plot(lamda_led1,m2,'b');
plot(lamda_led1,m3,'c');

```

```

plot(lamda_led1,m4,'m');
plot(lamda_led1,m5,'y');
hold off
xlim([585 595]);
xlabel('lamda LED'), ylabel('Slope');
legend('Rf0', 'Rf1', 'Rf2', 'Rf3', 'Rf4', 'Rf5');
grid on;

%Select an important wavelength to plot
WL_pointer = 2;
%WL_pointer = 1 for 588 nm; WL_pointer = 2 for 593 nm

%Obtain slope of reflectivity values of diferent pieces of fat at the
%selected wavelength
m_fat(1) = m0(WL_pointer);
m_fat(2) = m1(WL_pointer);
m_fat(3) = m2(WL_pointer);
m_fat(4) = m3(WL_pointer);
m_fat(5) = m4(WL_pointer);
m_fat(6) = m5(WL_pointer);

%Create a matrix of different number of fat pices
fat(1)= 0;
fat(2)= 1;
fat(3)= 2;
fat(4)= 3;
fat(5)= 4;
fat(6)= 5;

%Linear regression analysis of slope of reflectivity and number of fat
%pieces
stats = regstats(m_fat,fat,'linear');
yhat = stats.yhat;
strrsqr = num2str(stats.rsquare);

%Plot slope of reflectivity as a function of number of fat pieces along
%with linear regression line plot
plot(fat,m_fat,'o', fat,yhat,'--k');
hold on;
xlabel('Number of Fat Pcs.','fontsize',30,'fontweight','b','fontname','Times
New Roman');
ylabel('Slope of
Reflectivity','fontsize',30,'fontweight','b','fontname','Times New Roman');
legend('Slope of Reflectivity at 593 nm (LED)');
set(gca,'XTick',-1:1:6,'fontsize',30,'fontweight','b','fontname','Times New
Roman');
set(gca,'YTick',0.55:0.02:0.65,'fontsize',30,'fontweight','b','fontname','Tim
es New Roman');
text(2.5,m_fat(3),['\bf\fontsize{30}\fontname{Times New Roman} R^2 = '
strrsqr],'HorizontalAlignment','left');
xlim([-1 6]);
ylim([0.55 0.65]);
%End of program
%MATLAB program to calculate and plot NIR spectroscopy data%

%Clear MATLAB program memory and clear output window

```

```

clear;
clc;

%Acquire NIR reflectance data from Excel files
lamda_led = xlsread('Pure_fat.CSV', 1, 'A30:A11030');
I_Pure_fat = xlsread('Pure_fat.CSV', 1, 'B30:B11030');
I_lean_meat = xlsread('lean_meat.CSV', 1, 'B30:B11030');
I_fat1pc = xlsread('fat_1Pcs.CSV', 1, 'B30:B11030');
I_fat2pc = xlsread('fat_2Pcs.CSV', 1, 'B30:B11030');
I_fat3pc = xlsread('fat_3Pcs.CSV', 1, 'B30:B11030');
I_fat4pc = xlsread('fat_4Pcs.CSV', 1, 'B30:B11030');
I_fat5pc = xlsread('fat_5Pcs.CSV', 1, 'B30:B11030');
I_fat6pc = xlsread('fat_6Pcs.CSV', 1, 'B30:B11030');
I_fat7pc = xlsread('fat_7Pcs.CSV', 1, 'B30:B11030');
I_fat8pc = xlsread('fat_8Pcs.CSV', 1, 'B30:B11030');
I_fat9pc = xlsread('fat_9Pcs.CSV', 1, 'B30:B11030');
I_fat10pc = xlsread('fat_10Pcs.CSV', 1, 'B30:B11030');

%Set smoothing coefficient value
smoothing_coef=300;

%Apply smoothing on the reflectance data
I_Pure_fatf = smooth(I_Pure_fat,smoothing_coef);
I_lean_meatf = smooth(I_lean_meat,smoothing_coef);
I_fat1pcf = smooth(I_fat1pc,smoothing_coef);
I_fat2pcf = smooth(I_fat2pc,smoothing_coef);
I_fat3pcf = smooth(I_fat3pc,smoothing_coef);
I_fat4pcf = smooth(I_fat4pc,smoothing_coef);
I_fat5pcf = smooth(I_fat5pc,smoothing_coef);
I_fat6pcf = smooth(I_fat6pc,smoothing_coef);
I_fat7pcf = smooth(I_fat7pc,smoothing_coef);
I_fat8pcf = smooth(I_fat8pc,smoothing_coef);
I_fat9pcf = smooth(I_fat9pc,smoothing_coef);
I_fat10pcf = smooth(I_fat10pc,smoothing_coef);

%Plot reflectance intensity as a function of wavelength
plot
(lamda_led,I_lean_meatf,'r',lamda_led,I_fat1pcf,'g',lamda_led,I_fat2pcf,'b',l
amda_led,I_fat3pcf,'c',lamda_led,I_fat4pcf,'m',lamda_led,I_fat5pcf,'k',lamda_
led,I_fat6pcf,'--r',lamda_led,I_fat7pcf,'--g',lamda_led,I_fat8pcf,'--
b',lamda_led,I_fat9pcf,'--c',lamda_led,I_fat10pcf,'--m');
xlim([1100 1500]);
xlabel('Wavelength (nm)','fontsize',30,'fontweight','b','fontname','Times New
Roman');
ylabel('Intensity (counts)','fontsize',30,'fontweight','b','fontname','Times
New Roman');
legend('Int 0','Int 1','Int 2','Int 3','Int 4','Int 5','Int 6','Int 7','Int
8','Int 9','Int 10');
set(gca,'XTick',1100:50:1500,'fontsize',20,'fontweight','b','fontname','Times
New Roman');
grid off;
%End of program

%MATLAB program for Experiment performed on 17/11/10%

%Clear MATLAB program memory and clear output window

```

```

clear;
clc;

%Acquire VIS reflectance data from Excel files
lamda = xlsread('experiment12_11_2010.xlsx', 1, 'A4:A3651');
I_dark = xlsread('experiment12_11_2010.xlsx', 1, 'B4:B3651');
I_white = xlsread('experiment12_11_2010.xlsx', 1, 'BP4:BP3651');
I_fat0pc = xlsread('experiment12_11_2010.xlsx', 1, 'E4:E3651');
I_fat1pc = xlsread('experiment12_11_2010.xlsx', 1, 'H4:H3651');
I_fat2pc = xlsread('experiment12_11_2010.xlsx', 1, 'K4:K3651');
I_fat3pc = xlsread('experiment12_11_2010.xlsx', 1, 'N4:N3651');
I_fat4pc = xlsread('experiment12_11_2010.xlsx', 1, 'Q4:Q3651');
I_fat5pc = xlsread('experiment12_11_2010.xlsx', 1, 'T4:T3651');

%Acquire LED reflectance data from Excel files
I_leddark = xlsread('experiment_led17_11_2010.xlsx', 1, 'B4:B3651');
I_led605 = xlsread('experiment_led17_11_2010.xlsx', 1, 'E4:E3651');
I_led593 = xlsread('experiment_led17_11_2010.xlsx', 1, 'H4:H3651');
I_led588 = xlsread('experiment_led17_11_2010.xlsx', 1, 'K4:K3651');

%Apply smoothing on the VIS reflectance data
I_darkf = smooth(I_dark,51);
I_whitef = smooth(I_white,51);
I_fat0pcf = smooth(I_fat0pc,51);
I_fat1pcf = smooth(I_fat1pc,51);
I_fat2pcf = smooth(I_fat2pc,51);
I_fat3pcf = smooth(I_fat3pc,51);
I_fat4pcf = smooth(I_fat4pc,51);
I_fat5pcf = smooth(I_fat5pc,51);

%Apply smoothing on the LED reflectance data
I_leddarkf = smooth(I_leddark,11);
I_led588f = smooth(I_led588,11);
I_led593f = smooth(I_led593,11);
I_led605f = smooth(I_led605,11);

%Calculate normalized LED spectrum
I_led588fn = abs((I_led588f-I_leddarkf)/max(I_led588f-I_leddarkf));
I_led593fn = abs((I_led593f-I_leddarkf)/max(I_led593f-I_leddarkf));
I_led605fn = abs((I_led605f-I_leddarkf)/max(I_led605f-I_leddarkf));

%Calculate reflectivity after subtraction of dark current using integration
%method and multiply with 100 to obtain percentage reflectivity
Rf0(1) = (trapz(lamda, ((I_fat0pcf-
I_darkf).*I_led588fn))/trapz(lamda, ((I_whitef-I_darkf).*I_led588fn))*100;
Rf0(2) = (trapz(lamda, ((I_fat0pcf-
I_darkf).*I_led593fn))/trapz(lamda, ((I_whitef-I_darkf).*I_led593fn))*100;
Rf0(3) = (trapz(lamda, ((I_fat0pcf-
I_darkf).*I_led605fn))/trapz(lamda, ((I_whitef-I_darkf).*I_led605fn))*100;
Rf1(1) = (trapz(lamda, ((I_fat1pcf-
I_darkf).*I_led588fn))/trapz(lamda, ((I_whitef-I_darkf).*I_led588fn))*100;
Rf1(2) = (trapz(lamda, ((I_fat1pcf-
I_darkf).*I_led593fn))/trapz(lamda, ((I_whitef-I_darkf).*I_led593fn))*100;
Rf1(3) = (trapz(lamda, ((I_fat1pcf-
I_darkf).*I_led605fn))/trapz(lamda, ((I_whitef-I_darkf).*I_led605fn))*100;

```

```

Rf2(1) = (trapez(lamda, ((I_fat2pcf-
I_darkf).*I_led588fn))/trapez(lamda, ((I_whitef-I_darkf).*I_led588fn))*100;
Rf2(2) = (trapez(lamda, ((I_fat2pcf-
I_darkf).*I_led593fn))/trapez(lamda, ((I_whitef-I_darkf).*I_led593fn))*100;
Rf2(3) = (trapez(lamda, ((I_fat2pcf-
I_darkf).*I_led605fn))/trapez(lamda, ((I_whitef-I_darkf).*I_led605fn))*100;
Rf3(1) = (trapez(lamda, ((I_fat3pcf-
I_darkf).*I_led588fn))/trapez(lamda, ((I_whitef-I_darkf).*I_led588fn))*100;
Rf3(2) = (trapez(lamda, ((I_fat3pcf-
I_darkf).*I_led593fn))/trapez(lamda, ((I_whitef-I_darkf).*I_led593fn))*100;
Rf3(3) = (trapez(lamda, ((I_fat3pcf-
I_darkf).*I_led605fn))/trapez(lamda, ((I_whitef-I_darkf).*I_led605fn))*100;
Rf4(1) = (trapez(lamda, ((I_fat4pcf-
I_darkf).*I_led588fn))/trapez(lamda, ((I_whitef-I_darkf).*I_led588fn))*100;
Rf4(2) = (trapez(lamda, ((I_fat4pcf-
I_darkf).*I_led593fn))/trapez(lamda, ((I_whitef-I_darkf).*I_led593fn))*100;
Rf4(3) = (trapez(lamda, ((I_fat4pcf-
I_darkf).*I_led605fn))/trapez(lamda, ((I_whitef-I_darkf).*I_led605fn))*100;
Rf5(1) = (trapez(lamda, ((I_fat5pcf-
I_darkf).*I_led588fn))/trapez(lamda, ((I_whitef-I_darkf).*I_led588fn))*100;
Rf5(2) = (trapez(lamda, ((I_fat5pcf-
I_darkf).*I_led593fn))/trapez(lamda, ((I_whitef-I_darkf).*I_led593fn))*100;
Rf5(3) = (trapez(lamda, ((I_fat5pcf-
I_darkf).*I_led605fn))/trapez(lamda, ((I_whitef-I_darkf).*I_led605fn))*100;

%Plot filtered LED reflectance as a function of wavelength
plot (lamda,I_led588f,lamda,I_led593f,lamda,I_led605f);
xlabel('Wavelength (nm)', 'fontsize', 30, 'fontweight', 'b', 'fontname', 'Times New
Roman');
ylabel('Intensity (counts)', 'fontsize', 30, 'fontweight', 'b', 'fontname', 'Times
New Roman');
legend('Spectrum of 588 nm LED', 'Spectrum of 593 nm LED', 'Spectrum of 605 nm
LED');
set(gca, 'XTick', 500:20:700, 'fontsize', 30, 'fontweight', 'b', 'fontname', 'Times
New Roman');
xlim([500 700]);

%Plot normalized LED reflectance in terms of percentage as a function of
wavelength
plot (lamda, (I_led588fn*100), lamda, (I_led593fn*100), lamda, (I_led605fn*100));
xlabel('Wavelength (nm)', 'fontsize', 30, 'fontweight', 'b', 'fontname', 'Times New
Roman');
ylabel('Normalized Intensity
(%)', 'fontsize', 30, 'fontweight', 'b', 'fontname', 'Times New Roman');
legend('Spectrum of 588 nm LED', 'Spectrum of 593 nm LED', 'Spectrum of 605 nm
LED');
set(gca, 'XTick', 500:20:700, 'fontsize', 30, 'fontweight', 'b', 'fontname', 'Times
New Roman');
xlim([500 700]);
ylim([0 150]);

%Create LED wavelength matrix
lamda_led(1)= 588;
lamda_led(2)= 593;
lamda_led(3)= 605;

```

```

%Plot slope of reflectivity as a function of wavelength
plot
(lamda_led,Rf0,'r',lamda_led,Rf1,'g',lamda_led,Rf2,'b',lamda_led,Rf3,'c',lamda_led,Rf4,'m',lamda_led,Rf5,'k');
xlabel('Wavelength(LED) (nm)','fontsize',30,'fontweight','b','fontname','Times New Roman');
ylabel('Reflectivity (%)','fontsize',30,'fontweight','b','fontname','Times New Roman');
legend('Rf 0','Rf 1','Rf 2','Rf 3','Rf 4','Rf 5');
set(gca,'XTick',580:5:610,'fontsize',30,'fontweight','b','fontname','Times New Roman');
xlim([580 610]);

%Calculate slope of reflectivity by using dR/dlamda
m0 = diff(Rf0)./diff(lamda_led);
m1 = diff(Rf1)./diff(lamda_led);
m2 = diff(Rf2)./diff(lamda_led);
m3 = diff(Rf3)./diff(lamda_led);
m4 = diff(Rf4)./diff(lamda_led);
m5 = diff(Rf5)./diff(lamda_led);

%Obtain new wavelength range for slope of reflectivity data
lamda_led1 = ones(2,1);
for i=1:1:2
    lamda_led1(i)= lamda_led(i);
end

%Plot slope of reflectivity as a function of wavelength
plot(lamda_led1,m0,'r');
hold on
plot(lamda_led1,m1,'g');
plot(lamda_led1,m2,'b');
plot(lamda_led1,m3,'c');
plot(lamda_led1,m4,'m');
plot(lamda_led1,m5,'y');
hold off

%Select an important wavelength to plot
wl_pointer = 2;
%WL_pointer = 1 for 588 nm; WL_pointer = 2 for 593 nm

%Obtain slope of reflectivity values of diferent pieces of fat at the
%selected wavelength
m_fat(1) = m0(wl_pointer);
m_fat(2) = m1(wl_pointer);
m_fat(3) = m2(wl_pointer);
m_fat(4) = m3(wl_pointer);
m_fat(5) = m4(wl_pointer);
m_fat(6) = m5(wl_pointer);

%Create a matrix of different number of fat pices
fat(1)= 0;
fat(2)= 1;
fat(3)= 2;

```

```

fat(4)= 3;
fat(5)= 4;
fat(6)= 5;

%Linear regression analysis of slope of reflectivity and number of fat
%pieces
stats = regstats(m_fat,fat,'linear');
yhat = stats.yhat;
strrsqr = num2str(stats.rsquare);

%Plot slope of reflectivity as a function of number of fat pieces along
%with linear regression line plot
plot(fat,m_fat,'o',fat,yhat,'--k');
xlabel('Number of Fat Pcs.','fontsize',30,'fontweight','b','fontname','Times
New Roman');
ylabel('Slope of
Reflectivity','fontsize',30,'fontweight','b','fontname','Times New Roman');
legend('Slope of Reflectivity at 593 nm (LED)');
set(gca,'XTick',-1:1:6,'fontsize',30,'fontweight','b','fontname','Times New
Roman');
text(2,m_fat(2),['\bf\fontsize{30}\fontname{Times New Roman} R^2 = '
strrsqr],'HorizontalAlignment','left');
xlim([-1 6]);
ylim([0.3 0.8]);
%End of program

```

## Appendix C: Programs for Image Processing and Spectrum Data Calculation

```
%%%%%%%%%% VIS Spectroscopy data sorting and normalization%%%%%%%%%%

clear;
clc;

%Acquire VIS reflectance data from Excel files
Exl_FileName = 'Data Collection_111NV1.xlsx';
Exl_FileName1 = 'Data Collection_111NV3.xlsx';
sampleID = '111NV';
str_Range = '3';
counter_Range = 2;
for F1 = 1:1:4
    for F3 = 1:1:3
        for F2 = 1:1:4
            Exl_FileName(17) = num2str(F1);
            Exl_FileName(18) = num2str(F2);
            Exl_FileName(19) = num2str(F3);
            Exl_FileName1(17) = num2str(F1);
            Exl_FileName1(18) = num2str(F2);
            Exl_FileName1(19) = num2str(F3);
            sampleID = cellstr(Exl_FileName1(17:20));
            counter_Range = counter_Range+1;
            str_Range = num2str(counter_Range);

lamda = xlsread('Data Collection_111NV1.xlsx', 1, 'a422:a3294');

int_p1 = xlsread(Exl_FileName, 1, 'i422:i3294');
int_p3 = xlsread(Exl_FileName1, 1, 'i422:i3294');

int_wp1 = xlsread(Exl_FileName, 1, 'f422:f3294');
int_wp3 = xlsread(Exl_FileName1, 1, 'f422:f3294');

int_dp1 = xlsread(Exl_FileName, 1, 'b422:b3294');
int_dp3 = xlsread(Exl_FileName1, 1, 'b422:b3294');

%Calculate reflectivity and apply smoothing
reflvt_p1 = ((int_p1)./(int_wp1));
reflvt_p1s = smooth(reflvt_p1,50);

reflvt_p3 = ((int_p3)./(int_wp3));
reflvt_p3s = smooth(reflvt_p3,50);

%Calculate average reflectivity of different position readings
avg_reflvt = (reflvt_p1s+reflvt_p3s)/2;

%Store reflectivity data along with wavelength and sample ID to Excel file
xlswrite('VIS.xlsx', transpose(lamda), 1, 'B2');
```

```
xlswrite('VIS.xlsx', transpose(avg_reflvt), 1, ['B' str_Range]);  
xlswrite('VIS.xlsx', sampleID, 1, ['A' str_Range]);  
  
    end  
end  
end  
%End of program
```

```
%%%%%%%%% NIR spectroscopy data sorting and normalization%%%%%%%%%
```

```
clear;  
clc;
```

```
%Acquire NIR reflectance data from Excel files
```

```
Exl_FileName1 = '311NN1.CSV';  
Exl_FileName2 = '311NN3.CSV';  
Exl_FileNameew = '311NNW.CSV';  
str_Range = '3';  
counter_Range = 2;  
for F3 = 1:1:3  
    for F2 = 1:1:4  
        Exl_FileName1(2) = num2str(F2);  
        Exl_FileName1(3) = num2str(F3);  
        Exl_FileName2(2) = num2str(F2);  
        Exl_FileName2(3) = num2str(F3);  
        Exl_FileNameew(2) = num2str(F2);  
        Exl_FileNameew(3) = num2str(F3);  
        counter_Range = counter_Range+1;  
        str_Range = num2str(counter_Range);  
        sampleID = cellstr(Exl_FileName1(1:4));
```

```
lamda = xlsread(Exl_FileName1, 1, 'A3033:A10833');
```

```
int_1 = xlsread(Exl_FileName1, 1, 'B3033:B10833');  
int_2 = xlsread(Exl_FileName2, 1, 'B3033:B10833');
```

```
int_w = xlsread(Exl_FileNameew, 1, 'B3033:B10833');  
int_d = xlsread('Dark Current.CSV', 1, 'B3033:B10833');
```

```
%Reduce spectrum resolution to 1nm from 0.1nm
```

```
m_lamda=ones(760,1);  
for i= 0:1:759  
    m_lamda(i+1,1)= lamda((i*10)+1,1);  
end
```

```
m1=ones(760,1);  
for i= 0:1:759  
    m1(i+1,1)= int_1((i*10)+1,1);  
end
```

```
m2=ones(760,1);  
for i= 0:1:759  
    m2(i+1,1)= int_2((i*10)+1,1);  
end
```

```
m_w=ones(760,1);  
for i= 0:1:759  
    m_w(i+1,1)= int_w((i*10)+1,1);  
end
```

```
m_d=ones(760,1);  
for i= 0:1:759  
    m_d(i+1,1)= int_d((i*10)+1,1);
```

```

end

%Calculate reflectivity and apply smoothing
reflvt_1 = (abs((m1-m_d)./(m_w-m_d)));
reflvt_1s = smooth(reflvt_1,11);

reflvt_2 = (abs((m2-m_d)./(m_w-m_d)));
reflvt_2s = smooth(reflvt_2,11);

%Calculate average reflectivity of different position readings
reflvt_avg = (reflvt_1 + reflvt_2)/2;

%Store reflectivity data along with wavelength and sample ID to Excel file
xlswrite('NIR_test5.xlsx', transpose(round(m_lamda)), 1, 'B2');
xlswrite('NIR_test5.xlsx', transpose(reflvt_avg), 1, ['B' str_Range]);
xlswrite('NIR_test5.xlsx', sampleID, 1, ['A' str_Range]);

    end
end
%End of program

```

```

%%%%%%%%%%%%%%%%%%%%%%%%%%%%%%%%%%%%%%%%%%%%%%%%%%%%%%%%%%%%%%%%%%%%%%%% Image Processing%%%%%%%%%%%%%%%%%%%%%%%%%%%%%%%%%%%%%%%%%%%%%%%%%%%%%%%%%%%%%%%%%%%%%%%%

clear;
clc;

% Image data acquisition of two different position cropped image
f1 =(imread('343NS1.jpg'));
f3 =(imread('343NS3.jpg'));
figure(1);
subplot 121;
imshow(uint8(f1)); title('original image');
[M1,N1,O1] = size(f1);
figure(2);
subplot 121;
imshow(uint8(f3)); title('original image');
[M3,N3,O3] = size(f3);

%%%%%%%%%%%%%%%%%%%%%%%%%%%%%%%%%%%%%%%%%%%%%%%%%%%%%%%%%%%%%%%%%%%%%%%% Thresholding Image Position 1
g1 (M1,N1,O1)=zeros;
for i=1:1:M1
    for j=1:1:N1
        for k=1:1:O1
            if ((f1(i,j,1)>100) && (f1(i,j,2)<=95) && (f1(i,j,3)<=95))
                g1(i,j,k)=f1(i,j,k);
            end
        end
    end
end
h1=g1(:, :, 1);
figure(1);
subplot 122;
imshow(uint8(g1)); title('RED PIXEL');

%%%%%%%%%%%%%%%%%%%%%%%%%%%%%%%%%%%%%%%%%%%%%%%%%%%%%%%%%%%%%%%%%%%%%%%% Thresholding Image Position 3
g3 (M3,N3,O3)=zeros;
for i=1:1:M3
    for j=1:1:N3
        for k=1:1:O3
            if ((f3(i,j,1)>100) && (f3(i,j,2)<=95) && (f3(i,j,3)<=95))
                g3(i,j,k)=f3(i,j,k);
            end
        end
    end
end
h3=g3(:, :, 1);
figure(2);
subplot 122;
imshow(uint8(g3)); title('RED PIXEL');

%%%%%%%%%%%%%%%%%%%%%%%%%%%%%%%%%%%%%%%%%%%%%%%%%%%%%%%%%%%%%%%%%%%%%%%% Percentage fat area of image position 1
ImArea1 = M1*N1;
FatArea1 = 0;
for i=1:1:M1
    for j=1:1:N1

```

```

        if(h1(i,j)==0)
            FatArea1=FatArea1+1;

        end
    end
end
PrcFatArea1 = (FatArea1/ImArea1)*100;
display (PrcFatArea1);

%%%%%%%%%%%%%%%%%%%%%%%%%%%%%%%%%%%%%%%%%%%%%%%%%%%%%%%%%%%%%%%%%%%%%%%% Percentage fat area of image position 3
ImArea3 = M3*N3;
FatArea3 = 0;
for i=1:1:M3
    for j=1:1:N3
        if(h3(i,j)==0)
            FatArea3=FatArea3+1;

        end
    end
end
PrcFatArea3 = (FatArea3/ImArea3)*100;
display (PrcFatArea3);

%%%%%%%%%%%%%%%%%%%%%%%%%%%%%%%%%%%%%%%%%%%%%%%%%%%%%%%%%%%%%%%%%%%%%%%% Average Percentage fat area of two Image Position
PrcFatAreaAvg = ((FatArea1+FatArea3)/(ImArea1+ImArea3))*100;
display (PrcFatAreaAvg);
% End program

```

## Appendix D: Programs to Calculate L\*a\*b\* Value from Paper Model Sample Image

```
%%%%%%%%%%%%%%%%%%%%%%%%%%%%%%%%%%%%%%%%%%%%%%%%%%%%%%%%%%%%%%%%%%%%%%%% L*a*b* from paper model Image%%%%%%%%%%%%%%%%%%%%%%%%%%%%%%%%%%%%%%%%%%%%%%%%%%%%%%%%%%%%%%%%%%%%%%%%

clear;
clc;

% Image data acquisition from paper model image
f1 =(imread('CL1.jpg'));
figure(1);
subplot 121;
imshow(uint8(f1)); title('original image');

% Paper model image converted to L*a*b* format from RGB format
cform = makecform('srgb2lab');
lab_f1 = applycform(f1,cform);
figure(1);
subplot 122;
imshow(uint8(lab_f1)); title('L*a*b* image');

%%%%%%%%%%%%%%%%%%%%%%%%%%%%%%%%%%%%%%%%%%%%%%%%%%%%%%%%%%%%%%%%%%%%%%%% L*a*b* values dispalyed on the scree
L=lab_f1(228,228,1);
display(L);
A=lab_f1(228,228,2);
display(A);
B=lab_f1(228,228,3);
display(B);

%%%%%%%%%%%%%%%%%%%%%%%%%%%%%%%%%%%%%%%%%%%%%%%%%%%%%%%%%%%%%%%%%%%%%%%% RGB values displayed on the screen

R=f1(228,228,1);
display(R);
G=f1(228,228,2);
display(G);
Br=f1(228,228,3);
display(Br);

%%%%%%%%%%%%%%%%%%%%%%%%%%%%%%%%%%%%%%%%%%%%%%%%%%%%%%%%%%%%%%%%%%%%%%%% hsv values displayed on the screen
hsv_image = rgb2hsv(f1);
h=hsv_image(228,228,1);
display(h);
s=hsv_image(228,228,2);
display(s);
v=hsv_image(228,228,3);
display(v);
% End program
```

## Appendix E: Programs for Image Processing

```
%%%%%%%% Image processing of marked image%%%%%%%%

clear;
clc;

% Image data acquisition
f1 = (imread('111YG.jpg'));
[M1,N1,O1] = size(f1);

% Crop image
xx = round(15*N1/100);
yy = round(20*M1/100);
xt = round(N1-2*xx);
yt = round(M1-2*yy);
f1 = imcrop(f1,[xx yy xt yt]);
figure(1);
subplot 121;
imshow(uint8(f1)); title('original image');
[M1,N1,O1] = size(f1);

% Selecting boundary pixels
h1=ones(M1,N1,O1);
h1=h1*255;
g1 = f1;
for i=1:1:M1
    for j=1:1:N1
        for k=1:1:O1
            if ((f1(i,j,1)<=20) && (f1(i,j,2)<=20) && (f1(i,j,3)<=20))
                g1(i,j,1)=29;
                g1(i,j,2)=244;
                g1(i,j,3)=23;
                h1(i,j,k)=g1(i,j,k);
            end
        end
    end
end
figure(1);
subplot 122;
imshow(uint8(g1)); title('identified black circle');

%Select region of interest (ROI)
ROI = rgb2gray(uint8(h1));
threshold = graythresh(ROI);
ROI = im2bw(ROI,threshold);
ROI = ~ROI;
figure(2);
subplot 121;
imshow(ROI); title('ROI BW image');
```

```

ROI = bwareaopen(ROI,3000);
I1 = ROI;
ROI = imfill(ROI,'holes');
I2 = ~ROI;
ROI = ~(I1+I2);
ROI = bwareaopen(ROI,10^4);
figure(2);
subplot 122;
imshow(ROI); title('ROI');

% Crop region of interest (ROI)
b1 = f1;
for i=1:1:M1
    for j=1:1:N1
        for k=1:1:O1
            if((ROI(i,j)<1))
                b1(i,j,1)=0;
                b1(i,j,2)=0;
                b1(i,j,3)=0;
            end
        end
    end
end
figure(3);
subplot 121;
imshow(uint8(b1)); title('Cropped Image');

% Thresholding of ROI
c1(M1,N1,O1)=zeros;
g2=b1;
b2=b1;
Objectarea = 0;
Redpixel = 0;

for i=1:1:M1
    for j=1:1:N1
        for k=1:1:O1

if(((b1(i,j,1)>0)&&(b1(i,j,2)>0)&&(b1(i,j,3)>0))&&((b1(i,j,1)<225)&&(b1(i,j,2)
)<215)&&(b1(i,j,3)<200)))
            Objectarea = Objectarea+1;

if(((b1(i,j,1)<130)&&(b1(i,j,2)<100)&&(b1(i,j,3)<90))||((b1(i,j,1)>=130)&&(b1
(i,j,2)<110)&&(b1(i,j,3)<100)))
            c1(i,j,k)=b1(i,j,k);
            Redpixel = Redpixel+1;
            b2(i,j,1)=64;
            b2(i,j,2)=0;
            b2(i,j,3)=128;
        else
            g2(i,j,1)=0;
            g2(i,j,2)=128;
            g2(i,j,3)=128;
        end
    end
end
end

```

```

    end
end
figure(3);
subplot 122;
imshow(uint8(c1)); title('RED PIXEL');

figure(4);
subplot 121;
imshow(uint8(g2)); title('FAT REGION');

figure(4);
subplot 122;
imshow(uint8(b2)); title('MUSCLE REGION');

% Percentage fat area of ROI calculation
MuscleArea = Redpixel;
FatArea = Objectarea-Redpixel;
PrcFatArea = (FatArea/MuscleArea)*100;
display (PrcFatArea);
% End program

```

```

%%%%%%%% Image processing of whole sample image%%%%%%%%

clear;
clc;

% Image data acquisition
f1 =(imread('212YG.jpg'));%311, 112
[M1,N1,O1] = size(f1);

% Crop image
xx = round(15*N1/100);
yy = round(20*M1/100);
xt = round(N1-2*xx);
yt = round(M1-2*yy);
f1 = imcrop(f1,[xx yy xt yt]);
figure(1);
subplot 121;
imshow(uint8(f1)); title('original image');
[M1,N1,O1] = size(f1);
Ff1 = round(M1*N1/1500);
Ff2 = round(M1*N1/150);

% Selecting sample boundary pixels
T1(M1,N1,1)=zeros;
for i=1:1:M1
    for j=1:1:N1
        for k=1:1:O1
            if((f1(i,j,1)>120)&&(f1(i,j,2)<=140)&&(f1(i,j,3)<=130))
%311>>R>129 others >120
                T1(i,j,1)=1;
            end
            if((f1(i,j,1)>90)&&(f1(i,j,2)<70)&&(f1(i,j,3)<70))
                T1(i,j,1)=1;
            end
        end
    end
end
end
T1 = logical(T1);

% Filter image
T1 = bwareaopen(T1,Ff1);
T1 = imfill(T1,'holes');
T1 = bwareaopen(T1,Ff2);
T1 = imclearborder(T1, 6);
T1 = bwareaopen(T1,Ff2);
seD = strel('diamond',1);
T1 = imerode(T1,seD);
T1 = imerode(T1,seD);
T1 = imerode(T1,seD);
T1 = bwareaopen(T1,Ff2);
figure(4);
subplot 121;
imshow(T1); title('BW image');

% Sample isolation
u1 = f1;

```

```

for i=1:1:M1
    for j=1:1:N1
        for k=1:1:O1
            if((T1(i,j)<1))
                u1(i,j,1)=0;
                u1(i,j,2)=0;
                u1(i,j,3)=0;
            end
        end
    end
end
end
figure(4);
subplot 122;
imshow(uint8(u1)); title('separated Image');

% Thresholding of the selected sample image region
c1(M1,N1,O1)=zeros;
g1=u1;
b1=u1;
Objectarea = 0;
Redpixel = 0;
for i=1:1:M1
    for j=1:1:N1
        for k=1:1:O1

if(((u1(i,j,1)>0)&&(u1(i,j,2)>0)&&(u1(i,j,3)>0))&&((u1(i,j,1)<225)&&(u1(i,j,2)
)<215)&&(u1(i,j,3)<200)))
                Objectarea = Objectarea+1;

if(((u1(i,j,1)<130)&&(u1(i,j,2)<100)&&(u1(i,j,3)<90))||((u1(i,j,1)>=130)&&(u1
(i,j,2)<110)&&(u1(i,j,3)<100)))
                c1(i,j,k)=u1(i,j,k);
                Redpixel = Redpixel+1;
                b1(i,j,1)=64;
                b1(i,j,2)=0;
                b1(i,j,3)=128;
            else
                g1(i,j,1)=0;
                g1(i,j,2)=128;
                g1(i,j,3)=128;
            end
        end
    end
end
end
figure(1);
subplot 122;
imshow(uint8(c1)); title('RED PIXEL');

figure(5);
subplot 121;
imshow(uint8(g1)); title('FAT REGION');

figure(5);
subplot 122;
imshow(uint8(b1)); title('MUSCLE REGION');

```

```
% Percentage fat area calculation
MuscleArea = Redpixel;
FatArea = Objectarea-Redpixel;
PrcFatArea = (FatArea/MuscleArea)*100;
display (PrcFatArea);
% End program
```

## References

- Aalhus, J. L., Janz, J. A. M., Tong, A. K. W., Jones, S. D. M., and Robertson, W. M. 2001. The influence of chilling rate and fat cover on beef quality. *Canadian Journal of Animal Science* 81: 321–330.
- Aalhus, J. L., Jones, S., Tong, A., Jeremiah, L., Robertson, W., and Gibson, L. 1992. The combined effects of time on feed, electrical stimulation and aging on beef quality. *Canadian Journal of Animal Science* 72: 525-535.
- AMSA (American Meat Science Association). 1995. Research guidelines for cookery sensory evaluation and instrumental tenderness measurements of meat. American Meat Science Association and National Livestock Meat Board, Chicago, IL. Cong.
- Anderson, S. 2007. Determination of fat, moisture, and protein in meat and meat products by using the FOSS FoodScan™ near-infrared spectrophotometer with FOSS artificial neural network calibration model and associated database: collaborative study. *Journal of AOAC International* 90: 1073–1083.
- Andrés, S., Silva, A., Soares-Pereira, A. L., Martins, C., Bruno-Soares, A. M., and Murray, I. 2008. The use of visible and near infrared reflectance spectroscopy to predict beef M. longissimus thoracis et lumborum quality attributes. *Meat Science* 78: 217-224.
- Andrés, S., Murray, I., Navajas, E. A., Fisher, A. V., Lambe, N. R., and Bunger, L. 2007. Prediction of sensory characteristics of lamb meat samples by near infrared reflectance spectroscopy. *Meat Science* 76: 509–516.
- Anonymous. 2003. Crude Fat Determination using the Goldfish Extraction Apparatus. AFNS Standard/safe Operating Procedure. Revised September 2003.
- Anonymous. 1997. Goldfish Fat Extraction Apparatus: Model 35001 Instruction Manual. Labconco Corp. 35181 Revision I. 1997.
- AOAC. 1995. AOAC Official Method 960.39. Fat (crude) or ether extract in meat. Final Action, AOAC Official Methods of Analysis 1995, Association of Official Analytical Chemists, Arlington, VA.
- Asplund, K. M., Schenkman, K. A., Ciesielski, W. A., and Lorilee S. L. Arakaki, L. S. L. 2014. Photon path depth in tissue phantoms: a comparison of visible and near-infrared (NIR) wavelengths. *SPIE Proceedings* 8945: 89450D-10.
- Barlocco, N., Vadell, A., Ballesteros, F., Galiotta, G., and Cozzolino, D. 2006. Predicting intramuscular fat, moisture and Warner–Bratzler shear force in pork muscle using near infrared reflectance spectroscopy. *Animal Science* 82: 111–116.

- Bratzler, L. J. 1958. Fifty years of progress in meat research. *Journal of Animal Science* 17:1079-1087.
- Brooks, J. 1929. Postmortem formation of methemoglobin in red muscle. *Biochem. J.* 23: 1391-1400.
- Brooks, J. 1935. The oxidation of haemoglobin to methaemoglobin by oxygen. II. The relation between the rate of oxidation and the partial pressure of oxygen. *Proceedings Royal Society, London, Series.B* 118: 560–577.
- Bruce, H. L., and Ball, R. O. 1990. Postmortem interactions of muscle temperature pH and extension on beef quality. *Journal of Animal Science* 68: 4167-4175.
- Bruce, H. L., Scott, J.R., and Thompson, J. M. 2001. Application of an exponential model to early postmortem bovine muscle pH decline. *Meat Science* 58: 39-44.
- Bruce, H. L., Stark, J. L., & Beilken, S. L. 2004. The effects of finishing diet and postmortem ageing on the eating quality of the *M. longissimus thoracis* of electrically stimulated Brahman steer carcasses. *Meat Science* 67: 261-268.
- Byrne, C. E., Downey, G., Troy, D. J., and Buckley, D. J. 1998. Non-destructive prediction of selected quality attributes of beef by near-infrared reflectance spectroscopy between 750 and 1098 nm. *Meat Science* 49: 399–409.
- Chan, D. E., Walker, P. N., and Mills, E. W. 2002. Prediction of pork quality characteristics using visible and near-infrared spectroscopy. *Transactions of ASAE* 45: 1519-1527.
- Clerjon, S., Peyrin, F., and Lepetit, J. 2011. Frontal UV–visible fluorescence polarization measurement for bovine meat ageing assessment. *Meat Science* 88: 28-35.
- Cluff, K., Naganathan, G. K., Subbiah, J., Lu, R., Calkins, C. R., and Samal, A. 2008. Optical scattering in beef steaks to predict tenderness using hyperspectral imaging in the VIS-NIR region. *Sensing and Instrumentation for Food Quality* 2: 189-196.
- Degner, M., Damaschke, N., Ewald, H. and Lewis, E. 2010 . High resolution LED-spectroscopy for sensor application in harsh environment. *IEEE*. ISBN 978-1-4244-2833-5.
- Degner, M. and Ewald, H. 2012. LED-spectroscopy based on multi quantum well emitter. *IEEE*. ISBN 978-1-4673-0335-4.
- De Marchi, M., Berzaghi, P., Boukha, A., Mirisola, M., & Gallo, L. 2007. Use of near infrared spectroscopy for assessment of beef quality traits. *Italian Journal of Animal Science* 6: 421–423.
- De Marchi, M. 2013. On-line prediction of beef quality traits using near infrared spectroscopy. *Meat Science* 94: 455-460.

- Derington, A. J., Brooks, J. C., Garmyn, A. J., Thompson, L. D., Wester, D. B., and Miller M. F. 2011. Relationships of slice shear force and Warner-Bratzler shear force of beef strip loin steaks as related to the tenderness gradient of the strip loin. *Meat Science* 88: 203-208.
- Dian, P. H. M., Andueza, D., Jestin, M., Prado, I. N., and Prache, S. 2008. Comparison of visible and near infrared reflectance spectroscopy to discriminate between pastured and concentrate-fed lamb carcasses. *Meat Science* 80: 1157-1164.
- Downey, G., and Beauchêne, D. 1997. Discrimination between fresh and frozen-thawed beef m. longissimus dorsi by combined visible-near infrared reflectance spectroscopy: A feasibility study. *Meat Science* 45: 353-363.
- Dransfield, E. 1994. Optimisation of tenderisation, ageing and tenderness. *Meat Science* 36: 105-121.
- Ducastaing, A., Valin, C., Schollmeyer, J., and Cross, R. 1985. Effects of electrical stimulation on post-mortem changes in the activities of two calcium dependent neutral proteinases and their inhibitor in beef muscle. *Meat Science* 15: 193-202.
- Etherington, D. J. 1984. The contribution of proteolytic enzymes to postmortem changes in muscle. *Journal of Animal Science* 59: 1644-1650.
- Fowler, S. M., Schmidt, H., van de Ven, R., Wynn, P., & Hopkins, D. L. 2014. Predicting tenderness of fresh ovine semimembranosus using Raman spectroscopy. *Meat Science* 97: 597-601.
- George, A. R., Bendall, J. R., and Jones, R. C. D. 1980. The tenderising effect of electrical stimulation of beef carcasses. *Meat Science* 4: 51-68.
- George, P., and Stratmann, C. J. 1952. The oxidation of myoglobin to metmyoglobin by oxygen. *Biochem J.* 51: 103.
- Hildrum, K. I., Nilsen, B. N., Mielnik, M., and Næs, T. 1994. Prediction of sensory characteristics of beef by near-infrared spectroscopy. *Meat Science* 38: 67-80.
- Iwamoto, M., Norris, K. H., and Kimura, S. 1981. Rapid prediction of chemical compositions for wheat, soybean, pork and russet potatoes by near infrared spectrophotometric analysis. *Nippon Shokuhin Kogyo Gakkaishi.* 28: 85.
- Jeremiah, L. E., Martin, A. H., and Murray, A. C. 1985. The effects of various post-mortem treatments on certain physical and sensory properties of three different bovine muscles. *Meat Science* 12: 155-176.
- Kandaswamy, J., Apple, J. K., and Bajwa, S. G. 2005. Ability of Near-Infrared Reflectance Spectroscopy to Predict Fat, Cholesterol, and Caloric Content of Fresh and Cooked Ground Beef. Arkansas Animal Science Department Report 2005.

- Khatri, M., Phung, V. T., Isaksson, T., Sørheim, O., Slinde, E., and Egelanddal, B. 2012. New procedure for improving precision and accuracy of instrumental color measurements of beef. *Meat Science* 91: 223-231.
- Kruggel, W. G., Field, R. A., Riley, M. L., Radloff, H. D., and Horton, K. M. 1981. Near-infrared reflectance determination of fat, protein, and moisture in fresh meat. *Journal of the Association of Official Analytical Chemists* 64: 692.
- Krzywicki, K. 1979. Assessment of relative content of myoglobin, oxymyoglobin and metmyoglobin at the surface of beef. *Meat Science* 3: 1-10.
- Lanza, E. 1983. Determination of moisture, protein, fat, and calories in raw pork and beef by near infrared spectroscopy. *Journal of Food Science* 48: 471-474.
- Lawrie, R. A. 1964. *Meat science* (First edition). Pergamon, Oxford, 272.
- Lawrie, R. A. 1985. *Meat Science*. Pergamon Press, Oxford.
- Leroy, B., Lambotte, S., Dotreppe, O., Lecocq, H., Istasse, L., and Clinquart, A. 2003. Prediction of technological and organoleptic properties of beef *Longissimus thoracis* from near-infrared reflectance and transmission spectra. *Meat Science* 66: 45-54.
- Liu, Y., Barton, F. E., Lyon, B. G., Windham, W. R., and Lyon, C. E. 2004. Two-dimensional correlation analysis of visible/near-infrared spectral intensity variations of chicken breasts with various chilled and frozen storages. *J. Agric. Food Chem.* 52: 505-510.
- Liu, Y., Lyon, B. G., Windham, W. R., Realini, C. E., Pringle, T. D. D., and Duckett, S. 2003. Prediction of color, texture, and sensory characteristics of beef steaks by visible and near infrared reflectance spectroscopy. A feasibility study. *Meat Science* 65: 1107-1115.
- Livingston, D. J., and Brown, W. D. 1982. The chemistry of myoglobin and its reactions. *Food Technology* 35: 244-252.
- Locker, R. H., and Hagyard, C. J. 1963. A cold shortening effect in beef muscles. *Journal of the Science of Food and Agriculture* 14: 787-793.
- Luc, C., Clerjon, S., Peyrin, F., Lepetit, J., and Culioli, J. 2008. Sarcomere length determination using front-face fluorescence polarization. *Meat Science* 80: 814- 818.
- Lu, j., Tan, J., Shatadal, P., and Gerrard, D. E. 2000. Evaluation of pork color by using computer vision. *Meat Science* 56: 57-60.
- Maltin, C., Balcerzak, D., Tilley, R., and Delday, M. 2003. Determinants of meat quality: tenderness. *Proceedings of the Nutrition Society*, 62, 337-347.

- Mancini, R.A., and Hunt, M.C. 2005. Current research in meat color (Review). *Meat Science* 71: 100–121.
- Martens, H., and Næs, T. 1989. *Multivariate calibration*. Chichester, United Kingdom: John Wiley and Sons.
- Mitsumoto, M., Maeda, S., Mitsuhashi, T., and Ozawa, S. 1991. Near-infrared spectroscopy determination of physical and chemical characteristics in beef cuts. *Journal of Food Science* 56: 1493-1496.
- Moore, C. B., Bass, P. D., Green, M. D., Chapman, P. L., O'Connor, M. E., Yates, L. D., Scanga, J. A., Tatum, J. D., Smith, G. C., and Belk, K. E. 2010. Establishing an appropriate mode of comparison for measuring the performance of marbling score output from video image analysis beef carcass grading systems. *Journal of Animal Science* 88: 2464-2475.
- Morgan, J. B., Savell, J. W., Hale, D. S., Miller, R. K., Griffin, D. B., Cross, H. R., and Shackelford, S. D. 1991. National beef tenderness survey. *J. Anim. Sci.* 69: 3274–3283.
- Osborne, B. G. Principles and practice of near infra-red (NIR) reflectance analysis. 1981. *J. Food Technol.* 16:13-19.
- Osborne, B. G., Fearn, T., and Hindle, P. H. 1993. *Practical NIR Spectroscopy*. Longman Scientific & Technical, Harlow, UK.
- O'Sullivan, M. G., Byrne, D. V., Martens, H., Gidskehaug, G. H., Andersen, H. J., and Martens, M. 2003. Evaluation of pork color: Prediction of visual sensory quality of meat from instrumental and computer vision methods of color analysis. *Meat Science* 65: 909–918.
- Park, B., Chen, Y. R., Hruschka, W. R., Shackelford, S. D., and Koohmaraie, M. 1998a. Near-infrared reflectance analysis for predicting beef longissimus tenderness. *J. Anim. Sci.* 76: 2115-2120.
- Park, B., and Chen, Y. R. 1998b. Beef tenderness prediction by near-infrared reflectance spectroscopy. In *Proceedings SENSORAL 98: International Workshop on Sensing Quality of Agricultural Products*. Montpellier–Narbonne, France. 2: 485–495.
- Park, B., Chen, Y. R., Hruschka, W. R., Shackelford, S. D., and Koohmaraie, M. 2001. Principal component regression of near-infrared reflectance spectra for beef tenderness prediction. *American Society of Agricultural Engineers* 44: 609-615.
- Prevolnik, M., Candek-Potokar, M., and Skorjanc, D. 2004. Ability of NIR spectroscopy to predict meat chemical composition and quality – a review. *Czech Journal of Animal Science* 49: 500–510.

- Prevolnik, M., Čandek-Potokar, M., Škorjanc, D., Velikonja-Bolta, Š., Škrlep, M., Žnidaršič, T., and Babnik D. 2005. Predicting intramuscular fat content in pork and beef by near infrared spectroscopy. *Journal of Near Infrared Spectroscopy* 13: 77–85.
- Price, D. M., Hilton, G. G., VanOverbeke, D. L., and Morgan, J. B. 2008. Using the nearinfrared system to sort various beef middle and end muscle cuts into tenderness categories. *Journal of Animal Science* 86: 413-418.
- Price, J. P., and Schweigert, B. S. 1989. *The science of meat and meat products* third edition. Food & Nutrition Press, Inc. Westport, Connecticut 06880 USA, 200-201.
- Prieto, N., Andres, S., Giraldez, F. J., Mantecon, A. R., and Lavin, P. 2008. Ability of near infrared reflectance spectroscopy (NIRS) to estimate physical parameters of adult steers (oxen) and young cattle meat samples. *Meat Science*, 79, 692–699.
- Prieto, N., López-Campos, Ó., Aalhus, J.L., Dugan, M.E.R., Juárez, M., and Uttaro, B. 2014. Use of near infrared spectroscopy for estimating meat chemical composition, quality traits and fatty acid content from cattle fed sunflower or flaxseed. *Meat Science* 98: 279-288.
- Prieto, N., Roehe, R., Lavín, P., Batten, G., and Andrés, S. 2009. Application of near infrared reflectance spectroscopy to predict meat and meat products quality: a review. *Meat Science* 83: 175-186.
- Ripoll, G., Albertí, P., Panea, B., Olleta, J. L., and Sañudo, C. 2008. Near-infrared reflectance spectroscopy for predicting chemical, instrumental and sensory quality of beef. *Meat Science* 80: 697-702.
- Rodbotten, R., Mevik, B. H., and Hildrum, K. I. 2001. Prediction and classification of tenderness in beef from non-invasive diode array detected NIR spectra. *Journal of Near Infrared Spectroscopy* 9: 199–210.
- Rødbotten, R., Nilsen, B. N., and Hildrum, K. I. 2000. Prediction of beef quality attributes from early post mortem near infrared reflectance spectra. *Food Chemistry* 69: 427 – 436.
- Rosenvold, K., Micklander, E., Hansen P. W., Burling-Claridge, R., Challies, M., Devine, C., and North, M. 2009. Temporal, biochemical and structural factors that influence beef quality measurement using near infrared spectroscopy. *Meat Science* 82: 379-388.
- Rust, S. R., Price, D. M., Subbiah, J., Kranzler, G., Hilton, G. G., Vanoverbeke, D. L., and Morgan, J. B. 2008. Predicting beef tenderness using near-infrared spectroscopy. *Journal of Animal Science* 86: 211-219.
- Savell, J. W., and H. R. Cross. 1992. Value-based marketing: Current status. In *Proceedings: Annual Reciprocal Meat Conference of the American Meat Science Association*, 117–120.

- Sengupta, S. K., Farnham, J. M. and Whitten, J. E. 2005. A Simple Low-Cost Lock-In Amplifier for the Laboratory. *Journal of Chemical Education* 82: 9.
- Shackelford, S. D., Wheeler, T. L., King, D. A., and Koohmaraie, M. 2011. Field testing of a system for online classification of beef carcasses for longissimus tenderness using visible and near-infrared reflectance spectroscopy. *Journal of Animal Science* 90: 978-988.
- Shackelford, S. D., Wheeler, T. L., and Koohmarie, M. 2004. Development of optimal protocol for visible and near-infrared reflectance spectroscopic evaluation of meat quality. *Meat Science* 68: 371-381.
- Sierra, V., Aldai, N., Castro, P., Osoro, K., Coto-Montes, A., and Oliván, M. 2008. Prediction of the fatty acid composition of beef by near infrared transmittance spectroscopy. *Meat Science* 78: 248-255.
- Su, H., Sha, K. Zhang, L. Zhang, Q., Xu, Y., Zhang, R., Li, H., and Sun, B. 2014. Development of near infrared reflectance spectroscopy to predict chemical composition with a wide range of variability in beef. *Meat Science* 98: 110-114.
- Swatland, H. J. 1989. A review of meat spectrophotometry (300 to 800 nm). *Canadian Institute of Food Science and Technology Journal* 22: 390-402.
- Swatland, H. J. 2012. Optical properties of meat. *American Meat Science Association, 65th Annual Reciprocal Meat Conference*, 1-7.
- Togersen, G., Arnesen, J. F., Nielsen, B. N., and Hildrum, K. I. 2003. On-line prediction of chemical composition of semi-frozen ground beef by non-invasive NIR spectroscopy. *Meat Science* 63: 515-523.
- Venel, C., Mullen, A. M., Downey, G., and Troy, J. D. 2001. Prediction of tenderness and other quality attributes of beef by near infrared reflectance spectroscopy between 750 and 1100 nm. *Journal of Near Infrared Spectroscopy* 9: 185-198.
- Voisey, P. W. 1976. Engineering assessment and critique of instruments used for meat tenderness evaluation. *Journal of Texture Studies* 7: 11-48.
- Vote, D. J., Belk, K. E., Tatum, J. D., Scanga, J. A., and Smith, G. C. 2003. Online prediction of beef tenderness using a computer vision system equipped with a BeefCam module. *Journal of Animal Science* 81: 457-465.
- Wallace, W. J., Houtchens, R. A., Maxwell, J. C., and Caughey, S. 1982. Mechanism of autoxidation for hemoglobins and myoglobins. *Biochem. J.* 257: 4966-4977.
- Wheeler, T. L., Vote, D., Leheska, J. M., Shackelford, S. D., Belk, K. E., Wulf, D. M., Gwartney, B. L., and Koohmaraie, M. 2002. The efficacy of three objective systems for

- identifying beef cuts that can be guaranteed tender. *Journal of Animal Science* 80: 3315-3327.
- Wheeler, T. L., Shackelford, S. D., and Koohmaraie, M. 2000. Variation in proteolysis, sarcomere length, collagen content, and tenderness among major pork muscles. *Journal of Animal Science* 78: 958–965.
- Wulf, D. M., and Page, J. K. 2000. Using measurements of muscle color, pH, and electrical impedance to augment the current USDA beef quality grading standards and improve the accuracy and precision of sorting carcasses into palatability groups. *Journal of Animal Science* 78: 2595-2607.
- Wyle, A. M., Vote, D. J., Roeber, D. L., Cannell, R. C., Belk, K. E., Scanga, J. A., Goldberg, M., Tatum, J. D., and Smith, G. C. 2003. Effectiveness of the SmartMV prototype BeefCam System to sort beef carcasses into expected palatability groups. *Journal of Animal Science* 81: 441-448.
- Xia, J. J., Berg, E. P., Lee, J. W., and Yao, G. 2007. Characterizing beef muscles with optical scattering and absorption coefficients in VIS-NIR region. *Meat Science* 75: 78-83.
- Yancey, J. W. S., Apple, J. K., Meullenet, J.-F., and Sawyer, J. T. 2010. Consumer responses for tenderness and overall impression can be predicted by visible and near-infrared spectroscopy, Meullenet-Owens razor shear, and Warner-Bratzler shear force. *Meat Science* 85: 487-492.
- Zamarripa, J. A. P. 2014. Implications of Canada Grade and Early Post-Mortem Carcass Management on Beef Quality. Master of Science Thesis, University of Alberta, 1-191.